

Microbubble Formulations for Photoacoustic Imaging and Sonothrombolysis Applications

A Dissertation

Presented to
the faculty of the School of Engineering and Applied Science
University of Virginia

in partial fulfillment
of the requirements for the degree

Doctor of Philosophy

by

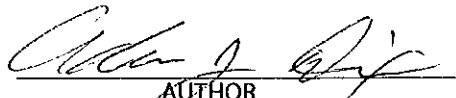
Adam Joseph Dixon

December

2016

APPROVAL SHEET

The dissertation
is submitted in partial fulfillment of the requirements
for the degree of
Doctor of Philosophy


AUTHOR

The dissertation has been read and approved by the examining committee:

John A. Hossack, Ph.D.

Advisor

Richard J. Price, Ph.D.

Alexander Klibanov, Ph.D.

Song Hu, Ph.D.

Coleen A. McNamara, M.D.

Accepted for the School of Engineering and Applied Science:



Craig H. Benson, Dean, School of Engineering and Applied Science

December
2016

Abstract

Microbubbles provide a versatile platform for both ultrasound-mediated therapy and imaging. This dissertation outlines the design and characterization of two novel microbubble formulations used in separate photoacoustic imaging and sonothrombolysis applications.

Microbubbles as Photoacoustic Imaging Contrast Agents

Photoacoustic imaging is a noninvasive imaging technique that provides high contrast images of optical absorption deep within living tissue. Dual-modality ultrasound and photoacoustic imaging can simultaneously evaluate anatomical tissue properties with ultrasound and molecular properties with photoacoustics. The two modalities utilize the same ultrasound receive instrumentation, which provides inherently co-registered images and permits the development of contrast agents that respond to both light and sound for molecular imaging applications. In this dissertation, the design, synthesis, and imaging performance of light-absorbing microbubbles bearing gold nanorods on their surface was evaluated *in vitro*, *in silico*, and *in vivo*. Two responses to pulsed laser excitation were identified – in response to high laser energy, explosive boiling at the nanoparticle surface resulted in rapid microbubble expansion and high amplitude, non-linear photoacoustic emissions; in response to lower laser energies, photoacoustic emissions scaled linearly with increasing laser fluence, and finite element modeling predicted nanoscale microbubble radius oscillations at the microbubble resonance frequency. Both of these responses may be utilized to separate the photoacoustic signal derived from the light-absorbing microbubble from spurious background tissue signals, thereby increasing the specificity of the imaging technique and enabling novel molecular imaging approaches.

Microfluidic Production of Microbubbles for Sonothrombolysis Applications

Intravenous or catheter-directed administration of recombinant tissue plasminogen activator (rtPA) remains the standard of care for many thrombo-occlusive diseases, including ischemic stroke, deep vein thrombosis, and pulmonary embolism. However, fewer than 5 % of ischemic stroke and deep vein thrombosis patients receive thrombolytic therapy due to strict eligibility criteria and risk of severe bleeding. An alternative approach that has been developed to address the pressing need for improved recanalization techniques is the combination of rtPA with adjuvant ultrasound and microbubbles, a technique known as sonothrombolysis. Sonothrombolysis accelerates recanalization and has been investigated as a means to remove blood clots using lower doses of thrombolytic agents, thereby reducing the risk of severe bleeding and increasing patient eligibility for treatment. In this dissertation, the feasibility of a catheter-directed sonothrombolysis platform was evaluated *in vitro* and *in vivo*. Microbubbles were produced in real-time at the distal end of the catheter by a flow-focusing microfluidic device, and significantly improved thrombolysis rates were observed in both *in vitro* and *in vivo* models. In particular, the potential for a 3.33 ± 2.16 fold rtPA dose reduction was observed in a rat model of ischemic stroke, and neurological deficit scores were also significantly improved following sonothrombolysis treatment. Together, these results suggest catheter-directed sonothrombolysis techniques may accelerate recanalization and permit rtPA dose reduction, thereby addressing two pressing clinical needs.

Acknowledgements

First, I would like to acknowledge Mr. Brian Shin, Mr. Vamsi Meka, Mr. Edwin Lu, Ms. Veronica Chang, Mr. Johnny L. Chen, Mr. John-Marschner Robert Rickel, Dr. Ali H. Dhanaliwala, Dr. Sunil Unnikrishnan, Dr. Shiyang Wang, Dr. Joseph P. Kilroy, and Dr. Bo Ning for their great contributions to this dissertation in terms of microfluidic device studies, animal studies, and photoacoustic studies.

Next, I would like to acknowledge my advisor, Dr. John A. Hossack for providing valuable mentorship, encouragement, and guidance in both my research and career. I would also like to thank Dr. Alexander L. Klibanov and Dr. Song Hu for their invaluable assistance with respect to the microbubble and photoacoustic studies described within this dissertation. Additionally, Dr. Richard J. Price and Dr. Coleen A. McNamara, who served on my dissertation committee, are acknowledged for their time and suggestions in shaping my dissertation.

I would like to also thank all the Hossack lab members, past and present for their support, suggestions, and contributions while I've worked in the lab – Dr. Frank W. Mauldin, Dr. Kevin Owen, Dr. Dan Lin, Mr. Sushanth Govinahallisathyanarayana, Ms. Elizabeth B. Herbst, and Mr. Colton Ladbury.

Last, but most certainly not least, I thank my family for supporting me from the beginning to the end of this dissertation; especially my partner, Kara Fitzgibbon, for her love and selfless support over the past several years.

This dissertation was supported by NIH R01 HL090700, S10 RR027333, and S10 RR025594 grants to the Hossack Lab and NSF Graduate Research Fellowship and Virginia Space Grant Consortium grants to support my research. The content is solely the responsibility of the author and does not necessarily represent the official views of the NIH, NSF, or VSGC.

Table of Contents

ABSTRACT.....	II
ACKNOWLEDGEMENTS.....	V
TABLE OF CONTENTS	VII
LIST OF FIGURES	X
LIST OF TABLES.....	XII
LIST OF EQUATIONS	XIII
LIST OF SOFTWARE	XIV
LIST OF NOMENCLATURE	XV
Mathematical Symbols	xv
Acronyms	xvii
CHAPTER 1. INTRODUCTION	1
1.1 Introduction to microbubbles.....	2
1.2 Photoacoustic imaging and photoacoustic contrast agents	3
1.3 Microbubbles for sonothrombolysis applications.....	5
1.4 Microbubble fabrication techniques	6
PART I: LIGHT ABSORBING MICROBUBBLES FOR PHOTOACOUSTIC IMAGING APPLICATIONS	10
Chapter 2. Investigation of optically absorbing microbubbles for in vitro and in vivo photoacoustic imaging	11
2.1 Abstract.....	11
2.2 Introduction.....	12
2.3 Materials and Methods.....	14
2.4 Results.....	20
2.5 Discussion	30
2.6 Conclusions.....	34
Chapter 3. Finite element modeling of optically absorbing microbubble oscillations in response to nanosecond pulsed laser excitation	36
3.1 Abstract.....	36
3.2 Introduction.....	37
3.3 Materials and Methods.....	38
3.4 Results	43
3.5 Discussion	47
3.6 Conclusions.....	52

PART II: MICROFLUIDIC PRODUCTION OF MICROBUBBLES FOR SONOTHROMBOLYSIS APPLICATIONS	55
Chapter 4. Development of a catheter-dimensioned microfluidic device for intravascular production of microbubbles	56
4.1 Abstract	56
4.2 Introduction	57
4.3 Materials and Methods	59
4.4 Results	62
4.5 Discussion	66
4.6 Conclusions	69
Chapter 5. In vitro sonothrombolysis efficacy of transiently stable microbubbles produced by a microfluidic device	70
5.1 Abstract	70
5.2 Introduction	71
5.3 Materials and Methods	73
5.4 Results	78
5.5 Discussion	84
5.6 Conclusions	89
Chapter 6. In vivo sonothrombolysis efficacy of microbubbles produced by a microfluidic device in a rat model of ischemic stroke	91
6.1 Abstract	91
6.2 Introduction	92
6.3 Materials and Methods	94
6.4 Results	99
6.5 Discussion	106
6.6 Conclusions	110
6.7 Appendix	110
Chapter 7. Conclusions and Future Directions	114
7.1 Conclusions	114
7.2 Future Directions	116
PEER-REVIEWED JOURNAL PUBLICATIONS	118
CONFERENCE ABSTRACTS AND PRESENTATIONS	120
PATENT APPLICATIONS	123
PART III: APPENDIX	125
Chapter A1. Development of an intravascular near-infrared fluorescence catheter with ultrasound guidance and blood attenuation correction	126
A1.1 Abstract	126
A1.2 Introduction	127
A1.3 Materials and Methods	129

A1.4 Results.....	137
A1.5 Discussion	144
A1.6 Conclusions.....	146
Chapter A2. Acoustic activation of phase change perfluorocarbon droplets containing solid mesoporous silica nanoparticles within their liquid cores	148
A2.1 Abstract	148
A2.2 Introduction.....	149
A2.3 Materials and Methods.....	150
A2.4 Results.....	153
A2.5 Discussion and Conclusions.....	156
Chapter A.3 PZFlex and MATLAB Code for AuMB Oscillation Simulations.....	157
REFERENCES.....	167

List of Figures

Figure 2-1: AuNR and AuMB optical absorption during AuMB preparation.....	15
Figure 2-2: Experimental apparatus for acquisition of high-speed camera and photoacoustic data from single AuMBs and AuNRs.....	16
Figure 2-3: Photoacoustic transients emblematic of vapor bubble formation around AuNR.....	17
Figure 2-4: Schematic and TEM characterization of AuMBs	20
Figure 2-5: High-speed and streak camera observations of AuMBs undergoing nanosecond pulsed laser excitation	23
Figure 2-6: Compilation of AuMB radial dynamics and photoacoustic properties following excitation by a nanosecond pulsed laser source.....	24
Figure 2-7: Nonlinear photoacoustic response of AuMBs with increasing laser fluence.....	25
Figure 2-8: in vitro ultrasound and photoacoustic images of AuMBs.....	28
Figure 2-9: in vivo imaging of murine kidney following injection of AuMBs	29
Figure 3-1: Finite element heat transfer model geometry and thermal fields.....	42
Figure 3-2. Thermal fields over time and with increasing laser pulse energies	43
Figure 3-3: Effect of distance between AuNR and gas/liquid interface on thermal field.....	44
Figure 3-4: Microbubble gas temperatures and simulated oscillatory frequencies	45
Figure 4-1: Design of a catheter-dimensioned flow focusing microfluidic device	60
Figure 4-2: Microbubble production characteristics for catheter-dimensioned FFMD.....	63
Figure 4-3: Still frame of catheter-dimensioned FFMD operation.....	64
Figure 4-4: Microbubble lifetime curves in air-saturated, mixed saline.....	65
Figure 4-5: Schematic of intended device operation and effect of low microbubble stability	67
Figure 5-1: Characteristics of microbubbles produced by flow-focusing microfluidic devices...	77
Figure 5-2: FFMD microbubble dissolution and acoustic properties	79
Figure 5-3: Schematic of in vitro sonothrombolysis assay and assay characterization.....	80
Figure 5-4: in vitro clot lysis curves for four experimental conditions	82
Figure 5-5: in vitro volumetric clot lysis rates for multiple experimental conditions	83
Figure 6-1: in vitro clot lysis curves for four experimental conditions	94
Figure 6-2: Schematic of rat surgery for administration of microbubbles and thrombus.....	97
Figure 6-3: TTC staining of brains sections from all rats included in the microbubble safety study	99
Figure 6-4: TTC staining of brains sections from all rats included in Group A (Control) of the ischemic stroke study.....	100
Figure 6-5: TTC staining of brains sections from all rats included in Group B (Low Dose rtPA) of the ischemic stroke study.....	101
Figure 6-6: TTC staining of brains sections from all rats included in Group C (High Dose rtPA) of the ischemic stroke study.....	102

Figure 6-7: TTC staining of brains sections from all rats included in Group D (Sonothrombolysis) of the ischemic stroke study.....	103
Figure 6-8: Boxplots of infarct volumes and NDS observed for each experimental group in the rat ischemic stroke study.....	104
Figure 7-1: Summary schematic of findings from Part I of this dissertation.....	114
Figure 7-2: Summary schematic of findings from Part II of this dissertation	115
Figure A1-1: Experimental apparatus and NIRF/IVUS scanning geometry	130
Figure A1-2: Schematic of one-dimensional light propagation model geometry.....	132
Figure A1-3: Schematic of IVUS image processing and vessel wall segmentation.....	135
Figure A1-4: In vitro NIRF/IVUS measurements of DiR concentrations	138
Figure A1-5: In vitro NIRF/IVUS measurements of DiR concentrations in vessel phantoms...	140
Figure A1-6: Ex vivo NIRF/IVUS measurements of DiR concentrations in excised porcine vessels	142
Figure A2-1: Schematic of synthesis of perfluorocarbon droplets with FMSNs in their core ...	151
Figure A2-2: Schematic of experimental apparatus used to observe droplet phase conversion.	152
Figure A2-3: Qualitative confirmation of silica nanoparticle fluorination.....	153
Figure A2-4: TEM imaging of perfluorocarbon droplets and FMSNs	154

List of Tables

Table 3-1: Thermal material properties used in finite element heat transfer model	40
Table 3-2: Microbubble properties used in modified Rayleigh-Plesset model.....	41
Table 4-1: Failure mode analysis for catheter-dimensioned microfluidic devices	63
Table 5-1: Parameters for different experimental in vitro sonothrombolysis conditions	81
Table 5-2: p-value for comparison of clot lysis rates under differing experimental conditions...	84
Table 5-3: Clot lysis rates relative to experimental Group B (1 μ g/ml rtPa alone).....	84
Table 6-1: Information on rats included in microbubble safety study.....	98
Table 6-2: Results of 1-way ANOVA and p-values for infarct volumes of rats in the ischemic stroke study	105
Table 6-3: Results of 1-way ANOVA and p-values for neurological deficit scores of rats in the ischemic stroke study.....	106
Table 6-4: Information on rats included in the rat ischemic stroke study	113
Table A1-1: Parameters for Model Fit to Equation A1-1	137

List of Equations

Equation 2-1: Velocity potential of oscillating microbubble.....	22
Equation 2-2: Pressure emitted by oscillating microbubble.....	22
Equation 3-1: Heat transfer equation for laser-heated gold nanorod.....	39
Equation 3-2: Heat transfer equation for water in contact with heated surface.....	39
Equation 3-3: Rate of heat loss from nanorod to it surrounding.....	39
Equation 3-4: Boundary conditions for heat transfer simulations.....	39
Equation 3-5: Modified Rayleigh-Plesset equation for microbubble oscillations.....	41
Equation 3-6: Gas pressure as a function of internal gas temperature.....	41
Equation 6-1: Calculation of mean from subtraction of two distributions.....	111
Equation 6-2: Calculation of variance from subtraction of two distributions.....	111
Equation 6-3: Calculation of mean and variance when dividing a distribution by a constant.....	111
Equation 6-4: Calculation of mean from ratio of two distributions.....	112
Equation 6-5: Calculation of variance from ratio of two distributions.....	112
Equation A1-1: Analytical model of light propagation and attenuation through blood.....	131
Equation A1-2: Analytical model of fluorescence emitted from homogeneous medium.....	132
Equation A1-3: Constant term derived from optical attenuation coefficients.....	133

List of Software

Software A3-1: PZFlex simulations for heating of gold nanorod near gas/liquid interface.....	157
Software A3-2: MATLAB helper-script for solving Rayleigh-Plesset equation.....	164
Software A3-3: MATLAB code to solve Rayleigh-Plesset equation.....	165

List of Nomenclature

Mathematical Symbols

Symbol	Description
$A_{surface}$	Surface area of nanoparticle
β	Thermal coefficient of volumetric expansion
d	Distance
d_b	Microbubble diameter
d_{MB}	Microbubble diameter
f	Frequency
f_b	Microbubble production rate
f_R	Resonant frequency
G	Thermal contact conductance
Gr	Grashof number
Γ	Grünesien parameter
g	Optical anisotropy
γ	Polytropic gas constant
H	Fractional hematocrit
k	Thermal conductivity
κ	Isothermal compressibility
κ_s	Dilational viscosity
λ	Wavelength
m	Mass
μ	Mean
μ_a	Optical absorption coefficient
μ_{eff}	Effective optical extinction coefficient
μ_s	Optical scattering coefficient
μ_s'	Reduced optical scattering coefficient

μ_L	Dynamic viscosity
c_p	Specific heat
p	Pressure
p_0	Photoacoustic pressure rise
Φ	Laser fluence
Φ	Fluorophore quantum yield
φ	Velocity potential
$\dot{\varphi}$	First derivative of velocity potential
Q_l	Liquid flow rate
Q	Heat
\dot{Q}	First time derivative of heat transfer
R	Microbubble radius
r	Distance from microbubble
R_0	Initial microbubble radius
R_{max}	Maximum microbubble radius
\dot{R}	First derivative of microbubble radius
\ddot{R}	Second derivative of microbubble radius
P	Power
ρ	Density
σ	Surface tension
σ_{abs}	Absorption cross section
T	Temperature
T_c	Critical temperature
t	Time
τ_p	Laser pulse width
V	Volume

Acronyms

Acronym	Description
AuMB	Gold nanorod coated microbubble
AuNR	Gold nanorod
CDT	Catheter-directed thrombolysis
CW	Continuous wave
DFB	Decafluorobutane
DFP	Dodecafluoropentane
DiR	1,1'-Dioctadecyl-3,3,3',3'-Tetramethylindotricarbocyanine Iodide
DSPC	1,2-distearoyl-sn-glycero-3-phosphocholine
DVT	Deep vein thrombosis
ECA	External carotid artery
FFMD	Flow-focusing microfluidic device
FMSN	Fluorinated mesoporous silica nanoparticle
FWHM	Full-width at half maximum
ICA	Internal carotid artery
ICH	Intracerebral hemorrhage
IVUS	Intravascular ultrasound
MB	Microbubble
MCA	Middle cerebral artery
mRS	Modified Rankin Scale
MSN	Mesoporous silica nanoparticle
NA	Numerical aperture
NIR	Near infrared
NIRF	Near infrared fluorescence
OCT	Optical coherence tomography
OPO	Optical parametric oscillator
PA	Photoacoustic
PCCA	Phase change contrast agent

PDE	Partial differential equation
PDMS	Polydimethylsiloxane
PDP	Polyvinylpyrrolidone
PE	Pulmonary embolism
PEG	Polyethylene glycol
PFB	Perfluorobutane
PFP	Perfluoropentane
PFOTS	1H,1H,2H,2H-perfluorooctyltriethoxysilane
PI	Pulse inversion
PNP	Peak negative pressure
PRP	Platelet-rich plasma
PTFE	Polytetrafluoroethylene
PTS	Post-thrombotic syndrome
RBC	Red blood cell
RMSE	Root mean square error
rtPA	Recombinant tissue plasminogen activator
SNR	Signal to noise ratio
TEM	Transmission electron microscopy
TICI	Thrombolysis in cerebral infarction
TTC	Triphenyltetrazolium chloride
US	Ultrasound

Chapter 1. Introduction

Ultrasound waves are longitudinal pressure waves that propagate through a medium via wavelike expansion and compression. Medical diagnostic ultrasound imaging is commonly performed using ultrasound frequencies between 1 – 15 MHz, permitting the evaluation of anatomical structures at depths between 0 – 20 cm in the human body. Acoustic waves are absorbed, reflected, refracted, and scattered as they propagate through tissue and interact with tissue structures. The reflected and scattered acoustic energy is detected by the ultrasound system and an image is made that represents the difference in acoustic reflectivity between neighboring tissue structures. Second to only X-ray imaging, ultrasound is one of the most commonly used imaging modalities for diagnostic, interventional, and therapeutic applications.⁶

Ultrasound offers significant advantages over other medical imaging modalities, including high portability, real-time imaging, non-ionizing imaging, and comparably low cost. Unlike computed tomography and X-ray, ultrasound is capable of real-time Doppler imaging of blood flow without the introduction of vascular contrast agents. However, Doppler blood flow signals can be enhanced by the introduction of ultrasound contrast agents, which extends the clinical utility of blood flow imaging to smaller blood vessels and permits the assessment of tissue perfusion.^{7,8} To date, ultrasound contrast agents are approved in the United States for contrast enhancement in liver and cardiac imaging applications and are under investigation in on-going clinical trials for molecular imaging and therapeutic applications.^{9,10}

The most common ultrasound contrast agents are microbubbles, which are gas bubbles with diameters of 1 – 4 μm and a stabilizing lipid, protein, or polymer surfactant shell.^{11,12} Microbubbles provide a versatile platform for both imaging and therapy, and this dissertation evaluates the design and characterization of two novel microbubble formulations for use in separate photoacoustic

imaging and thrombolysis applications. Accordingly, the dissertation is divided into two separate sections – one for each specific application enabled by each unique microbubble formulation.

1.1 Introduction to microbubbles

Microbubbles used for diagnostic imaging applications are conventionally designed to provide circulation lifetimes on the order of approximately 10 minutes. This constrains their design to incorporate a stabilizing shell (most commonly a lipid monolayer) and a low-solubility gas to limit gas diffusion and prolong circulation lifetimes. The primary modes of clearance from the circulation are thought to be filtration by small lung capillaries, dissolution due to gas diffusion, and phagocytosis by immune cells, including splenic macrophages, neutrophils, and hepatic Kupffer cells.¹³⁻¹⁶ The primary clinical indications in which microbubbles are used are left ventricle opacification, myocardial perfusion imaging, and hepatic cell carcinoma screening.^{8,17}

The acoustic signature of microbubbles may be specifically detected within ultrasound images on the basis of their unique frequency response. In response to ultrasound excitation, microbubbles oscillate at the frequency of the acoustic wave and emit acoustic energy at both sub-harmonic and harmonic frequencies due to the high compressibility of the gas core. Under certain imaging conditions and using specific beamforming approaches, these emissions at non-fundamental frequencies may be specifically detected to distinguish between the emissions from microbubbles and soft-tissue with high sensitivity and specificity.¹⁸⁻²⁰ Microbubbles also exhibit a resonant frequency that is a function of the microbubble radius and the viscoelastic properties of its surfactant shell. Microbubble oscillations and acoustic scattering are strongest when the microbubble is excited at its resonance frequency, which is often in the range of 5 – 10 MHz, conveniently in the range of diagnostic ultrasound imaging frequencies.²¹ Collectively, these

1.2 Photoacoustic imaging and photoacoustic contrast agents

properties make microbubbles excellent ultrasound contrast agents for diagnostic imaging applications.

The microbubble shell provides a scaffold upon which targeting moieties, drugs, and other payloads may be attached to endow the microbubble with additional functionality. A common application is the placement of antibodies or peptides on the microbubbles surface that are targeted to cell-surface receptors that are of interest to a specific disease state. The targeted microbubble binds to the cell-surface receptor and the microbubble signal can be used as a surrogate within the ultrasound image to gauge the expression of the cell-surface receptor.^{10,22} Of particular interest is the detection of cell-surface receptors governing angiogenesis in cancer microvasculature, an application currently under study in the prostate and breast in early-stage clinical trials.¹⁰

Microbubbles oscillate under ultrasound exposure, causing rapid movements of the microbubble shell that cause mechanical perturbations in the surrounding medium. Under certain conditions, microbubbles that oscillate in close proximity to cells can cause temporary perforation of the cell membrane through a process known as sonoporation.²³ Sonoporation enables the delivery of drugs to cells or organs that otherwise could not pass through the cell membrane or organ boundary.^{24,25} Drugs can be incorporated within the microbubble shell or attached to the microbubble in liposomes to promote highly localized drug delivery at the site of focused ultrasound exposure and microbubble rupture.²⁶⁻²⁹ Enhanced chemotherapeutic drug delivery via sonoporation has recently been demonstrated in pancreatic cancer patients, marking the first utilization of this technique in humans.⁹

1.2 Photoacoustic imaging and photoacoustic contrast agents

Photoacoustic imaging describes an imaging modality in which the deposition of optical energy within a material elicits a rapid thermal expansion and a broadband acoustic transient.

1.2 Photoacoustic imaging and photoacoustic contrast agents

These acoustic transients may be detected by conventional ultrasound imaging systems to produce images that are representative of the optical absorption of the material at the wavelength of optical excitation. Spectroscopic imaging techniques acquire separate images at different optical wavelengths as a means to characterize the materials contained within the image on the basis of their optical absorption spectrum. Photoacoustic imaging is promising for measuring blood oxygenation on the basis of the differing optical absorption spectra of oxy- and deoxy-hemoglobin and the presence of lipid within atherosclerotic plaque, among other applications.^{30 31,32}

Beyond the endogenous sources of optical contrast (e.g. hemoglobin, melanin, lipid), photoacoustic imaging also utilizes optically absorbing contrast agents to enable molecular imaging and other applications. Clinically approved dyes include methylene blue and a fluorophore called indocyanine green.^{33,34} As discussed above, these contrast agents often require spectroscopic imaging techniques to enable their detection, as the emitted photoacoustic signals are weak and attenuate in the medium before they reach the ultrasound receive system. To circumvent these limitations, contrast agents based on gold nanoparticles have been developed that produce photoacoustic responses that are significantly stronger than endogenous sources and injected dyes.³ While not clinically approved, these agents have provided utility in preclinical models.³⁵

A limitation of most photoacoustic contrast agents is that, to first order, they produce acoustic emissions with similar frequency content and their photoacoustic emissions scale linearly with increasing laser amplitude. These limitations mean that photoacoustic contrast agents may only be detected based on their differing optical absorption spectra and, unlike microbubbles, not on the basis of their acoustic emissions. In effect, this means that multi-wavelength lasers and spectroscopic imaging techniques must be employed, which adds significant cost and time to

photoacoustic image acquisition. Alternatively, if a photoacoustic contrast agent emitted a unique acoustic signature, then it could be differentiated from the background tissue signal on the basis of its acoustic emission and not its optical absorption. Part I of this thesis explores the properties of a light-absorbing microbubble for use in photoacoustic imaging applications and demonstrates two potential modes of specific detection of these agents from background sources of photoacoustic signals.

1.3 Microbubbles for sonothrombolysis applications

In addition to the therapeutic applications introduced in Section 1.2, the combination of ultrasound and microbubbles has also been investigated as a means to accelerate blood clot lysis in patients with thrombo-occlusive diseases, including ischemic stroke, deep vein thrombosis, and pulmonary embolism.³⁶⁻³⁸ This therapy is known as sonothrombolysis, and can accelerate clot lysis through multiple mechanisms. When exposed to ultrasound, momentum is transferred to the microbubble, resulting in the ultrasound wave pushing the microbubble in the direction of wave propagation.³⁹ This pushing effect, a result of acoustic radiation force, causes microbubbles to tunnel within the fibrin mesh of the blood clot, exposing more surface area to thrombolytic drug and damaging the mechanical integrity of the clot.⁴⁰⁻⁴² In addition, microbubble cavitation events – a process in which microbubbles collapse violently after exposure to ultrasound excitation – have been shown to remove material from both the surface and interior of the clot.^{43,44}

Sonothrombolysis as a therapy for ischemic stroke has been evaluated in multiple clinical studies.^{36,38,45} Overall, these studies demonstrated accelerated thrombolysis rates when using sonothrombolysis instead of intravenous tissue plasminogen activator, but also found an increased risk of intracerebral hemorrhage – a finding that severely tempered enthusiasm for the therapeutic approach. The underlying cause of hemorrhagic transformation was unknown, but it was thought

to have resulted from standing wave formation in the patient's skull and the effects of off-target microbubble-ultrasound interactions away from the location of the occlusion. Strategies to increase the localization of therapeutic delivery to avoid these off-target effects may reduce the incidence of intracerebral hemorrhage, but they have not been evaluated clinically.^{46,47}

Aside from ischemic stroke, sonothrombolysis-based therapies may find application for deep vein thrombosis or pulmonary embolism applications.⁴⁸ These conditions often require catheter-directed thrombolysis (CDT) based approaches, in which thrombolytic drug is slowly administered from the distal end of a catheter placed in close proximity of the occluding thrombus.⁴⁹⁻⁵¹ While effective in many patients at lysing the thrombus, catheterization and hospitalization times up to 48 – 96 hours are not uncommon, and many patients return with repeat thrombosis or post-thrombotic syndrome (PTS), a condition marked by swelling of the extremities and severe pain.⁴⁹⁻⁵¹ Therefore, DVT, in particular, may be well suited for acceleration of thrombus removal by sonothrombolysis-based approaches.

In Part II of this thesis, a design for a catheter-based sonothrombolysis administration system is presented. The system was validated *in vitro*, and the fundamental basis of the technology was evaluated in a rat model of ischemic stroke. However, as discussed above, this platform could be extendable to other thrombo-occlusive diseases.

1.4 Microbubble fabrication techniques

Microbubbles are most commonly fabricated via agitation or sonication of a gas-saturated solution containing the microbubble shell material (e.g. lipid). These techniques produce a large number (> 1 billion) of stable microbubbles with a wide range of diameters (e.g. 0.5 – 10 μm). This production technique is well-suited to bedside production of microbubbles for diagnostic imaging studies, in which a large number of microbubbles are required for intravenous injection

and stability is required for long circulation lifetimes.⁵² However, these properties are not necessarily well-matched to therapeutic applications, as discussed above in the context of ischemic stroke and hemorrhagic transformation due to off-target ultrasound-microbubble interactions.

An alternative approach is to fabricate microbubbles using microfluidic devices, in which pressurized streams of liquid and gas are combined with high precision and repeatability within microchannels to produce microbubbles.⁵³ Microbubbles produced within microfluidic devices have near-uniform diameters immediately after production, which can be beneficial for imaging applications by improving SNR of contrast-enhanced ultrasound imaging.⁵⁴ In addition, microfluidic devices can produce targeted or drug-loaded microbubbles via on-chip processes, thereby reducing processing steps required to attach targeting moieties or drug to the microbubble shell post-production.^{55,56}

However, rather than replicating microbubbles that can be produced easily by agitation or sonication, one of the more interesting capabilities of microfluidic devices is the production of microbubbles made of unconventional materials that are not widely used in commercial microbubble formulations. Because the mixing is precisely controlled within the microfluidic device, the gas and liquid phases meet under precisely known conditions, thereby presenting the opportunity to make microbubbles from gas or liquid phases that otherwise would be unsuitable for microbubble production but may impart advantageous properties. For instance, microbubbles with short-lifetimes, if produced directly within the vasculature, would be active only near the intended therapeutic target site and would dissolve further downstream, thereby mitigating potential off-target effects.⁵⁷ Microfluidic devices are capable of making such low-stability microbubbles from high solubility gases and weak surfactant shells in large number with relatively uniform properties.^{58,59} This thesis demonstrates that microfluidic bubble fabrication technology

can be miniaturized to a catheter of human-compatible dimensions for microbubble production directly within the vasculature. The underlying hypothesis of this work is that, when placed near a thrombus, the microbubbles produced by the catheter would actively degrade the thrombus and dissolve further downstream, potentially increasing the safety of catheter-directed sonothrombolysis techniques.⁵⁷

1.4 Microbubble fabrication techniques

Part I: Light Absorbing Microbubbles for Photoacoustic Imaging Applications

Chapter 2. Investigation of optically absorbing microbubbles for *in vitro* and *in vivo* photoacoustic imaging¹

2.1 Abstract

Microbubbles bearing plasmonic nanoparticles on their surface provide contrast enhancement for both photoacoustic and ultrasound imaging. In this work, the responses of microbubbles with surface-bound gold nanorods – termed AuMBs – to nanosecond pulsed laser excitation were studied using high-speed microscopy and photoacoustic imaging. In response to laser fluences below 5 mJ cm^{-2} , AuMBs produce weak photoacoustic emissions and exhibit negligible microbubble wall motion. However, in response to fluences above approximately 5 mJ cm^{-2} , AuMBs undergo dramatically increased thermal expansion and emit nonlinear photoacoustic waves of over 10-fold greater amplitude than would be expected from freely dispersed gold nanorods. At these higher fluences, explosive boiling may occur at the nanorod surface, producing vapor nanobubbles that contribute to rapid AuMB expansion. The results of this study indicate that AuMBs are capable of producing acoustic emissions of significantly higher amplitude than those produced by conventional sources of photoacoustic contrast. *In vivo* imaging performance of AuMBs in a murine kidney model suggests that AuMBs may be an effective alternative to existing contrast agents for non-invasive photoacoustic and ultrasound imaging applications.

¹ This chapter contains content drawn from the following peer-reviewed conference and journal publications:
 AJ Dixon, S Hu, AL Klibanov, JA Hossack, “Oscillatory dynamics and *in vivo* photoacoustic imaging performance of plasmonic nanoparticle-coated microbubbles.” *Small*, 11(25), 3066-3077, 2015.
 AJ Dixon, S Hu, AL Klibanov, JA Hossack, “Empirical and theoretical study of the interaction between plasmonic-nanoparticle coated microbubbles and nanosecond pulsed laser excitation.” 21st European Symposium on Ultrasound Contrast Agents (2016), Rotterdam, The Netherlands.
 AJ Dixon, S Hu, AL Klibanov, JA Hossack, “Photoacoustic properties of plasmonic nanoparticle coated microbubbles.” IEEE International Ultrasonics Symposium (2015), Taipei, Taiwan.

2.2 Introduction

Photoacoustic imaging is a noninvasive imaging technique that provides high contrast images of optical absorption within living tissue.³⁰ Photoacoustic signals arise from the conversion of absorbed optical energy to heat, causing transient thermoelastic expansion and subsequent wideband ultrasonic emission.^{60,61} While first explored for the detection of endogenous sources of optical contrast (e.g. hemoglobin, melanin), photoacoustic imaging has been extended to molecular imaging applications through the use of exogenous contrast agents, such as dyes and nanoparticles.^{33,62-66} In particular, plasmonic metal nanoparticles exhibit optical absorption cross-sections that are orders of magnitudes higher than those of endogenous tissue chromophores and are effective molecular imaging agents when functionalized with moieties targeted to specific molecules.^{64,65,67-69}

The sensitivity, specificity, and imaging depth of photoacoustics are limited by the efficiency with which optical absorbers convert light energy to sound.³⁰ The origin of biomedical photoacoustic signals has historically been restricted to photothermal expansion of liquid or solid materials that possess relatively small coefficients of thermal expansion. The acoustic transients produced by these materials are weak, which significantly limits the signal-to-noise ratio (SNR) and penetration depth of *in vivo* photoacoustic imaging.^{30,33,70} While the introduction of plasmonic nanoparticles has enhanced the sensitivity of photoacoustic imaging on account of their greatly increased optical absorption, their photoacoustic emissions are still derived from thermoelastic expansion, which fundamentally limits the magnitude of the photoacoustic transient.^{71,72} However, new classes of photoacoustic contrast agents that utilize vaporization and gaseous expansion for photoacoustic signal generation have recently demonstrated photoacoustic emissions several orders of magnitude greater than those typically encountered in biomedical photoacoustic

imaging.⁷¹⁻⁷⁴ Furthermore, some formulations of these new contrast agents enhance photoacoustic emissions at laser fluences below the current safety limits for laser irradiation, thereby enabling optically-guided, deep tissue therapy and imaging.⁷¹⁻⁷⁶

Photoacoustic signal generation via gaseous expansion is achieved by using either a liquid perfluorocarbon precursor that vaporizes upon laser excitation or a preformed gaseous microbubble.^{71-75,77-81} Preformed microbubbles bearing gold nanoparticles on their surface produce significant photoacoustic signal enhancement when compared to freely dispersed gold nanoparticles.^{75,78} These agents are referred to as AuMBs, and unlike phase-change perfluorocarbon nanodroplets, increased pressures are not derived from the vaporization of a liquid perfluorocarbon precursor.⁷¹⁻⁷⁴ The exact mechanisms underlying photoacoustic signal enhancement from AuMBs are not well characterized. However, Dove *et al* recently demonstrated that, for AuMBs bearing 5 nm diameter gold nanospheres on their surface, conductive heat transfer from the nanospheres to the gaseous core induces AuMB oscillations that enhance the photoacoustic response by approximately 8-fold relative to freely dispersed gold nanospheres.^{44,75}

In this work, we propose an additional mechanism for the photoacoustic enhancement observed from AuMBs and describe a fluence-dependent nonlinear behavior that has not been previously reported. High-speed video microscopy and photoacoustic imaging results confirm that that when the gold nanoparticles are heated to higher temperatures, AuMBs exhibit radial expansion dynamics that scale nonlinearly with laser fluence. In this nonlinear regime, conductive heat transfer cannot confer enough energy to the gaseous core to account for the up to 3-fold increase in AuMB radius that was observed experimentally. Rather, these results suggest that AuMB expansion in response to high laser fluence is driven by vapor-bubble formation on the gold nanoparticle surface and rapid mass-transfer from the vapor bubbles to the expanding AuMB.^{[26-}

^{30]} Indeed, altered heat-transfer dynamics at the nanoparticle-microbubble interface may promote nanobubble formation at lower fluence than is typically required for homogeneous nucleation of vapor bubbles, thereby enabling high-SNR, vaporization-based photoacoustic imaging at safe laser fluence.^{72,82-85}

2.3 Materials and Methods

2.3.1 Synthesis and Characterization of AuMBs

PDP-microbubbles were comprised of DSPC (2 mg ml^{-1}) and PDP-PEG2000-DSPE (1 mg ml^{-1}) (Avanti Polar Lipids) in aqueous saline and were fabricated by dispersing decafluorobutane (DFB) gas in the lipid micellar aqueous media. Following fabrication, the microbubbles were subjected to centrifugal flotation to remove excess free lipid not associated with the microbubble shell. AuNRs ($10 \text{ nm} \times 35 \text{ nm}$, Nanopartz, Inc) with 750 nm peak optical absorption and a neutral surface charge were centrifuged three times in fresh saline at $12000 \times g$ for 10 min to remove excess stabilizing ligands from solution.⁸⁶ To complete the conjugation, approximately 9×10^{12} AuNRs were incubated with 5×10^8 microbubbles under a DFB gas headspace for 24 hr under gentle agitation. Unattached AuNRs were removed by a final series of gravitational floatation steps (see Figure 2-1). Floatation separation was performed until the optical density of the supernatant was less than 0.05 , indicating the removal of freely dispersed AuNRs.⁸⁶ The surface charges of microbubbles, AuMBs, and AuNRs in $0.9\% \text{ NaCl}$ were measured by a Zetasizer Nano S (Malvern). Transmission electron microscopy (JEOL 2000-FX) was performed on a dilute suspension of AuMBs. Prior to placement in the TEM sample chamber, the AuMBs were incubated with $2\% \text{ uranyl acetate}$ for 30 s to provide a negative stain.

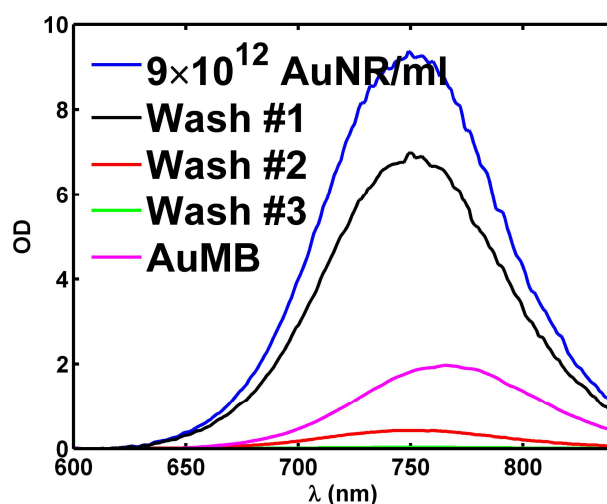


Figure 2-1: AuNR and AuMB optical absorption during AuMB preparation

The blue curve is the optical absorption of 9×10^{12} AuNR prior to incubation with 5×10^8 microbubbles. The black, red, green curves are the optical absorption of the three washes following incubation. Note that the OD is less than 0.05 following the third wash, indicating that the majority of unbound AuNRs have been removed. The pink curve is the optical absorption of AuMBs, prepared as described in the methods section.

2.3.2 Determination of AuNR Loading Efficiency on AuMBs

Conjugation of AuNRs was performed by incubating 9×10^{12} AuNRs with 1×10^9 microbubbles overnight in a glass vial with decafluorobutane (DFB) headspace as described in the methods section. Prior to incubation, the optical density of 9×10^{12} AuNR/ml was measured using a NanoDrop 2000c. A concentration of 9×10^{12} AuNR/ml repeatedly yielded a peak optical density of 9.7 ± 0.3 ($n=6$ trials). Following incubation, AuNRs that were not associated with AuMBs were removed by floating the AuMBs to the top of the vial and removing the remaining infranatant containing unbound AuNRs. Floatation and separation of the AuMBs and freely dispersed AuNR fractions was performed a minimum of three times to ensure removal of unbound AuNRs. The optical densities of each infranatant fraction were measured and are shown in Figure 2-1 to demonstrate removal of unbound AuNRs through the serial wash steps. The optical density of the AuNRs remaining in the AuMB fraction was measured by collapsing the AuMBs via repeated over-and under-compression in a syringe. This process destroys the gas microbubbles but leaves

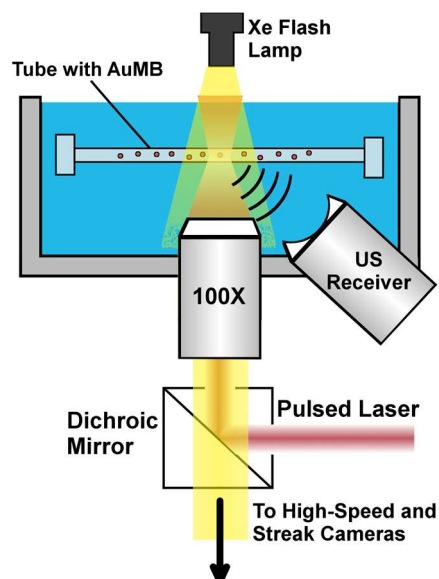


Figure 2-2: Experimental apparatus for acquisition of high-speed camera and photoacoustic data from single AuMBs and AuNRs.

The samples were placed in a 200 μm diameter cellulose tube and light was focused onto the sample using a 100X water immersion objective. Photoacoustic waves were recorded by a 10 MHz ultrasound transducer and high speed cameras were used to record the images produced by the 100X objective. The optical and acoustic foci were aligned on a 200 μm cellulose tube containing the sample. Note: not to scale.

the lipid shell and gold nanorods in solution, thereby eliminating the optical scattering caused by the microbubbles. The peak optical density of the collapsed AuMBs measured 1.9 ± 0.2 ($n=6$), corresponding to a concentration of 1.9×10^{12} AuNR/ml, and exhibited a small red-shift, as shown in Figure 1e. In addition, the number of AuMBs remaining from the initial 5×10^8 microbubbles were counted using a Microsizer 3 Coulter Counter (Beckman Coulter). On average $4.0 \times 10^8 \pm 2.1 \times 10^7$ AuMBs remained following all incubation and wash steps, corresponding to an AuNR load of approximately 4300 ± 710 AuNR per AuMB.

2.3.3 Determination of the Threshold Fluence for Vapor Nanobubble Formation

The onset of cavitation for single AuMBs and freely dispersed AuNRs were (1×10^{12} AuNR/ml) studied separately in the experimental setup shown in Figure 2-2. Fluences above $\sim 5 \text{ mJ cm}^{-2}$ caused permanent photobleaching of the AuNRs, so the solution in the tube was circulated to ensure that new AuNRs were studied with each laser pulse. The formation of a vapor bubble was

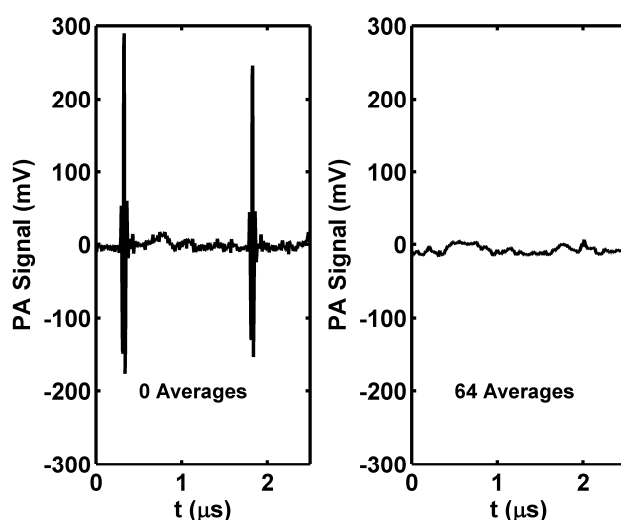


Figure 2-3: Photoacoustic transients emblematic of vapor bubble formation around AuNR

(Left) Acoustic signal from a cavitation event around AuNRs (1×10^{12} AuNR/ml, 80 mJ/cm^2 fluence, 0 averages). (Right) Acoustic signal from a non-cavitation event around gold nanorods (1×10^{12} GNR/ml, 1 mJ/cm^2 fluence, 64 averages).

confirmed based on the transient acoustic emission detected from this region. Vaporization events produced a high-amplitude acoustic transient that was well above the noise floor of the detection system, while non-vaporization events produced weak acoustic transients that often required signal averaging to detect clearly (Figure 2-3). A vaporization event was defined as one in which the acoustic signal within the recording time window exceeded a threshold voltage set at twice the voltage that would be expected of a linear contrast agent. The vaporization probability is defined as the number of cavitation events detected divided by the total number of laser shots.

2.3.4 High-speed microscopic and photoacoustic observation of AuMB Dynamics

The experimental configuration is shown in Figure 2-2. Excitation light produced by a pulsed optical parametric oscillator (OPO) laser (Spectra Physics, Newport Corp.) operating at 750 nm wavelength, 20 Hz pulse repetition frequency, and 5 ns pulse width was passed through the back lightport of an inverted microscope (IX51, Olympus) and focused through a 100X water-immersion objective (NA=1.0) to a spot size of 9 μm radius. A 200 μm diameter cellulose tube

(Spectrum Labs) was positioned in the optical focus and contained a dilute suspension of AuMBs. The acoustic focus of a 10 MHz, 0.5 inch diameter ultrasound transducer (V303, Panametrics, Olympus) was co-aligned with the optical focus, and photoacoustic waveforms were received and amplified (40 dB) by a 5900PR pulser-receiver (Panametrics, Olympus) and digitized by an oscilloscope at a 200 MHz sampling frequency (LC334AL, LeCroy). Optical energy density incident on the cellulose tube was measured by a pulsed optical power meter (918D, Newport Corp). Pulse-to-pulse variation in laser output was approximately 11% and did not vary with fluence. The pulsed laser triggered the acquisition of 24 two-dimensional high-speed camera images (SIMD24, Specialised Imaging) and a single one-dimensional streak camera image (OptoScope, Optronis GmbH). The 2-dimensional images had user-selected interframe times of 10-50 ns and the streak camera had a user-selected temporal resolution of between 200 and 600 ps. A xenon flash-lamp was used to provide high-intensity illumination for the short exposure, high-speed imaging. Microbubble radii were measured manually in MATLAB from streak images and automatically on the 2D images using a snake-based image segmentation algorithm in MATLAB.⁸⁷

2.3.5 Multimodality *in vitro* and *in vivo* imaging

All B-Mode, pulse inversion, and photoacoustic images were acquired using a CL15-7 transducer connected to a Verasonics V-1 programmable ultrasound imaging system with 128 transmit and 64 receive channels (Verasonics, Redmond, WA). B-mode imaging (1 cycle pulse, 15 dB gain) was performed with a transmit frequency of 15 MHz and images were formed by spatially compounding seven separate acquisitions acquired at transmit steering angles between ± 12 degrees to reduce speckle and improve image quality. Pulse inversion (2 cycle pulse, 15 dB gain) imaging was performed using a transmit frequency of 7 MHz and a bandpass filter with

cutoff frequencies at 8 and 15 MHz to suppress tissue signal and preferentially retain higher frequency harmonic emissions from the AuMBs.¹⁹ Photoacoustic imaging was performed by coupling excitation light produced by a pulsed optical parametric oscillator (OPO) laser (Spectra Physics, Newport Corp.) into the common end of a bifurcated fiber bundle (CeramOptec) and aligning the output of the fiber bundle with the imaging plane of the CL15-7 linear array ultrasound transducer. All ultrasound and photoacoustic data was acquired with a sampling frequency of 45 MHz and the mechanical index (MI) at the elevational focus of the transducer was approximately 0.4 for both B-mode and PI imaging.

For the *in vitro* imaging study, a 1% agar / 5% gelatin flow-phantom was formed by placing 2 mm diameter PTFE tubes in the gelatin while it cured. The tubes were removed once the gelatin solidified to reveal the empty channels. The contrast agents, in concentrations stated in section 2.5, were flowed through the channels at a flow velocity of 0.1 mm/s by a syringe pump (PHD 2000, Harvard Apparatus). Photoacoustic images (5 mJ cm⁻² fluence, $\lambda = 750$ nm) were averaged 9 times while pulse inversion acquisitions were not averaged.

2.3.6 *In Vivo* Imaging of AuMBs

For the *in vivo* imaging study, a female C57BL/6 mouse was anesthetized using 1.5% isoflurane and 98.5% room air following proper animal care and use protocols (approved by University of Virginia Animal Care and Use Committee [ACUC]). The kidney was located on the imaging system using B-Mode ultrasound, and 50 million AuMBs in a volume of 100 μ l were administered via retro-orbital injection. B-Mode, pulse-inversion, and photoacoustic (5 mJ cm⁻² skin fluence, 9 averages per image) radiofrequency data were acquired immediately following AuMB injection. Raw radiofrequency data was beamformed, IQ-demodulated, logarithmically compressed, and normalized to the maximum value in each image prior to being displayed on an

image grid with isotropic resolution. Images are presented on a dB scale with linear color maps. The kidney was manually segmented and its outline was overlaid on the pulse-inversion and photoacoustic images for reference.

2.4 Results

2.4.1 Synthesis and Characterization of AuMBs

Microbubbles were comprised of 1,2-distearoyl-*sn*-glycero-3-phosphocholine (DSPC) and 1,2-distearoyl-*sn*-glycero-3-phosphoethanolamine-N- [PDP (polyethylene glycol) - 2000] (PDP-PEG2000-DSPE) lipid with a decafluorobutane (DFB) gas core. The presence of the PDP group enabled direct gold-thiol linkage of AuNRs to the surface of the microbubble, as depicted in Figure

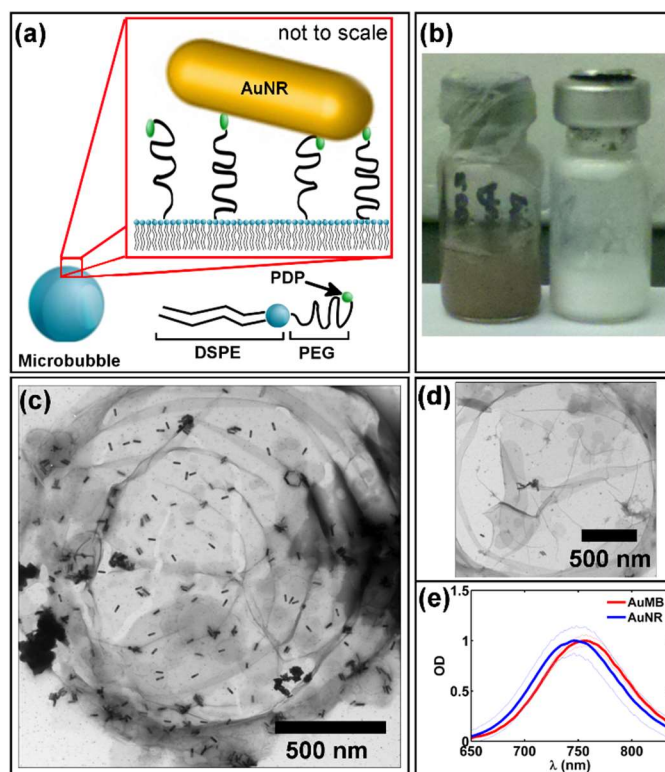


Figure 2-4: Schematic and TEM characterization of AuMBs

(a) Schematic of AuNR linkage to microbubble surface. (b) Suspensions of AuMBs (left) and plain microbubbles (right). (c) Representative TEM image of AuNRs on the microbubble surface. Note the presence of both AuNR clusters and single AuNRs. (d) Significantly reduced AuNR loading on surface of microbubble with no PDP group. (e) Optical absorption spectra of freely dispersed AuNRs and AuNRs bound to AuMBs. Note the red-shift of the longitudinal plasmon resonance observed for AuMBs

5-4A.⁸⁶ After overnight incubation with AuNRs, the microbubble suspension turned from opaque white to dark brown, indicating a change in optical absorption (Figure 2-4B). Following a series of wash-steps to remove unbound AuNRs, an estimated 4300 ± 710 AuNRs were associated with each microbubble, corresponding to a loading efficiency of $19 \pm 3\%$ (Figure 2-1). Direct binding of AuNRs to the microbubble surface was confirmed by transmission electron microscopy (TEM, Figure 2-4C). AuNRs associated with the microbubble shell as both single AuNRs and AuNR aggregates of varying size and orientation. AuMBs exhibited a statistically significant red-shift in peak absorbance from 749.0 ± 1.9 nm to 757.5 ± 3.1 nm, which may be the result of refractive index change related to the lipid shell or plasmonic coupling between AuNRs ($n = 6$, $p < 0.05$, Figure 1e).^{3,88} Notably, far fewer AuNRs associated with microbubbles lacking PDP on their surface, suggesting that the presence of PDP was required for association of the AuNRs with the microbubble shell (Figure 2-4D). The surface zeta-potentials for the AuNRs and microbubbles were 0.10 ± 0.51 and -0.35 ± 0.83 mV, respectively, ruling out a strong electrostatic coupling mechanism.

2.4.2 AuMB Responses to Nanosecond Pulsed Laser Excitation

AuMB responses to single 5-ns laser pulses were recorded by high-speed photography and photoacoustic emissions were simultaneously measured by a focused 10 MHz ultrasound transducer. Two distinct behaviors were observed that were dependent upon the laser fluence. Below approximately 5 mJ cm^{-2} , no microbubble wall motion was observable in the microscopy images, although low amplitude photoacoustic emissions were detected.⁷⁵ However, above 5 mJ cm^{-2} , single AuMBs rapidly expanded and contracted, producing strong photoacoustic responses. Figure 2-5A,D,G show 1-D streak camera images and temporally registered 2-D snap-shots of single AuMB responses to 20, 10, and 5 mJ cm^{-2} laser fluences, respectively. Each AuMB radial

response is marked by a rapid expansion and contraction, although some AuMBs (Figure 2-5A,D) exhibited a prolonged compressional phase relative to their initial rate of expansion. Rapid AuMB expansion following laser excitation was observed more frequently at higher fluences and resulted in higher AuMB wall velocities and larger amplitude photoacoustic waves.

Radius-time and wall-velocity curves for each AuMB are presented in Figure 2-5B,D,H, and the measured photoacoustic emissions are presented in Figure 2-5C,F,I. As shown by the radius-time and velocity curves, peak AuMB wall velocities occur within the first 50 ns following the laser pulse or upon AuMB compression. According to potential flow theory, the acoustic pressure emitted by an oscillating bubble may be expressed as a function of its velocity potential:

$$\phi = -R^2 \dot{R} r^{-1} \quad \text{Equation 2-1}$$

$$p(r, t) = -\rho_w \dot{\phi} = \rho_w \frac{R(t)}{r} (\dot{R}(t) \ddot{R}(t) + 2\dot{R}(t)) \quad \text{Equation 2-2}$$

where ϕ is the velocity potential, ρ_w is the density of water, $R(t)$, $\dot{R}(t)$, and $\ddot{R}(t)$ are the bubble radius and its time derivatives, and r is the recording distance.⁴⁴ The calculated acoustic response for each bubble is presented by red waveforms in Figure 2-5C,F,I. The agreement between the measured and calculated acoustic signals suggests that the acoustic emission may be accurately described by potential flow theory, even though AuMB expansion was triggered by rapid heat deposition on the AuMB surface rather than an externally applied pressure source.^{44,89}

AuMB radial dynamics were investigated further for fluences of 5, 10, and 20 mJ cm⁻². Similar to vapor bubble formation around plasmonic nanoparticles, the average relative radial expansion, $\frac{R_{max}}{R_0}$ (Figure 2-6A), bubble expansion lifetime (Figure 5-6B), and wall velocities increased with increasing laser fluence.⁸⁹⁻⁹² A strong positive correlation between peak wall velocity and $\frac{R_{max}}{R_0}$ was also observed ($r^2=0.71$, Figure 2-6E), while the AuMB initial radius did not appear to impact

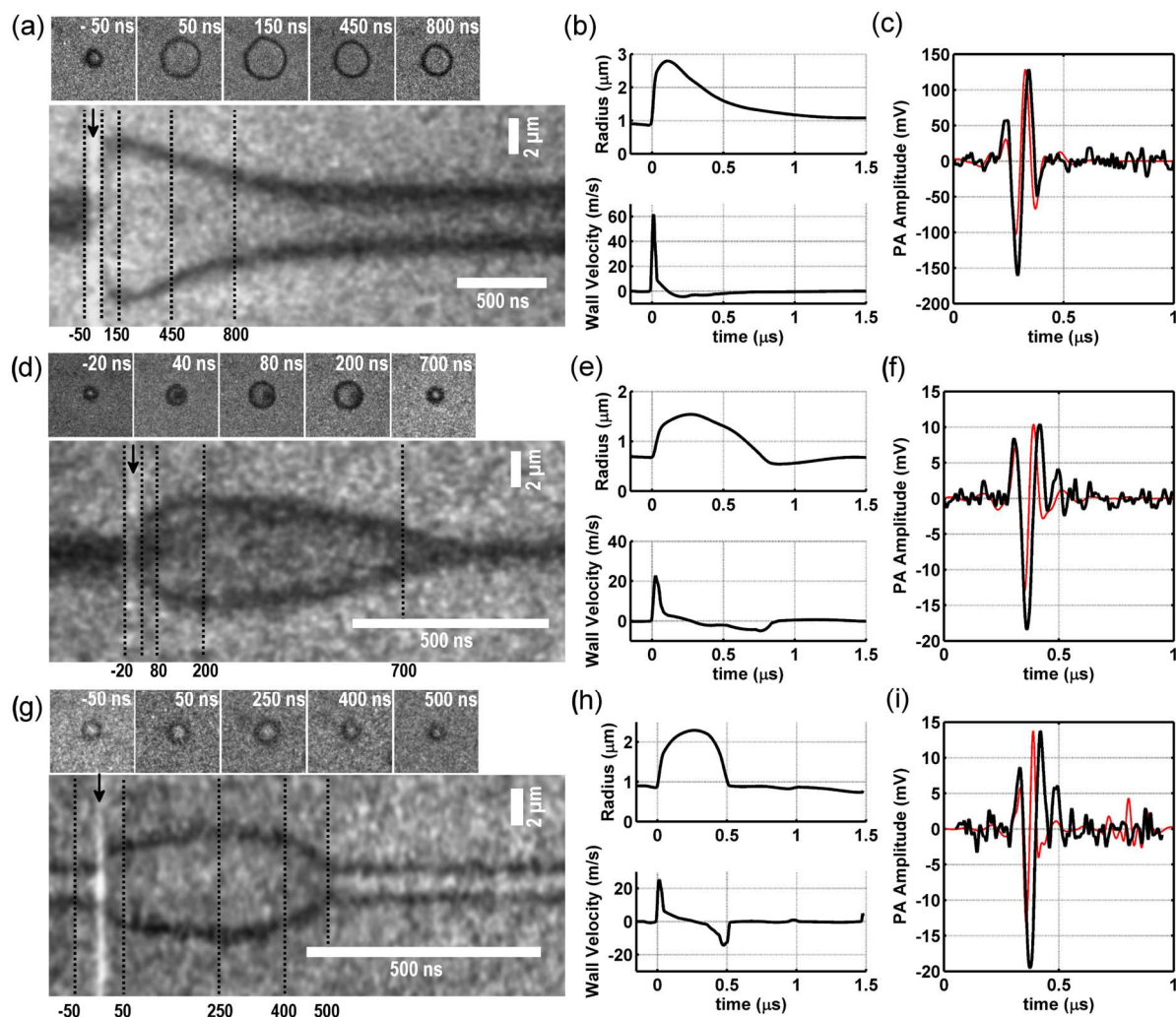


Figure 2-5: High-speed and streak camera observations of AuMBs undergoing nanosecond pulsed laser excitation

(a,d,g) Streak camera and temporally registered 2-D snapshots for single AuMBs exposed to single laser pulses of 20, 10, and 5 mJ/cm² fluence, respectively. The x-axis of these 2D plots is time (ns), while the y-axis is distance (μm). The black, vertical dotted lines on the streak images indicate when the corresponding 2-D snapshot was acquired, and the black arrows indicate the time at which the laser pulse was applied. (b,e,h) Radius and wall velocity curves as a function of time for each AuMB. (c,f,i) Measured acoustic emission from each AuMB (black curve) along with the calculated acoustic emission derived from Equations 2-1 and 2-2 (red curve).

AuMB wall velocities (data not shown). Notably, in all cases, the AuMB remained intact following laser irradiation, however, on average, the final AuMB radius decreased following laser exposure in a fluence-dependent manner (Figure 2-6D).⁷⁹ Also, as predicted by Equation 2-2, a positive correlation was observed between the measured photoacoustic signal amplitude and the microbubble wall velocity ($r^2 = 0.63$, Figure 2-6F).^{44,92,93}

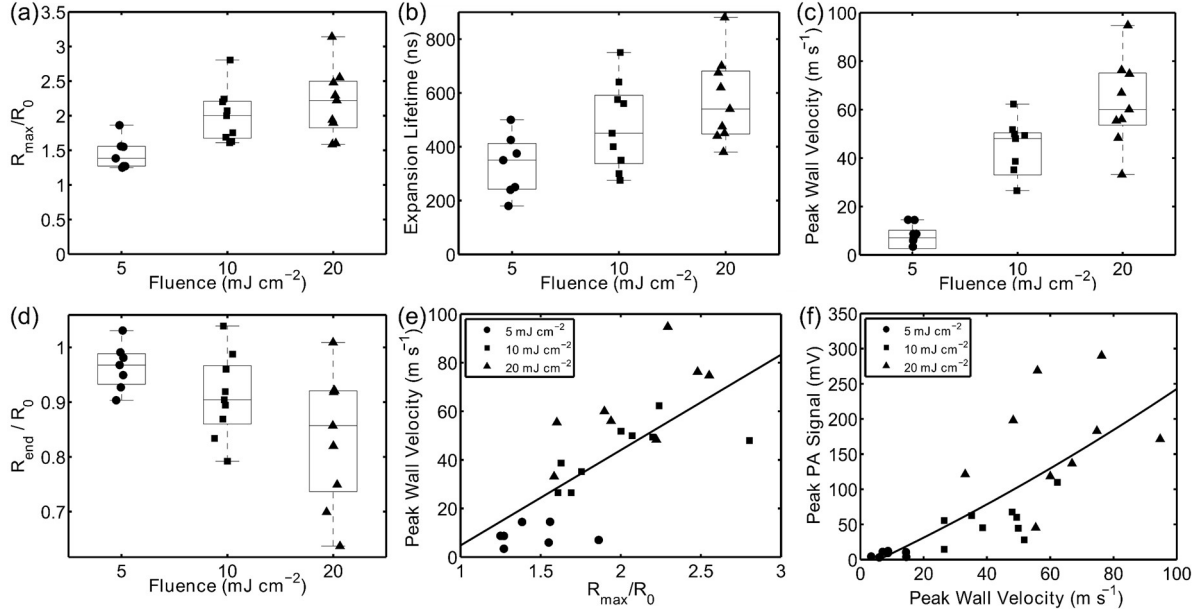


Figure 2-6: Compilation of AuMB radial dynamics and photoacoustic properties following excitation by a nanosecond pulsed laser source

Compiled results of high-speed camera and photoacoustic observation of single AuMB interactions with 5-ns duration laser pulses. (a) Relative AuMB radial expansion, (b) AuMB expansion lifetime, (c) peak wall velocity, and (d) relative change in AuMB radius following laser excitation as a function of laser fluence. (e) Peak AuMB wall velocities as a function R_{\max}/R_0 and (f) peak photoacoustic signal as a function of peak AuMB wall velocity.

2.4.3 Photoacoustic Emission from AuMBs

Individual AuMBs and freely dispersed AuNRs (1×10^{13} AuNR/ml, OD = 10) were exposed to 5 ns duration laser pulses at fluences between 0.1 and 50 mJ cm^{-2} , and the peak-to-peak amplitude of the photoacoustic signal as a function of fluence was recorded (Figure 2-6A). This concentration of freely dispersed AuNRs was chosen for comparison with single AuMBs because approximately 3000 – 6000 AuNRs were contained in the optical focus of the 100X objective, which is comparable to the number of AuNRs on a single AuMB. Below approximately 5 mJ cm^{-2} , both AuMBs and freely dispersed AuNRs behave as linear photoacoustic contrast agents, which produce a pressure rise, p_0 , in response to pulsed laser excitation: $p_0 = \frac{\beta(T) \Delta T}{\kappa} = \Gamma \mu_a \Phi$, where $\beta(T)$ is the thermal coefficient of volumetric expansion, ΔT is the local temperature increase, κ is the isothermal compressibility, Γ is the dimensionless Grünesien parameter of the surrounding

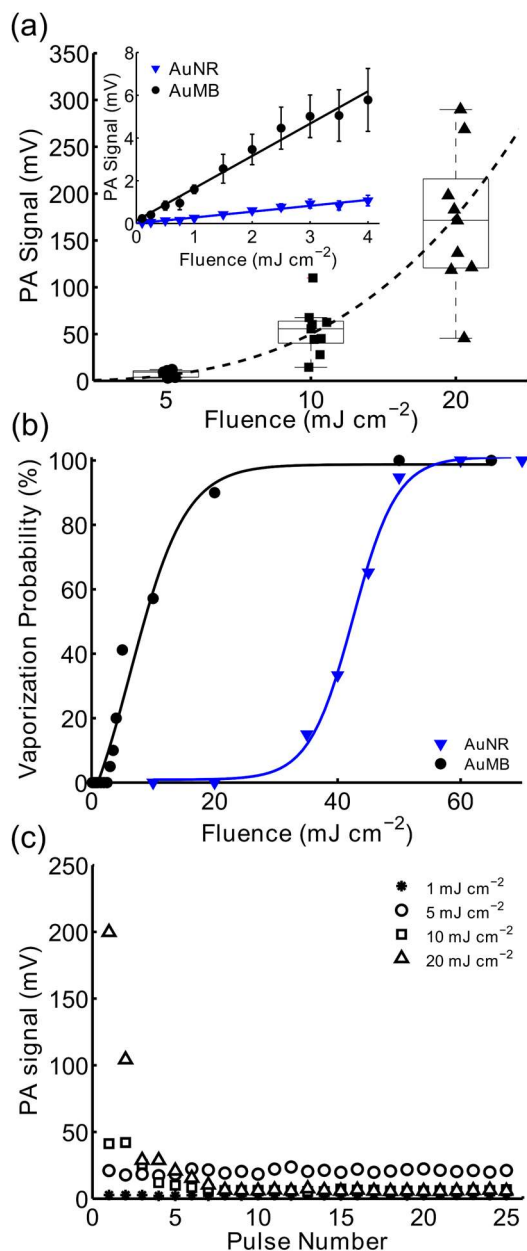


Figure 2-7: Nonlinear photoacoustic response of AuMBs with increasing laser fluence

(a) Peak-to-peak photoacoustic signal amplitudes of single AuMBs and freely dispersed AuNRs (inset) versus laser fluence. (b) Probability of photoacoustic cavitation as a function of fluence for AuMBs and freely dispersed AuNRs. Note the reduction in fluence required to initiate cavitation in AuMBs versus AuNRs (c) Photoacoustic amplitude of a single AuMB exposed to 25 laser pulses at varying fluence. Note that different AuMBs were used at each fluence due to AuNR conversion to gold nanospheres.

medium, μ_a is the absorption coefficient of the nanoparticle, and Φ is the laser fluence.^{30,35,93,94}

For fluences up to approximately 5 mJ cm^{-2} , the photoacoustic signal from single AuMBs scales linearly with increasing fluence and is 5.4 ± 0.6 fold greater than the signal recorded from the

freely dispersed AuNRs (Figure 2-7A, inset). However, above 5 mJ cm^{-2} , the photoacoustic amplitude scales nonlinearly with increasing laser fluence due to rapid AuMB expansion, as described above.^{44,92,93,95,96} At these increased fluences, the relationship between fluence and photoacoustic amplitude is best described by a nonlinear power law relation, $y = ax^k$, with $k = 3.1$. As a result of this nonlinear relationship, the median photoacoustic amplitude at 20 mJ cm^{-2} is 5.8-fold higher than would be expected if photoacoustic amplitudes continued to scale linearly with fluence above 5 mJ cm^{-2} .

In addition, the threshold fluence for homogenous nucleation of vapor nanobubbles on the surfaces of AuNRs was studied. The presence of nanobubble formation within the optical focal region was determined based on the magnitude of the acoustic emission detected from this region (Figure 2-3). The homogeneous nucleation threshold fluence is defined as the fluence at which nanobubble formation occurs 50% of the time.⁹⁵ The probability of nanobubble formation as a function of fluence for single AuMBs and freely dispersed AuNRs is shown in Figure 2-7B. Association of the AuNRs on the AuMB surface reduced the fluence threshold for nanobubble formation from approximately 42 mJ cm^{-2} to 8 mJ cm^{-2} , consistent with the results of previous studies on aggregated plasmonic nanoparticles.^{35,90,92,97}

Finally, photoacoustic signals were recorded for single AuMBs exposed to multiple laser pulses at fluences of 1, 5, 10, and 20 mJ cm^{-2} (Figure 2-7C). The photoacoustic signal of AuMBs exposed to fluences up to 5 mJ cm^{-2} are relatively stable, but photoacoustic signal enhancement only persists for 1 to 2 laser pulses above 5 mJ cm^{-2} due to permanent photothermal conversion of AuNRs to gold nanospheres.^{98,99} Notably, while the photoacoustic signal decayed rapidly over multiple pulses at high fluence, the AuMBs persisted as intact microbubbles, although with

substantially decreased optical absorption at 750 nm and with a decreased radius following laser excitation (Figure 2-6D).

2.4.4 *In vitro* Multi-modality Imaging of AuMBs

In vitro photoacoustic and ultrasound pulse inversion imaging performance was assessed by placing AuMBs (10×10^6 per ml), freely dispersed AuNRs (5×10^{10} per ml), or freely dispersed AuNRs (5×10^{10} per ml) plus non-PDP microbubbles (10×10^6 per ml) into separate flow channels molded into a gelatin phantom. The sample of freely dispersed AuNRs and non-PDP microbubbles was prepared by adding the AuNRs to the microbubbles immediately prior to imaging so as to limit any interactions between the two contrast agents. As shown in Figure 2-8B,C both channels containing microbubbles provided approximately 31.6 ± 4.7 dB increased contrast in pulse inversion imaging mode, while the center of the channel containing freely dispersed AuNRs provided no contrast above background. Note that the pulse inversion imaging mode specifically detects microbubbles by canceling out linear acoustic backscatter from tissue and preferentially retaining non-linear acoustic signals produced by microbubble oscillations.¹⁹

Conversely, all three samples provided photoacoustic imaging contrast, although with markedly different image characteristics. First, the freely dispersed AuNRs generated a photoacoustic image consistent with illuminating a cylindrical target with homogenous optical absorbance (Figure 2-8A).⁶⁰ As shown, no contrast enhancement was observed in the lumen of the channel, but signals from the top (17.3 ± 3.2 dB) and bottom (13.1 ± 2.9 dB) interfaces are clearly distinguishable. The AuMBs also produced a strong photoacoustic signal from the top interface (15.6 ± 2.7 dB) and additionally provided enhanced contrast in the center of the lumen (11.9 ± 3.1 dB) (Figure 2-8B), implying heterogenous optical and acoustic absorption and scattering conditions within the channel.⁶⁰ Finally, the sample of freely dispersed AuNRs and non-PDP

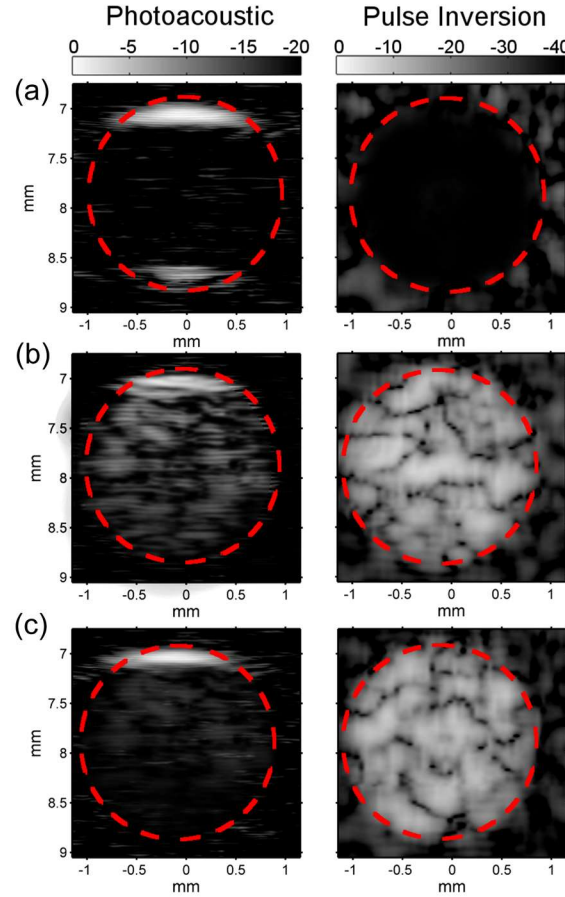


Figure 2-8: *in vitro* ultrasound and photoacoustic images of AuMBs

(a) PA and PI images of freely dispersed AuNRs (5×10^{10} per ml) within a gelatin flow phantom. (b) PA and PI images of AuMBs (1×10^7 per ml) within a gelatin flow phantom. (c) PA and PI images of microbubbles (1×10^7 per ml) and freely dispersed AuNRs within a gelatin flow phantom. All PA data was taken with the following parameters: $\lambda = 750$ nm, 5 mJ cm^{-2} fluence, image comprised of 9 PA averages. PA and PI images are displayed on a linear scale with 20 and 40 dB of dynamic range, respectively.

microbubbles also produced a photoacoustic signal from the top interface (13.7 ± 2.1 dB), but the signal from the lumen was of significantly lower amplitude (4.4 ± 1.7 dB) than the signal produced by the AuMBs ($p < 0.01$).

2.4.5 *In Vivo* Multi-modality Imaging of AuMBs

Approximately 50×10^6 AuMBs were administered to a C57BL/6 mouse via retro-orbital injection to assess the *in vivo* imaging potential of AuMBs. B-mode, pulse-inversion, and photoacoustic images of AuMBs circulating in the murine kidney vasculature are shown in Figure

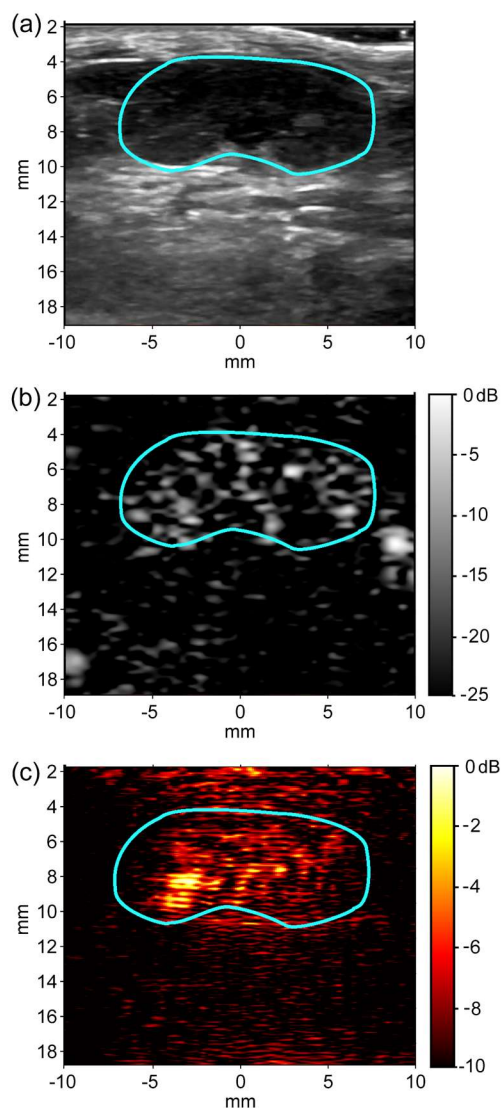


Figure 2-9: *in vivo* imaging of murine kidney following injection of AuMBs

(a) 15 MHz B-mode image of murine kidney (outlined in blue) prior to AuMB administration displayed with 60 dB dynamic range. (b) Pulse-inversion image of kidney demonstrating approximately 20 dB peak-ultrasound contrast enhancement by AuMBs in the renal vasculature. (c) Simultaneously acquired photoacoustic image of AuMBs circulating in kidney demonstrating approximately 5.7 dB average photoacoustic contrast enhancement ($\lambda=750$ nm, 5 mJ cm^{-2} skin fluence, image comprised of 9 photoacoustic averages).

2-9. As shown in Figure 2-9B, the AuMBs enhance the ultrasound contrast by 16.8 ± 3.7 dB in the kidney vasculature, confirming that the presence of the AuNRs on the AuMB surface does not significantly impact their ability to provide acoustic contrast.^{75,78} Additionally, the AuMBs provided an average of 5.7 ± 1.6 dB photoacoustic contrast (skin fluence = 5 mJ cm^{-2}) that was spatially co-registered with the AuMB signal in the pulse inversion image. Ultrasound contrast

enhancement persisted for approximately twelve minutes, while photoacoustic contrast enhancement only lasted approximately three minutes. The mouse experienced no short-term adverse effects to heart or respiration rates as a result of AuMB administration.

2.5 Discussion

2.5.1 AuMB Response in the Linear Regime

In the linear regime, the amplitude of AuMB photoacoustic emissions scales linearly with increasing laser fluence. This behavior mimics that of AuNRs, with the exception that the AuMBs studied in this work produced photoacoustic emissions of 5.4-fold greater amplitude than highly concentrated AuNRs ($1 \times 10^{13} \text{ ml}^{-1}$, $\text{OD} \cong 10$). A similar result was first reported by Dove *et al*, who measured an 8-fold increase in photoacoustic signal amplitude from AuMBs templated with 5 – 7 nm gold nanospheres.⁷⁵ Photoacoustic signal enhancement from AuMBs is probably due to a combination of factors, not least of which is the reduced inter-particle spacing when AuNRs are attached to the microbubble surface. As an example, the freely dispersed AuNRs studied in this work have an approximate inter-particle spacing of 570 nm ($1 \times 10^{13} \text{ ml}^{-1}$). The TEM results presented in Figure 2-4 indicate that AuNRs are spaced much more closely on the AuMB surface (average inter-particle distance $\ll 100$ nm). Therefore, the microbubble acts as a scaffold for preferentially arranging AuNRs at significantly reduced inter-particle distances, which is known to permit thermal field overlap and produce enhanced photoacoustic emissions.^{84,90,100}

Another possible mechanism for photoacoustic enhancement is AuMB expansion and oscillation in response to laser excitation.^{79,101,102} Dove *et al* empirically demonstrated that, in response to low-fluence excitation, AuMBs bearing 5 – 7 nm diameter gold nanospheres on their surface oscillated at or near the resonance frequency of the microbubble. In their study, AuMB radial oscillations ranged between 2 – 10 nm, and the AuMB response from several hundred

thousand consecutive laser pulses was averaged to enable the measurement.⁷⁹ The requirement for stability over this many laser pulses limited the maximum fluence that each AuMB could be exposed to before new nonlinear behaviors, such as those reported in the present study, adversely affected the measurement.

2.5.2 AuMB Response in the Non-Linear Regime

At fluences above approximately 5 mJ cm^{-2} , AuMB photoacoustic amplitudes and radial dynamics begin to scale nonlinearly with increasing laser fluence. Rapid AuMB expansion in this nonlinear regime may be driven by a combination of microbubble gas core expansion and vapor nanobubble formation on the surface of the AuNRs. In this scenario, as the wall of the microbubble core rapidly expands due to conductive heating, it envelopes vapor nanobubbles as they form in response to heating above the homogenous nucleation temperature. Homogeneous nucleation begins to occur at temperatures around $80\% \cdot T_c$ and produces vapor nanobubbles of diameters between $10 - 1000 \text{ nm}$.^{5,103} Large AuMB expansion at fluences below that which is required to elicit homogeneous nucleation may result from the presence of AuNR clusters on the AuMB surface, which are known to reduce the fluence required for vapor nanobubble formation.^{84,90,100}

Interestingly, AuMB expansion in this nonlinear regime resulted in approximately spherically symmetric expansion and compression in close to 70% of AuMBs studied. This is in contrast to polymeric microcapsules recently described by Lajoinie *et al*, which exhibited discrete gas nucleation sites located within a dye-loaded, thick polymer shell.⁸⁹ Symmetric AuMB expansion may suggest relatively uniform AuNR loading on the AuMB surface, and observed departures from this behavior may indicate the presence of large AuNR clusters acting as discrete nucleation sites on the AuMB surface.^{84,90,100} In any case, the formation of a large secondary vapor nanobubble of $\approx 1 \text{ }\mu\text{m}$ diameter on the surface of an AuMB, provides direct evidence in support of

our hypothesis that vapor nanobubble formation plays a role in the rapid AuMB expansion observed in the nonlinear regime.

While AuMB expansion and compression is a violent process, with wall velocities up to 94 m s⁻¹, it was not observed to cause fragmentation of the AuMBs at fluences up to 20 mJ cm⁻². Chomas *et al* conducted detailed studies on the acoustic destruction threshold of microbubble contrast agents and determined that wall speeds up to several hundred meters per second and relative radial expansions exceeding 3-fold were required for consistent destruction of lipid-shelled microbubbles.¹⁰⁴⁻¹⁰⁶ In this study, no AuMBs exposed to fluences below 20 mJ cm⁻² reached these limits, and as a result, remained intact following laser excitation. However, these wall speeds are probably sufficient to temporarily permeabilize cell membranes via sonoporation and mobilize small particles via acoustic radiation force, enabling the delivery of membrane impermeable drugs to cells with fine spatiotemporal control.^{23,85,107,108}

2.5.3 *In Vitro and In Vivo Imaging with AuMBs*

Deploying optical contrast agents on the surface of microbubbles preserves the concomitant advantages that microbubbles afford to ultrasound imaging, primarily: contrast enhancement, therapeutic enhancement via sonoporation, manipulation by acoustic radiation force, and endothelial-cell specific molecular imaging.^{12,23,107,109-114} Both acoustic and photoacoustic contrast enhancement was observed from AuMBs *in vitro* (Figure 2-8), with AuMBs providing significantly more contrast enhancement within the lumen than either freely dispersed AuNRs or a suspension of unbound AuNRs with microbubbles. In addition, AuMBs provided approximately 7.5 ± 2.6 dB enhanced contrast when compared to the suspension of freely dispersed AuNRs and microbubbles, providing further evidence of photoacoustic signal enhancement derived from AuNR aggregation on the microbubble shell.

The *in vivo* pulse inversion images (Figure 2-9B) confirm that AuMBs provide 16.8 ± 3.7 dB ultrasound contrast enhancement, and individual vessels within the murine kidney are easily resolved. Photoacoustic signal enhancement of 5.7 ± 1.6 dB by AuMBs up to an imaging depth of 10 mm (Figure 2-9C) demonstrates suitable photoacoustic imaging signal for *in vivo* applications. Individual blood vessels are not resolvable in the photoacoustic images, primarily due averaging data across multiple photoacoustic acquisitions to achieve suitable SNR. Ultrasound contrast enhancement persisted for approximately twelve minutes, while photoacoustic contrast enhancement only lasted approximately three minutes. Reduced photoacoustic contrast duration may be a result of the lower sensitivity inherent to photoacoustic imaging and photothermal conversion of AuNRs to nanospheres, which reduces the magnitude of the longitudinal plasmon resonance at $\lambda = 750$ nm.⁹⁸ However, it should be noted that photothermal conversion is a limitation that may be overcome by coating AuNRs in a rigid, melt resistant, silica shell, as described by Chen *et al.*⁹⁹

A total of 50×10^6 AuMBs carrying approximately 2×10^{11} AuNRs (0.5 nM) were injected, which is considerably fewer AuNRs than was required to provide photoacoustic contrast in comparable *in vivo* imaging settings.⁶⁵ Increased photoacoustic contrast at lower AuNR concentrations may result from a combination of enhancement inherent to AuMBs, differing biodistribution patterns, and altered clearance mechanisms from the blood stream.^{13,115-117} The optical power output of the linear-array photoacoustic imaging system (5 mJ cm^{-2} skin fluence at $\lambda = 750$ nm) was probably insufficient to cause widespread vapor nanobubble formation on the surface of AuMBs in the murine kidney, however, these results are the first demonstration of simultaneous *in vivo* ultrasound and photoacoustic imaging with AuMBs, confirming the feasibility of the multimodality imaging technique.

2.5.4 Limitations

The magnitude of the photoacoustic emission was observed to increase with increasing laser fluence, AuMB wall velocity, and relative AuMB expansion. However, the acoustic emission during rapid expansion or compression cycles is broadband, and neither the 10 MHz single-element transducer nor the CL15-7 linear array transducer were able to adequately sample the entire photoacoustic waveform generated by the AuMBs. Thus, the reported increase in photoacoustic amplitude may be an underestimation due to the bandwidth limitations of the ultrasound instrumentation.

The AuMBs studied in this report utilize AuNRs to confer optical absorbance at near-infrared wavelengths and permit deep tissue *in vivo* imaging. Relative to gold nanospheres, AuNRs exhibit enhanced optical absorption and improved heat transfer properties, which permits enhanced photoacoustic signal generation and nanobubble formation on the AuNR surface at lower fluence.^{35,90} Therefore, the laser fluence required for a transition into the nonlinear regime may have been significantly higher if small gold nanospheres were used instead of AuNRs. However, the inverse is also true, in that the transition to nonlinear AuMB behavior may be achieved at even lower fluence by replacing AuNRs with nanoparticles that exhibit enhanced optical absorption (e.g. gold nanocages, golden carbon nanotubes).

2.6 Conclusions

AuMBs exhibited two distinct behaviors that were a function of laser fluence. In the linear regime, individual AuMBs produced photoacoustic waves with 5.4-fold increased amplitude relative to highly concentrated freely dispersed AuNRs, although no AuMB oscillations were detected microscopically. Above fluences of approximately 5 mJ cm^{-2} , AuMBs rapidly expanded and produced large amplitude photoacoustic waves that scaled nonlinearly with laser fluence. The

increase in photoacoustic amplitude may be explained by a combination of properties inherent to AuMBs. First, the AuMB surface provides a scaffold for AuNR aggregation at small inter-particle spacing that permits thermal field overlap and increased water temperatures. Second, heat transfer into the AuMB gaseous core causes thermal expansion of the gas phase, giving rise to large amplitude photoacoustic emissions due to an increase coefficient of thermal expansion. Third, close placement of AuNRs to the liquid-gas interface on the AuMB surface increases local water temperatures to the point that homogeneous nucleation occurs, resulting in the formation of vapor nanobubbles that contribute to AuMB expansion. Finally, a pilot *in vivo* imaging study with a linear-array photoacoustic imaging system achieved 16.8 ± 3.7 dB ultrasound and 5.7 ± 1.6 dB photoacoustic contrast enhancement from AuMBs, demonstrating their potential as effective multimodality contrast agents for deep tissue ultrasound and photoacoustic imaging.

Chapter 3. Finite element modeling of optically absorbing microbubble oscillations in response to nanosecond pulsed laser excitation²

3.1 Abstract

Optically absorbing microbubbles are comprised of a surfactant-shelled gas microbubble with optically absorbing dyes or nanoparticles located within or on the surface of the microbubble shell. These agents exhibit unique photoacoustic properties and have recently been shown to oscillate at or near the resonance frequency of the microbubble following nanosecond pulsed laser excitation. Oscillation is driven by heat transfer from the optically absorbing material into the gaseous core of the microbubble, causing rapid thermal expansion of the gas. In this work, the optically driven microbubble oscillations are modeled using a combination of finite element analysis and an analytical model. First, the heat transfer from gold nanorods to the microbubble gas core is modeled over nanosecond timescales using finite element analysis to determine the energy transferred into the gas core. Second, the microbubble's response to heating of its gaseous core is modelled analytically by a modified Rayleigh-Plesset model of microbubble oscillations in which gas temperature is the driving term. The combined model recapitulates the results of a recently published empirical study of optically-driven microbubble oscillations. Specifically, maximal

² This chapter contains content drawn from the following peer-reviewed conference and journal publications:
 AJ Dixon, S Hu, AL Klibanov, JA Hossack, "Oscillatory dynamics and *in vivo* photoacoustic imaging performance of plasmonic nanoparticle-coated microbubbles." *Small*, 11(25), 3066-3077, 2015.
 AJ Dixon, S Hu, AL Klibanov, JA Hossack, "Empirical and theoretical study of the interaction between plasmonic-nanoparticle coated microbubbles and nanosecond pulsed laser excitation." 21st European Symposium on Ultrasound Contrast Agents (2016), Rotterdam, The Netherlands.
 AJ Dixon, S Hu, AL Klibanov, JA Hossack, "Photoacoustic properties of plasmonic nanoparticle coated microbubbles." IEEE International Ultrasonics Symposium (2015), Taipei, Taiwan.

radial excursions are shown to be on the order of 10 to 100 nm and the microbubble oscillates at its resonant frequency, as determined by the microbubble radius and the viscoelastic properties of its surfactant coating.

3.2 Introduction

Photoacoustic imaging is a noninvasive imaging technique that provides high contrast images of optical absorption deep within living tissue. Although first investigated for the detection of endogenous chromophores, PA imaging has been extended to molecular imaging applications through the use of exogenous contrast agents that are targeted to specific extracellular or intracellular molecules.³⁰ Photoacoustic contrast agents, ranging from dyes to plasmonic nanoparticles, are often designed to strongly absorb light in the near-infrared (NIR) wavelengths, where the optical absorption of native tissue chromophores is at a minimum.

Detection of exogenous photoacoustic contrast agents *in vivo* is typically achieved by acquiring multiple photoacoustic images over a range of light wavelengths near the contrast agent's optical absorption maximum.^{65,70} Photoacoustic waves are recorded by conventional ultrasound receive instrumentation, and the magnitude of the measured pressure wave is used to identify the presence of the contrast agent. However, acoustic waves encode more information than just magnitude. Frequency and phase information have long been used for ultrasonic tissue characterization¹¹⁸ and contrast enhanced ultrasound imaging,¹¹⁹ and may find use in photoacoustic imaging applications.

The frequency content of photoacoustic waves has not been thoroughly studied, even though Diebold *et al* experimentally validated that the shape of the photoacoustic pressure wave is a function of both the shape of the optical absorber and the shape of the optical pulse.^{60,120} More recently, others have demonstrated that frequency-domain based analyses of the received photoacoustic wave can be used to characterize endogenous microstructures in biological

samples¹²¹ and distinguish between healthy and cancerous tissues.¹²² In addition, Dove *et al* and Dixon *et al* have designed microbubble-based photoacoustic contrast agents to produce photoacoustic emissions with known frequency content.^{79,123} The underlying hypothesis is that these optically absorbing microbubbles can be specifically detected on the basis of their unique frequency response, rather than on the basis of their optical absorption, like conventional dye or nanoparticle-based photoacoustic contrast agents.

The purpose of this work was to simulate the photoacoustic emissions arising from optically absorbing microbubbles. The photoacoustic response of these agents has been simulated analytically by others, but existing models predict microbubble radial excursions of up to two orders of magnitude larger than what has been observed empirically or make unrealistic assumptions to ease simulation, such as assuming the optically absorbing material is uniformly distributed within the gaseous phase.^{101,102} To improve on existing models, we employ finite element analysis to simulate the heating of gold nanorods in response to nanosecond pulsed laser excitation. The gold nanorods are located on the microbubble shell, approximately 10 nm from the gaseous core, so heat dissipation from the nanorod is altered by the liquid/gas interface – an effect that has not been previously considered. Ultimately, heat transfer into the gas core is modelled numerically, and heating of the gas core is used as a driving function to analytically model microbubble oscillations in a modified Rayleigh-Plesset model.¹²⁴

3.3 Materials and Methods

3.3.1 Finite element heat transfer model

The heat transfer equations for a single gold nanorod (AuNR) and its surrounding medium during a nanosecond duration laser pulse are:^{93,125-127}

$$\rho_p c_p(T_p) \frac{\partial T_p}{\partial t} = k_p(T_p) \nabla T_p + \frac{\sigma_{abs} F_{pulse}}{V_p \tau_{pulse}} \quad \text{Equation 3-1}$$

$$\rho_w c_w(T_w) \frac{\partial T_w}{\partial t} = k_w(T_w) \nabla T_w \quad \text{Equation 3-2}$$

where p denotes properties of the particle, w denotes properties of the water, ρ is density, $c(T)$ is specific heat, T is temperature, k is thermal conductivity, σ_{abs} is the nanoparticle absorption cross section, F_{pulse} is laser fluence, V_p is particle volume, and τ_p is laser pulse width. This formulation assumes that the laser energy is absorbed homogeneously throughout the AuNR volume and that there is no mass transfer. The rate of heat loss from the nanoparticle to its surroundings is calculated by taking into account the thermal interface conductance by:^{5,82,128}

$$\dot{Q}_w = A_{surface} \cdot G \cdot (T_p - T_{w,surface}) \quad \text{Equation 3-3}$$

where $A_{surface}$ is the surface area of the AuNR, G is the thermal contact conductance, and $T_{w,surface}$ is the water temperature at the AuNR surface. The thermal conductance is a coupling parameter between the AuNR and water energy equations and is the source of a temperature discontinuity at the AuNR surface.

Thermal continuity and conductive heat transfer boundary conditions are enforced at the water – gas boundary:

$$T_g(t) = T_w(t); k_g(T_g) \nabla T_g = k_w(T_w) \nabla T_w \quad \text{Equation 3-4}$$

where subscript g denotes properties of the gas. Estimates of the total energy transferred from the water to the microbubble gas core are computed by integrating the heat flux across this boundary over the entire duration of the simulation. The simulation does not explicitly model expansion of the gas phase as it increases in temperature, but $k_g(T_g)$ decreases as a function of temperature. The model assumes that the gas core is comprised completely of decafluorobutane, although it is known that vapor and other gases are also present in the microbubble core.

Table 3-1: Thermal material properties used in finite element heat transfer model

Parameter	Symbol	Unit	Value
Gold density	ρ_g	kg m ³	193×10^4
Gold specific heat	c_{pg}	J kg ⁻¹ K ⁻¹	$111.6515 + 0.066T - 2.6554 \times 10^{-6}T^2$
Gold thermal conductivity	k_g	W m ⁻¹ K ⁻¹	$3335.4544 - 5.8253 \times 10^{-2}T - 7.4773 \times 10^{-6}T^2$
Nanorod absorption cross-section	C_{abs}	nm ²	2450, Ref [3]
Thermal contact conductance	G	W m ⁻² K ⁻¹	105×10^6 , Ref [5]

Equations 3-1 through 3-4 have temperature dependent coefficients and must be solved numerically. The solution to these equations has been implemented in a finite element solver using a non-linear, iterative conjugate gradient descent solver (PZFlex, Weidlinger Associates, Mountain View, CA), which is a general purpose technique for accurately solving PDEs. The computational grid spanned a $400 \times 200 \times 200$ nm volume meshed with $0.5 \times 0.5 \times 0.5$ nm cubic elements. The gas core comprised $200 \times 200 \times 200$ nm of the model, while the remaining $200 \times 200 \times 200$ nm was water and contained the AuNR. The model and mesh size were refined until the solution was invariant to mesh density changes. Infinite thermal boundary conditions were enforced on all six faces of the computational grid by forcing the potential function to zero at infinity.^{129,130} The numerical simulation code (PZFlex) for a representative simulation is given in Appendix A.3.

All thermal properties for water and superheated water above its usual boiling point were taken from the NIST Chemistry WebBook, the thermal properties for gaseous decafluorobutane were taken from Ref. [131], and the thermal properties for gold are given in Table 3-1.¹³²

3.3.2 Estimating AuMB Radial Wall Motion

Radial expansion of a lipid-shelled microbubble may be estimated by the modified Rayleigh-Plesset equation:^{44,133,134}

$$\frac{p_g(t) - p_\infty}{\rho_L} = R \frac{d^2 R}{dt^2} + \frac{3}{2} \left(\frac{dR}{dt} \right)^2 + \frac{4\mu_L}{R} \frac{dR}{dt} + \frac{2\sigma}{\rho_L R} + \frac{4\kappa_s}{R^2} \frac{dR}{dt} \quad \text{Equation 3-5}$$

where the time-varying gas pressure is given by:

$$p_g(t) = \left(p_\infty + \frac{2\sigma}{R_0} \right) \left(\frac{R_0}{R} \right)^{3\gamma} \left(\frac{T_g(t)}{T_0} \right) \quad \text{Equation 3-6}$$

and p_∞ is ambient pressure, ρ_L is water density, R is microbubble radius, μ_L is water viscosity, σ is surface tension at the liquid-gas interface, κ_s is the dilational viscosity from the lipid monolayer, γ is the ratio of the gas specific heats, and T_0 is the initial gas temperature. This formulation of the Rayleigh-Plesset equation assumes mass transfer in and out of the microbubble is negligible, which is approximately true for rapid microbubble expansion. Furthermore, there is no acoustic driving term, $p_{ac}(t)$, as is often found in the Rayleigh-Plesset equation, as microbubble oscillations in this model are driven by changes in gas temperature, $T_g(t)$. $T_g(t)$ is assumed to be homogenous throughout the microbubble volume and changes to $T_g(t)$ result exclusively from heat transferred from the water into the gas core. $T_g(t)$ at each time step is calculated from the results of the heat

Table 3-2: Microbubble properties used in modified Rayleigh-Plesset model

Parameter	Symbol	Unit	Value
Water density	ρ_L	kg m ³	999.97
Water viscosity	μ_L	Pa s	8.9×10 ⁻⁴
Surface tension	σ	N m ⁻¹	0.02, Ref [1]
Lipid monolayer dilational viscosity	κ_s	kg s ⁻¹	7.2 ×10 ⁻⁹ Ref [2]
Ratio of decafluorobutane specific heats	γ	None	1.07

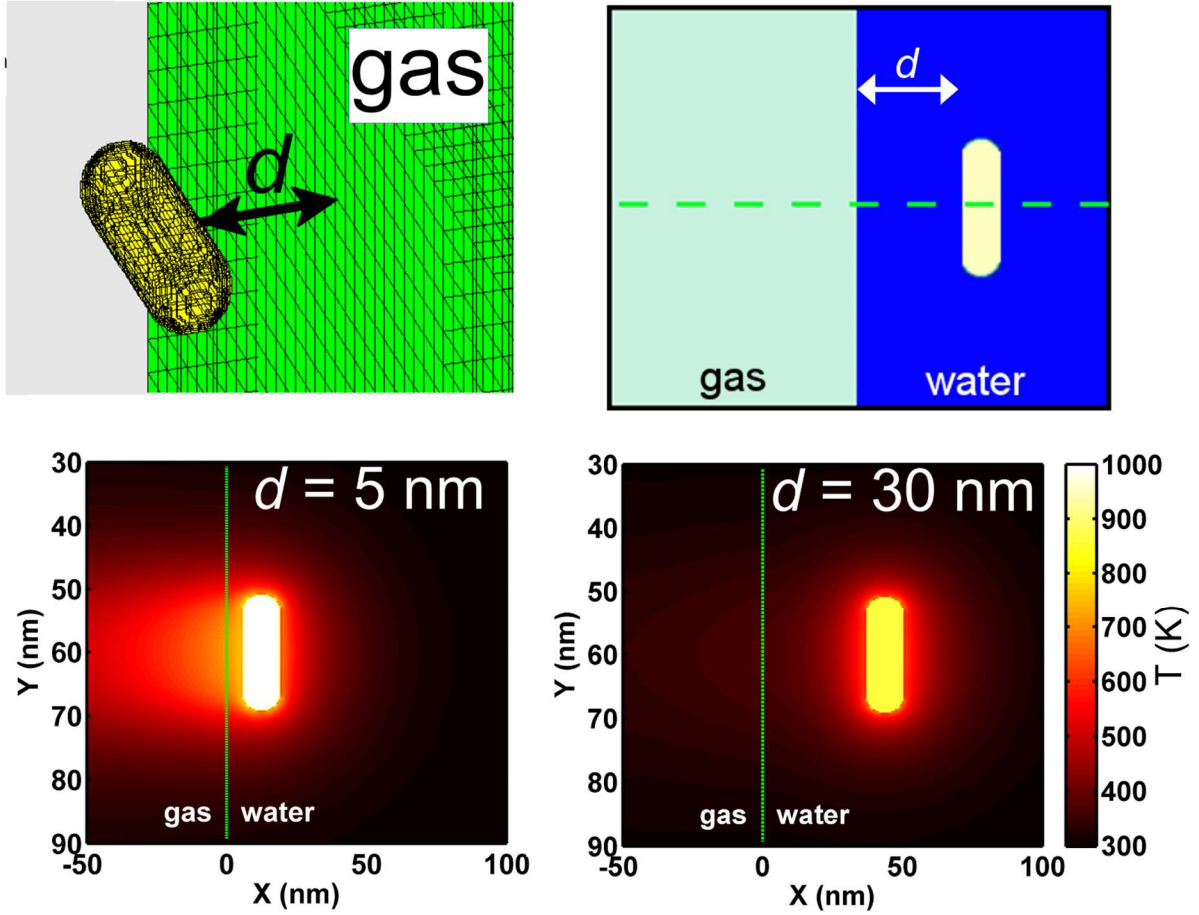


Figure 3-1: Finite element heat transfer model geometry and thermal fields

(Top Left) 3D model geometry of an AuNR placed d nm from the liquid/gas interface. The liquid nodes are not shown. The gas nodes are green. (Top Right) 2D cross-section of 3D heat transfer model. The dashed green line is the cross-section of thermal profiles shown in Figure 6-2 and 6-3. (Bottom Left) Thermal field immediately following laser pulse when AuNR is 5 nm from liquid/gas interface. (Bottom Right) Thermal field immediately following laser pulse when AuNR is 30 nm from liquid/gas interface.

transfer simulations by $Q(t) = mC_p(T_g(t) - T_0)$, where m is the mass of the gas core and C_p is the specific heat at constant pressure. The solution to Equation 3-5 was solved using MATLAB's ode45 differential equation solver. Microbubble parameters used in the simulations are given in Table 3-2.

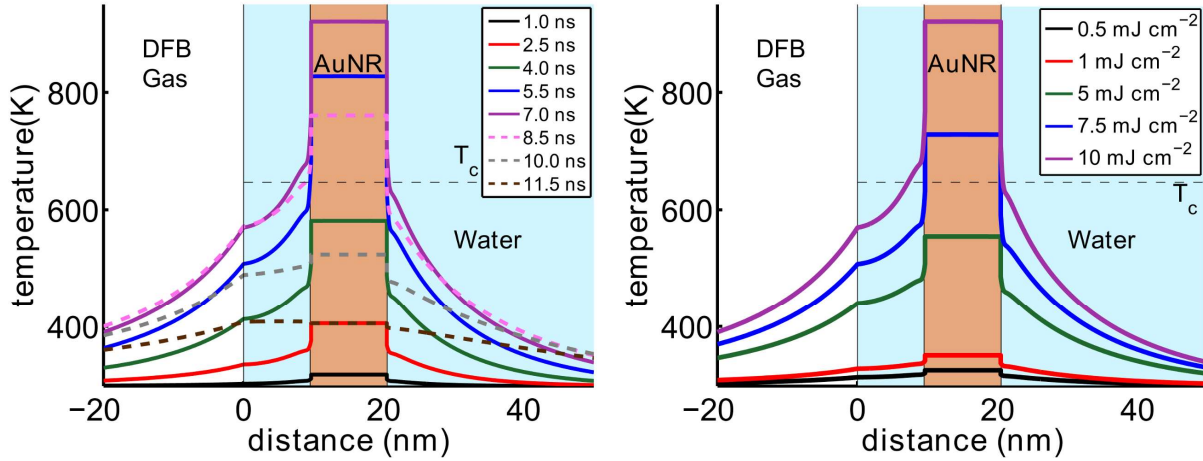


Figure 3-2. Thermal fields over time and with increasing laser pulse energies

(Left) Simulated temperature profiles between 1 – 11.5 ns for an AuNR placed 10 nm from the liquid-gas interface. The laser energy was 10 mJ cm⁻² (Right) Simulated temperature profiles for an AuNR placed 10 nm from the liquid-gas interface and exposed to varying fluence. These profiles were captured at $t = 7$ ns, when the peak AuNR temperature occurred.

3.4 Results

3.4.1 Thermal Analysis at the AuMB Surface

The enhanced photoacoustic signal produced by AuMBs and the transition to a nonlinear relationship between laser fluence and photoacoustic amplitudes is hypothesized to result from both thermal-field overlap between closely-spaced AuNRs on the AuMB surface and modified heat transfer dynamics in the vicinity of the liquid-gas interface.^{75,79,123} The effect of thermal field overlap and plasmonic nanoparticle aggregation has been considered previously.^{84,90,100} To determine the impact of the liquid-gas interface, a 3D finite-element model was developed to study the thermal effects of coupling a single AuNR to the microbubble shell.^{125,126} Given the small length scales involved, the primary mode of heat transfer between the AuNR, water, and the gas core is conduction. This may be verified by consideration of the Grashof number ($Gr = \frac{g\beta\Delta TV}{\nu^2}$) for this system, which indicates that viscous forces dominate buoyant forces at these dimensions.¹²⁸

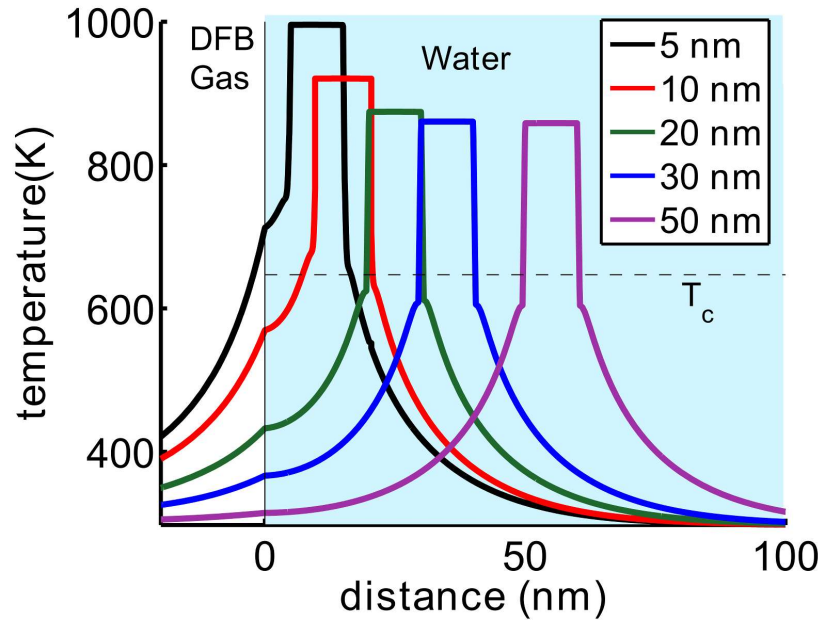


Figure 3-3: Effect of distance between AuNR and gas/liquid interface on thermal field

Simulated temperature profiles as the distance between the AuNR and the liquid/gas interface is increased. Laser fluence was 10 mJ cm^{-2} in all simulations.

The model geometry and representative two-dimensional heat transfer results from a single plane in the 3D model are shown in Figure 3-1.

In the simulations, a Gaussian-shaped laser pulse with 5 ns duration (FWHM) was applied to a single AuNR placed at varying distances, d , from the liquid-gas interface. The laser pulse was centered at 7 ns, and thermal profiles of the AuNR, water, and gas core at varying time steps are shown in Figure 3-2. For an AuNR placed 10 nm from the liquid-gas interface, peak AuNR temperatures occur at approximately 7 ns, while peak gas temperatures occur at 8.5 ns. The effect of increasing the laser fluence applied to an AuNR placed 10 nm from the liquid-gas interface is also shown in Figure 3-2. As shown, water temperatures in between the gas and AuNR are between 8-12% higher than water temperatures on the opposite side of the AuNR on account of reduced heat transfer into the gas core. Note that water temperatures begin to reach temperatures (80% ·

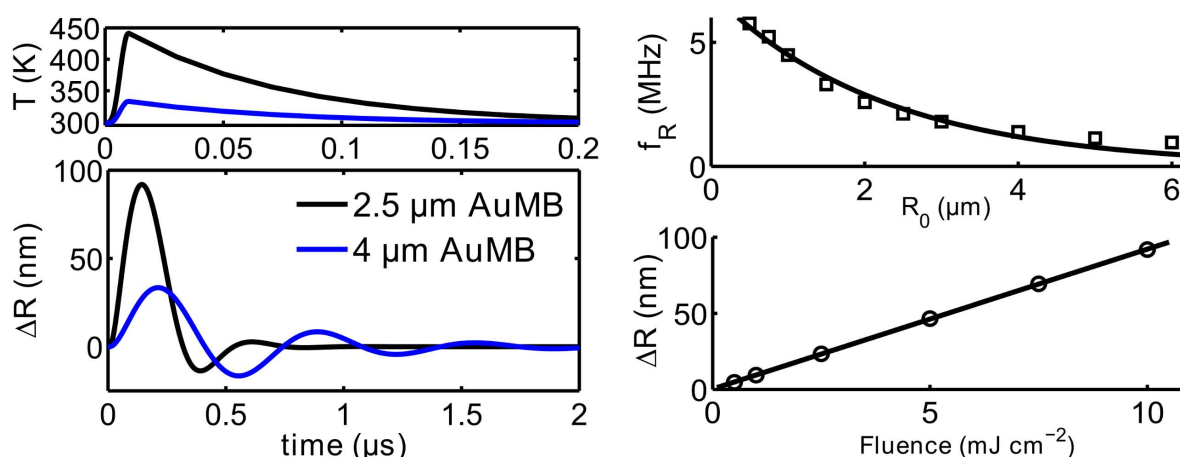


Figure 3-4: Microbubble gas temperatures and simulated oscillatory frequencies

(Left Top) Microbubble gas temperatures following a laser pulse with fluence of 10 mJ cm^{-2} . The black curve is for a microbubble with $2.5 \mu\text{m}$ diameter and the blue curve is for a microbubble with $4 \mu\text{m}$ diameter. (Left Bottom) Simulated change in microbubble radii for $2 \mu\text{s}$ following laser excitation. (Right Top) Simulated oscillation frequency of optically excited microbubbles of varying radii. (Right Bottom) Simulated maximum radial excursions of a $2.5 \mu\text{m}$ with increasing laser fluence.

T_c) that could result in homogenous nucleation of vapor nanobubbles at fluences above 7.5 mJ cm^{-2}

2,5,82,103

The effect of increasing the distance of the AuNR from the liquid-gas interface is shown in Figure 3-3. The AuNR reaches significantly higher temperatures when placed closer to interface (16% higher at $d=5 \text{ nm}$ vs $d=50 \text{ nm}$), which translates to increased heat transfer into the microbubble core and increased probability of water vaporization at reduced laser fluence. At distances above approximately 30 nm , thermal interactions between the AuNR and the gas core are significantly reduced.⁹⁶ Given the lengths of the lipid monolayer and PEG-2000 spacer, the AuNRs on the AuMBs used in the experimental studies are approximately $5 - 15 \text{ nm}$ from the liquid-gas interface, depending on whether PEG-2000 exists in the brush-like or mushroom-like conformation.^{12,135}

3.4.2 Optically Driven Microbubble Oscillations

The heat transfer simulations were used to estimate the total amount of energy transferred from the AuNR into the gas core. If the gas core is assumed to heat homogenously such that its time-varying temperature may be written as $T_g(t)$ and the effects of mass transfer and vapor pressure are assumed to be negligible, then AuMB radial wall motions may be estimated by the modified Rayleigh-Plesset equation (Equation 3-5). The total energy transferred from the AuNR into the AuMB was computed at each time step of the heat transfer simulations in order to estimate $T_g(t)$. Overall, between 0.2 – 4.8% of the energy deposited in the AuNR is transferred into the gas core, depending on the distance between the AuNR and the liquid/gas interface (0.2% corresponds to a distance of 50 nm, while 4.8% corresponds to a distance of 10 nm). The simulated gas temperatures and radial perturbations of two AuMBs containing 5000 AuNRs on their respective surfaces are presented in Figure 3-4. Regardless of AuMB size, the peak gas temperature is reached at approximately 8.5 ns and decays to T_0 over the next 200 ns. The 4 μm diameter AuMB exhibits lower amplitude radial oscillations than the 2 μm diameter AuMB on account of its gas core reaching lower temperatures. Furthermore, the AuMBs oscillate at different frequencies, as is expected based on the difference in their resonance frequencies.⁷⁹ Finally, a compilation of simulation results at varying fluence and AuMB radii is shown in Figure 3-4. As discussed, the AuMBs oscillate according to their resonance frequency (f_R), and maximum radial excursions (ΔR) approach 100 nm for a 2.5 μm diameter AuMB exposed to 10 mJ cm^{-2} laser fluence. The simulation results are in good agreement with the experimental results of Dove *et al*, who measured ΔR up to 10 nm for AuMBs coated with weakly-absorbing 5 - 7 nm diameter gold nanospheres at low laser fluence.⁷⁹

3.5 Discussion

3.5.1 Finite Element Heat Transfer Model

Finite element modeling is regularly employed to simulate the laser-induced heating of plasmonic nanoparticles, in large part due to the difficulty of empirically studying the heating of nanometer-sized particles on nanosecond (or shorter) timescales. Much has been learned through optical and thermal modeling of photon interactions with plasmonic nanoparticles, including the properties of electron thermalization (also known as lattice heating),¹²⁸ heat transport into the surrounding medium,^{96,128,136} heat transport between aggregates of particles,^{100,136} and nanoparticle fragmentation.^{98,137} In particular, Pitsillides *et al* calculated that the temperature of the surrounding fluid falls to $1/e$ of the surface temperature of the nanoparticle at a distance of approximately one particle radius (15 nm).⁹⁶ The surface temperature of the particle reaches several hundreds of Kelvin above ambient, even in response to relatively low laser energies, due to the high extinction coefficient inherent to plasmonic nanoparticles and limited electron-phonon coupling, which limits heat transfer out of the particle into its surrounding medium.^{3,138,139} Specifically, absorbed energy is rapidly converted to heat via electron thermalization, but the thermal contact resistance at the boundary between the metal nanoparticle and its liquid surroundings limits the maximal rate of heat transfer from the particle,^{103,139,140} thereby significantly increasing the nanorod temperature. Explosive boiling occurs at the surface of the nanoparticle when its surface temperature reaches approximately 80 % of the fluid's critical temperature (T_c), at which point finite element techniques can no longer reliably predict the system's thermal or mechanical properties on account of phase transition of the fluid immediately surrounding the nanoparticle.¹⁰³ However, finite element modeling is able to predict laser fluences at which explosive boiling can occur and accurately recapitulates the temperature of the materials surrounding the nanoparticle.

This work represents the first finite element model to consider the thermal effects of a gas/liquid interface in close proximity to a laser-heated gold nanoparticle. This is a unique scenario on the surface of a bubble, but is of relevance to better understand the properties of optically absorbing microbubbles as photoacoustic contrast agents. Heat transfer across the gas/liquid interface is governed by a conductive heat transfer mechanism given the time and short lengths scales involved.^{93,94} Thus, the thermal conductivity of each medium dominates, and the gas phase acts as a thermally insulating barrier, serving to increase local water temperatures. This effect is intensified when the nanorod is placed in closer proximity to the gas/liquid interface (Figure 3-3), possibly explaining why the photoacoustic amplitudes observed from optically absorbing microbubbles is higher than what is observed from freely dispersed nanorods.^{75,123} Specifically, the peak water temperature is predicted to increase from approximately 605 K to 780 K when the nanorod is moved from 50 nm to 5 nm away from the liquid gas interface, thereby accounting for a potential 28% increase in photoacoustic amplitudes. This result, in particular, provides motivation for nanoscale-level design of AuMBs and suggests that heat transfer and photoacoustic amplitudes may be modified by altering the length of the PEG spacer. Additional increases in the photoacoustic amplitude observed when imaging optically absorbing microbubbles is likely explained by thermal field overlap from aggregated nanoparticles on the microbubble surface. This effect was not explicitly studied in this work, but has been widely considered elsewhere.^{3,90,100,141}

3.5.2 Optically Driven Microbubble Oscillations

The response of optically absorbing microbubbles to pulsed laser excitation is dependent upon laser fluence. In response to high fluence, the nanoparticle temperature exceeds the threshold for explosive boiling and the photoacoustic response is broadband and is dominated by vapor bubble formation on the surface of the microbubble as described by Dixon *et al.*¹²³ However, in response

to lower fluence, the nanoparticle temperature does not approach the threshold for explosive boiling, and the photoacoustic response is due to a combination of thermal expansion of the surrounding water and thermally-driven oscillations of the microbubble.^{79,123} In this regime, the amplitude of optically absorbing microbubble photoacoustic emissions scales linearly with increasing laser fluence, much like that of freely dispersed nanorods. However, multiple investigations have established intensified photoacoustic emissions when nanorods or nanospheres are templated on the surface of the microbubble.^{75,78,123} As discussed above, this effect is probably due to a combination of thermal and acoustic factors, including increased temperatures due to nanoparticle aggregation and proximity to an insulating gas/liquid interface.

Increased photoacoustic amplitudes may also arise due to the unique frequency response of optically absorbing microbubbles.^{79,123} Dove *et al* empirically demonstrated that nanoparticle-coated microbubbles undergo nanometer-scale radial oscillations in response to pulsed laser excitation, and that the frequency of oscillation is governed by the resonant frequency of the microbubble.⁷⁹ The simulation results of this work support Dove *et al*'s findings and place an upper limit on the magnitude of microbubble oscillations of approximately 100 nm, before explosive boiling is predicted to occur at the nanoparticle/liquid interface. However, these radial oscillations are sufficient to produce local pressure disturbances on the order of hundreds of kilopascals emanating from the microbubble, which is of a sufficient magnitude for detection by sensitive photoacoustic instrumentation. In particular, if the microbubble resonance is matched to the bandwidth of the photoacoustic receive system, then significant gains in photoacoustic signal amplitude compared to the emissions of freely dispersed nanorods may result.^{79,123}

Another potential benefit of tuning the frequency response of photoacoustic emissions by selecting a specific microbubble radius is the ability to perform multi-target photoacoustic

molecular imaging with a single wavelength laser. The majority of the cost and equipment associated with photoacoustic imaging systems is attributable to the tunable wavelength lasers, which are required for spectroscopic molecular imaging. However, if molecular targets could be discriminated based on the frequency of photoacoustic emissions produced by optically absorbing microbubbles of differing size, then multi-target photoacoustic imaging could potentially be performed without the need for expensive laser systems with large footprints. This is a future direction that warrants further investigation.

Finally, although the results of this study are similar to the empirical results acquired by Dove *et al.*,⁷⁹ they do not closely match existing analytical models of optically absorbing microbubble oscillations.^{101,102} Both Firouzi *et al* and Sassaroli *et al* predict microbubble radial oscillations in excess of 500 nm in response to pulsed laser excitation, but this is two orders of magnitude greater than oscillations observed by Dove *et al* and almost an order of magnitude larger than the upper bound predicted in this study.^{101,102} The primary discrepancies between the existing models and the model presented herein are the amount of thermal energy that is assumed to transfer to the gaseous phase of the microbubble and considerations related to the onset of explosive boiling and vapor bubble formation. The simulation results of this study indicate that, on average, less than 5% of the energy absorbed by the nanorod is transferred into the gaseous phase, which places a limit on the maximum radius of microbubble excursion. Similarly, arbitrarily high laser fluences are not possible in reality due to the onset of vapor bubble formation – an effect considered by the present model but not considered by others.

3.5.3 Limitations

The model developed in this work has several limitations that must be considered when interpreting its results. First, optically absorbing microbubbles contain several thousand plasmonic

nanoparticles on their surface,^{75,79,123} but the finite element model only considered the heat transfer from a single nanorod into the gaseous core. Microbubble oscillation in response to a temperature rise was derived based on the assumption that the thermal contribution from all nanorods on the microbubble shell could be extrapolated from the model of the single nanorod. While this assumption is probably true to first-order, it should be noted that it does not take into account the effects of nanorod aggregation, which will produce local hot-spots on the microbubble surface and may produce asymmetrical oscillations.¹⁰⁰ The model also only considered one orientation of the nanorod with respect to the microbubble shell, but each nanorod is free to assume any orientation in 3D space relative to the shell. Thus, nanorods with less surface area oriented parallel to the microbubble shell would contribute less to microbubble heating and oscillation.

In addition, the analytical model of microbubble oscillations assumes that the gas temperature, T_g , is uniform throughout the entire gaseous core and that gas expansion and compression is a polytropic, isentropic process with polytropic index, n , equal to γ , the ratio of the specific heats.⁴⁴ The primary limitation of these assumptions is that the temperature of the gas is only accurate for small microbubble radial oscillations. As the microbubble expands or contracts, the microbubble gas temperature is expected to cool or heat, respectively, but this is not explicitly modeled. Instead, all thermal fluctuations of the gas temperature are driven by heat transfer from the nanorods on the microbubble surface. The decision to neglect modelling the thermal effects of expansion and cooling was driven by the observation that the expected microbubble radial oscillations were very small (less than 5% of the microbubble resting diameter) and the fact that the maximum gas temperature rise from heated nanorods was less than 200 K. For reference, the effects of bubble expansion and contraction with respect to internal gas temperatures and heat transfer to the surrounding medium has been widely studied in the context of sonoluminescence, in which the

goal was to model temperature rises of several thousand Kelvin in a rapidly contracting bubble.¹⁴²⁻

146

Finally, although the finite element model considers the temperature dependence of the thermal conductivities of all materials (e.g. water, gold, gas), the analytical model of microbubble oscillations does not take temperature variations into account. Given the high temperatures in the vicinity of the lipid shell, it is probable that the viscoelastic properties of the lipid membrane are altered. In particular, the dilational viscosity, κ_s , and surface tension, σ , are expected to vary with temperature such that at high temperatures, especially those above the gel temperature of the lipid, the microbubble is expected to take on properties of an unshelled bubble. This would reduce the dampening in the system and drive longer, higher amplitude microbubble oscillations, as has been observed empirically by Dove *et al.*⁷⁹ In fact, the primary discrepancy between the results of this model and the published empirical results is that the model predicts only a few microbubble oscillations following laser excitation on account of the highly damped nature of the microbubble shell, while empirical results have demonstrated significantly more oscillations. This discrepancy may be reconciled in future versions of the model by accounting for temperature effects on the viscoelastic properties of the lipid shell.^{147,148}

3.6 Conclusions

The radial microbubble oscillations arising from nanosecond pulsed laser excitation of optically absorbing microbubbles were simulated using a combination of finite element and analytical modeling techniques. The finite element heat transfer model determined that between 0.2 and 4.8 % of energy absorbed by nanorods on the microbubble surface was transferred into the microbubble gas core to drive microbubble oscillations. Microbubbles were determined to oscillate at their resonant frequency following laser excitation, with radial oscillations between 1 and 100

nm. The scale of microbubble oscillations and frequencies determined by this modeling framework closely match recently published empirical results of similar agents – microbubbles with gold nanospheres on their surfaces – thereby providing direct, independent validation to the results of this model.

Part II: Microfluidic Production of Microbubbles for Sonothrombolysis Applications

Chapter 4. Development of a catheter-dimensioned microfluidic device for intravascular production of microbubbles³

4.1 Abstract

Catheter-based interventions have been widely investigated for the treatment of thrombo-occlusive diseases, including stroke, deep vein thrombosis, and pulmonary embolism. The mechanisms of thrombus removal employed by these catheters vary, from mechanical extraction (e.g. stentriever) to agitation-based approaches that accelerate clot dissolution *in situ*. In this work, we developed a catheter-dimensioned microfluidic device to produce microbubbles in real-time within the vasculature. Our intent was to demonstrate technical proof-of-concept for intravascularly administered sonothrombolysis as a means to accelerate thrombus dissolution. The prototype catheter was fabricated using soft lithography to mold 25 μm wide channels into an elastomeric polydimethylsiloxane (PDMS) substrate for conveyance of liquid and gas phases. The two-dimensional footprint of the microfluidic device, including the inlet ports and microbubble outlet port, was 540 μm wide by 3020 μm long. The overall dimensions of the device were 800 μm wide by 4000 μm long by 400 μm tall. Microbubbles with a non-crosslinked albumin stabilizing shell and a nitrogen gas core were fabricated with diameters between 8 and 28 μm at

³ This chapter contains material from the following peer-reviewed conference and journal publications:

AJ Dixon, B Shin, V Meka, JP Kilroy, AL Klibanov, JA Hossack, "Large diameter microbubbles produced by a catheter-based microfluidic device for sonothrombolysis applications." IEEE International Ultrasonics Symposium (2015), Taipei, Taiwan.

AJ Dixon, JP Kilroy, AL Klibanov, JA Hossack, "Microbubbles produced by a catheter-based microfluidic device for sonothrombolysis applications." 20th European Symposium on Ultrasound Contrast Imaging (2015), Rotterdam, The Netherlands.

AJ Dixon, B Shin, JMR Rickel, AL Klibanov, JA Hossack, "Development of a catheter-dimensioned microfluidic device for intravascular production of microbubbles" in preparation.

production rates between approximately 5.6×10^3 and 118×10^3 microbubbles per second. Notably, this represents the first demonstration of microbubble fabrication by a microfluidic device with dimensions necessary to permit *in situ* microbubble production directly within a blood vessel.

4.2 Introduction

Thrombolysis mediated by intravenous administration of recombinant tissue plasminogen activator (rtPA) is the primary therapy for accelerating the removal of blood clots from occluded blood vessels. However, rtPA is only effective in approximately 30% of ischemic stroke patients and is contraindicated for many others due to an increased risk of intracranial hemorrhage (ICH) and severe off-target bleeding.^{149,150} The increased risk of severe bleeding coupled with the inability to predict which patients will respond favorably to rtPA has limited its use in the United States to only ~5% of ischemic stroke patients.¹⁵¹ In addition, rtPA is only safely administered to patients with deep vein thrombosis (DVT) or pulmonary embolism (PE) via a catheter-directed method, in which a catheter is placed within the occluded vessel and slowly emits rtPA over a period of up to 96 hours.^{50,51,152}

The limitations associated with rtPA have motivated the development of catheters that mechanically retrieve blood clots or accelerate clot dissolution within occluded blood vessels.¹⁵³⁻¹⁵⁵ In the context of ischemic stroke, current generation thrombectomy catheters have demonstrated recanalization rates approaching 90%, but only achieve complete restoration of perfusion in distal capillary beds in 60% of cases.¹⁵⁶ This observation may explain why only 40% of patients treated with endovascular thrombectomy devices receive “good” scores on the modified Rankin Scale (mRS) after 90 days.^{154,156-158} Successful recanalization is not the only factor that influences long-term clinical outcomes, as the time to recanalization, the site of vascular occlusion, and the presence of distal emboli are also known to be important parameters.¹⁵⁹ In the context of

DVT, the findings of the Catheter-directed Venous Thrombolysis (CaVenT) study suggested that an additional 20% reduction in post-thrombotic syndrome (PTS) may be achieved through the use of catheter-directed thrombolysis (CDT) as compared to conventional anticoagulant therapies. While this is a notable reduction in PTS, 40% of patients still presented with PTS at 24-months and approximately 10% of patients who underwent CDT therapy experienced clinically relevant bleeding complications during the procedure that required immediate medical intervention. Thus, there still exists a significant opportunity to improve long-term clinical outcomes by developing new technologies that not only accelerate and improve recanalization of the primary occlusion but also reduce or eliminate the use of rtPA to decrease the risk of off-target hemorrhage and bleeding.

An approach intended to address the multiple elements of revascularization is the combination of rtPA with ultrasound and microbubbles, a technique known as sonothrombolysis. When applied as a combination therapy, rtPA, ultrasound, and microbubbles improved recanalization rates from approximately 30% to 60% in ischemic stroke patients, and the time to recanalization was also significantly reduced. In total, clinical sonothrombolysis for ischemic stroke has been evaluated in four clinical trials (e.g. CLOTBUST,³⁶ TUCSON,³⁸ TRUMBI,¹⁶⁰ and DUET¹⁶¹), all of which reported accelerated recanalization rates accompanied by an increased risk of off-target bleeding or ICH. A limitation of these trials is that the microbubbles were administered intravenously, so the majority of the microbubble dose never reached the occluded blood vessel, and the ultrasound used was supplied by a diagnostic imaging rather than therapeutic ultrasound system. Significant improvements may be achieved by administering microbubbles directly within the occluded vessel to ensure their proximity to the blood clot and by using a therapeutic ultrasound regimen.

In this work, we describe the design, fabrication, and operation of a catheter-dimensioned microfluidic device that produces microbubbles in real-time with tunable composition, dimension,

and stability. Producing microbubbles directly within the vasculature removes the requirement for long-circulation lifetimes and small diameters that is needed for intravenous administration, and permits the study of large-diameter, low-stability microbubbles that are therapeutically active immediately after production and dissolve as they migrate downstream. It is hypothesized that these properties may reduce the occurrence of off-target hemorrhage and bleeding associated with the use of conventional microbubbles for sonothrombolysis applications.

4.3 Materials and Methods

4.3.1 Microfluidic Catheter Design and Fabrication

A flow-focusing microfluidic device (FFMD) was designed with dimensions of approximately 400 μm wide and 800 μm long (Figure 4-1A). Gas and liquid channels were 25 μm wide and all channels were 20 – 22 μm tall. Liquid and gas inlets were placed at the same end of the device to permit liquid and gas entry from the proximal end of the catheter. The flow-focusing nozzle doubled back into the center of the device as a means to reduce the device's footprint and produced microbubbles into the outlet channel.

Fabrication of the microfluidic device was performed by first manufacturing a SU-8 mold on a silicon wafer using photolithography techniques.⁵⁷ SU-8 was chosen as the photoresist because it allows for high aspect-ratio features to be produced down to a minimum feature-size of 3 – 5 micrometers. The microfluidic device channels were cast in polydimethylsiloxane (PDMS) by pouring PDMS over the mold to a depth of 250 μm and curing it at 70 C for 30 minutes. However, prior to pouring PDMS into the mold, short lengths of 90 μm diameter optical fibers (Polymicro, Molex Inc) were laid across the gas and liquid inlets as a means to cast pre-formed inlet channels in which to place the gas and liquid inlet tubing. After the PDMS had fully cured, the optical fibers were removed from the PDMS leaving the channel imprints behind. The result was a 250 μm thick

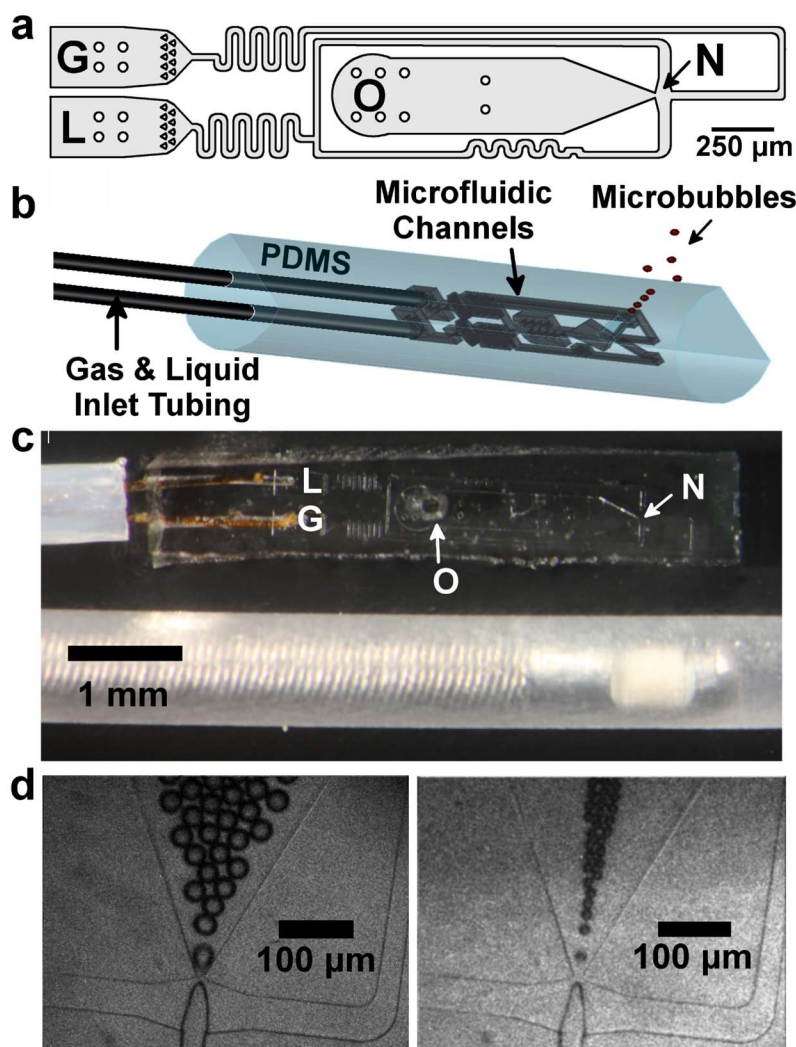


Figure 4-1: Design of a catheter-dimensioned flow focusing microfluidic device

(a) Two-dimensional schematic of the catheter-dimensioned FFMD. The device is $540\ \mu\text{m}$ wide and $3020\ \mu\text{m}$ long, while the narrowest channels are $25\ \mu\text{m}$ wide. The gas (G) and liquid (L) inlets are on the left side of the device, while the nozzle (N) and microbubble outlet (O) fold back towards the center of the device. (b) A three-dimensional rendering of the completed device, showing the gas and liquid inlet tubing, along with the microbubble outlet. (c) Fabricated catheter showing brown capillary tube inlets, microfluidic channels, the nozzle, and the microbubble outlet port. (d) High speed camera images showing approximately $20\ \mu\text{m}$ and $8\ \mu\text{m}$ diameter microbubble production.

piece of cured PDMS with the design of the device imprinted upon one of its sides. To complete fabrication, two key steps needed to follow: binding of the PDMS to a blank piece of PDMS and a creation of a hole on top the output portion of the design on the PDMS in order to allow the microbubbles to exit the outlet channel of the device. Binding the piece of PDMS imprinted with the channels to another blank piece creates a completely closed channel through which gas and

liquid can flow. Bonding was performed by placing both pieces of PDMS in an oxygen plasma oven to activate the surface of the PDMS. After treatment, the PDMS pieces were joined to form a semi-permanent bond. A 200 μm diameter hole was punched into the outlet channel of the device using a 200 μm biopsy punch (Item #57391, Stoelting, Co). The final step of device assembly was the insertion of fused silica capillary tubes (O.D. = 110 μm , Polymicro, Molex Inc) with a reinforced polyimide coating into the gas and liquid interconnect channels to convey the gas and liquid phases into the device.

4.3.2 Microfluidic Device Operation and Characterization

Microbubbles were produced using 99.998% N_2 or 99.99% CO_2 gas (GTS Welco, Richmond, VA) and a liquid phase comprised of 4% w/v bovine serum albumin (BSA) and 10% w/v dextrose in 0.9% saline. The liquid phase was prepared by mixing its components overnight at 4C – no effort was made to degas the liquid phase prior to injection into the microfluidic device. The liquid phase was pressurized using a syringe pump (PhD 2000, Harvard Apparatus, Holliston, MA) and a 20 mL metal syringe capable of withstanding high pressures (KD Scientific, Holliston, MA). The liquid phase was filtered by 0.2 μm nylon filters prior to use in the FFMD. The gas pressure was regulated by a digital manometer (06-664-22, Fisher Scientific, Waltham, MA). Liquid flow rates varied between 10 – 60 $\mu\text{L}/\text{min}$ and gas pressures varied between 43.8 and 89.6 kPa. Microfluidic microbubble production was monitored by a high-speed camera (SIMD24, Specialised Imaging, Tring, UK) and production rate and diameter were measured in ImageJ.

4.3.3 Microbubble Characterization

Microbubble lifetime after exiting the microfluidic device was measured using a Z2 Coulter Counter (Beckman Coulter, Brea, CA).⁵⁹ A catheter-dimensioned FFMD producing microbubbles of approximately 20 μm diameter was placed in 20 mL of air saturated saline. After

10 s, the FFMD was removed and the saline was sampled by the Z2 Coulter Counter every 15 s over a period of 120 s. The saline was continuously stirred during measurement to limit microbubble aggregation and to ensure adequate mixing. Microbubble size distribution and number as reported by the Z2 Coulter Counter were analyzed to determine the microbubble half-life in a well-mixed, air-saturated, saline environment.

4.4 Results

4.4.1 Microfluidic device fabrication and characterization

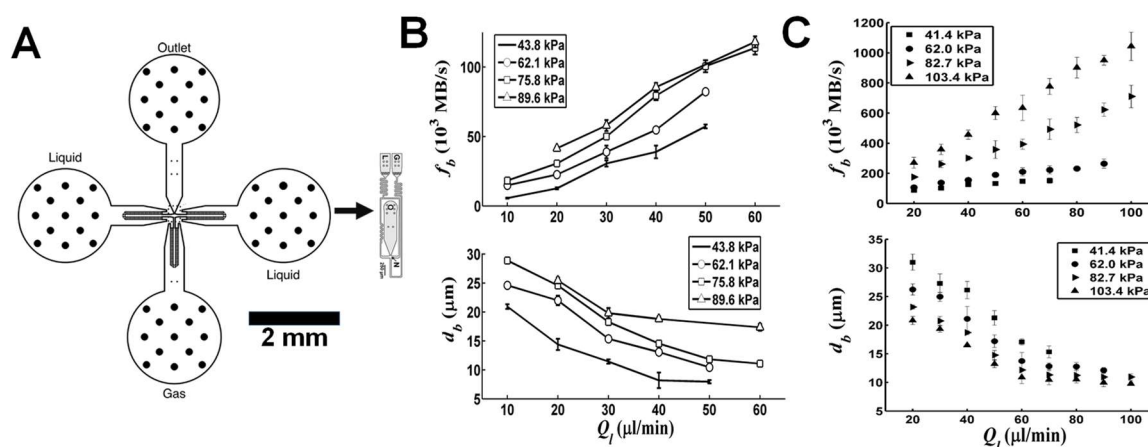
The distal end of a completed catheter-dimensioned microfluidic device is depicted in Figure 4-1C. The devices were hand-fabricated and several failure modes were observed due to the variability in fabrication methods. First, manual alignment of biopsy punch (diameter = 250 μm) with the outlet channel (width = 310 μm) was difficult and often resulted in destruction of the nearby gas and liquid channels. Second, the gas and liquid inlets often clogged due to the small diameter of the of inlet tubing. The particles responsible for the blockage were most often small pieces of PDMS that became dislodged upon placement of the gas and liquid inlet tubes.

Ten catheter-sized devices were tested to determine the gas and liquid pressures at which device failure was observed. Five devices were exposed to increasing gas pressures and five were exposed to increasing liquid flow rates until failure was observed. The gas pressure was incremented by 6.9 kPa every five minutes and the liquid flow rate was incremented by 5 $\mu\text{l}/\text{min}$ every five minutes. If the gas pressure was under evaluation, then the liquid inlet was completely closed, and vice versa. The purpose was to place an upper operating limit on gas and liquid pressure for the device. A summary of failure modes and the pressures/flow rates at which failure occurred is given in Table 4-1. The most common failure mode was gas or liquid seepage between the PDMS and polyimide coating of the inlet tubing. This interface can only withstand a finite pressure

Table 4-1: Failure mode analysis for catheter-dimensioned microfluidic devices

Device	Gas Pressure At Failure (kPa)	Liquid Flow Rate At Failure ($\mu\text{l}/\text{min}$)	Failure Mode
1	96.5	—	Gas seepage from inlet
2	110.3	—	Gas seepage from inlet
3	103.4	—	Gas seepage from inlet
4	106.8	—	Gas seepage from inlet
5	100.0	—	Gas seepage from inlet
6	—	90	Liquid seepage from inlet
7	—	110	PDMS bond failure
8	—	105	PDMS bond failure
9	—	85	Liquid seepage from inlet
10	—	95	Liquid seepage from inlet
Average	103.4 ± 4.9	97.0 ± 9.3	

before gas or liquid will pass through the friction seal. The second most common failure mode was due to separation of the PDMS-to-PDMS bond located in between the liquid and gas inlet channels. Liquid over-pressure occurred at an average liquid flow rate of $97.0 \pm 9.3 \mu\text{l}/\text{min}$ while gas over-pressure occurred at an average pressure of $103.4 \pm 4.9 \text{ kPa}$. For this reason, future characterization of the device was performed below these upper limits.

**Figure 4-2: Microbubble production characteristics for catheter-dimensioned FFMD**

(A) Comparison in dimensions between two FFMDs for microbubble production. The device on the left has three inlets and one outlet, and the footprint of its microfluidic channels is $6.6 \text{ mm} \times 6.6 \text{ mm}$. The catheter-dimensioned microfluidic device is shown next to the large device for comparison. The catheter-dimensioned has two inlets and one outlet, as shown in Figure 2-1A. (B) Production rates (top) and microbubble diameters (bottom) achieved by the catheter-dimensioned microfluidic device at a range of operating gas pressures and liquid flow rates (Q_l). (C) Production rates (top) and microbubble diameters (bottom) achieved by the larger microfluidic device at a range of operating gas pressures and liquid flow rates (Q_l).

This micrograph shows a microfluidic device with several labeled components:

- Nozzle:** Indicated by a black arrow pointing to the narrow opening where the gas and liquid channels meet.
- Gas channel:** The upper channel through which gas is introduced.
- Liquid channel:** The lower channel through which liquid is introduced.
- Microbubble stream:** Indicated by a white arrow pointing to the dark, elongated region where gas and liquid are mixed.
- Outlet hole:** Indicated by a black arrow pointing to the circular opening where the microbubbles exit the device.

A single frame (60 FPS) of catheter-dimensional FFMD operation. Individual microbubbles exit the nozzle too quickly to be resolved, but this frame shows multiple rows of microbubbles developing as the nozzle expands towards the outlet. The black area around the outlet hole is the stream of microbubbles exiting the device. Also shown are the gas and liquid channels. For scale, the width of the gas channel at the top of the image is 25 μm .

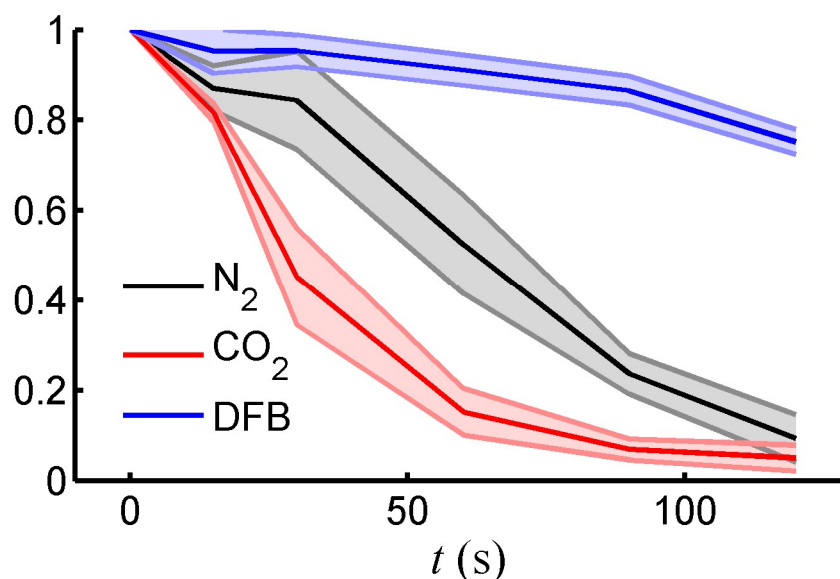


Figure 4-4: Microbubble lifetime curves in air-saturated, mixed saline

Microbubble lifetime curves as measured by a Coulter counter in a well-mixed, air-saturated environment for microbubbles produced with N₂, CO₂, and DFB gasses. The shaded error regions are \pm SEM, and the Y-axis is fraction of remaining microbubbles after the initial measurement at $t = 0$.

operation. As shown, the microbubbles exit the nozzle faster than can be resolved by the camera, and stream out of the device through the outlet hole.

4.4.3 *In vitro* microbubble stability

Microbubbles were produced by the catheter-dimensioned FFMD with gases of either N₂, CO₂, or decafluorobutane (DFB) and identical albumin/dextrose shells. The solubility of each of these gases in water at 25 C is 0.019 g N₂/kg H₂O, 1.69 g CO₂/kg H₂O, and 0.0015 g DFB/kg H₂O. Thus, the relative solubility of each gas is CO₂: 1126, N₂: 12.6, DFB: 1.0. The catheter-dimensioned FFMD was placed in 20 mL air-saturated saline and produced microbubbles for 30 seconds, after which point the saline was sampled by a Coulter counter to determine microbubble number. The saline was stirred during the measurement by a magnetic stir bar. The results of the Coulter measurements for each gas is shown in Figure 4-4 (average of 3 separate measurements through time). As shown, the microbubble half-life for CO₂ gas was approximately 28 ± 4 s, the half-life

for N₂ gas was 64 ± 9 s, and the half-life of DFB gas microbubbles exceeded the 120 s measurement period. All of these half-life measurements are statistically significantly different ($p < 0.05$). Note that in these experiments, efforts were made to keep microbubble production rates and diameters within 10% of each other for each gas and each replicated measurement.

4.5 Discussion

Microfluidic devices are aptly named because they are capable of transporting, mixing, and reacting microliter and nanoliter volumes of fluids and gases with high precision, repeatability, and control. However, in most instances, only the channels within the microfluidic device may be considered as miniature, while the device itself, its interconnects, and accessory sensing equipment are often orders of magnitude larger than the channels. This is not a limitation for many applications, but is often a consideration for devices intended to operate *in situ*, such as implantable biomedical sensors,¹⁶³ drug dispensers,¹⁶⁴ blood dialyzers,¹⁶⁵ or in the case of this work, an intravascular catheter. The catheter-dimensioned flow-focusing microfluidic device (FFMD) developed in this work is the smallest FFMD ever reported, as most have been developed for benchtop operation rather than direct *in vivo* deployment.^{162,166-170} Miniaturization was enabled by reducing number of interconnects and decreasing each interconnect's size by employing 100 μm diameter capillary tubing. Further miniaturization may be possible by decreasing interconnect and channel size, but modifications must be made with the understanding that additional miniaturization compromises device performance and robustness.

The catheter-dimensioned devices withstood moderate liquid and gas pressures, as evidenced by the failure analysis results shown in Table 4-1. As is often the case, the weakness in the design was the interconnects, where the polyimide-coated fused silica capillary tubes were in contact with the PDMS channel walls. Migrating the device to an all-glass design with annealed interconnects

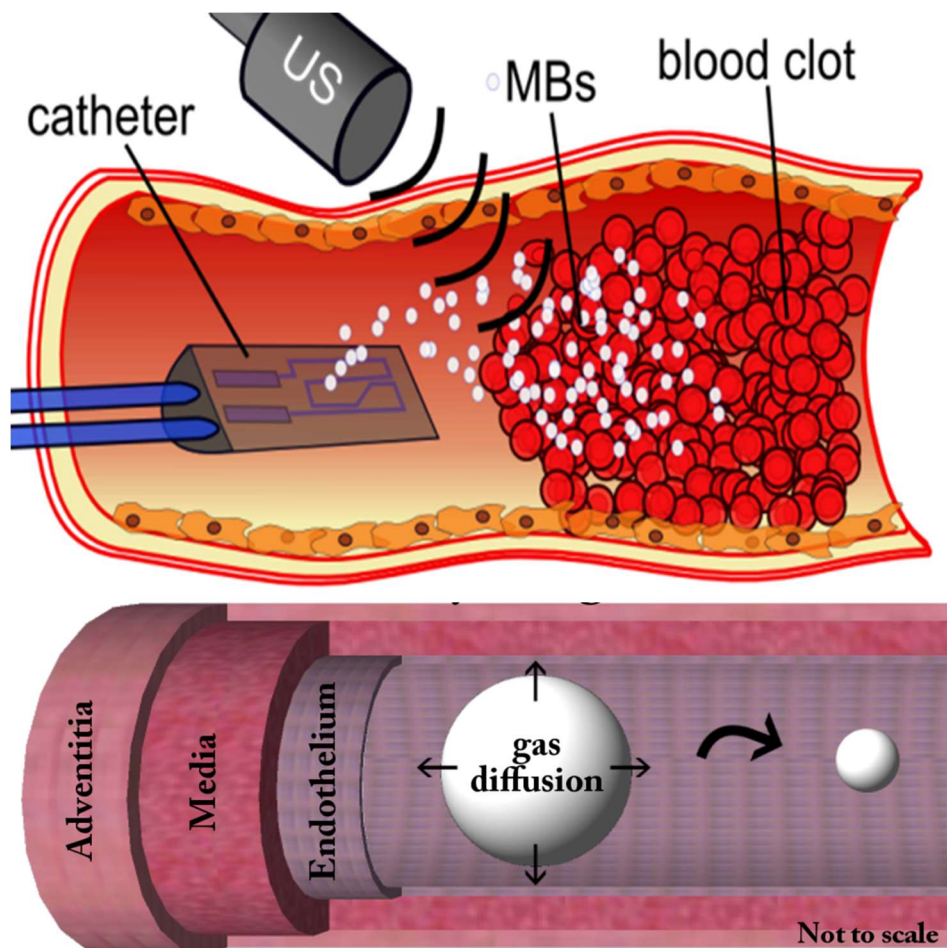


Figure 4-5: Schematic of intended device operation and effect of low microbubble stability

(Top) Schematic of intravascular deployment of the catheter-based FFMD. Microbubbles are produced in close proximity to the thrombus, and ultrasound is applied either directly from the catheter or transcutaneously. (Bottom) Intentionally using microbubbles composed of high solubility gases causes the microbubble to shrink as it moves away from the therapeutic target, thus reducing the incidence of potential adverse off-target effects. Note: the contributions of Ali Dhanaliwala, M.D., Ph.D. are acknowledged for the creation of the bottom figure.

would increase device robustness, permit operation at significantly higher pressures, and increase the safety factor for eventual *vivo* deployment.¹⁷¹ However, the PDMS device developed in this work was able to produce microbubbles at rates that are likely suitable for *in situ* intravascular delivery, thereby establishing proof-of-concept that a device of this size is capable of producing a sufficient number of microbubbles. Notably, the catheter-dimensioned device produced microbubbles at approximately 1/10th the rate of larger PDMS devices, primarily due to the increased hydrodynamic resistance associated with the significantly smaller channels and

interconnect tubing in the catheter-dimensioned device (hydrodynamic resistance scales with $1/r^4$, where r is the channel radius).

As stated in the introduction, the motivation for developing this catheter stemmed from the desire to accelerate clot lysis rates in patients with thrombo-occlusive diseases. Sonothrombolysis is known to accelerate clot lysis in ischemic stroke patients, but increased risks of off-target hemorrhage have tempered enthusiasm for its use.⁴⁵ Thus, techniques to constrain the effects of sonothrombolysis to the diseased vessel and limit their off-target effects are required for future clinical translation. Catheters are already widely employed to treat these diseases via a variety of mechanisms, so development of a sonothrombolysis catheter was a natural extension of other catheter-based techniques. Of course, this work has demonstrated only that an FFMD of catheter-compatible dimensions can produce microbubbles in real-time, and but has not evaluated the efficacy of these microbubbles for sonothrombolysis.

Central to implementing sonothrombolysis via catheter-produced microbubbles is the notion that microbubbles must now only persist within the diseased vessel for a short period of time, which removes constraints associated with the gases and shell materials conventionally used. In particular, innocuous materials such as albumin, dextrose, saline, and breathable gases may now be employed to increase safety. Further, these formulations can be designed so that microbubble concentration in the diseased vessel can be very high to elicit maximal therapy and very low elsewhere via rapid microbubble dissolution, as diagrammed in Figure 4-5.

Further, the results of varying gas composition presented in Figure 4-4 demonstrate that by simply modifying the gas, the microbubble half-life can be modulated by at least an order of magnitude. A limitation of this evaluation was that microbubble lifetimes were evaluated in air-saturate saline at 25 C, whereas blood gases and temperatures are expected to be quite variable,

depending on the gasses inhaled by the patient and their physiological condition.¹⁷² Nevertheless, the solubility of each gas in water is a good surrogate measure for establishing an expected trend of microbubble lifetimes in solution, and the ability to mix gases is expected to enable even more tunability for application-specific requirements.

4.6 Conclusions

We have demonstrated technical proof-of-concept for microbubble production by a catheter-dimensioned flow-focusing microfluidic device. The device was fabricated out of PDMS with fused silica capillary interconnects, and its overall dimensions were 800 μm wide by 4000 μm long by 400 μm tall. The device produced microbubbles with a non-crosslinked albumin stabilizing shell and nitrogen, carbon dioxide, and decafluorobutane gas cores. The microbubbles were fabricated with diameters between 8 and 28 μm at production rates between approximately 5.6×10^3 and 118×10^3 microbubbles per second. Notably, this represents the first demonstration of microbubble fabrication by a microfluidic device with dimensions necessary to permit *in situ* microbubble production directly within a blood vessel.

Chapter 5. *In vitro* sonothrombolysis efficacy of transiently stable microbubbles produced by a microfluidic device⁴

5.1 Abstract

Therapeutic approaches that enhance thrombolysis by combining recombinant tissue plasminogen activator (rtPA), ultrasound, and/or microbubbles (MBs) are known as sonothrombolysis techniques. To date, sonothrombolysis approaches have primarily utilized commercially available MB formulations (or derivatives thereof) with diameters in the range 1 – 4 μm and circulation lifetimes between 5 – 15 min. In this study, we evaluated the *in vitro* sonothrombolysis efficacy of large diameter MBs ($d_{\text{MB}} \geq 10 \mu\text{m}$) with much shorter lifetimes that were produced in real-time and in close proximity to the blood clot by a flow focusing microfluidic device. MBs with a N_2 gas core and a non-crosslinked bovine serum albumin shell were produced with diameters between 10 – 20 μm at rates between $50 - 950 \times 10^3$ per second. Use of these large MBs resulted in approximately 4 – 8 fold increases in thrombolysis rates compared to a clinical rtPA dose and approximately 2 – 4 fold increases in thrombolysis rates compared to sonothrombolysis techniques using conventional MBs. The results of this study indicate that the large diameter microbubbles with transient stability are capable of significantly enhanced *in vitro*

⁴ This chapter contains material from the following peer-reviewed conference and journal publications:

AJ Dixon, B Shin, V Meka, JP Kilroy, AL Klibanov, JA Hossack, “Large diameter microbubbles produced by a catheter-based microfluidic device for sonothrombolysis applications.” IEEE International Ultrasonics Symposium (2015), Taipei, Taiwan.

AJ Dixon, JP Kilroy, AL Klibanov, JA Hossack, “Microbubbles produced by a catheter-based microfluidic device for sonothrombolysis applications.” 20th European Symposium on Ultrasound Contrast Imaging (2015), Rotterdam, The Netherlands.

AJ Dixon, B Shin, JMR Rickel, AL Klibanov, JA Hossack, “Accelerated *in vitro* sonothrombolysis facilitated by large-diameter microbubbles produced by a flow-focusing microfluidic device.” in preparation.

sonothrombolysis rates when delivered directly to the clot immediately following production by a flow focusing microfluidic device.

5.2 Introduction

Ischemic stroke, venous thromboembolism, and pulmonary embolism result from blood vessel occlusion caused by either *in situ* thrombus formation or by migration of a thrombus from an upstream blood vessel to a smaller downstream vessel.^{48,173} Together, these conditions affect over 1.3 million individuals in the United States and over 20 million worldwide each year.¹⁷⁴ Intravenous or intra-arterial administration of recombinant tissue plasminogen activator (rtPA), either peripherally or through a catheter, remains the most common therapeutic intervention for these conditions.^{49,50,175,176} Unfortunately, rtPA is ineffective in many individuals, and the majority of patients presenting with stroke or venous thromboembolism are contraindicated for the full course of rtPA therapy due to bleeding and hemorrhagic risk.^{150,151} Therefore, there is a significant need for improved therapeutic interventions across the entire spectrum of diseases that result from thromboembolisms.

Thrombolysis assisted by ultrasound and/or microbubbles (MBs), termed sonothrombolysis, has been studied extensively in both *in vitro* and *in vivo* settings as a means to safely accelerate thrombolysis. In clinical ischemic stroke studies, sonothrombolysis improved recanalization rates from approximately 30% to 60%, and the time to recanalization was also significantly reduced. Clinical sonothrombolysis has been evaluated in multiple clinical trials (e.g. CLOTBUST,³⁶ TUCSON,³⁸ TRUMBI,¹⁶⁰ and DUET¹⁶¹), all of which reported accelerated recanalization rates accompanied by an increased risk of off-target bleeding or ICH. Given that each trial used ultrasound parameters and MB designs optimized for diagnostic imaging, and not for therapy, there remains an opportunity to increase recanalization rates and mitigate the risk of off-target

bleeding by designing an ultrasound parameter set and MB platform specifically for localized therapeutic delivery for thrombolysis applications.

The presence of MBs reduces the acoustic pressure required for cavitation, and it has been posited that MB cavitation, in combination with MB tunneling through clots, accelerates thrombolysis by mechanically disrupting the fibrin mesh, increasing fluid mixing via MB microstreaming, and exposing deeper regions of the fibrin mesh for rtPA enzymatic activity.^{42,45-47,177,178} Significant effort has been placed on determining optimal ultrasound parameters for sonothrombolysis, including ultrasound frequency, duty factor, pressure, cycle length and how all of these parameters influence MB cavitation, acoustic radiation force, and MB interactions with the clot and its fibrin mesh.^{36,38,41-43,45-47,177-189} However, apart from an *in vitro* study by Borrelli *et al*, which demonstrated improved clot lysis efficacy by 3 μm MBs versus 1 μm MBs, MB design parameters (e.g. size, composition, stability) remain largely unexplored.¹⁹⁰ In short, the requirement for intravenous administration of long-circulating, small diameter MBs has limited the field to studying commercially available MB formulations that have been optimized for diagnostic imaging rather than therapeutic efficacy. Nevertheless, large diameter MBs have been associated with increased bioeffects in therapeutic applications including sonothrombolysis,¹⁹⁰ sonoporation-mediated drug delivery,^{59,107,191} and blood brain barrier disruption.¹⁹²

With this in mind, it was the intent of this study to evaluate the sonothrombolysis performance of MBs with design parameters in a previously unexplored region of the potential parameter set (diameter $> 5 \mu\text{m}$, lifetime $< 90 \text{ s}$, N_2 gas core). We hypothesized that large diameter MBs would confer enhanced bioeffects in the form of accelerated thrombolysis rates, while also mitigating the risk of gas embolism due to the propensity of this MB formulation to dissolve shortly after administration.^{58,59,193} The MBs in this study were fabricated in real time (i.e. immediately before

intended use) by a flow-focusing microfluidic device (FFMD) and were administered to the *in vitro* sonothrombolysis model as though they were fabricated by a catheter-mounted FFMD placed in close proximity to the blood clot.¹⁹⁴ In this way, the short-lived MBs had time to interact with the blood clot before dissolving farther downstream. In addition, a new *in vitro* sonothrombolysis model is presented that permits the assessment of volumetric clot lysis rates by measuring the concentration of hemoglobin released from the clot during the thrombolysis process.

5.3 Materials and Methods

5.3.1 Microfluidic device fabrication

A custom chrome-metal photolithography mask (Applied Image, Inc, Rochester, NY) was used to fabricate an SU-8 mold of the microfluidic channel geometry on a silicon wafer.¹⁶² Flow-focusing microfluidic devices (FFMD) were cast from the SU-8 mold in polydimethylsiloxane (PDMS) (Sylgard 184, Dow Corning Corp., Midland, MI) and bound to a clean PDMS substrate using oxygen plasma. The nominal device channel dimensions were: height – 20 μm , nozzle width – 8 μm , liquid channel width – 50 μm , and gas channel width – 30 μm (Figure 5-1A). Note that these nominal dimensions varied $\pm 5\%$ from device to device. The overall dimension of the device used in this study was $10 \times 4 \times 8$ mm.

5.3.2 Microfluidic microbubble production and characterization

Microbubbles were produced by precise mixing of separate gas and liquid phases at the FFMD nozzle. The gas phase was comprised of 99.998% nitrogen gas (GTS Welco, Richmond, VA) and its pressure was regulated by a gas regulator and digital monometer (Model 06-664-21, Fisher Scientific, Waltham, MA). The liquid phase was a solution of 4% (w/v) bovine serum albumin (BSA) and 10% (w/v) dextrose in isotonic saline (0.9%)⁵⁸. All chemicals were purchased from

Sigma Aldrich (St. Louis, MO). The liquid phase was advanced into the microfluidic device channels through PTFE microbore tubing connected to a digital syringe pump (PHD2000 Harvard Apparatus, Holliston, MA). A high-speed camera (SIMD24, Specialised Imaging, Tring, United Kingdom) connected to an inverted microscope was used to measure microbubble production rates and diameters as previously described (Figure 5-1B).^{58,59,162} All stated average diameters in this work were accurate to $\pm 1 \mu\text{m}$ and all production rates were accurate to $\pm 5\%$ of the stated value.

Microbubble lifetime after exiting the microfluidic device was measured using a Z2 Coulter Counter (Beckman Coulter, Brea, CA).⁵⁹ An FFMD producing microbubbles of approximately 20 μm diameter was placed in 20 mL of air saturated saline. After 10 s, the FFMD was removed and the saline was sampled by the Z2 Coulter Counter every 15 s over a period of 120 s. The saline was continuously stirred during measurement to limit microbubble aggregation and to ensure adequate mixing. Microbubble size distribution and number as reported by the Z2 Coulter Counter were analyzed to determine the microbubble half-life in a well-mixed, air-saturated, saline environment.

Stable and inertial microbubble cavitation induced by acoustic excitation was characterized using a method described by Datta *et al.*¹⁹⁵ Long-pulse acoustic excitation (1000 cycle, 1 MHz) at varying peak-negative-pressure (PNP) was applied from a single element ultrasound transducer (V303 Olympus Panametrics, Waltham, MA) onto a 2 mm diameter PTFE tube containing slowly-flowing microbubbles produced by an FFMD. The acoustic backscatter from the microbubbles was measured by a calibrated polyvinylidene difluoride (PVDF) hydrophone (GL-0200, Onda Corp., Sunnyvale, CA) and the frequency content of the acoustic backscatter was analyzed to monitor for signs of stable and inertial cavitation. Stable cavitation is identified by the onset of the

ultraharmonic response while inertial cavitation is detected by an increase in broadband acoustic noise above the baseline noise level.^{185,195}

5.3.3 *In vitro* sonothrombolysis model and optical assay

Blood clots used for these experiments were comprised of 35% (v/v) citrated human red blood cells (RBC) and 65% (v/v) citrated platelet-rich plasma (PRP, $> 5 \times 10^6$ platelets/ μ l).¹⁹⁶ This blood mixture was placed within glass tubes of 2.5 mm inner diameter and vinyl sutures were threaded through the tubes. Introducing CaCl_2 at a concentration of 15 mM initiated the clotting process, which was allowed to proceed for 4 hours at 37 °C. After 4 hours, the clots were stored at 4°C for three days to promote clot retraction. Prior to experimentation, the clots were removed from the glass tubes but remained attached to the vinyl suture. Excess clot was removed from the suture so that all clots were 2 cm long and 2.3 ± 0.1 mm in diameter. All human blood products were procured from Virginia Blood Services (Richmond, VA).

The blood clot was placed within an *in vitro* sonothrombolysis experimental apparatus, as shown in Figure 5-2A. The apparatus contained a flow loop (3 mm I.D) that was surrounded by a bath thermostatically maintained at 37 ± 2 °C. Human plasma (30 ml) was circulated within the flow loop at an average flow velocity of 10 cm/s by a peristaltic pump (NE-9000B, New Era Pump Systems, Inc.). The plasma was maintained at 37 ± 2 °C by a hot plate and was continuously stirred by a magnetic stir bar. Recombinant tissue plasminogen activator (rtPA, Activase, Genentech, South San Francisco, CA) was added as a bolus to the circulating plasma in either 0, 0.1, or 1 μ g/ml concentrations. An 18 μ m nylon mesh filter (Tisch Scientific, Cleaves, OH) was placed in the flow loop to trap large clot fragments for additional analysis.

The blood clot was secured within the flow loop and was aligned within the acoustic beam of a single element 1 MHz ultrasound transducer with a 2.54 cm diameter (V302-SU Olympus

Panametrics, Waltham, MA). A single set of ultrasound parameters was used for all sonothrombolysis experiments in this study: 1 MHz center frequency, 100 cycle pulses, 1 kHz pulse repetition frequency, with a 2 s on / 2 s off pulsing pattern to allow for microbubble replenishment on the clot face.^{184,186} The peak negative pressure (PNP) at the surface of the clot closest to the ultrasound transducer was measured to be 500 kPa (Mechanical Index = 0.5). The sinusoidal excitation was supplied by an arbitrary waveform generator (AFG 3022B, Tektronix, Beaverton, OR) and was amplified by a 60 dB RF amplifier (A-500, ENI Ltd., Rochester, NY).

A FFMD continuously produced microbubbles that were introduced to the flow loop through a microbore PTFE tube (30G, Cole-Parmer, Vernon Hills, IL). The distal end of the tube was placed approximately 2 cm upstream from the clot. The FFMD was kept under continuous microscopic observation to monitor microbubble production rates and diameters over the course of the experiment. In some experiments, microbubbles produced via tip sonication of a decafluorobutane (C_4F_{10}) saturated solution of 4% BSA and 10% dextrose were used as a means to evaluate sonothrombolysis efficacy of conventionally sized microbubbles. These microbubbles were sized and counted by a Coulter counter, and were infused continuously through the same microbore PTFE tube by a syringe pump.

Sonothrombolysis with varying rtPA, ultrasound, and MB conditions was performed for 30 minutes ($N \geq 4$ for each experimental condition). The volumetric clot lysis rate was quantified via an optical absorption assay that measured the concentration of hemoglobin present in the circulating plasma over time. Every 3 minutes, a 1 ml sample of the circulating plasma was removed, placed in a 2 ml Eppendorf tube, and kept on ice. At the completion of the 30 minute sonothrombolysis experiment, the entirety of the clot that remained on the suture was lysed by the addition of 1 μ g/ml rtPA in a total volume of 2 mL plasma within an Eppendorf tube. This served

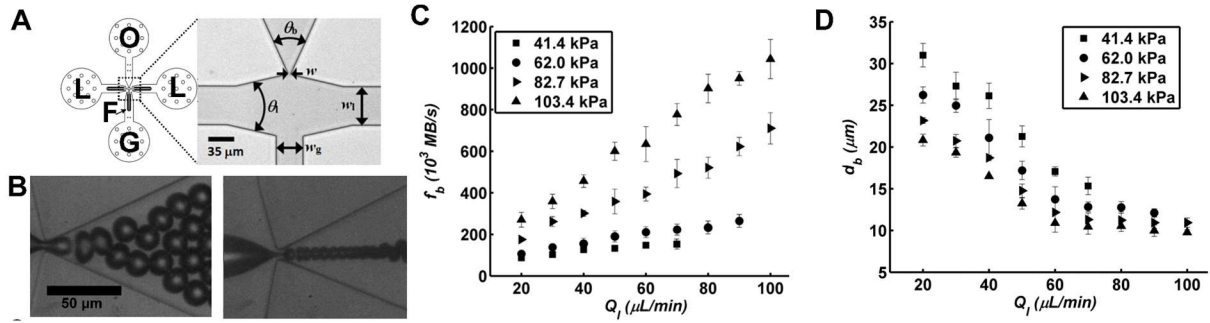


Figure 5-1: Characteristics of microbubbles produced by flow-focusing microfluidic devices

(A) (Left) Schematic of the flow-focusing microfluidic device (FFMD). There are two liquid inlets (L), one gas inlet (G), filters to prevent the nozzle from clogging (F), and an outlet where MBs are emitted (O). (Right) 20X magnified view of the device nozzle. Dimensions are $w_g = 30 \mu\text{m}$, $w_l = 50 \mu\text{m}$, $w = 8 \mu\text{m}$, $\theta_l = 25^\circ$, $\theta_b = 50^\circ$. (B) High speed images of the FFMD producing 20 μm (left) and 10 μm (right) diameter MBs. (C) MB production rates as a function of liquid flow rate, Q_l , for four different gas pressure. (D) MB diameter as a function of liquid flow rate, Q_l , for four different gas pressures.

to liberate all RBCs contained within the clot into solution for the following analysis (Fig 5-2A): each Eppendorf tube containing plasma plus free RBCs was lightly centrifuged to pellet the RBCs, and all plasma was removed. The RBCs were lysed in distilled water to release free hemoglobin into solution (total volume 100 μL). The samples were centrifuged at high centrifugal force one final time to remove RBC membranes from the hemoglobin. The concentration of hemoglobin in each sample was measured via optical absorption ($A_{540\text{nm}}$) in a 96 well plate reader (FLUOStar Optima, BMG Labtech) and compared against the optical absorption of a reference concentration of human hemoglobin (Sigma Aldrich, St. Louis, MO). Thus, the circulating hemoglobin concentration was quantified every three minutes during the sonothrombolysis experiment, and the total amount of hemoglobin within the fraction of the clot that remained on the suture was also measured. Together, these measurements permitted the calculation of the rate at which hemoglobin was removed from the clot through time, which was considered to be a volumetric measurement of the clot lysis rate. Least-squares linear regression was performed on the time-series data to derive a volumetric clot lysis rate for each experimental condition. Statistical significance between

slopes was determined using two-sided t-tests ($\alpha=0.05$). All statistical analysis was performed in MATLAB (Mathworks, Natick, MA).

5.4 Results

5.4.1 FFMD microbubble production and characterization

A schematic and description of the microfluidic channel geometry is illustrated in Figure 3-1A. MBs of diameters between 9.8 ± 0.3 and 31.1 ± 1.4 μm were produced at rates between $87.7 \pm 4 \times 10^3$ and $1043 \pm 94 \times 10^3$ MB/s (Figure 5-1 B,C,D). Gas pressures ranged from approximately 40 to 110 kPa and liquid flow rates were varied between 20 and 110 $\mu\text{l}/\text{min}$. The MB production characteristics at discrete gas pressures and liquid flow rates, as shown in Figure 5-1C and 5-1D, were acquired from a single FFMD operated on three separate days to gauge reproducibility.

MB stability was assessed by monitoring the change in MB size and number following production by the FFMD. The data shown in Fig 5-2A were acquired from an FFMD producing 20 μm diameter MBs at a rate of approximately 225×10^3 MB/s. As shown, the initial distribution at 0 s has a primary peak at approximately 20 μm that flattens through time as MBs dissolve, expand, coalesce, and aggregate. Through time, the average MB diameter, d_{MB} , remained approximately constant near 20 μm , however the standard deviation of d_{MB} measurements increases from 2.2 μm at 0 s to 5.9 μm at 120 s. The half-life of these 20 μm diameter MBs in a well-mixed saline environment was measured to be 65 ± 27 s across three separate measurements. The onset of stable and inertial MB cavitation in response to acoustic excitation was characterized by analyzing the frequency content of acoustic backscatter from MBs ensonified by long-pulse acoustic excitation at 1 MHz. A representative power-spectra of a suspension of FFMD-produced MBs with 15 μm diameter is shown in Figure 5-2B. Ultraharmonics were not observed at a PNP of 50 kPa, but were observed at PNP of 250 kPa and 500 kPa. A significant increase (approx. 10

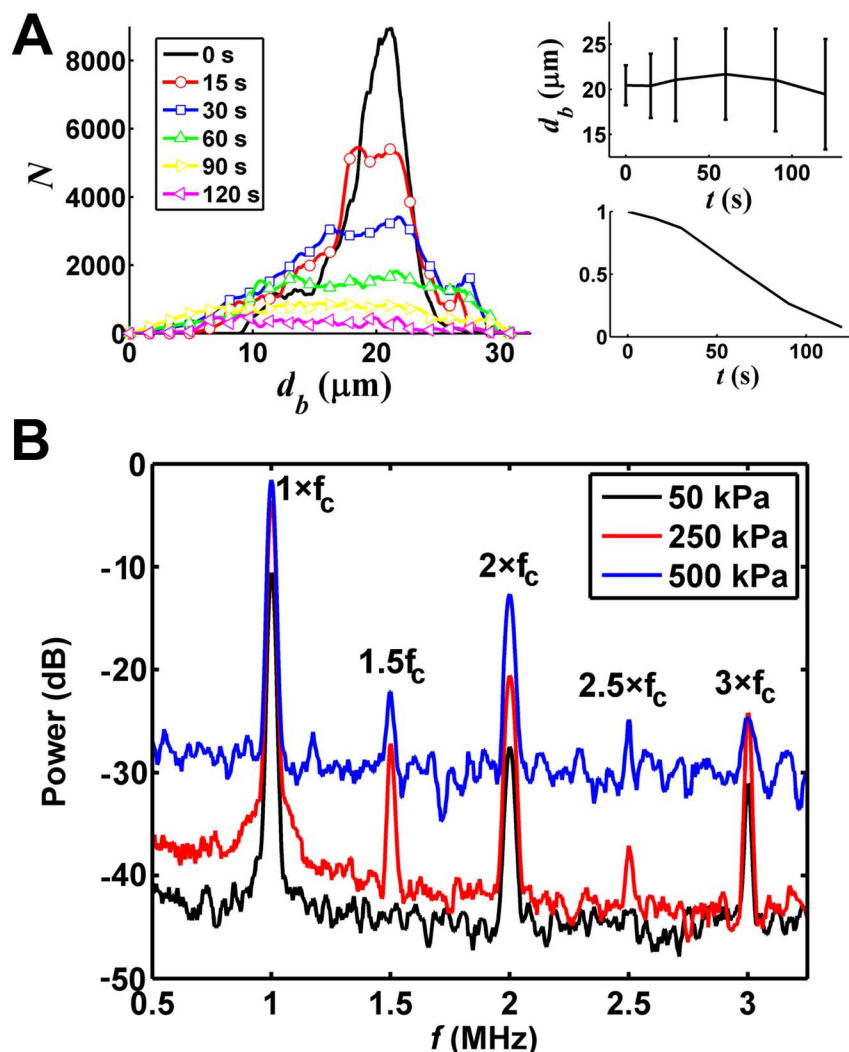


Figure 5-2: FFMD microbubble dissolution and acoustic properties

(A) (left) MB distributions over time as measured by a Coulter counter immediately after production by a flow-focusing microfluidic device (FFMD). MB diameters were confirmed via optical microscopy to be approximately 20 μm . (Right) Change in MB diameter (top) and number (bottom) over time, as measured from the Coulter distributions. (B) Frequency analysis of the acoustic backscatter from 15 μm diameter MBs produced by a FFMD when exposed to long-pulse acoustic excitation at 1 MHz and three different pressures. The generation of ultraharmonic responses (e.g. 1.5, 2.5 MHz) is associated with stable MB cavitation. Increase in broadband noise is associated with the onset of inertial cavitation.

– 15 dB) in broadband acoustic noise was observed when increasing the PNP from 250 kPa to 500 kPa, which corresponds to the onset of inertial cavitation. Thus, based on this analysis, both stable and inertial cavitation was observed at 500 kPa for FFMD produced MBs of 15 μm diameter.¹⁹⁵ A similar analysis for sonication-produced MBs ($d_{\text{MB}} = 2.8 \pm 1.7 \mu\text{m}$) confirmed that both stable and inertial cavitation also occurred at 500 kPa (data not shown). In addition, long-pulse 500 kPa PNP

excitation was confirmed to result in significant primary radiation force that pushed MBs out of the stream of flow and onto the clot face during the sonothrombolysis experiments.

5.4.2 *In vitro* sonothrombolysis assay

A schematic depiction of the colorimetric assay utilized to measure volumetric clot lysis rates is shown in Figure 5-3A. To determine the sensitivity of this assay, 10 blood clots of uniform size and composition were completely lysed by 1 $\mu\text{g}/\text{ml}$ rtPA in a 30 ml volume of human plasma for 4 hours at 37 C. Following complete lysis, the free RBCs were centrifuged, plasma was removed, and the pelleted RBCs were lysed to release free hemoglobin in distilled water. The optical absorption ($A_{540\text{nm}}$) of a dilution series of the free hemoglobin, from 50% to 0.097%, was measured

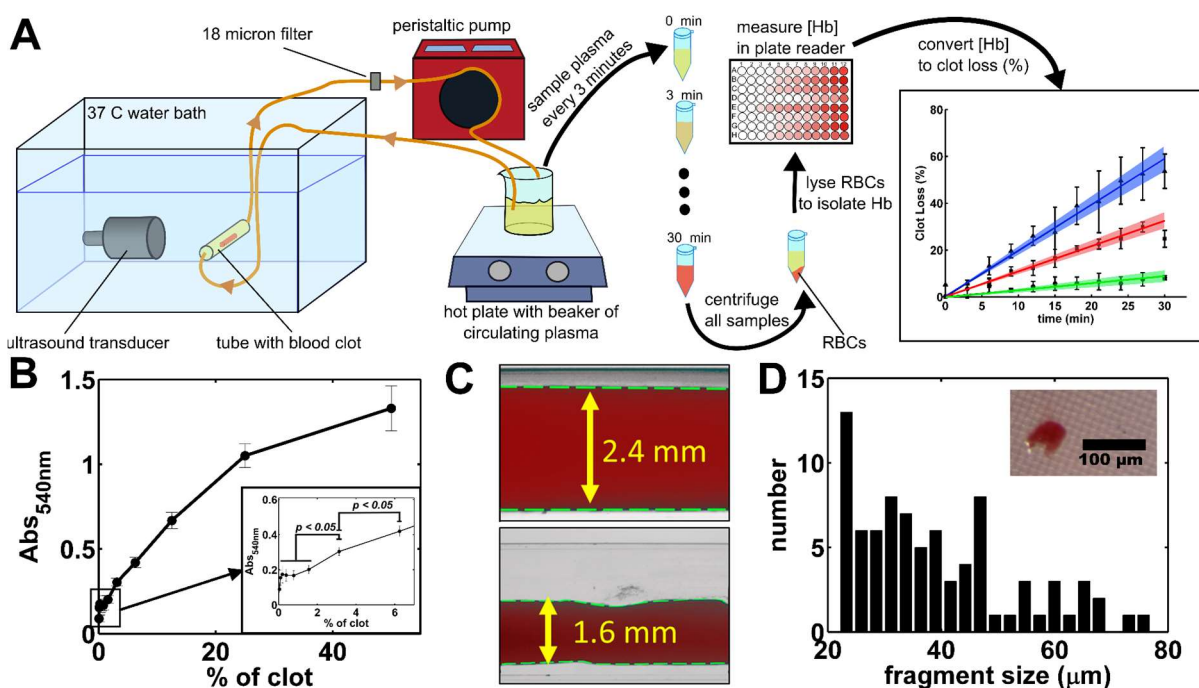


Figure 5-3: Schematic of *in vitro* sonothrombolysis assay and assay characterization

(A) Schematic of *in vitro* sonothrombolysis assay. Briefly, a blood clot was placed in a circulating flow loop and was exposed to ultrasound, microbubbles, and rtPA. The circulating plasma was sampled every minute and hemoglobin concentration was quantified using a plate reader. Changes in hemoglobin concentrations over time were used to derive a volumetric clot lysis rate for each experimental condition. (B) Sensitivity of the assay to percentage of the initial clot volume based on [Hb]. The assay is able to detect hemoglobin concentrations corresponding to greater than 1.5% of the initial clot volume. (C) Representative image of a clot prior to (top) and after (bottom) 30 min of sonothrombolysis. (D) Distribution of clot fragments observed on the 18 micrometer nylon mesh filter across all clots studied.

Table 5-1: Parameters for different experimental *in vitro* sonothrombolysis conditions

Group	[rtPa] ($\mu\text{g/ml}$)	US	MB production method	MB conc. (ml^{-1})	MB production rate ($1 \times 10^3 \text{ s}^{-1}$)	MB diameter (μm)	MB gas volume (μl)
A	0	–	–	–	–	–	0
B	1	–	–	–	–	–	0
C	1	Yes	Sonication	1×10^6	–	2.8 ± 1.7	1.4
D	1	Yes	Sonication	1×10^8	–	2.8 ± 1.7	140
E	1	Yes	FFMD	–	50	15	160
F	1	Yes	FFMD	–	250	15	800
G	1	Yes	FFMD	–	950	15	3020
H	1	Yes	FFMD	–	850	10	800
I	1	Yes	FFMD	–	100	20	800
J	0	Yes	FFMD	–	250	15	800
K	0.1	Yes	FFMD	–	250	15	800

to determine the smallest fraction of eroded clot that could be measured accurately by the assay. As shown in Figure 5-3B, hemoglobin concentrations corresponding to less than 1.5% of the total clot could not be distinguished from one another as the absorption measurement was too close to the sensitivity limit of the plate reader. Fractions above 1.5% of the total clot could be accurately and significantly detected ($p < 0.05$).

Images of the clot at 4X magnification were acquired by a microscope-mounted camera, as shown in Figure 5-3C, although these images were not used to quantify volumetric clot lysis rates. As shown, clot erosion occurred approximately uniformly along the clot face, and no large clot fragments were observed to be released from the clot. This observation is further strengthened by an analysis of clot fragments observed on the 18 μm nylon mesh filter. Figure 5-3D is a histogram of all clot fragments contained on the mesh filter across all clots and across all experimental conditions (described below). The largest clot fragment was 78 μm , as measured along its longest dimension.

5.4.3 *In vitro* sonothrombolysis with MBs produced by FFMD

The sets of experimental sonothrombolysis conditions that were evaluated in this study are given in Table 5-1. Two conditions without MBs and two conditions with MBs produced via

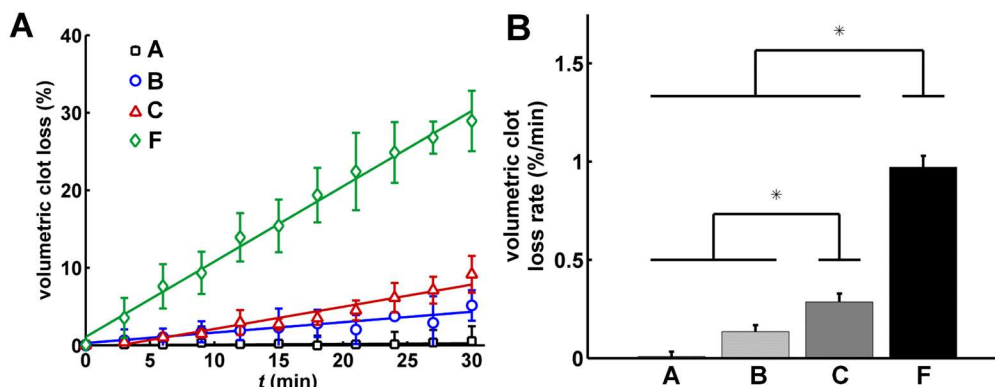


Figure 5-4: *in vitro* clot lysis curves for four experimental conditions

(A) Clot lysis curves for experimental groups A, B, C, F. Data points are mean \pm S.E. (B) Volumetric clot lysis rates for the four experimental groups shown in (A). * indicates $p < 0.05$.

sonication were evaluated in order to establish a baseline control for comparison to the MBs produced by the FFMD. The approximate volume of gas introduced into the flow loop over the entire 30 min experiment is also listed in the table (C₄F₁₀ or N₂).

Volumetric clot lysis curves for four experimental conditions are shown in Figure 5-4A. In all cases, the volumetric erosion rates were observed to be approximately linear over 30 minutes. The slopes derived from a linear regression of these four datasets correspond to the volumetric clot lysis rates (% of clot per minute) and are presented as a bar graph in Figure 5-4B. Clot lysis in the absence of rtPA, ultrasound, or MBs (Group A) was below the sensitivity of the assay (less than 1.5% of clot eroded over 30 minutes). To approximate a clinical-dose of rtPA,¹⁷⁶ 1 μ g/ml rtPA was circulated in the flow loop (Group B), and the clot lysis rate was 0.13 ± 0.03 %/min. Sonication-produced MBs (1×10^6 MB/ml, $d_{MB} = 2.8 \pm 1.7$ μ m) and 1 MHz ultrasound were added to 1 μ g/ml rtPA to match approximate clinical sonothrombolysis conditions (Group C³⁶⁻³⁸) and the clot lysis rate approximately doubled to 0.29 ± 0.04 %/min. When FFMD-produced MBs with $d_{MB} = 15$ μ m and a production rate of 250×10^3 MB/s were used with 1 μ g/ml rtPA and 1 MHz ultrasound (Group F), the clot lysis rate was 0.97 ± 0.06 %/min.

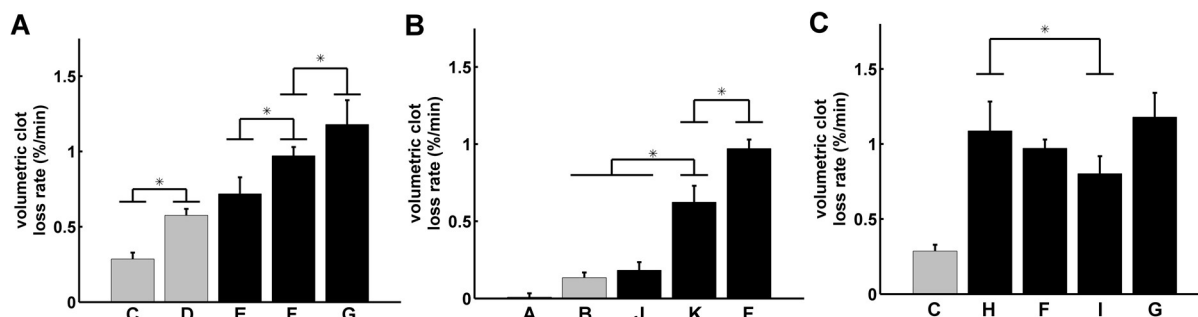


Figure 5-5: *in vitro* volumetric clot lysis rates for multiple experimental conditions

(A) Volumetric clot lysis rates for experimental groups that investigate the effect of changes in MB concentration and production rate. (B) Volumetric clot lysis rates that investigate the effect of changes in rtPA concentration. (C) Volumetric clot lysis rates that investigate the effect of changing MB diameter. * indicates $p < 0.05$.

Additional studies were performed to evaluate the effects of MB concentration, rtPA concentration, and MB diameter on rate on the sonothrombolysis process. Figure 5-5A shows the sonothrombolysis rates observed as the MB concentration (Groups C, D) or the FFMD production rates were increased (Groups E, F, G). As shown, sonothrombolysis rates increased as FFMD production rate increased, and rates observed for Groups F and G were significantly greater than Group D, which represented an approximate 100-fold greater MB dose than clinical MB dose. The effect of increasing rtPA concentration on sonothrombolysis rates is shown in Figure 5-5B. As expected, sonothrombolysis rates increased with increasing rtPA dose across Groups J, K, F. Finally, the effect of MB diameter was investigated and results are shown in Figure 5-5C. The approximate volume of gas administered in groups H, F, I was held constant while the MB diameter was varied across the range 10, 15, and 20 μm . The sonothrombolysis rates decreased with increasing MB diameter, but this effect may be due to the dramatic decrease in MB number as the MB diameter increased. When the production rates of 10 and 15 μm diameter MBs were approximately the same (Groups H and G), the observed sonothrombolysis rates were not significantly different ($p = 0.377$).

Table 5-2: *p*-value for comparison of clot lysis rates under differing experimental conditions.

	A	B	C	D	E	F	G	H	I	J	K
A	–	< 0.001	< 0.001	< 0.001	< 0.001	< 0.001	< 0.001	< 0.001	< 0.001	< 0.001	< 0.001
B	–	–	0.0241	< 0.001	0.113	< 0.001	< 0.001	< 0.001	< 0.001	0.457	< 0.001
C	–	–	–	< 0.001	< 0.001	< 0.001	< 0.001	< 0.001	< 0.001	0.0238	< 0.001
D	–	–	–	–	0.124	0.084	0.0481	< 0.001	0.003	< 0.001	0.183
E	–	–	–	–	–	0.017	< 0.001	< 0.001	0.312	< 0.001	0.0387
F	–	–	–	–	–	–	0.042	0.214	0.009	< 0.001	< 0.001
G	–	–	–	–	–	–	–	0.377	< 0.001	< 0.001	< 0.001
H	–	–	–	–	–	–	–	–	0.289	< 0.001	< 0.001
I	–	–	–	–	–	–	–	–	–	< 0.001	0.441
J	–	–	–	–	–	–	–	–	–	–	0.008
K	–	–	–	–	–	–	–	–	–	–	–

Significant differences, $p < 0.05$, are italicized.

p-values were computed to test for similarity among the experimental conditions and are listed in Table 5-2 (two-tailed t-test). The ratio of clot lysis rates for all experimental conditions relative to an approximate clinical dose of rtPA (Group B, 1 µg/ml) are listed in Table 5-3.

5.5 Discussion

5.5.1 *In vitro* sonothrombolysis model

The *in vitro* sonothrombolysis model presented in this study measured clot erosion down to 1.5% of the total clot volume, which was sufficient to study a wide range of experimental conditions. A benefit of this model was the ability to derive volumetric clot erosion rates from multiple time-points, which significantly increased the confidence in the measured

Table 5-3: Clot lysis rates relative to experimental Group B (1 µg/ml rtPa alone).

Group	Ratio of Clot Lysis Rates
A	0.06 (0, 0.11)
B	–
C	2.1 (1.9, 2.4)
D	4.3 (3.9, 4.7)
E	5.4 (4.8, 6.0)
F	7.3 (6.6, 8.0)
G	8.8 (7.9, 9.8)
H	8.1 (7.2, 9.1)
I	6.0 (5.4, 6.7)
J	1.4 (1.2, 1.6)
K	4.7 (4.2, 5.2)

Relative rates presented as mean (95% C.I.).

sonothrombolysis rates compared to models that rely on measurements taken at a single time point at the end of the study (for instance, models in which clots are weighed before and after treatment).^{190,197,198} The sonothrombolysis experiments were performed for 30 minutes because this was sufficient for evaluating a statistically significant difference in lysis rates and because the lysis rates were approximately linear for the first 30 minutes. However, it is not expected that these approximately linear lysis rates continue for entire duration of the clot lysis process. As shown by Petit et al. in a similar sonothrombolysis model, lysis rates are approximately linear at the beginning of the process and decrease as the clot erodes.¹⁸⁵

The sonothrombolysis model used in this work produced results that are in broad agreement with those presented in the literature. As shown in Figure 3-4, adding ultrasound and sonicated MBs at a concentration of 1×10^6 MB/ml increased the *in vitro* thrombolysis rate by 2.1-fold (95% C.I. 1.9 – 2.4) relative to thrombolysis rates observed when using rtPA alone at an approximate clinical dose (e.g. 1 µg/ml). Previously reported results for similar experimental conditions demonstrated increased thrombolysis rates of approximately 1.5 and 3-fold, depending on ultrasound conditions and the composition of the blood clot.^{181,182,184-187,190}

The composition of the blood clot greatly impacts the efficacy of thrombolysis by rtPA, with or without the addition of MBs or ultrasound.¹⁹⁷ The *in vitro* clot formulation used in this study was intended to simulate the average composition of clots retrieved from 50 ischemic stroke patients, which were determined via histology to be comprised of 61 ± 21 % fibrin/platelets, 34 ± 21 % RBCs, and 4 ± 2 % white blood cells.¹⁹⁶ Accordingly, the thrombus composition used in this study was comprised of 65 % platelet-rich plasma and 35 % RBC in order to simulate ‘white clots’ (platelet rich), which are more likely to be observed *in vivo* than red clots, which are rich in RBCs and fibrin.¹⁹⁹ The high platelet content is associated with reduced thrombolysis rates compared to

the RBC-rich blood clots formed from whole blood that are often studied in *in vitro* sonothrombolysis models.¹⁹⁷

Finally, the model permitted the evaluation of clot fragmentation, which is of concern in the context of ischemic stroke, as clot fragments that migrate downstream may cause distal emboli and restrict flow to distal regions of the brain.^{159,179} Few clot fragments above 20 μm in diameter remained on the nylon mesh filter at the end of the studies, which may indicate that sonothrombolysis does not result in significant clot fragmentation. However, this may also be a result of circulating rtPA that could have dissolved fragments that were caught on the mesh but remained in the flow loop for the duration of the experiment. No obvious trends could be established regarding which experimental conditions produced the most clot fragmentation because few clot fragments above 20 μm in diameter were retained on the nylon mesh.

5.5.2 Sonothrombolysis with MBs produced by FFMDs

Increased MB concentrations are associated with accelerated sonothrombolysis rates but may also increase the incidence of undesirable off-target effects (e.g. hemorrhage, hemolysis).^{45,178,186,190} Thus, we sought to develop a MB delivery technique and formulation that would permit high MB concentrations in the vicinity of the thrombus but low concentrations elsewhere. Accordingly, we hypothesized that placement of a catheter near the blood clot would permit the use of large, transiently stable MBs that dissolve downstream and potentially reduce the incidence of off-target effects.^{194,200} MB production by a FFMD at the site of therapeutic delivery is hypothesized to permit real-time adjustment of MB size, concentration, composition, and stability in order to modulate sonothrombolysis efficacy and safety.^{57,193} The N_2 gas MBs used in this work exhibited a half-life of 65 ± 27 s in well-mixed saline and were also observed to dissolve within minutes in the sonothrombolysis experiments (Figure 5-3A).^{58,59} Notably, this

same FFMD MB formulation was evaluated in a mouse model, and circulation half-lives of less than 30 s were observed.¹⁹³ The stability of FFMD-produced MBs can be tuned to a specific application by changing the shell material (e.g. using a lipid^{56,201}) or by using a gas with different solubility in water (e.g. decafluorobutane⁵⁹ or CO₂).

MB gas volumes introduced into the sonothrombolysis assay over 30 minutes ranged from 1.4 µl to 3 ml, and sonothrombolysis rates were observed to increase with increasing MB gas volume, MB concentration, and MB production rates (Figure 5-5A). The condition in which 3 ml N₂ gas was administered (Group G) represents the upper limit of MB production rates attainable by the FFMD, and the safety of administration of these large gas volumes must be considered when translating this technique to *in vivo* models. Rapid intra-arterial administration of even 1 ml of air is considered unsafe due to the risk of gas embolism,²⁰² but smaller volumes (e.g. 100 µl) have been administered safely in rabbit models,^{203,204} suggesting that several milliliters of high solubility gas could be administered intra-arterially over a long time period. In contrast, venous administration of large gas volumes poses much less of a risk, so this technique may be more translatable for the treatment of venous thromboembolisms than for stroke. In any case, additional study of the use of large volumes of high solubility gases in *in vivo* models is required to determine if this approach is feasible *in vivo*.

As shown in Figure 5-5B, sonothrombolysis rates were found to increase with increasing rtPA dose (Groups J, K, F). The results suggest that accelerating thrombolysis with MBs produced by FFMDs may provide the opportunity for rtPA dose reduction because the thrombolysis rates for Group B (rtPA dose of 1 µg/ml) and Group J (rtPA dose of 0 µg/ml) were statistically similar ($p = 0.457$). This also implies a significant degree of mechanical disruption from MB interactions with the clot, given that limited enzymatic breakdown of the fibrin mesh could occur in Group J.

This observation is consistent with previous findings that have described significant clot erosion from MBs and ultrasound alone, especially when using ultrasound parameters that elicit both stable and inertial cavitation (Figure 5-2).^{178,185,195} In addition, a 10-fold increase in rtPA dose from 0.1 µg/ml (Group K) to 1 µg/ml (Group F) was associated with only a 40% increase in sonothrombolysis rate, potentially a sign of diminishing returns. Developing thrombolysis techniques that utilize reduced rtPA doses, or even no rtPA, is of significant clinical importance given that many patients presenting with stroke or venous thromboembolisms are contraindicated for rtPA therapy.^{150,151}

Sonothrombolysis rates were also evaluated when the diameter of FFMD-produced MBs was varied from 10 to 20 µm and the total amount of gas held constant at approximately 800 µl. The sonothrombolysis rates decreased with increasing MB diameter (Figure 5-5C), but this effect may be due to the decrease in MB number and concentration as the MB diameter increased. In support of this view, when the production rates of 10 and 15 µm diameter MBs were approximately the same (Groups H and G), the observed sonothrombolysis rates were not significantly different ($p = 0.377$). In addition, Groups D and E were performed to compare sonothrombolysis rates in approximately gas volume-matched conditions for sonication-produced MBs of diameter 2.8 ± 1.7 µm and FFMD-produced MB of 15 µm. The sonothrombolysis rates were not statistically different ($p = 0.124$), but Group D is representative of a 100-fold increase in the clinically permitted concentration of high-stability MBs, which may be prohibitive *in vivo*. This result suggests that, on a per-MB basis, the larger FFMD-produced MBs may be more effective at accelerating sonothrombolysis rates, but there is a need for additional study to establish optimal MB size and concentration for accelerating thrombolysis.

Overall, the results of this study suggest that the larger MBs produced by the FFMD are capable of significantly enhanced sonothrombolysis rates compared to conditions in which only clinical doses of either rtPA or rtPA with small MBs were used (i.e. 2 – 8 fold enhanced sonothrombolysis rates, Table 5-3). The notion that large MBs confer enhanced bioeffects is supported by experimental and theoretical studies that demonstrate higher energy inertial cavitation,²⁰⁵⁻²⁰⁷ larger microstreaming fields,²⁰⁸⁻²¹⁰ more violent jetting,^{205,211,212} and increased acoustic radiation forces^{110,213} from MBs of large diameter compared to MBs of small diameter. Further enhancement of sonothrombolysis rates may be possible by matching the ultrasound frequency to the resonance frequency of the MB, as MBs undergo larger amplitude radial oscillations^{44,214} and exhibit a lower pressure threshold for cavitation when excited near their resonant frequency;^{134,215} all factors that may increase their ability to tunnel into and disrupt the fibrin mesh.¹⁷⁸ It should be noted that most clinical applications of sonothrombolysis for ischemic stroke therapy have utilized ultrasound frequencies between 1 – 3 MHz^{36-38,200} and that lower frequencies have been linked to standing wave formation and increased hemorrhagic transformation.^{180,216} Thus, while the safety of in vivo administration of this MB formulation has been evaluated in a mouse model,¹⁹³ additional study is required in large animal in vivo models to balance thrombolysis efficacy with safety concerns related to gas embolism, hemorrhage, and potentially destructive bioeffects caused by cavitating MBs.

5.6 Conclusions

This study evaluated the *in vitro* sonothrombolysis efficacy of large, transiently stable microbubbles produced by a flow-focusing microfluidic device. The use of large diameter microbubbles ($d_{MB} = 10 - 20 \mu\text{m}$) produced in real-time at production rates between $50 - 950 \times 10^3$ per second by a flow-focusing microfluidic device resulted in approximately 4 – 8 fold

increases in sonothrombolysis rates compared to a clinical rtPA dose. Additionally, the sonothrombolysis rates observed with microbubbles produced by a flow-focusing microfluidic device resulted in approximately 2 – 4 fold increases in sonothrombolysis rates compared to a peripheral I.V. infusion of a clinical dose of conventional microbubbles and a clinical dose of rtPA. Overall, the results of this study indicate that the large diameter microbubbles produced by a flow-focusing microfluidic device are capable of significantly enhanced *in vitro* sonothrombolysis rates. Additional testing is required to optimize the use of this microbubble formulation and to evaluate its efficacy *in vivo*.

Chapter 6. *In vivo* sonothrombolysis efficacy of microbubbles produced by a microfluidic device in a rat model of ischemic stroke⁵

6.1 Abstract

Sonothrombolysis traditionally uses microbubble formulations comprised of low solubility gases with diameters between 1–4 μm . Microbubbles with parameters outside of this range have not been explored for sonothrombolysis due to embolic risks associated with large diameter gas bubbles. However, a growing body of evidence suggests that larger microbubbles confer increased bioeffects when excited acoustically, as has been demonstrated in blood brain barrier disruption, sonoporation, and sonothrombolysis studies. In this work, we used a flow-focusing microfluidic device to produce microbubbles comprised of a non-crosslinked albumin shell with a nitrogen gas core. These microbubbles had diameters between 10 – 20 μm and have previously been shown to exhibit *in vivo* circulation half-lives of less than 60 s. The efficacy of these microbubbles at accelerating clot lysis via sonothrombolysis was evaluated in a rat model of ischemic stroke ($n = 32$). The microbubbles were produced in real-time and were administered via a catheter to the internal carotid artery for direct delivery to the occluded middle cerebral artery, while ultrasound was administered through the skull and rtPA was administered intravenously via a tail-vein catheter. The results demonstrate that larger-diameter microbubbles comprised of high solubility

⁵ This chapter contains material from the following peer-reviewed conference and journal publications:

AJ Dixon, JP Kilroy, AL Klibanov, JA Hossack, “Microbubbles produced by a catheter-based microfluidic device for sonothrombolysis applications.” 20th European Symposium on Ultrasound Contrast Imaging (2015), Rotterdam, The Netherlands.

AJ Dixon, J Li, JMR Rickel, B Shin, Z Zuo, JA Hossack, “Sonothrombolysis efficacy of microbubbles produced by a microfluidic device in a rat ischemic stroke model.” IEEE International Ultrasonics Symposium (2016), Tours, France.

AJ Dixon, J Li, JMR Rickel, B Shin, Z Zuo, JA Hossack, “Sonothrombolysis efficacy of microbubbles produced by a microfluidic device in a rat ischemic stroke model.” in preparation.

gases can be safely administered intra-arterially to deliver a sonothrombolytic therapy. Further, sonothrombolysis using these large microbubbles reduced cerebral infarct volumes by up to approximately 50% versus no therapy and permitted a rtPA dose reduction of 3.3 (95% C.I. 1.8 – 3.8) fold when compared to therapy with intravenous rtPA alone.

6.2 Introduction

Early recanalization of the large occluded arteries in the brain is an essential component of treatment after the onset of acute ischemic stroke. Intravenous administration of recombinant tissue plasminogen activator (rtPA) only achieves complete recanalization in approximately 30% of patients, which has motivated the development of alternative recanalization techniques.^{149,217} Current generation thrombectomy catheters, known as “stentriever”, have recently achieved primary vessel recanalization rates approaching 90% and complete restoration of perfusion in distal capillary beds in close to 60% of cases.^{156,218} These results, reported by multiple independent trials (MR CLEAN²¹⁹, SWIFT PRIME¹⁵⁶, ESCAPE²²⁰, REVASCAT²²¹, EXTEND-IA²²²), represent a significant improvement over intravenous rtPA therapy and strongly support the use of interventional endovascular approaches for treating acute ischemic stroke patients.²²³

However, despite successful recanalization of the primary vessel, a subset of patients still fail to achieve clinical improvement. One possible explanation for this may be microcirculation no-reflow, a situation in which major vessel recanalization does not result in microvascular reperfusion.^{224,225} Indeed, while improved outcomes of recent trials were strongly linked to improved recanalization rates, the 90-day outcomes of patients whose distal perfusion was not restored (i.e. TIC1 0/1/2a scores) were significantly worse than the outcomes of patients whose distal perfusion was completely restored were completely recanalized (34% vs 49% functional 90-day mRS score, respectively).^{226,227} Therefore, given the recent success of stent retrievers for

treating the primary occlusion, the focus must now turn to extending the “reach” of these catheters to address distal occlusions in M2 segment of the MCA (and beyond) that contribute to poor revascularization in the remaining ~30% of ischemic stroke patients.

Multiple reports have suggested that the use of adjuvant ultrasound (with or without microbubbles) improves rtPA efficacy and distal reperfusion.²²⁸⁻²³¹ In a clinical trial, ischemic stroke patients treated with a combination of rtPA, transcranial ultrasound, and microbubbles had significantly higher rates of complete recanalization (55% vs 24%) and greater clinical improvement (54.9% vs 31.1%) compared with patients who received rtPA alone.²³¹ Notably, the observed rate of complete recanalization was similar to that achieved by the recent stentriever trials discussed above. However, a limitation of these sonothrombolysis-based approaches was an increased risk of off-target intracerebral hemorrhage (ICH), which led at least one clinical study to early termination.²³² Thus, methods must be developed to confine the effects of sonothrombolysis to the primary occluded vessel and its downstream capillary bed to limit these off-target deleterious effects in otherwise unaffected regions of the brain.

In this work, we evaluated a catheter-based sonothrombolysis treatment method that used large-diameter microbubbles for accelerating primary vessel recanalization in a rat model of ischemic stroke. The development of this method was informed by the clinical findings in support of endovascular interventions for acute ischemic stroke and the growing body of evidence indicating that larger microbubbles produce enhanced bioeffects due to increased microstreaming,²³³⁻²³⁶ increased momentum transfer via acoustic radiation force,^{39,237,238} and higher-energy cavitation events.^{206,207,239} Thus, we hypothesized that off-target hemorrhage could be mitigated by directing the delivery of microbubbles to the occluded blood vessel while

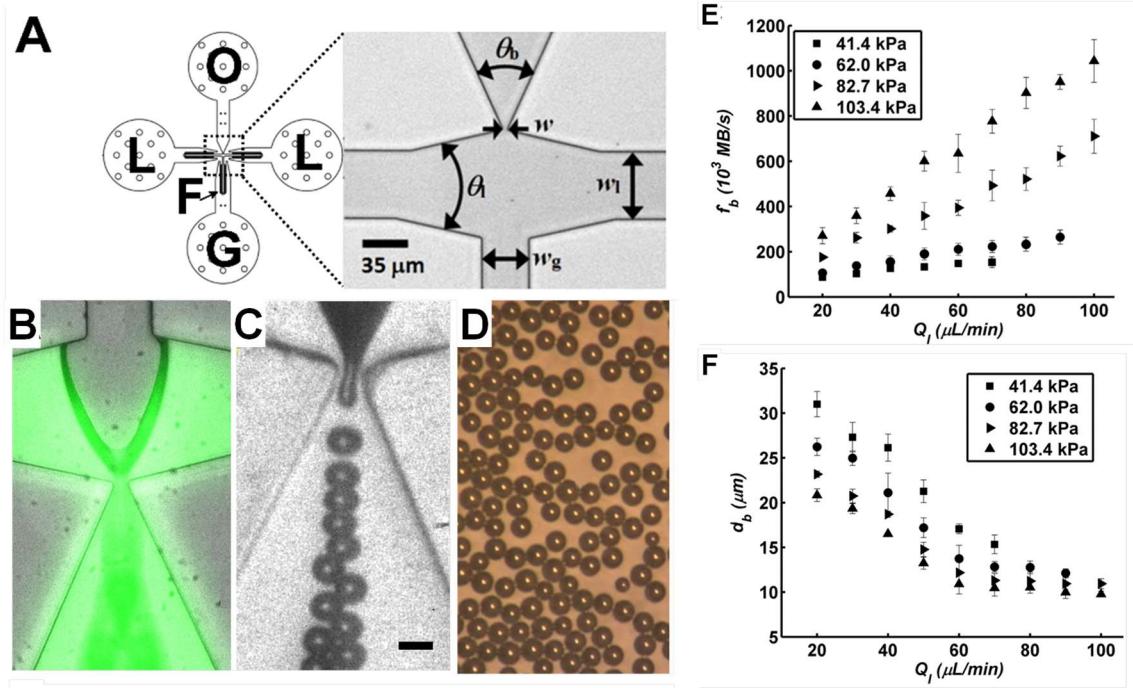


Figure 6-1: *in vitro* clot lysis curves for four experimental conditions

(A) (Left) Schematic of the flow-focusing microfluidic device (FFMD). There are two liquid inlets (L), one gas inlet (G), filters to prevent the nozzle from clogging (F), and an outlet where MBs are emitted (O). (Right) 20X magnified view of the device nozzle. Dimensions are $w_g = 30 \mu m$, $w_l = 50 \mu m$, $w = 8 \mu m$, $\theta_l = 25^\circ$, $\theta_b = 50^\circ$. (B & C) High speed images of the FFMD producing 10 μm diameter MBs. The liquid phase (green) is easily distinguished from the gas phase in B. (D) Monodisperse microbubbles imaged immediately after exiting the microfluidic device. Scale bar in (B,C,D) is 10 μm . (E) MB production rates as a function of liquid flow rate, Q_l , for four different gas pressure. (F) MB diameter as a function of liquid flow rate, Q_l , for four different gas pressures.

enhancing the thrombolytic effect of sonothrombolysis by using larger microbubbles with enhanced bioeffects.

6.3 Materials and Methods

6.3.1 Microfluidic device fabrication and microbubble production

A custom SU-8 mold with the flow-focused microfluidic device (FFMD) channel design was manufactured by photolithography, as previously described.^{58,59} Devices were cast in polydimethylsiloxane (PDMS) and bound to a clean PDMS substrate using oxygen plasma. The final device had a channel height of 22 micrometers and a nozzle width of 8 micrometers, while

the liquid and gas channels were 50 and 30 micrometers wide, respectively. All stated dimensions are accurate to ± 1 micrometers. A schematic of the FFMD is shown in Figure 6-1.

Microbubbles were produced using 99.998% N₂ (GTS Welco, Richmond, VA) and a liquid phase comprised of 4% w/v bovine serum albumin (BSA) and 10% w/v dextrose in 0.9% saline. The liquid phase was prepared by mixing its components overnight at 4C – no effort was made to degas the liquid phase prior to injection into the microfluidic device. The liquid phase was pressurized using a syringe pump (PhD 2000, Harvard Apparatus, Holliston, MA). The liquid phase was filtered by 0.2 μ m nylon filters prior to use in the FFMD. The gas pressure was regulated by a digital manometer (06-664-22, Fisher Scientific, Waltham, MA). Microbore PTFE tubing of 762 μ m outer diameter (Cole-Parmer, Vernon Hills, IL) was used to convey the gas and liquid phases into the device. Liquid flow rates varied between 30 – 90 μ L/min and gas pressures varied between 43.8 and 89.6 kPa. Microfluidic microbubble production was monitored by a high-speed camera (SIMD24, Specialised Imaging, Tring, UK) and production rate and diameter were measured in ImageJ.

6.3.2 Safety evaluation of intra-arterial administration of FFMD-produced microbubbles

All animal protocols were approved by the University of Virginia Animal Use and Care Committee. Prior to conducting the ischemic stroke studies described below, a small study was conducted to evaluate the safety of intra-arterial delivery of the large microbubbles produced by the FFMD. On the day of surgery, male Sprague-Dawley rats weighing between 350 – 500 g were anesthetized with 5 vol% isoflurane in medical air, intubated, and ventilated artificially throughout the experiment using an anesthesia ventilator. Isoflurane was reduced to 2 vol% in medical air after intubation for the remainder of the experiment. The external carotid artery (ECA) was catheterized and a PE-10 tube was inserted to the junction of the ECA and the internal carotid

artery (ICA). Microbubbles of approximately 15 μm diameter produced at three different production rates were administered continuously to the rat ECA through the PE-10 tube for 15 minutes. Rats were monitored for changes in respiration or heart rate during microbubble administration. After 15 minutes of microbubble administration, rats were allowed to wake from anesthesia and a neurological deficit score was measured immediately after recovering from anesthesia and 24 hours later.²⁴⁰ At the 24 hr time point, the rats were sacrificed, their brains excised, fixed in paraformaldehyde, sliced into 2 mm thick sections, and stained with triphenyltetrazolium chloride (TTC) to evaluate the brain infarct volume. Brain infarct volume was measured by an anesthesiologist who was blinded to the study groups.

The neurological deficit scoring system is as follows: 0, no apparent deficits; 1, failure to extend left forepaw fully; 2, decreased grip of the left forelimb; 3, spontaneous movement in all directions, contralateral circling only if pulled by the tail; 4, circling or walking to the left; 5, walking only if stimulated; 6, unresponsiveness to stimulation and with depressed level of consciousness; 7, dead.²⁴⁰

6.3.3 Rat model of ischemic stroke

On the day of surgery, the rats were anesthetized with 5 vol% isoflurane in medical air, intubated, and ventilated artificially throughout the experiment using an anesthesia ventilator. Isoflurane was reduced to 2 vol% in medical air after intubation for the remainder of the experiment. Blood acquired from the tail vein of a donor rat was clotted in a PE-50 tube and kept at 4C for up to 48 hr prior to experimentation. Ischemic stroke was simulated in the rat by administering the blood clot into the middle cerebral artery via catheterization of the ECA, as described above. The clot was administered via a PE-10 tube and was allowed to sit in the MCA for 15 minutes prior to a therapeutic intervention. The total volume of clot administered to each

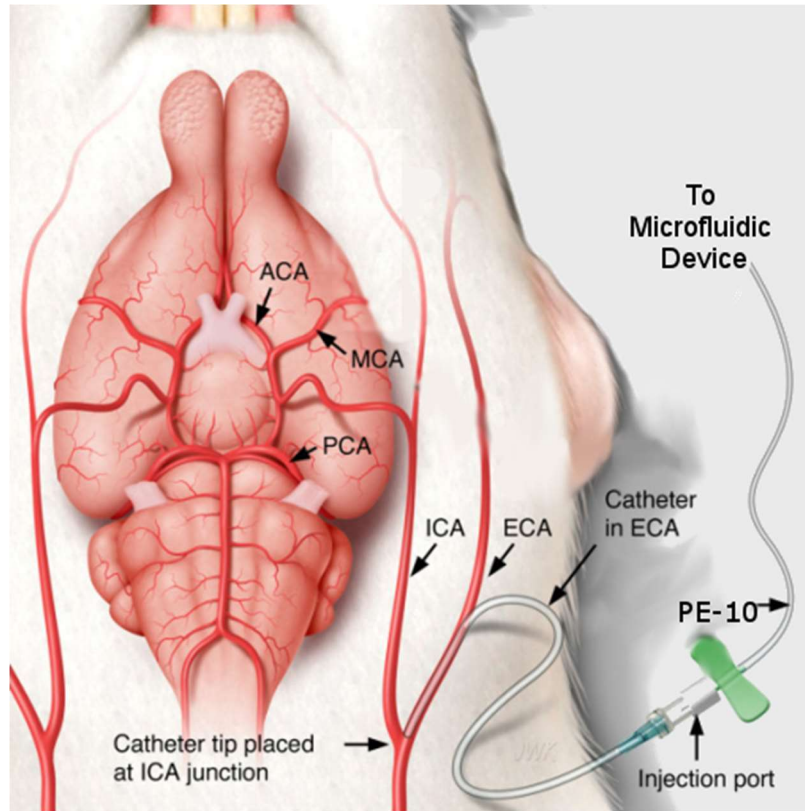


Figure 6-2: Schematic of rat surgery for administration of microbubbles and thrombus

The ECA was catheterized and the catheter was placed at the junction of the ICA and ECA. Microbubbles were administered through a PE-10 tube that was connected to the outlet of the FFMD and to the catheter by a tubing connector. In the ischemic stroke studies, the clot resided where the ICA intersects the Circle of Willis and occluded both the MCA and PCA. Figure adapted and modified from Crumrine RC *et al*⁴ under the guidelines of the Creative Commons Public License (CCPL) 2.0 for Open Access Images. CCPL 2.0 license may be found at the following link: <https://creativecommons.org/licenses/by/2.0/legalcode>. The original figure may be found at this link: https://openi.nlm.nih.gov/detailedresult.php?img=PMC3184064_2040-7378-3-10-3&req=4

rat was the same, and was measured to be approximately 16 μ l. All animals also received a tail-vein catheter for administration of thrombolytic drugs, if applicable.

Animals were randomized to four different therapeutic interventions. Group A animals received a 2 ml intravenous injection of saline via the tail vein catheter (sham). Group B animals received a 2 ml intravenous injection of rtPA (0.9 mg/kg) in saline via the tail vein catheter (representative of a clinical dose).²⁴¹ Group C animals received 1/10th of the rtPA dose of Group 2 animals (0.09 mg/kg) in saline via the tail vein catheter. Group D animals also received 1/10th of the rtPA dose of Group B animals (0.09 mg/kg) via the tail vein catheter and sonothrombolysis

therapy as described below. In all Groups, the tail vein injection was performed via continuous infusion using a syringe pump over a period of 30 minutes.

In Group D animals, microbubbles produced in real time by the FFMD were administered via the ECA catheter that was previously used to place the blood clot. The microbubble outlet channel of the FFMD was connected directly to the ICA catheter to administer microbubbles into the rat. Ultrasound was applied by a single element ultrasound transducer coupled to the skull of the rat by ultrasound gel (1 MHz center frequency, V302-SU, Olympus Panametrics, Waltham, MA). The hair on the rat's head was removed to expose the bare skin to facilitate acoustic coupling. Acoustic pulses of 100 cycles were applied at 10% duty factor with peak negative pressures of 500 kPa (as measured in a water tank). Ultrasound and microbubbles were administered for a total of 30 minutes. Ultrasound was administered continuously while microbubbles were administered for 30 s every 4.5 minutes. Microbubble administration could not be continuous because administration through the internal carotid artery catheter blocked blood flow to the brain, and blood flow could not be blocked for the entire 30 minute intervention. All microbubble production rates quoted in

Table 6-1: Information on rats included in microbubble safety study

Rat Number	MB Dose	Weight (g)	MB Diameter (µm)	MB Production Rate (MB/s)	Total Gas Volume (µl)	Neurological Score Immediately Following MB Administration	Percent Infarct Volume
101	Control	481	N/A	N/A	N/A	0	0
102	Control	511	N/A	N/A	N/A	1	0
103	Low	429	15	150,000	240	3	1.5
104	Low	440	15	150,000	240	1	0
105	Low	437	15	150,000	240	2	0
106	Medium	478	15	500,000	800	3	3.5
107	Medium	529	15	500,000	800	4	7.9
108	Medium	465	15	500,000	800	3	8.4
109	High	479	15	1,200,000	1910	5	13.7
110	High	495	15	1,200,000	1910	7	N/A*

* Rat #110 died prior to the 24 hr timepoint and TTC staining could not be performed

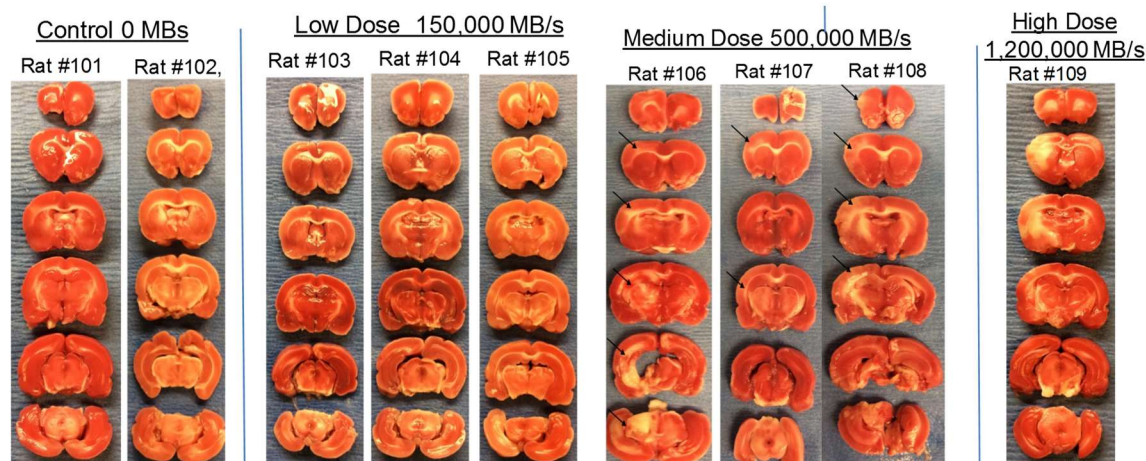


Figure 6-3: TTC staining of brains sections from all rats included in the microbubble safety study
Regions of infarct may be detected as white or light shades of pink whereas non-infarcted tissue stains pink. Areas of small infarcts that are difficult to identify, but were identified by the blind expert observer are indicated by black arrows. Obvious infarct zones are not explicitly highlighted. The Rat number associated with each brain corresponds to the rat number in Table 6-1.

the rat studies were accurate to approximately $\pm 20\%$, while all microbubble diameters stated for the rat studies were accurate to approximately $\pm 10\%$. A schematic of the surgery is shown in Figure 6-2.

Following the intervention, the catheters were removed from the rats and the rats were allowed to recover from anesthesia. Immediately following recovery from anesthesia, a neurological deficit score was measured based on the rat's ability to walk and feel pain.²⁴⁰ The neurological deficit was also evaluated 24 hr after the intervention. At the 24 hr time point, the rats were sacrificed, their brains excised, fixed in paraformaldehyde, sliced into 2 mm thick sections, and stained with triphenyltetrazolium chloride (TTC) to evaluate the brain infarct volume. Brain infarct volume was measured by an anesthesiologist who was blinded to the study groups.

6.4 Results

6.4.1 Microbubble production by FFMD

A schematic and description of the microfluidic channel geometry is illustrated in Figure 6-1. MBs of diameters between 9.8 ± 0.3 and 31.1 ± 1.4 μm were produced at rates between 87.7 ± 4

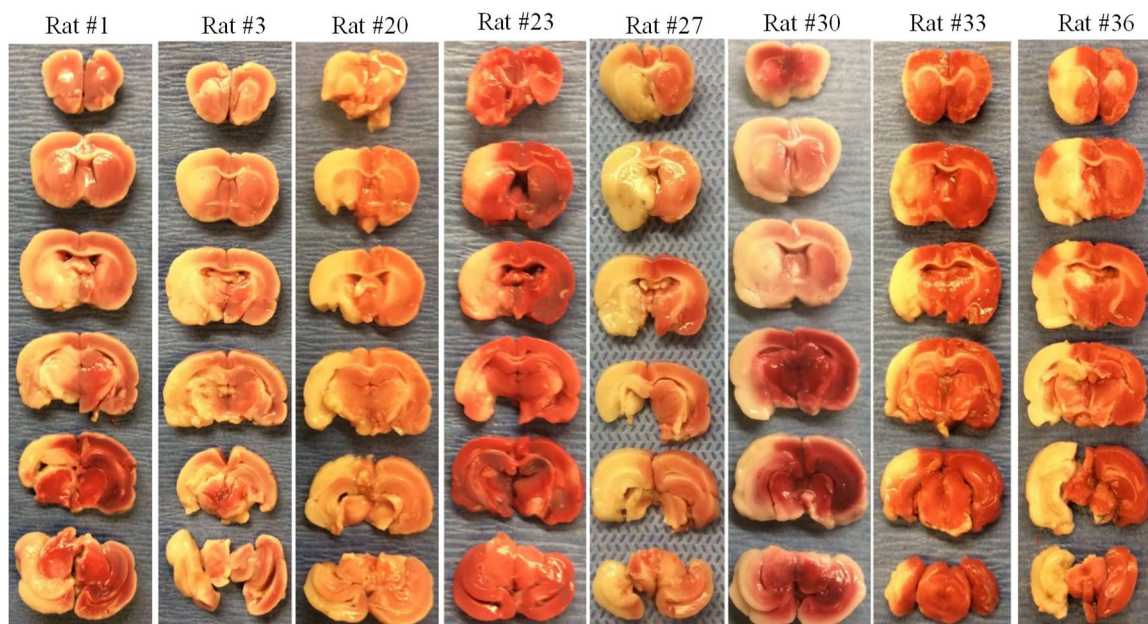


Figure 6-4: TTC staining of brains sections from all rats included in Group A (Control) of the ischemic stroke study

Regions of infarct may be detected as white or light shades of pink whereas non-infarcted tissue stains pink. Several of these rats died prior to the 24 hour time point, so the healthy tissue did not stain as well, accounting for the color variations. The Rat number associated with each brain corresponds to the Rat number in Table 6-4.

$\times 10^3$ and $1043 \pm 94 \times 10^3$ MB/s. Gas pressures ranged from approximately 40 to 110 kPa and liquid flow rates were varied between 20 and 110 $\mu\text{L}/\text{min}$. The MB production characteristics at discrete gas pressures and liquid flow rates, as shown in Figure 6-1, were acquired from a single FFMD operated on three separate days to gauge reproducibility. A still image of monodisperse microbubbles that was captured immediately after the microbubbles had left the microfluidic device is also shown in Figure 6-1.

6.4.2 Safety study of intra-arterial microbubble administration

Microbubbles produced by an FFMD were continuously administered to the rat brain via the ECA catheter for 15 mins to evaluate the safety of intra-arterial MB administration. Microbubbles had an average diameter of 15 μm (maximum: 20 μm , minimum 10 μm) and were produced at three different production rates: 150,000, 500,000 and 1,200,000 MB/s. These doses corresponded to total injected gas volumes of approximately 240, 800, and 1900 μL . Infarct volumes were

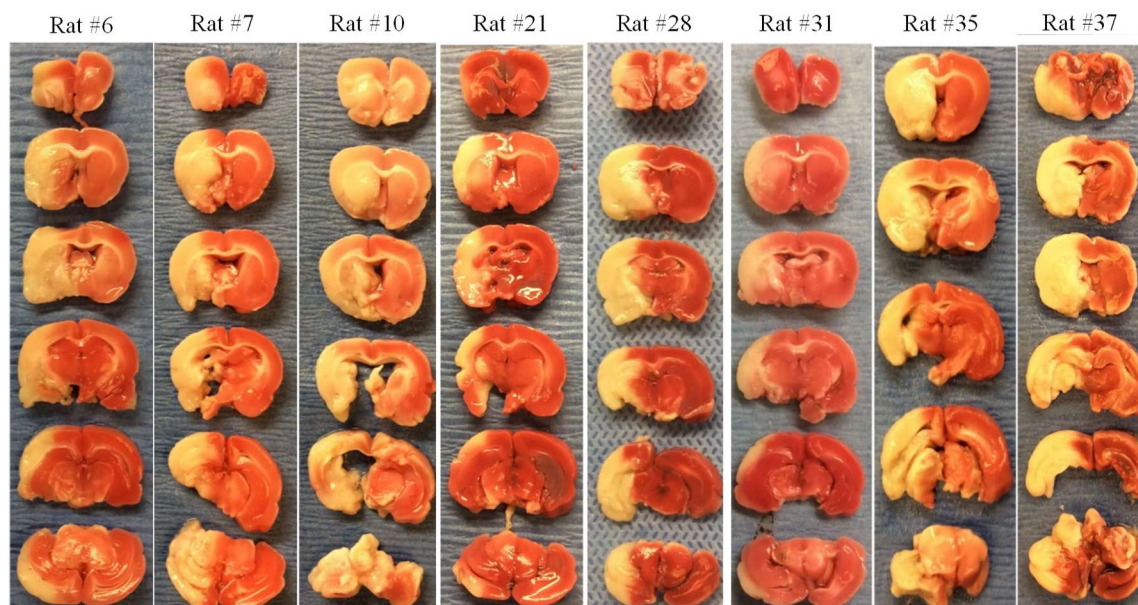


Figure 6-5: TTC staining of brains sections from all rats included in Group B (Low Dose rtPA) of the ischemic stroke study

Regions of infarct may be detected as white or light shades of pink whereas non-infarcted tissue stains pink. Rat #37 was dead at 24 hours after surgery. The Rat number associated with each brain corresponds to the Rat number in Table 6-4.

assessed 24 hr following the administration of MBs to assess damage caused by gas embolization of the cerebral vasculature. Results of TTC-staining for each rat brain are shown in Figure 6-3. Rats receiving the highest MB doses showed small areas of localized infarct on the side of the brain corresponding to the side of the animal that was catheterized. Rats that received the lowest MB dose (150,000 MB/s) and no MBs (saline sham injection) showed no signs of infarct. Rats that received a medium dose of microbubbles exhibited an average of 6.6 ± 2.7 % infarct. One rat that received a high dose of microbubbles exhibited 13.7 % infarct, while a second rat that received the same dose exhibited respiratory distress and died 4 – 8 hours after microbubble administration. It was observed that this rat struggled to breath upon waking from anesthesia, perhaps due to microbubbles that migrated to the heart through the common carotid artery rather than into the brain through the ICA. A summary of infarct measurement results and information about each rat included in the safety study is given in Table 6-1. All rats that were alive at 24 hours had a

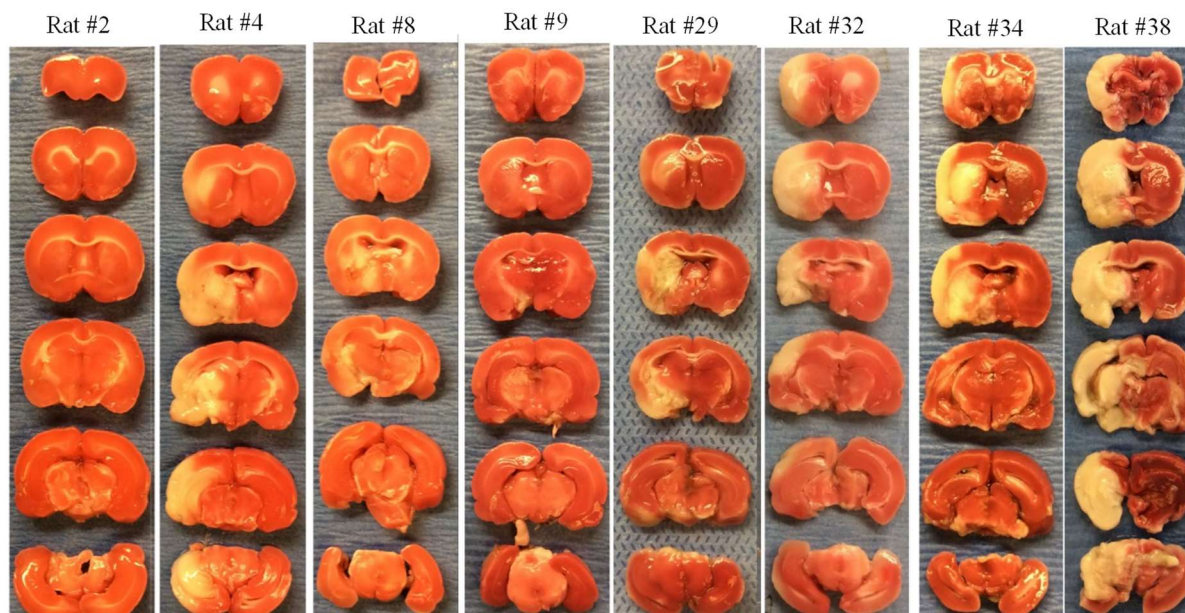


Figure 6-6: TTC staining of brains sections from all rats included in Group C (High Dose rtPA) of the ischemic stroke study

Regions of infarct may be detected as white or light shades of pink whereas non-infarcted tissue stains pink. Rat #38 was dead at 24 hours after surgery. The Rat number associated with each brain corresponds to the Rat number in Table 6-4.

neurological deficit score of 0, except the rat the received the highest dose of microbubbles (Rat #109), which had a neurological deficit score of 2.

6.4.3 Rat ischemic stroke model

The microbubbles used for the sonothrombolysis intervention in Group D were produced at a rate of 250,000 microbubbles per second and had average diameters of 15 μm when measured at the nozzle of the microfluidic device. A total of approximately 80 μl N_2 gas was administered to each animal over the 30 minute intervention. In no cases did the rats appear to suffer from respiratory or cardiac distress directly from the administration of microbubbles or the application of ultrasound. No rats exhibited intracranial bleeding as would be observed in the histology prior to TTC staining.²⁴²

Infarct volumes were measured for rats in each group (N = 8 rats in Groups A and B, and N = 7 for Groups C and D). Results of TTC staining for each rat included in the study are given in

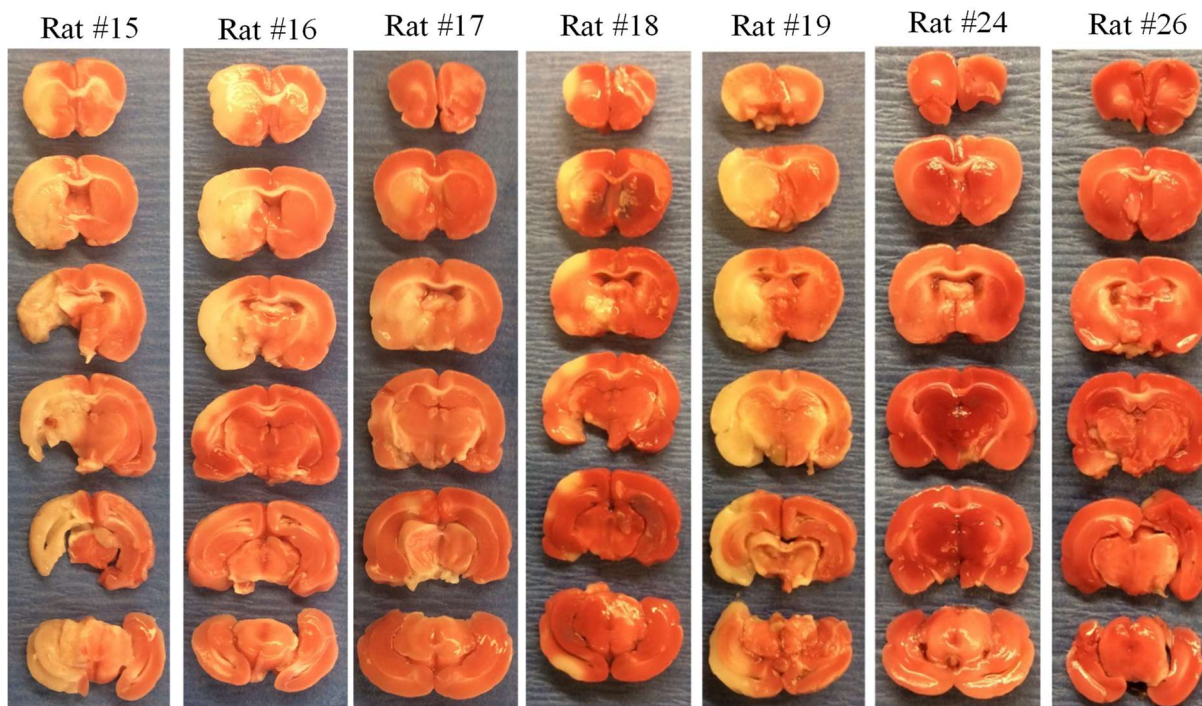


Figure 6-7: TTC staining of brains sections from all rats included in Group D (Sonothrombolysis) of the ischemic stroke study

Regions of infarct may be detected as white or light shades of pink whereas non-infarcted tissue stains pink. Eight rats were performed in this group, but one rat was found dead 24 hours after surgery and its brain could not be excised for TTC staining. Rat #38 was dead at 24 hours after surgery. The Rat number associated with each brain corresponds to the Rat number in Table 6-4.

Figures 6-4, 6-5, 6-6, and 6-7, and a summary of information about each rat is given in Table 6-4.

Quantified infarct volumes for all groups are shown as box plots in Figure 6-8. Infarct volumes measured for each group were (mean \pm std. dev.): control – 60.6 ± 19.7 %, low dose rtPA (0.09 mg/kg) – $63.6 \pm 22.0\%$, high dose rtPA (0.9 mg/kg) – $23.3 \pm 15.9\%$, and sonothrombolysis plus low dose rtPA (0.09 mg/kg) – 32.3 ± 20.1 %. Note that Rat #38 in Group C (high dose rtPA) was excluded from analysis because it was a significant outlier on account of its death at 24 hours (the statistical basis for outlier detection was evaluation of Pierce’s criterion for outliers).²⁴³ Similarly, Rat #25 in Group D had died by the 24 hour time point and its brain could not be extracted for TTC staining.

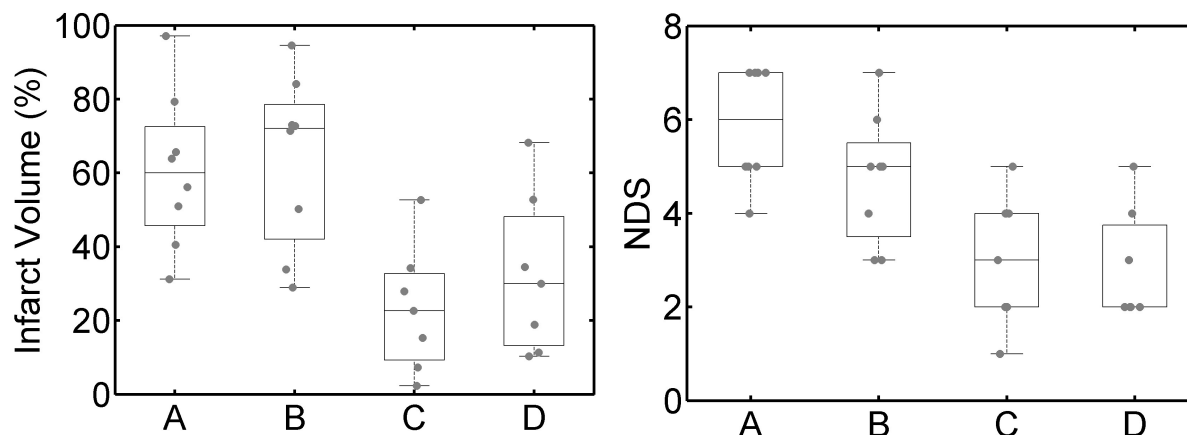


Figure 6-8: Boxplots of infarct volumes and NDS observed for each experimental group in the rat ischemic stroke study

(Left) Boxplot of infarct volumes and (Right) boxplot of NDS for each rat in the stroke study. The central line in each box is the median, while the bottom and top edges of the box are the first and third quartile, respectively. The bottom and top of each whisker is the minimum and maximum observed value in each group. Gray dots overlapping each box plot are individual measurements from single rats. Statistical significance for each group is given in Table 6 – 2 and Table 6 – 3.

Statistical significance among groups was determined using a 1-way ANOVA and Tukey-Kramer multiple comparisons test with $\alpha = 0.05$. Results of the 1-way ANOVA and p -values for each individual comparison among groups are given in Table 6-2. The infarct volume results for the control and low-dose rtPA groups were not significantly different ($p > 0.05$). The measured infarct volumes for the high dose rtPA group was significantly different from the control and low-dose rtPA groups ($p < 0.05$), but not the sonothrombolysis group ($p = 0.805$). The measured infarct volumes for the sonothrombolysis group was significantly different only from the low-dose rtPA group ($p = 0.0476$), but not from the control group ($p = 0.0887$) or high-dose rtPA group ($p = 0.805$).

The average neurological deficit scores measured at 24 hr post-intervention for Groups A, B, C, and D are given in Table 6 – 3. Also given in Table 6 – 3 is a 1-way ANOVA analysis and p -values for statistical comparison amongst the groups. The NDS results for the control and low-dose rtPA groups were not significantly different ($p > 0.05$). The NDS for the high dose rtPA group was significantly different from the control group, but not the low-dose rtPA ($p = 0.073$) or the

Table 6-2: Results of 1-way ANOVA and *p*-values for infarct volumes of rats in the ischemic stroke study

	Group A	Group B	Group C	Group D
Infarct volume (%)	60.6 ± 19.7	63.6 ± 22.0	23.3 ± 15.9	32.3 ± 20.1

1- way ANOVA						
<i>Source of Variation</i>	<i>SS</i>	<i>df</i>	<i>MS</i>	<i>F</i>	<i>P-value</i>	<i>F crit</i>
Between Groups	0.898253	3	0.299418	6.473186	0.002028	2.975154
Within Groups	1.202632	26	0.046255			
Total	2.100886	29				

Tukey-Kramer Multiple Comparison Test (<i>p</i> values)				
Group	A	B	C	D
A	–	0.392	<i>0.0121</i>	0.0887
B	–	–	<i>0.00629</i>	<i>0.0476</i>
C	–	–	–	0.805
D	–	–	–	–

Significant differences, $p < 0.05$, are italicized.

sonothrombolysis group ($p = 0.899$). The NDS for the sonothrombolysis group was significantly different from both the control and low-dose rtPA groups ($p < 0.05$), but not from the high-dose rtPA group ($p = 0.805$).

The experiment was designed to permit the calculation of a rtPA dose response, using the low-dose rtPA and high-dose rtPA groups to establish the effect of increasing rtPA dose. The measured infarct volume was assumed to scale linearly with increasing rtPA dose, such that the infarct volume decreased from $63.6 \pm 22.0\%$ at 0.09 mg/kg to $23.3 \pm 15.9\%$ at 0.9 mg/kg, or approximately a reduction of $4.9 \pm 0.9\%$ per each additional 0.1 mg/kg injected dose. The sonothrombolysis group exhibited an infarct volume of $32.3 \pm 20.1\%$, representing a decrease of $31.3 \pm 29.8\%$ relative to the low dose rtPA group. Based on the linear relationship between rtPA dose and infarct volume, the introduction of sonothrombolysis was equivalent to the effect of an additional rtPA dose of 0.63 ± 0.18 mg/kg. This equates to a potential rtPA dose reduction of 3.3 – fold (95% C.I.: 1.8 – 4.8) required to reach the performance of 0.9 mg/kg rtPA. Put another way,

Table 6-3: Results of 1-way ANOVA and *p*-values for neurological deficit scores of rats in the ischemic stroke study

	Group A	Group B	Group C	Group D
NDS	5.875 ± 1.25	4.75 ± 1.39	3.00 ± 1.41	2.86 ± 1.22

1- way ANOVA						
<i>Source of Variation</i>	<i>SS</i>	<i>df</i>	<i>MS</i>	<i>F</i>	<i>P-value</i>	<i>F crit</i>
Between Groups	47.57	3	15.85	9.11	0.0003	2.975154
Within Groups	45.23	26	1.74			
Total	92.80	29				

Tukey-Kramer Multiple Comparison Test (<i>p</i> values)				
Group	A	B	C	D
A	–	0.341	<i>0.00144</i>	<i>0.001</i>
B	–	–	0.0733	<i>0.0469</i>
C	–	–	–	0.899
D	–	–	–	–

Significant differences, $p < 0.05$, are italicized.

sonothrombolysis plus approximately 0.27 ± 0.18 mg/kg rtPA would be expected to match the performance of 0.9 mg/kg rtPA alone in this experimental model. Please reference the appendix to Chapter 6 for a thorough explanation of the statistical analysis.

6.5 Discussion

This was the first study designed to evaluate the *in vivo* safety and efficacy of large-diameter microbubbles produced in real-time by a flow-focusing microfluidic device for a therapeutic application. Microbubbles of similar composition and origin have previously been evaluated for sonoporation-mediated *in vitro* drug delivery^{58,59} and *in vivo* contrast enhancement in a murine model.¹⁹³ In prior sonoporation studies, microfluidically-produced microbubbles with N₂ gas cores, weak-stabilizing shells, and diameters greater than 10 μm were observed to induce sonoporation-mediated drug delivery at peak negative pressures that were significantly lower than pressures that are widely reported to induce sonoporation with smaller, lipid shelled microbubbles of 1 – 4 μm diameter.^{23,59,107,244} These observations were corroborated by other findings that

suggested larger microbubbles elicited stronger bioeffects than smaller microbubbles in the context of multiple therapeutic applications, including sonoporation,¹⁰⁷ blood brain barrier disruption,¹⁹² and sonothrombolysis studies.¹⁹⁰ Notably, these other studies compared microbubbles of 1 – 2 μm diameter to microbubbles of 2 – 4 μm diameter and could not evaluate large microbubbles due to embolic risk associated with larger diameter, long-circulating microbubbles. Despite this limitation, however, significantly stronger bioeffects were observed between the two differently sized microbubble populations.

The motivation to evaluate even larger microbubbles for therapeutic applications stems from the observations stated above and the understanding that larger microbubbles produce enhanced bioeffects due to increased microstreaming,²³³⁻²³⁶ increased momentum transfer via acoustic radiation force,^{39,237,238} and higher-energy cavitation events.^{206,207,239} Sonothrombolysis is a natural application for enhanced therapeutic efficacy derived from large diameter microbubbles because thrombolytic therapy must be administered quickly and, if possible, with as little thrombolytic agent as is necessary to reduce the risk of severe off-target bleeding. Until now, the primary limitation for the use of large microbubbles for therapeutic applications has been the risk of gas embolism associated with microbubbles of diameters larger than the smallest lung capillaries. The innovation in this work is the use of microbubbles with short circulation half-lives derived from their composition of high solubility gases and a weak surfactant shell. In a previous study, these microbubbles were observed to exhibit circulation half-lives of approximately 21 s when administered intravenously in a murine model, with almost all microbubbles observed to be cleared by the lungs with no respiratory or cardiac distress.¹⁹³

6.5.1 Safety of intra-arterial microbubble administration

In this work, the safety of intra-arterial administration of large diameter, microfluidically produced microbubbles was evaluated to determine a safe dosing limit in the rat model. Microbubbles were administered continuously for 15 min, with total injected N₂ gas volumes of approximately 240 µl, 800 µl, or 1910 µl. Small, localized infarct zones were observed to result from gas emboli in rats receiving 800 and 1910 µl N₂ doses, while no gross infarct or neurological deficit was observed at the lowest dose. These results are broadly in line with those of Helps *et al*, who observed that rapid injection of 400 µl air into the rabbit cerebral vasculature resulted in disrupted cerebral blood flow for approximately 180 min, but caused no lasting neurological effect.^{203,245} Their dose corresponded to roughly 180 µl air/kg, which is less than the safe dose observed in this rat study – 600 µl/kg. Although, the discrepancies between injection duration (immediate versus 15 min) and animal models (rabbit versus rat) make direct comparisons difficult, there is precedent for safe intra-arterial injection of gas volumes on this order of magnitude.

In the stroke model, microbubbles were administered directly to the occluded blood vessel via a catheter placed at the junction of the ICA/ECA. It was our intent to simulate the targeted clinical condition in which a catheter would be placed directly in the occluded vessel of a stroke patient. A limitation of using the rat model was that microbubbles could not be administered continuously, as the catheter occluded blood flow towards the brain and prevented microbubbles from reaching the clot while the catheter was in place. Further, microbubbles were administered directly into a vessel with occluded flow, so it took longer for the microbubbles to flow out of the ICA and into the brain than in the rats without an occlusive thrombus that were evaluated in the microbubble safety study. So, microbubbles were administered for 30 s every 4.5 min over the course of the 30

min procedure. The selection of this dosing pattern was based on the time required for the ICA to completely clear of microbubbles, which indicated that the microbubbles had either dissolved or migrated towards the clot and out of view of the surgical microscope. In total, approximately 80 μ l of gas was administered in the stroke animals, which was less than the safe dose established in the safety study. However, injection directly into an occluded vessel limited the total number of microbubbles that could be effectively administered in this model.

6.5.2 rtPA dose reduction

The infarct volume results of the stroke study indicated that the sonothrombolysis treatment with 0.09 mg/kg rtPA (approximately 1/10th clinical dose) was more effective than 0.09 mg/kg rtPA alone, but was not as effective as 0.9 mg/kg rtPA. This was the expected result of this study's design and permitted the calculation of the effective rtPA dose-reduction enabled by sonothrombolysis treatment method. As stated in the results, sonothrombolysis using the large diameter, transiently stable microbubbles permitted a dose reduction of approximately 0.63 ± 0.18 mg/kg, corresponding to a 3.3 – fold (95% C.I.: 1.8 – 4.8) dose reduction. This degree of rtPA dose reduction is significant because many stroke patients are contraindicated for rtPA due to bleeding risks and are therefore left with limited treatment options (fewer than 5% of ischemic stroke patients receive rtPA).¹⁵¹ Therefore, it is the goal of many interventions to either eliminate or greatly reduce the required rtPA dose.

In addition to the limitations already stated, this study only considered thrombolysis of clots formed from whole blood, which are considered to be erythrocyte-rich and comparatively easy to lyse.¹⁹⁷ While the clots were allowed to harden and retract over 48 hrs, their composition was not reflective of many platelet-rich clots that are often recovered from ischemic stroke patients.^{196,246} In addition, as this was a pilot study intended to evaluate the baseline efficacy of this new approach,

a comparison of the large, transiently stable microbubbles to conventionally sized microbubbles was not made. However, several other investigators have established the performance of sonothrombolysis with conventionally sized microbubbles in human studies and rabbit and rat models that the results of this study can be compared to.^{38,181,183,188,229,242,247} Finally, although no large-scale intracerebral hemorrhage was observed in the rat brain sections, future studies must be specifically designed to evaluate hemorrhagic risk and effects that these large microbubbles may cause to the microvasculature.

6.6 Conclusions

This study was the first to evaluate an *in vivo* therapeutic application of microfluidically-produced microbubbles that dissolve quickly due to their transient stability. It was demonstrated that microbubbles with diameters between 10 – 20 μm comprised of N_2 gas with a non-crosslinked albumin shell could be administered safely intra-arterially up to a dose of 240 μl gas over a 15 minute period. The results of the ischemic stroke study indicated that sonothrombolysis using these large, transiently stable microbubbles permitted a 3.3 – fold (95% C.I. 1.8 – 4.8) rtPA dose reduction relative to intravenous rtPA therapy alone.

6.7 Appendix

6.7.1 Statistical determination of dose reduction

The relationship between rtPA dose and infarct volume was determined via the following calculations. Care must be taken when applying arithmetic operations to distributions of data to correctly calculate the variance of the resulting distributions. All percentages are converted to fractions between 0 and 1 for the calculations in this section. The subscripts, *B*, *C*, and *D* denote

which experimental group the data came from. Variables derived from the source data are represented by Greek characters.

Step 1: Determine linear relationship between rtPA dose and infarct volume

<u>rtPA Dose</u>	<u>Infarct Volume</u>
0.09 mg/kg	$\mu_B = 0.636, Var(B) = 0.0484$
0.9 mg/kg	$\mu_C = 0.233, Var(C) = 0.0252$

The first step is to determine the difference between the two distributions via subtraction and then divide the resulting distribution by the difference in rtPA dose. In this way, an ‘infarct volume per rtPA dose’ metric is computed. When subtracting two distributions to yield a new distribution, α , the mean and variance must be handled in the following way:

$$E[\alpha] = E[B] - E[C] \quad \text{Equation 6-1}$$

$$Var[\alpha] = Var[B] + Var[C] \quad \text{Equation 6-2}$$

When applied to the data above, $E[\alpha] = 0.403$ and $Var[\alpha] = 0.073$. Next, the α distribution must be divided by the difference in rtPA doses (0.81 mg/kg) to establish the linear relationship. When dividing a distribution by a constant, K , the mean and variance must be handled in the following way:

$$E[\beta] = \frac{\mu_\alpha}{K}, Var[\beta] = \frac{\sigma_\alpha^2}{K^2} \quad \text{Equation 6-3}$$

When applied to the α distribution to yield the β distribution, $E[\beta] = 0.0498$, $Var[\beta] = 0.000081$. Note that the divisor, K , used above was not 0.81 mg/kg, but rather 8.1 ‘100 μ g/kg’ so that the slope of the regression line is: 4.98 ± 0.9 % infarct volume per 100 μ g/kg rtPA.

Step 2: Determine equivalent rtPA dose of sonothrombolysis treatment

Step 1 derived a linear relationship between infarct volume and rtPA dose. Step 2 will use this relation to determine the effect of sonothrombolysis treatment in terms of an equivalent rtPA dose.

To do this, use the following data:

<u>rtPA Dose</u>	<u>Sonothrombolysis?</u>	<u>Infarct Volume</u>
0.09 mg/kg	No	$\mu_B = 0.636, Var(B) = 0.0484$
0.09 mg/kg	Yes	$\mu_C = 0.323, Var(C) = 0.0403$

As above, subtract the two distributions using the rules given in Equations 6-1 and 6-2 to yield a new distribution that reflects the difference in the distributions, γ : $E[\gamma] = 0.313$, $Var[\gamma] = 0.0887$.

Now, take a ratio between the γ and β distributions to determine the equivalent rtPA dose of sonothrombolysis. To do this, the mean and variance must be handled using the following equations:

$$E[\delta] = \frac{\mu_\gamma}{\mu_\beta} \quad \text{Equation 6-4}$$

$$Var[\delta] = Var\left[\frac{\gamma}{\beta}\right] = \frac{1}{\mu_\beta^2} Var[\gamma] + \frac{\mu_\gamma^2}{\mu_\beta^4} Var[\beta] - 2 \frac{\mu_\gamma}{\mu_\beta^3} Cov[\gamma, \beta] \quad \text{Equation 6-5}$$

When these equations are applied, assuming independence (i.e. $Cov[\gamma, \beta] = 0$), then the following is computed for δ : $E[\delta] = 6.291$, $Var[\delta] = 3.081$. The interpretation is that sonothrombolysis accounted for a reduction in infarct volumes equivalent to 6.291 ± 1.756 '100 $\mu\text{g/kg}$ ', or stated in mg/kg as $0.6291 \pm 0.1756 \text{ mg/kg}$.

Step 3: Calculate fold dose reduction

Using the statistical tools described above, the fold dose reduction is computed by dividing the maximum dose, 0.9 mg/kg , by the effective dose required to match its level of performance when used with sonothrombolysis (i.e. $0.9 \text{ mg/kg} - 0.6291 \pm 0.1756 \text{ mg/kg} = 0.27 \pm 0.1756 \text{ mg/kg}$). Propagating the variance as described above for a division of a distribution, this yields a new distribution, ϵ , with the following statistics: $E[\epsilon] = 3.33$, $Var[\epsilon] = 4.66$.

6.7.2 Summary of Results of Rat Ischemic Stroke Model

Table 6-4: Information on rats included in the rat ischemic stroke study

Rat Number	Weight (g)	MB Gas Volume (µl)	rtPA Dose (mg/kg)	Neurological Score @ 24 hr	Percent Infarct Volume
Group A - Control					
1	410	–	0	7	65.7
3	462	–	0	7	56.1
20	409	–	0	7	63.9
23	479	–	0	5	31.2
27	500	–	0	5	97.1
30	508	–	0	4	51.0
33	554	–	0	5	40.5
36	655	–	0	7	79.3
Group B – Low Dose rtPA (0.09 mg/kg)					
6	542	–	0.09	5	50.3
7	528	–	0.09	4	84.1
10	535	–	0.09	6	71.3
21	452	–	0.09	3	28.9
28	500	–	0.09	5	72.9
31	453	–	0.09	3	33.9
35	620	–	0.09	5	72.7
37	560	–	0.09	7	94.5
Group C – High Dose rtPA (0.9 mg/kg)					
2	502	–	0.9	1	2.3
4	445	–	0.9	5	52.7
8	458	–	0.9	4	15.3
9	495	–	0.9	2	7.2
29	510	–	0.9	2	22.6
32	523	–	0.9	4	34.2
34	651	–	0.9	3	28.0
38	582	–	0.9	7*	78.8*
Group D – Low Dose rtPA (0.09 mg/kg) plus Sonothrombolysis					
15	505	80	0.09	5	68.2
16	493	80	0.09	2	34.4
17	503	80	0.09	2	18.8
18	433	80	0.09	3	30.0
19	480	80	0.09	4	52.8
24	457	80	0.09	2	10.3
25	486	80	0.09	7*	–*
26	435	80	0.09	2	11.3

* Denotes outliers as detected by Pierce's criterion

Chapter 7. Conclusions and Future Directions

7.1 Conclusions

This thesis presented two microbubble formulations customized for separate photoacoustic imaging and sonothrombolysis therapeutic applications. Together, both parts of this thesis demonstrate the versatility of microbubble contrast agents for imaging and therapeutic applications. In Part I, the design, synthesis, and imaging performance of light-absorbing microbubbles was evaluated *in vitro*, *in silico*, and *in vivo*, as summarized in Figure 7 – 1. Two

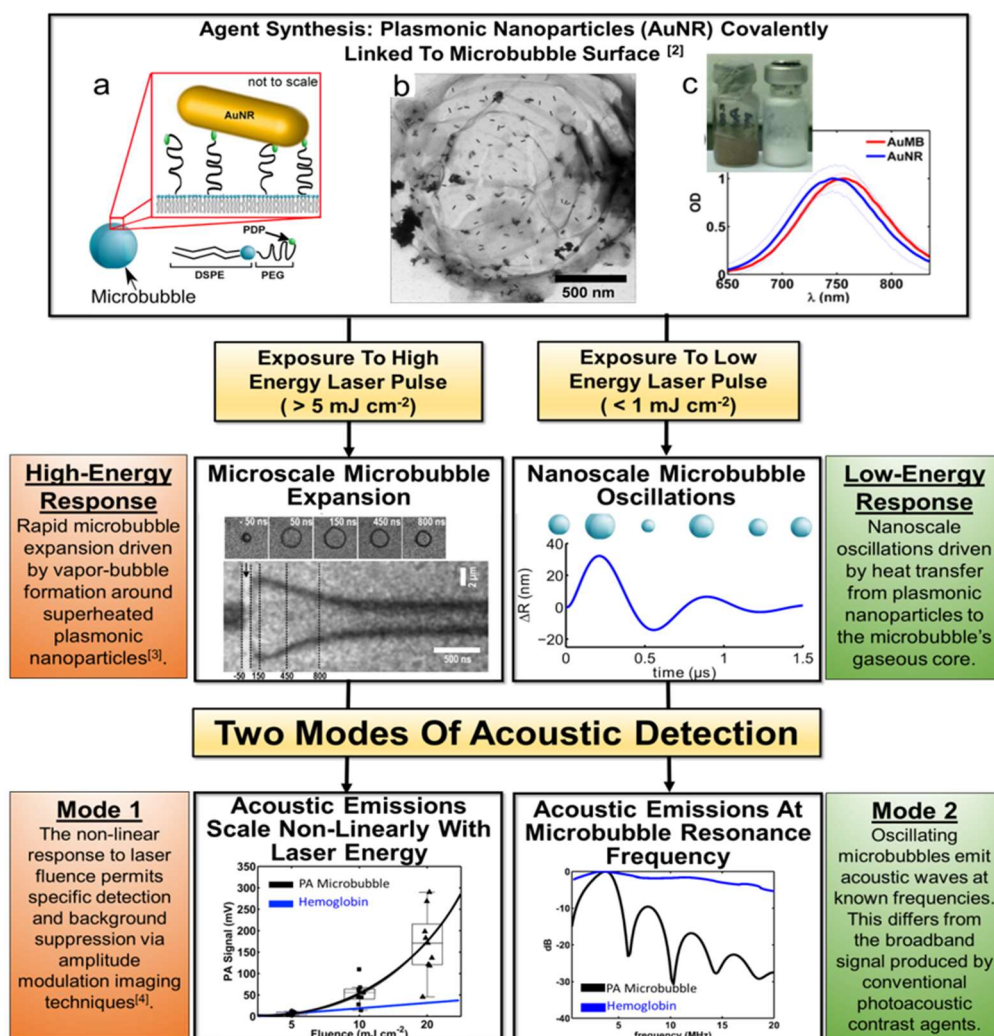
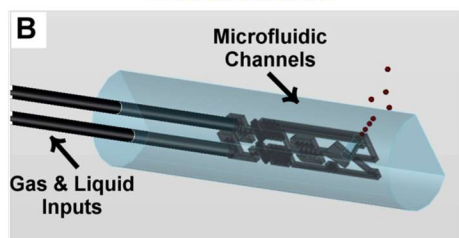


Figure 7-1: Summary schematic of findings from Part I of this dissertation

responses to pulsed laser excitation were identified – in response to high energy, explosive boiling at the nanoparticle surface resulted in rapid microbubble expansion and high amplitude, non-linear photoacoustic emissions; in response to lower laser energies, photoacoustic emissions scaled linearly with increasing laser fluence, and finite element modeling predicted nanoscale microbubble radius oscillations at the microbubble resonance frequency. Notably, these simulations results have been supported by recent empirical results of similar light-absorbing microbubbles,⁷⁹ adding independent validation to the modelling work presented in Chapter 3.

In Part II, a catheter-dimensioned flow-focusing microfluidic device was designed, fabricated, and tested *in vitro* to establish feasibility of *in situ* microbubble production within the vasculature. The catheter-dimensioned device produced microbubbles at production rates and diameters that

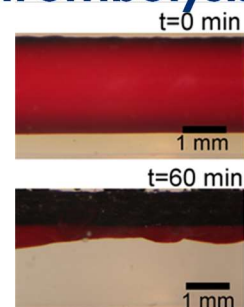
Human-Dimensioned Catheter



MBs safely administered



~ 8X Enhanced *In Vitro* Sonothrombolysis Rate



3.3 fold rtPA dose reduction

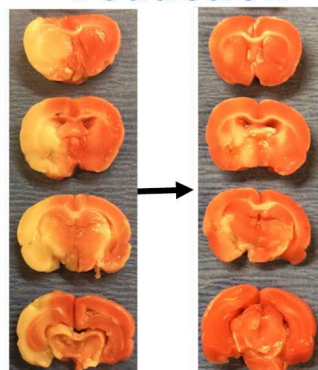


Figure 7-2: Summary schematic of findings from Part II of this dissertation

are expected to be suitable for eventual *in vivo* application. The sonothrombolysis performance of the microfluidically-produced microbubbles was evaluated in both *in vitro* and *in vivo* models, with both establishing significantly improved sonothrombolysis rates compared to representative controls. In particular, the potential for a 3.33 ± 2.16 fold rtPA dose reduction was demonstrated in the rat model of ischemic stroke, and neurological deficit scores were also significantly improved following sonothrombolysis treatment. A graphical summary of key findings from Part II of this thesis is shown in Figure 7-2.

7.2 Future Directions

There are several future directions that may be pursued based on the results of this dissertation:

- 1) *In vivo* imaging of high- and low-fluence AuMB photoacoustic responses: this dissertation established that AuMBs exhibit two responses following laser excitation, but did not demonstrate improved sensitivity or specificity of AuMB detection based on these modes *in vivo*. Targeted molecular imaging is a natural extension of the work presented in this dissertation, either in a linear array photoacoustic setting or optical-resolution photoacoustic microscopy.
- 2) Finite element modeling of light-absorbing microbubbles of differing compositions: the finite element model presented in Chapter 3 of this dissertation studied only the response of gold nanorods attached to the microbubble shell, but other optically absorbing particles and molecules may be able to confer similar properties to the microbubble. In particular, simulating microbubble oscillations resulting from laser-heated gold nanospheres or dye-loaded liposomes is a possible future direction.

- 3) Evaluation of sonothrombolysis in other models: the sonothrombolysis studies presented in Part II of this dissertation evaluated the thrombolysis of soft, RBC-rich blood clots in either *in vitro* or *in vivo* settings. These were appropriate models for feasibility and proof-of-concept studies using microfluidically-produced microbubbles for sonothrombolysis, but RBC-rich blood clots are not representative of all clinical thrombi. While most thrombi responsible for DVT may be classified as RBC-rich, only approximately 30 % of thrombi that cause ischemic stroke are RBC-rich. Future work must evaluate the thrombolysis of platelet-rich blood clots, both *in vitro* and *in vivo*, to establish the limits of the techniques efficacy.
- 4) Robust fabrication of catheter-based FFMDs: the catheter-dimensioned FFMD presented in Chapter 4 was fabricated from PDMS, in part due to ease and low cost of fabrication during the prototyping phase. Yet, PDMS does not offer a significant safety margin, as the devices may catastrophically fail if exposed to high gas or liquid pressures. Fabrication of the catheter-based device out of glass or quartz would result in a far more robust catheter, but at added fabrication cost and time. However, any future translational application, or even validation in larger animal models, must consider the material properties of the microfluidic substrate and select an appropriate material.

Peer-Reviewed Journal Publications

- [1] AA Bogdanov, Jr, AJ Dixon, S Gupta, L Zhang, S Zheng, MS Shazeeb, S Shang, AL Klibanov, “Synthesis and testing of multiplexed dual-modality magnetic resonance and photoacoustic imaging nanoparticles,” *Bioconjugate Chemistry*, 27(2), 383-90, 2016.
- [2] T Wang, R Cao, B Ning, AJ Dixon, JA Hossack, AL Klibanov, Q Zhou, A Wang, S Hu, “All-optical photoacoustic microscopy based on plasmonic detection of broadband ultrasound.” *Applied Physics Letters*, 107(15), 153702, 2015.
- [3] AJ Dixon, S Hu, AL Klibanov, JA Hossack, “Oscillatory dynamics and in vivo photoacoustic imaging performance of plasmonic nanoparticle-coated microbubbles.” *Small*, 11(25), 3066-3077, 2015.
- [4] AJ Dixon, AH Dhanaliwala, JP Kilroy, JL Chen, M Ragosta, L Phillips, AL Klibanov, BR Wamhoff, JA Hossack, “Microbubble-mediated intravascular ultrasound imaging and drug delivery.” *IEEE Transactions on Ultrasonics, Ferroelectrics, and Frequency Control*, 62(9), 1674-1685, 2015.
- [5] AH Dhanaliwala, AJ Dixon, D Lin, JL Chen, AL Klibanov, JA Hossack, “In vivo imaging of microfluidic-produced microbubbles.” *Biomedical Microdevices*, 17(1):9914, 2015.
- [6] B Ning, MJ Kennedy, AJ Dixon, N Sun, R Cao, BT Soetikno, R Chen, Q Zhou, KK Shung, JA Hossack, S Hu. “Simultaneous photoacoustic microscopy of microvascular anatomy, oxygen saturation, and blood flow,” *Optics Letters*, 40(6), 910-913, 2015.
- [7] JL Chen, AH Dhanaliwala, AJ Dixon, AL Klibanov, JA Hossack, “Synthesis and characterization of transiently stable albumin-coated microbubbles via a flow-focusing microfluidic device for intravascular applications.” *Ultrasound in Medicine and Biology*, 40(2), 400-9, 2014.

- [8] AJ Dixon and JA Hossack, “Intravascular near-infrared fluorescence catheter with ultrasound guidance and blood attenuation correction.” *Journal of Biomedical Optics*, 18(5), 056990, 2013.
- [9] AJ Dixon, AH Dhanaliwala, JL Chen, JA Hossack, “Enhanced intracellular delivery of a model drug using microbubbles produced by a microfluidic device.” *Ultrasound in Medicine and Biology*, 39(7), 1267-76, 2013.
- [10] AJ Dixon, J Li, JMR Rickel, B Shin, Z Zuo, JA Hossack, “Sonothrombolysis efficacy of microbubbles produced by a microfluidic device in a rat ischemic stroke model.” in preparation.
- [11] AJ Dixon, B Shin, JMR Rickel, AL Klibanov, JA Hossack, “Accelerated in vitro sonothrombolysis facilitated by large-diameter microbubbles produced by a flow-focusing microfluidic device.” in preparation.
- [12] AJ Dixon, B Shin, JMR Rickel, AL Klibanov, JA Hossack, “Development of a catheter-dimensioned microfluidic device for intravascular production of microbubbles” in preparation.

Conference Abstracts and Presentations

- [1] AJ Dixon, S Hu, AL Klibanov, JA Hossack, “Empirical and theoretical study of the interaction between plasmonic-nanoparticle coated microbubbles and nanosecond pulsed laser excitation.” 21st European Symposium on Ultrasound Contrast Agents (2016), Rotterdam, The Netherlands.
- [2] AJ Dixon, J Farry, JL Chen, JA Hossack, AL Klibanov, “Photoacoustic imaging of stimuli-responsive red blood cell drug delivery agents,” IEEE International Ultrasonics Symposium (2016), Tours, France.
- [3] AJ Dixon, JR Rickel, BD Shin, JA Hossack, “Sonothrombolysis efficacy of microbubbles produced by a microfluidic device in a rat ischemic stroke model.” IEEE International Ultrasonics Symposium (2016), Tours, France.
- [4] AJ Dixon, E Lu, V Chang, JA Hossack, “Synthesis and acoustic conversion of perfluorocarbon nanodroplets containing solid nanoparticles within their liquid cores.” International Ultrasonics Symposium (2016), Tours, France.
- [5] AJ Dixon, S Hu, AL Klibanov, JA Hossack, “Photoacoustic properties of plasmonic nanoparticle coated microbubbles.” IEEE International Ultrasonics Symposium (2015), Taipei, Taiwan. ***Student Paper Competition Winner***
- [6] AJ Dixon, B Shin, V Meka, JP Kilroy, AL Klibanov, JA Hossack, “Large diameter microbubbles produced by a catheter-based microfluidic device for sonothrombolysis applications.” IEEE International Ultrasonics Symposium (2015), Taipei, Taiwan.
- [7] AJ Dixon, JP Kilroy, AL Klibanov, JA Hossack, “Microbubbles produced by a catheter-based microfluidic device for sonothrombolysis applications.” 20th European Symposium

on Ultrasound Contrast Imaging (2015), Rotterdam, The Netherlands. ***Oral Competition Finalist***

- [8] AA Bogdanov, Jr, AJ Dixon, S Zheng, AL Klibanov, S Gupta, MS Shazeeb, L Zhang, S Zhang, “Hybrid metal nanoparticles for photoacoustic multiplexing and magnetic resonance imaging.” World Molecular Imaging Congress (2014), Seoul, South Korea.
- [9] AJ Dixon, AH Dhanaliwala, D Lin, AL Klibanov, JA Hossack, “Ultrasound imaging of microfluidic-produced microbubbles directly injected into a mouse via a tail vein catheter.” Ultrasound Session, Biomedical Engineering Society (2014), San Antonio, TX, USA.
- [10] S Wang, C Wang, AJ Dixon, FW Mauldin, JA Hossack, “Relationship between Secondary Radiation Force, Targeted Adhesion, and Microbubbles Acoustic Response in Large Blood Vessels.” Ultrasound Session, Biomedical Engineering Society (2014), San Antonio, TX, USA. ***Reviewer Choice Award***
- [11] AJ Dixon, AH Dhanaliwala, D Lin, AL Klibanov, JA Hossack, “In vivo acoustic contrast enhancement via simultaneous production and injection of microfluidic-produced microbubbles.” IEEE International Ultrasonics Symposium (2014), Chicago, IL, USA.
- [12] JL Chen, AJ Dixon, AH Dhanaliwala, JA Hossack, “Quantification of ultrasound-mediated drug delivery using an in vitro flow chamber.” Society for Biomaterials Annual Conference (2013), Boston, MA, USA.
- [13] AJ Dixon, WH Guilford, JA Hossack, “Intravascular near-infrared fluorescence imaging with intravascular ultrasound guidance.” Diagnostic and Therapeutic Applications of Light in Cardiology, SPIE Photonics West (2013), San Francisco, CA, USA.

- [14] AH Dhanaliwala, JL Chen, AJ Dixon, AL Klibanov, JA Hossack, “Production of albumin-stabilized microbubbles for ultrasound imaging and therapy via a microfluidic device. World Molecular Imaging Congress, (2013), Savannah, GA, USA.
- [15] AJ Dixon, AH Dhanaliwala, JL Chen, AL Klibanov, JA Hossack, “Transiently stable microbubbles produced by a microfluidic device for therapeutic applications.” 18th European Symposium on Ultrasound Contrast Imaging (2013), Rotterdam, The Netherlands. *Best Poster Award*
- [16] AJ Dixon, AH Dhanaliwala, JL Chen, AL Klibanov, BR Wamhoff, JA Hossack, “In Situ Produced Microbubbles via a Microfluidic Device for Enhanced Drug Delivery,” 3rd International Symposium on Current and Future Applications of Focused Ultrasound (2012), Washington DC, USA.
- [17] AJ Dixon, AH Dhanaliwala, JL Chen, AL Klibanov, JA Hossack, “Model Drug Delivery via In Situ Production of Microbubbles by a Microfluidic Device.” Drug-Delivery Technologies, Biomedical Engineering Society (2012), Atlanta, GA, USA.
- [18] AJ Dixon, WH Guilford, AL Klibanov, JA Hossack, “Monitoring of Ultrasound Mediated Drug Delivery with a Fluorescence Detection Catheter.” Image-Guided Therapy, Biomedical Engineering Society (2012), Atlanta, GA, USA.

Patent Applications

- [1] AJ Dixon, AL Klibanov, M Wintermark, JA Hossack, “Method and Apparatus for Accelerated Disintegration of Blood Clot.” US Patent Application No. 62/049,338, Filed 11 September 2014.

Part III: Appendix

Chapter A1. Development of an intravascular near-infrared fluorescence catheter with ultrasound guidance and blood attenuation correction⁶

A1.1 Abstract

Intravascular near-infrared fluorescence (NIRF) imaging offers a new approach for characterizing atherosclerotic plaque, but random catheter positioning within the vessel lumen results in variable light attenuation and can yield inaccurate measurements. We hypothesized that NIRF measurements could be corrected for variable light attenuation through blood by tracking the location of the NIRF catheter with intravascular ultrasound (IVUS). In this study, a combined NIRF-IVUS catheter was designed to acquire co-registered NIRF and IVUS data, an automated image processing algorithm was developed to measure catheter-to-vessel wall distances, and depth-dependent attenuation of the fluorescent signal was corrected by an analytical light propagation model. Performance of the catheter sensing distance correction method was evaluated in coronary artery phantoms and *ex vivo* arteries. The correction method produced NIRF estimates of fluorophore concentrations in coronary artery phantoms with an average RMSE of 17.5%. In addition, the correction method resulted in a statistically significant improvement in correlation

⁶ This chapter contains content drawn from the following peer-reviewed conference and journal publications:
 AJ Dixon and JA Hossack, "Intravascular near-infrared fluorescence catheter with ultrasound guidance and blood attenuation correction." *Journal of Biomedical Optics*, 18(5), 056990, 2013.
 AJ Dixon, WH Guilford, JA Hossack, "Intravascular near-infrared fluorescence imaging with intravascular ultrasound guidance." *Diagnostic and Therapeutic Applications of Light in Cardiology*, SPIE Photonics West (2013), San Francisco, CA, USA.
 AJ Dixon, WH Guilford, AL Klibanov, JA Hossack, "Monitoring of Ultrasound Mediated Drug Delivery with a Fluorescence Detection Catheter." *Image-Guided Therapy*, Biomedical Engineering Society (2012), Atlanta, GA.

between spatially resolved NIRF measurements and known fluorophore spatial distributions in *ex vivo* arteries (from $r = 0.24$ to $r = 0.69$, $p < 0.01$, $n = 6$). This work demonstrates that catheter-to-vessel wall distances measured from IVUS images can be employed to compensate for inaccuracies caused by variable intravascular NIRF sensing distances.

A1.2 Introduction

Acute coronary events are primarily caused by thrombogenesis following vulnerable atherosclerotic plaque rupture and are the leading cause of sudden cardiac death in the United States.²⁴⁸ Recent advances in intravascular imaging techniques have provided new insights into the mechanisms underlying the development of unstable atherosclerotic lesions, however, these studies have not produced systematic approaches capable of identifying high-risk plaques prior to rupture.²⁴⁹ It is increasingly probable that combined information on anatomical and physiological parameters is required to determine whether a specific lesion is susceptible to rupture, and several of these parameters may be evaluated through catheter-based intravascular imaging approaches.²⁵⁰⁻²⁵⁵

Intravascular ultrasound (IVUS) has been widely adopted by the clinical community and is capable of assessing tissue properties within the vessel wall through IVUS elastography^{251,252,256} and virtual histology techniques.²⁵⁷ Optical coherence tomography (OCT) provides a resolution of 10-15 μm , approximately five times better than 40 MHz IVUS, and can evaluate clinically important plaque structural features such as the thickness of fibrous caps and the presence of a necrotic core or lipid deposits.²⁵⁸ While these approaches have demonstrated potential for systematically characterizing the structural components of atherosclerotic plaque,²⁵⁹⁻²⁶¹ they often fail to provide insight into physiological and biochemical processes that may be precursors to plaque rupture.^{262,263} To address this deficiency, fluorescence, photoacoustic, and spectroscopic

catheters have been developed to optically detect the molecular signatures of vulnerable plaque.^{34,264-269} Plaque characterization via these optical techniques relies on the detection of endogenous molecules within the plaque or exogenous probes that are either targeted to extracellular ligands or are activated by physiological processes within the vessel wall.^{31,34,270,271} Both approaches enable direct monitoring of physiological function rather than anatomical structure, which is hypothesized to further improve the detection and specialized treatment of vulnerable atherosclerotic plaque.²⁷²

Intravascular near-infrared fluorescence (NIRF) imaging has emerged as a robust approach for molecular imaging of atherosclerosis due to continued development of targeted imaging agents, high inherent detection sensitivities (nM), relatively low light attenuation through blood, and low background fluorescence from endogenous molecules in the vessel wall.^{34,266-268,273} NIRF catheters have been employed to study atherosclerosis in animal models and have demonstrated the capacity to identify regions of atheroma formation using FDA-approved exogenous fluorophores.³⁴ However, intravascular NIRF acquisition systems cannot acquire anatomical images of the vessel wall and lack a direct means of correcting for light attenuation through unknown quantities of luminal blood. Together, these limitations compromise the accuracy of diagnostic conclusions regarding the risk of vulnerable plaque and are an impediment to future clinical translation of the technique.

Interpretation of NIRF measurements is complicated by the distance-dependent attenuation of light through blood. Catheter-to-vessel wall distances cannot be determined directly from NIRF measurements, but can be estimated from co-registered IVUS images if NIRF and IVUS capabilities are integrated into a single catheter. Precedence exists for using ultrasound ranging data to detect optical sensing distances,²⁷⁴ and while other multi-modality catheters have been

presented in the literature,^{261,275,276} none have demonstrated the capacity to acquire co-registered imaging data for the purposes of correcting for random catheter positioning within the vessel lumen.

In this work, we describe the design of a combined NIRF-IVUS catheter for the correction of distance dependent attenuation of light through luminal blood. IVUS and NIRF components are rotated independently of one another, allowing for coincident acquisition of high frame rate IVUS images and long exposure NIRF measurements. Spatial registration of NIRF-IVUS data is achieved by image post-processing steps that map NIRF measurements to discrete sections of the vessel wall. Catheter-to-vessel wall distance is estimated from IVUS data and is incorporated into a light propagation model in order to correct NIRF measurements for variable sensing distances. In this study, we demonstrate the use of this instrument to correct for variable catheter sensing distances in coronary vessel phantoms and *ex vivo* porcine arteries using the exogenous fluorophore DiR as a NIRF imaging agent.

A1.3 Materials and Methods

A1.3.1 Combined NIRF-IVUS Catheter

Light from a 750 nm CW laser (BWF1-750, B&W Tek, Newark, DE) was focused into the proximal end of a 200 μ m diameter, 0.22 NA, multimode optical fiber (AFS200/220A, Fiberguide Industries, Stirling, NJ) and was reflected at a 90° angle from the fiber axis by an aluminum-coated microprism (NT66-768, Edmund Optics, Barrington, NJ). Fluorescence emission was collected by the same side-viewing optical fiber and was passed through a 770 nm dichroic mirror and a 750 nm band-stop filter to attenuate residual 750 nm excitation light (Iridian Spectral Optics, Ottawa, Ontario, CA). Emission channel leakage was approximately 2-4% of excitation power and was caused primarily by back-reflection of excitation light from the proximal face of the optical fiber.

Emission light was passed through a prism-based spectrophotometer to improve detection sensitivity by separating fluorescence signal from residual excitation light and was detected by a CCD camera (C4742-95, Hamamatsu, Bridgewater, NJ). A separate photodiode monitored laser power in order to correct NIRF measurements for deviations in excitation power.

A schematic of the NIRF-IVUS catheter is shown in Figure A1-1A. The NIRF optical fiber was bound to the sheath of a commercially available IVUS catheter and extended 1 mm beyond

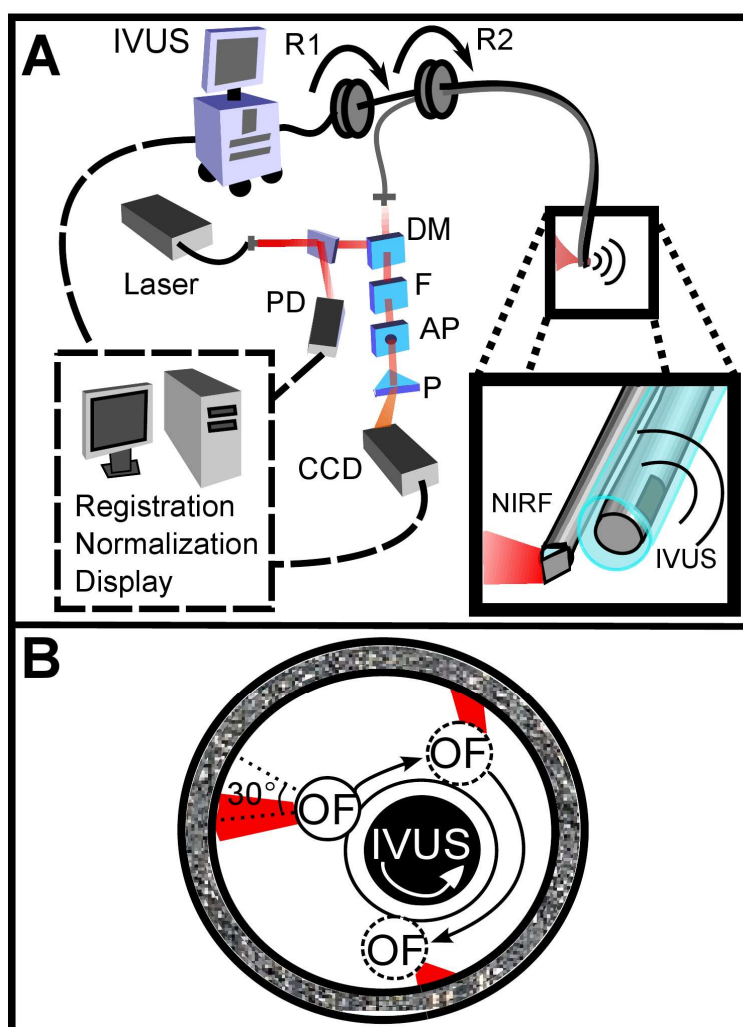


Figure A1-1: Experimental apparatus and NIRF/IVUS scanning geometry

(A) Schematic of the prototype NIRF-IVUS imaging system. The IVUS element is rotated by rotation motor R1. The IVUS sheath and NIRF optical fiber are rotated by rotation motor R2. Optical components are abbreviated as follows: PD, photodiode; DM, dichroic mirror; F, filter; AP, aperture; P, prism. **(B)** The IVUS element rotates about its axis and the optical fiber is advanced to new angular sensing positions as the catheter sheath is rotated by rotation motor R2.

the single-element ultrasound transducer (Revolution 45 MHz, Volcano Corp., San Diego, CA). Adjustment of the NIRF field-of-view was achieved by rotating the IVUS catheter sheath in discrete increments with a separate rotation motor, as shown in Figure A1-1B. The position of the NIRF optical fiber at the time of NIRF sensing was determined by tracking the center of an acoustic reverberation artifact caused by the optical fiber within the IVUS field-of-view. The NIRF field-of-view was fixed at a 30° angle relative to an imaginary line drawn between the centers of the IVUS and optical fiber (Figure A1-3). The IVUS element was rotated within the catheter sheath by a Volcano In-Vision Gold 3 imaging device. The combined NIRF-IVUS catheter had an outer diameter of 1.4 mm (4.2 F).

IVUS images were captured at frame rates exceeding 30 frames per second with a 4 mm radial imaging depth. NIRF measurements were acquired with 50 ms exposure times with 7 mW power. IVUS images were downloaded to a PC from the IVUS imaging system and were processed in conjunction with NIRF measurements using custom algorithms written in MATLAB (Mathworks Inc, Natick, MA).

A1.3.2 Analytical Light Propagation Model and Fluorescence Estimation

A two-layer analytical model of light propagation was developed to correct NIRF measurements for variable sensing distances through blood. The geometry of the two-layer model is illustrated in Figure A1-2. Light propagation through blood was modeled by the following equation, which was originally derived by Twersky^{277,278} and has proven accurate across physiological ranges of hematocrit and blood oxygenation:²⁷⁹⁻²⁸¹

$$P = P_0 e^{-\mu_a d} \left(e^{-sH(1-H)d} + q \left(1 - e^{-sH(1-H)d} \right) \right) \quad \text{Equation A1-1}$$

where P is the transmitted power, P_0 is the excitation power, μ_a is the absorption coefficient of hemoglobin, d is the propagation distance of light, H is the fractional hematocrit, and s and q are

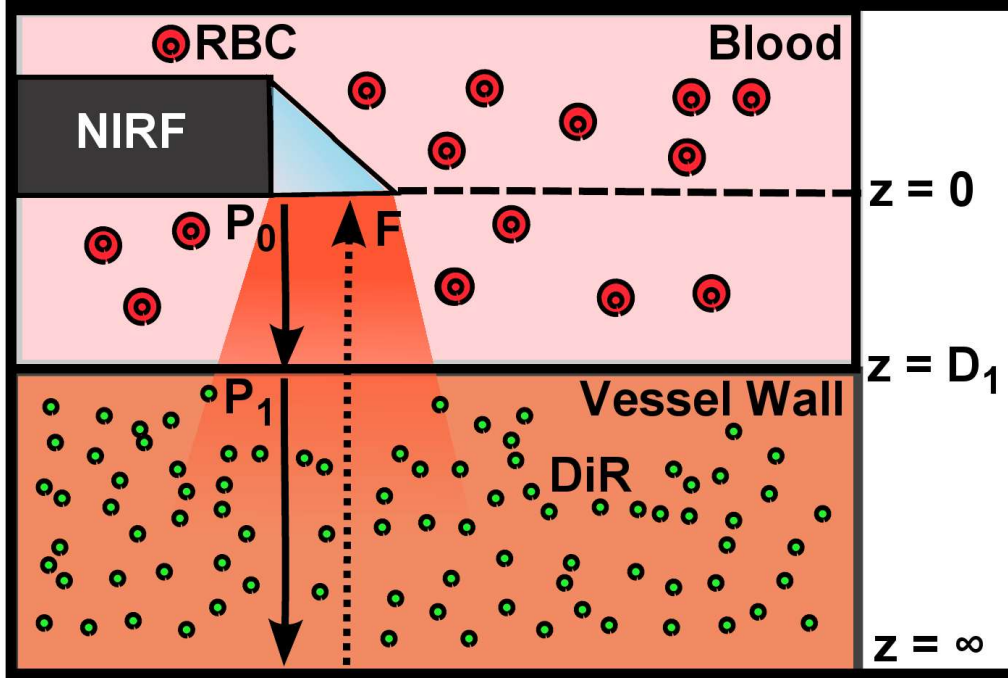


Figure A1-2: Schematic of one-dimensional light propagation model geometry

One-dimensional model of light propagation. Subscripts denote excitation power, P , at the beginning of each layer and cumulative fluorescence intensity, F , sensed by the optical fiber. Attenuation through blood is governed by Equation A1-1 and fluorescence emission from the vessel wall is estimated by Equation A1-2.

constants related to scattering and detection geometry. This framework resolves the total attenuation from blood into two distinct parts: absorption caused by hemoglobin and light attenuation due to scattering. Hemoglobin-specific attenuation (μ_a) was calculated using the extinction coefficient of hemoglobin,²⁸² and scattering is a function of H , which is known, and s and q , which are determined by fits to experimental data.

Emitted fluorescence was modeled by Equation A1-2, which is derived from one-dimensional diffusion theory by using the Eddington approximation to model fluorescence emission from a homogenous, semi-infinite, and turbid medium:²⁸³

$$F(\lambda_x, \lambda_m) = \int_0^{\infty} \mu_{a,f,x} \cdot \Phi \cdot C(\lambda_m) \cdot e^{-\mu_{\text{eff}}(\lambda_m)z} \cdot \left([4\pi A(\lambda_x) + P] \cdot e^{-\mu_t(\lambda_x)z} + 4\pi \cdot C_2(\lambda_x) e^{-\mu_{\text{eff}}(\lambda_x)z} \right) dz$$

Equation A1-2

where $\mu_{a,f,x}$ is the absorption coefficient of the fluorophore, Φ is the fluorophore quantum yield, $\mu_{eff} = [3 \cdot \mu_a \cdot (\mu_a + \mu_s')]^{1/2}$, P is the power of the excitation light incident on the vessel wall, $A(\lambda)$ and $C_2(\lambda)$ are the general and particular solutions of the diffusion equation,²⁸⁴ μ_t is the total extinction coefficient ($\mu_t = \mu_a + \mu_s$), and

$$C(\lambda_m) = 3 \cdot \left[\frac{\mu_a(\lambda_m) + \mu_s'(\lambda_m)}{3 \cdot [\mu_a(\lambda_m) + \mu_s'(\lambda_m)] + 2 \cdot \mu_{eff}(\lambda_m)} \right]. \quad \text{Equation A1-3}$$

In Equations A1-2 and A1-3, the subscripts x and m refer to excitation and emission wavelengths, respectively, and μ_s' is the reduced scattering coefficient ($\mu_s' = \mu_s \cdot (1-g)$ where g is the optical scattering anisotropy). Optical parameters at excitation and emission wavelengths were assumed to be equal in Equation A1-2. Equation A1-2 models attenuation of the excitation light, fluorescence conversion, and attenuation of fluorescence emission within the vessel wall. The fluorescence intensity sensed by the optical fiber is approximated by multiplication with a constant related to the acceptance angle of the optical fiber.²⁸⁵

Fluorescence intensity is related to fluorophore concentration by the absorption coefficient, $\mu_{a,f,x}$, and the quantum yield, Φ , such that values of $\mu_{a,f,x} \cdot \Phi$ scale linearly with changes in fluorophore concentration if no quenching occurs. Thus, relative fluorophore concentration within the vessel wall is proportional to the magnitude of $\mu_{a,f,x} \cdot \Phi$, which can be determined using an inverse-estimation approach when solving Equation A1-2, assuming that all other parameters in Equations A1-1 and A1-2 are known. In inverse estimation, the value of $\mu_{a,f,x} \cdot \Phi$ that best fits the mathematical model to experimental NIRF data is determined in an iterative least-squares optimization process. A trust-region-reflective algorithm was used in this work. After calibration to known fluorophore concentrations in tissue-mimicking phantoms, estimated values of $\mu_{a,f,x} \cdot \Phi$ can be used to determine the concentration of unknown fluorescent samples.²⁸⁶

A1.3.3 NIRF-IVUS Phantom Studies

Four concentrations of the fluorophore DiR (excitation: 750 nm, emission: 780 nm) were prepared in a tissue mimicking medium comprised of 3.5% v/v Intralipid and 0.05% v/v India Ink ($\mu_a = 2 \text{ cm}^{-1}$, $\mu_s = 150 \text{ cm}^{-1}$, $g = 0.85$).²⁸⁷ The optical parameters of the tissue-mimicking medium were intended to model the intimal layer of the vessel wall.²⁸⁸ DiR samples were placed in cuvettes of varying thickness and were surrounded by whole bovine blood with fractional hematocrits of 0.40, 0.45, and 0.50. Hematocrit was measured by centrifugation of heparinized blood. Co-registered NIRF and IVUS measurements were acquired at increasing sensing distances from the fluorescent samples. Sensing distances measured manually from the IVUS images were validated against ground-truth sensing distances provided by a calibrated motion stage.

A1.3.4 NIRF-IVUS Catheter Validation

A schematic of the vessel phantom is shown in Figure A1-5A. A transparent PTFE tube with a 3.1 mm inner diameter and 100 μm thick walls served as the vessel lumen and was filled with whole bovine blood with 0.40, 0.45, or 0.50 fractional hematocrit. Four borosilicate glass tubes filled with DiR in the tissue-mimicking medium were placed around the circumference of the PTFE tube to simulate discrete fluorescent targets within the phantom. Fluorophore concentrations were estimated for each sample of DiR from rotational NIRF-IVUS measurements acquired within the vessel phantom. All data is reported as mean \pm standard error of the mean (SEM). Paired two-sample *t*-tests were performed to determine whether the NIRF correction method produced a statistically significant improvement in fluorophore concentration estimation for each concentration tested.

A1.3.5 Image Processing

The vessel wall was segmented using an active contours segmentation framework.⁸⁷ IVUS images were preprocessed using a 2D bilateral filter²⁸⁹ to suppress speckle and by a Sobel operator to detect the edges of the vessel wall. It was assumed that there was a sufficient difference in image contrast between the blood-filled lumen and the vessel wall to enable robust edge detection. Iterative gradient vector flow (GVF) was performed on the edge-enhanced image to produce an external force term to guide contour evolution.²⁹⁰ A circular contour was initialized in the center of the IVUS image and iteratively evolved until a minimum energy condition was reached that preferentially guided the contour to the edges of the vessel wall.

The location of the optical fiber was automatically determined through a series of thresholding steps that segmented the acoustic reverberation artifact caused by the optical fiber from the dark background of the blood-filled vessel. NIRF catheter-to-vessel wall distances were measured

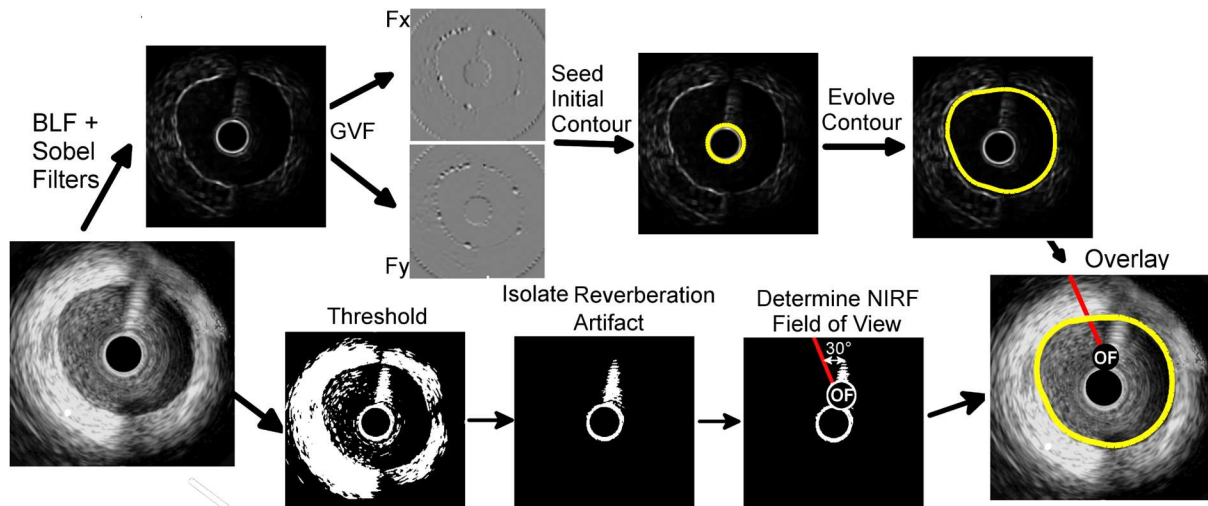


Figure A1-3: Schematic of IVUS image processing and vessel wall segmentation

Image processing steps employed to measure NIRF sensing distances from IVUS data. The top path shows intermediate images formed to produce external energy images, F_x and F_y , for the active contours algorithm. The initial contour is seeded around the circumference of the null space in the IVUS image and evolves until the termination condition is met. The bottom path shows thresholding and morphological steps used to isolate the reverberation artifact caused by the optical fiber.

automatically by finding the intersection of the contour outlining the vessel wall and the line depicting the NIRF field-of-view.

A1.3.6 Ex Vivo Artery Studies

Ex vivo porcine carotid arteries ranging in size between 3 and 5 mm in internal diameter were acquired from a local abattoir. The arteries were harvested proximal to the carotid bifurcation and were immediately stored in a physiological saline solution at 4°C.²⁹¹ DiR (100 μ M) was applied to one section of the vessel wall to simulate a non-uniform fluorescent target within each artery. DiR was selected for use in this study due to its low toxicity and propensity to integrate directly into cell membranes without migrating from cell to cell.²⁹² Thus, once applied to a specific region of the vessel, DiR does not disperse to label other sections of the vessel. Furthermore, the quantum yield of DiR significantly increases following incorporation into lipid bilayers, which ensures low background fluorescence from DiR that may have remained in solution following staining. Carbocyanine dyes, like DiR, have been used extensively in preclinical animal models, and DiR exhibits comparable fluorescence excitation and emission spectra to indocyanine green, an FDA approved fluorophore.

NIRF-IVUS measurements were acquired at multiple axial positions along the length of each artery to simulate a catheter pull-back procedure. Following NIRF-IVUS imaging, each artery was cut open and laid flat on a microscope slide (*en face*). *En face* fluorescence microscopy images of the inner vessel wall supplied relative estimates of local fluorophore spatial distributions within the artery. Accurate registration of fluorescence microscopy images and NIRF-IVUS catheter measurements was achieved by using needles to mark axial locations where NIRF-IVUS imaging was performed.

A1.4 Results

A1.4.1 NIRF-IVUS Phantom Studies

Four parameters must be determined to model light attenuation through blood using Equation A1-1 (μ_a , H , s , and q). Values of μ_a used to model hemoglobin absorption at 750 nm (excitation) and 780 nm (fluorescent emission) are shown in Table A1-1 and are derived from measurements made by Cope *et al.*²⁸² Estimates of s and q from Equation A1-1 were determined by measuring the transmission of 750 nm light through blood at three hematocrit levels (0.40, 0.45, and 0.50) and fitting the results to Equation A1-1 via least-squares optimization. In the fitting process, it was assumed that the value of q ranged between 0 and 0.2, as q broadly describes the fraction of scattered photons that are received by the NIRF optical fiber and has been previously shown to fall within this range.^{277-279,281} The value of s was allowed to assume any non-negative value, and it was assumed that the values of q and s did not vary within the narrow wavelength range considered in this work.

Table A1-1: Parameters for Model Fit to Equation A1-1

Hematocrit	$\mu_{a,750} \text{ (cm}^{-1}\text{)}$	$\mu_{a,780} \text{ (cm}^{-1}\text{)}$	H	s	q
0.40	2.48	3.30	0.40	29.7	0.126
0.45	2.77	3.71	0.45	29.7	0.126
0.50	3.08	4.13	0.50	29.7	0.126

Similarly, the transmission of 750 nm light was measured through the tissue-mimicking medium. Values of μ_a , μ_s' , and g for the tissue-mimicking phantom were taken from the literature²⁸⁷ and resulted in a theoretical value of 27.6 cm^{-1} for μ_{eff} . The experimentally determined value of μ_{eff} as calculated by Beer's Law ($P = P_0 e^{-\mu_{eff}d}$) was $29.4 \pm 0.87 \text{ cm}^{-1}$.

Four known concentrations of DiR in the tissue-mimicking medium were imaged with the NIRF-IVUS catheter through three different whole blood samples with fractional hematocrits of

0.40, 0.45, and 0.50. NIRF measurements were acquired at increasing sensing distances, and the experimental results and light propagation model fits are shown in Figure A1-4A-C ($r^2 = 0.92$). NIRF sensing distances were measured manually on IVUS images and resulted in a 3.9% RMSE when compared to ground-truth sensing distances provided by a calibrated motion stage. The same

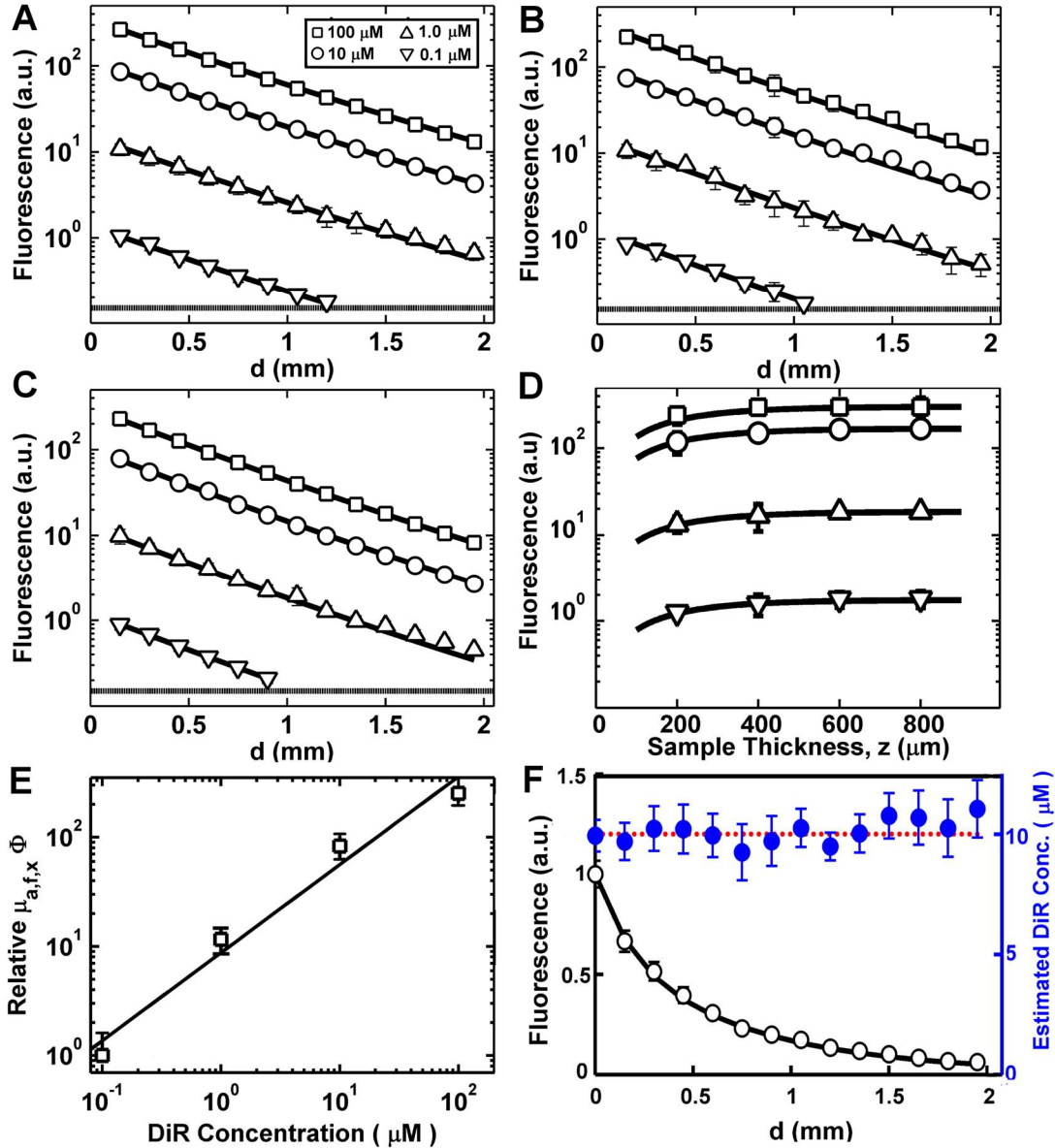


Figure A1-4: *In vitro* NIRF/IVUS measurements of DiR concentrations

Light propagation model fits to NIRF measurements from four different concentrations of DiR imaged through whole bovine blood with (A) 0.40, (B) 0.45, and (C) 0.50 fractional hematocrit. The dashed line represents the approximate noise floor of the NIRF instrumentation. (D) Light propagation model fits to NIRF measurements of DiR samples of different thicknesses. (E) Calibration curve (linear fit) derived from experimental NIRF measurements relating model estimates of $\mu_{a,f,x} \Phi$ to known concentrations of DiR. (F) Estimated DiR concentration of a 10 μM sample of DiR imaged through whole bovine blood with 0.45 fractional hematocrit.

DiR samples were placed in cuvettes of different thicknesses and were measured from a constant NIRF sensing distance of 500 μm through whole blood with a fractional hematocrit of 0.45. The majority of the fluorescent light was generated within the first 200 μm of the sample. Experimental results and light propagation model fits are shown in Figure A1-4D ($r^2 = 0.96$).

A calibration curve showing the relationship between values of $\mu_{a,f,x} \cdot \Phi$ estimated by the light propagation model and DiR concentrations sensed through the three different whole blood samples is presented in Figure A1-4E. Values of $\mu_{a,f,x} \cdot \Phi$ scaled linearly with increasing DiR concentration between 0.1 μM and 10 μM ($r^2 = 0.91$) and varied only slightly with changes in the fractional hematocrit (differences were not significant, $p > 0.05$). The calibration curve was used to map estimates of $\mu_{a,f,x} \cdot \Phi$ derived from raw NIRF measurements to DiR concentrations in subsequent vessel phantom experiments.

An example result of the concentration estimation procedure is shown in Figure A1-4F. The fluorescence from a 10 μM sample of DiR was measured with the NIRF-IVUS catheter at increasing sensing distances through whole blood with 0.45 fractional hematocrit. Values of $\mu_{a,f,x} \cdot \Phi$ were derived by the light propagation model for each data point using the optical parameters that were previously determined. The values of $\mu_{a,f,x} \cdot \Phi$ were used to estimate DiR concentrations using the calibration curve in Figure A1-4E. DiR concentrations were estimated with an average root mean square error (RMSE) of 6.3%.

A1.4.2 NIRF-IVUS Validation in Vessel Phantoms

Co-registered NIRF-IVUS imaging was performed in vessel phantoms, and catheter-to-vessel wall distances for each NIRF acquisition were measured manually on IVUS images. The measured catheter-to-vessel wall distances supplied the value for d within Equation A1-1 of the light

propagation model, and the value of $\mu_{a,fx} \cdot \Phi$ was calculated for each NIRF-IVUS measurement taken within the vessel phantom.

NIRF sensing distances for a complete 360° acquisition in the 3.1 mm diameter vessel phantom are shown in Figure A1-5B. The average NIRF sensing distance for the single trial presented in Figure A1-5B was 540 μm with a minimum and maximum of 305 μm and 785 μm , respectively. Minimum and maximum NIRF sensing distances for all trials performed were 220 μm and 1210 μm . Raw fluorescence intensities and estimated fluorophore concentrations for the same 360°

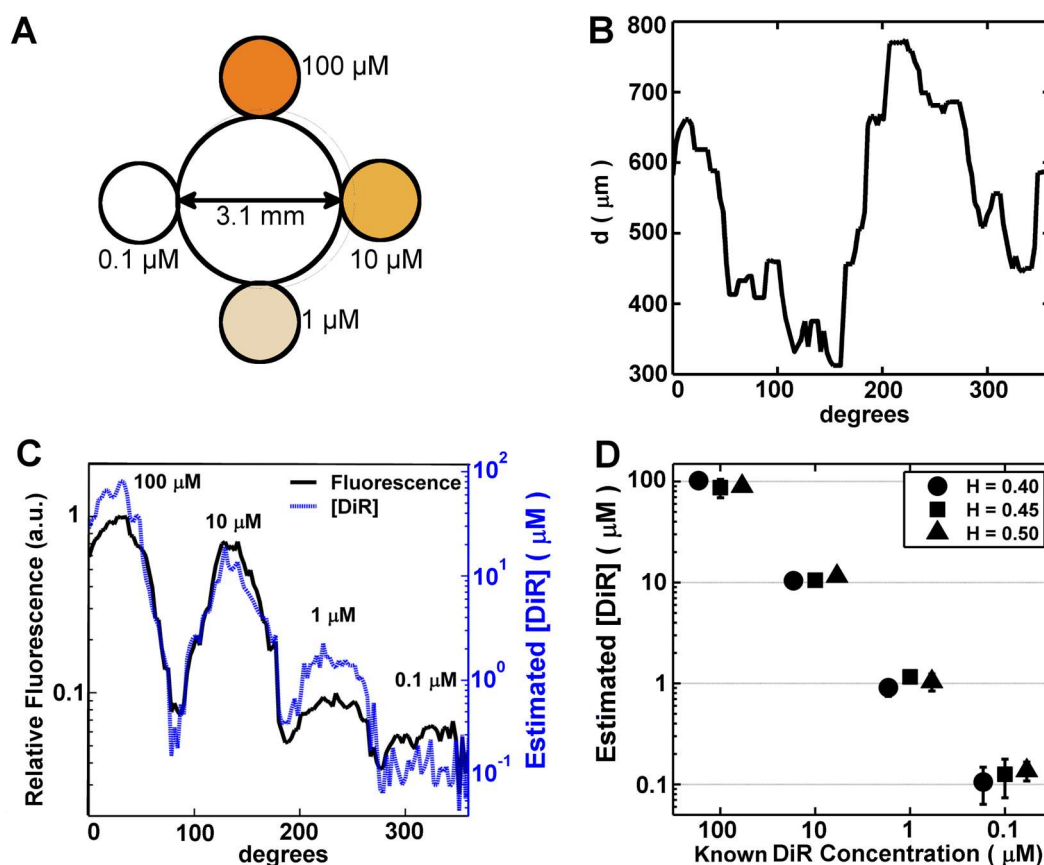


Figure A1-5: *In vitro* NIRF/IVUS measurements of DiR concentrations in vessel phantoms

(A) Axial schematic of the vessel phantom. Whole bovine blood was placed within the 3.1 mm diameter lumen and four different concentrations of DiR were placed in tubes surrounding the vessel lumen. (B) NIRF sensing distances as measured manually on IVUS images for a single 360° acquisition within a vessel phantom. (C) Raw fluorescence intensities and estimates of DiR concentration for each fluorescent target within the vessel phantom for the same 360° NIRF-IVUS acquisition presented in (B). (D) Estimated concentrations of fluorescent targets within the vessel phantom at three different blood hematocrits. The NIRF correction method resulted in a statistically significant improvement in fluorophore concentration estimates for each concentration tested ($p < 0.05$).

acquisition are presented in Figure A1-5C. Each fluorescent target produced a fluorescence intensity peak with a full-width-half-maximum of approximately 50 degrees.

A comparison between estimated and known concentrations for each DiR sample within the vessel phantom is presented in Figure A1-5D. RMSE for concentration estimates derived by the light propagation model were 16.5%, 17.0%, 19.0%, and 45.4% for the 100 μM , 10 μM , 1 μM , and 0.1 μM DiR samples, respectively. These RMSE values are compiled from all measurements taken through whole blood with hematocrits of 0.40, 0.45, and 0.50. Differences in RMSE between the three different hematocrit values were not statistically significant ($p > 0.05$), demonstrating the ability of the model to correct for variable catheter sensing distances through whole blood with varying hematocrit. Measurements of the 0.1 μM DiR sample were obscured by sensitivity limits of the NIRF instrumentation and were excluded from further analysis.

In addition, DiR concentration estimates were made using raw fluorescence intensities by normalizing each uncorrected NIRF measurement to the average fluorescence intensity of the 10 μM DiR sample. RMSE for these concentration estimates with no corrections were 92%, 41.6%, 138%, and 272% for the 100 μM , 10 μM , 1 μM , and 0.1 μM DiR samples, respectively. These large and unpredictable errors are the result of random sensing distances within the vessel phantom, which significantly limits the usefulness of conclusions drawn from uncorrected NIRF measurements.

A1.4.3 Fluorescence Estimation in Ex Vivo Arteries

Ex vivo arteries were stained with DiR and underwent NIRF-IVUS imaging. Representative results of the automated image processing algorithm are shown in Figure A1-6A. The outline of the vessel wall was generated using an active contours segmentation algorithm and the position of the NIRF optical fiber was determined by tracking its acoustic reverberation artifact. A comparison

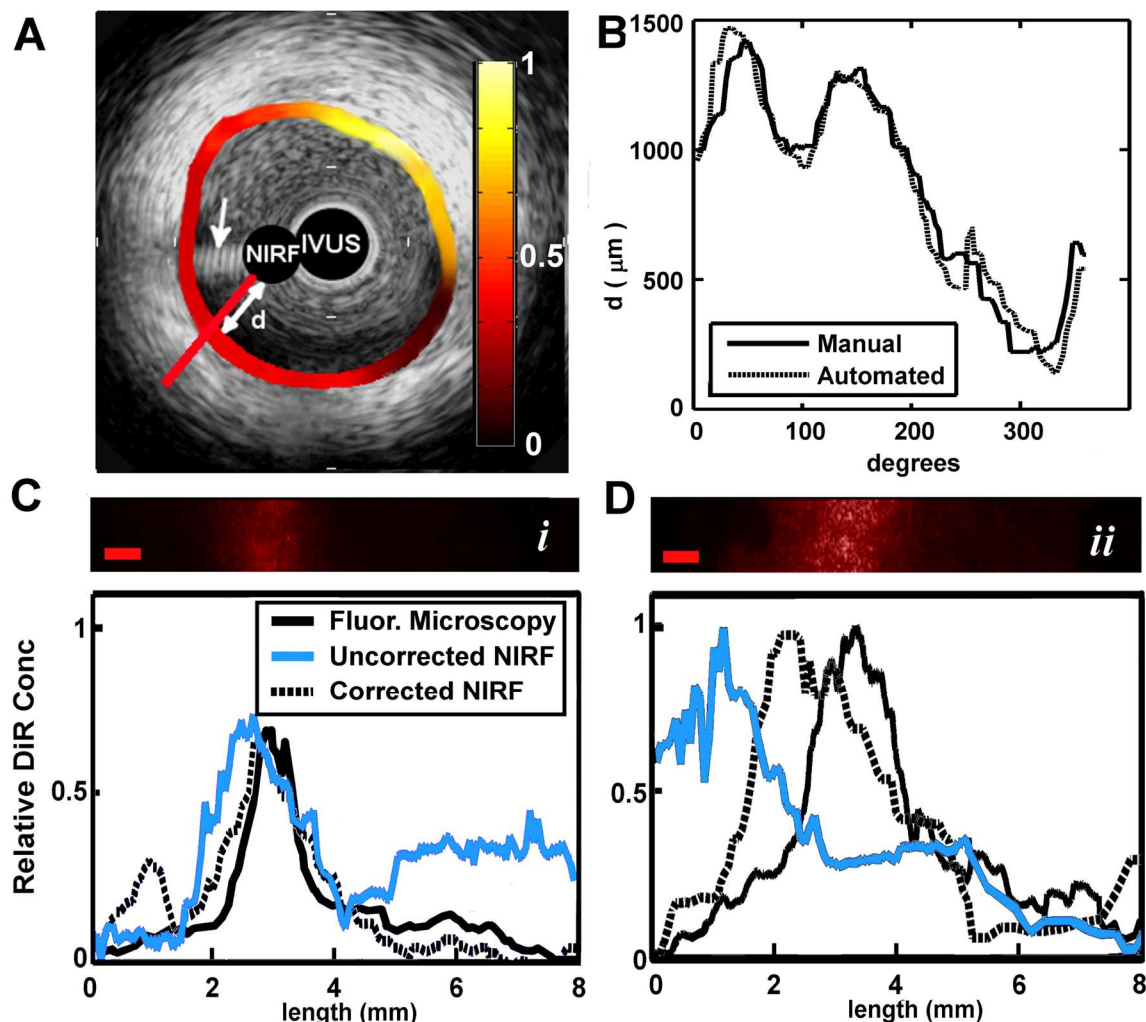


Figure A1-6: *Ex vivo* NIRF/IVUS measurements of DiR concentrations in excised porcine vessels
(A) IVUS image of an *ex vivo* porcine carotid artery with co-registered NIRF overlay. The NIRF optical fiber caused an acoustic reverberation artifact marked by the white arrow. The white double-headed arrow shows the NIRF sensing distance, d . Colorbar corresponds to normalized relative fluorescence sensed by NIRF catheter. **(B)** Comparison between manual and automatic measurement of NIRF sensing distances for a single 360° NIRF-IVUS acquisition. **(C & D)** (Top) Two rows, *i* and *ii*, of fluorescence microscopy images of an *ex vivo* artery stained with DiR (scale bar = 1 mm). (Bottom) Relative fluorescence intensities measured from fluorescence microscopy and NIRF across rows *i* and *ii*.

of manually and automatically measured NIRF sensing distances is shown in Figure A1-6B for a single 360° NIRF-IVUS acquisition. Average RMSE between manual and automated measurements was 8.2%, suggesting that the proposed NIRF correction can be performed automatically with minimal user interaction.

Co-registered NIRF-IVUS data was acquired from two *ex vivo* arteries with inner diameters of 3.9 mm and 4.3 mm. NIRF-IVUS acquisitions were captured at different axial locations along the length of each artery to simulate a pullback procedure. Representative fluorescence microscopy results for two locations in the 3.9 mm artery, *i* and *ii*, are shown in Figure A1-6C,D. Robust DiR staining was localized to approximately one-third of the vessel circumference at depths up to 50 μm , as determined by confocal microscopy. Accordingly, optical parameters of the intima were used to model the vessel wall in the light propagation model ($\mu_a = 2 \text{ cm}^{-1}$, $\mu_s = 150 \text{ cm}^{-1}$, $g = 0.84$).²⁸⁸

Figure A1-6C,D shows relative DiR concentrations derived from fluorescence microscopy, uncorrected NIRF, and corrected NIRF measurements for axial locations *i* and *ii*. Spatial correlation coefficients between fluorescence microscopy and NIRF estimates of DiR spatial distributions improved from 0.34 to 0.66 for location *i* and from 0.13 to 0.73 for location *ii* following correction of the NIRF measurements.

Spatial correlation between NIRF and fluorescence microscopy results was assessed for all artery locations examined by the NIRF-IVUS catheter ($n = 6$). Correlation coefficients were transformed into a new variable, the Fisher Z value, in order to calculate average correlation coefficients and 95% confidence intervals for uncorrected and corrected NIRF measurements.²⁴³ The average correlation coefficient between uncorrected NIRF and fluorescence microscopy measurements was 0.24 with a 95% confidence interval between 0.19 and 0.30. The average correlation coefficient between corrected NIRF and fluorescence microscopy measurements was 0.69 with a 95% confidence interval between 0.67 and 0.72. These results demonstrate that correcting NIRF measurements for variable catheter-to-vessel wall sensing distances resulted in a

statistically significant improvement ($p < 0.01$, $n = 6$) in the correlation between NIRF-IVUS and fluorescence microscopy estimates of local fluorescence intensities in *ex vivo* arteries.

A1.5 Discussion

A combined NIRF-IVUS catheter was developed to provide intravascular anatomical and molecular imaging of the vessel wall and to determine whether correcting for variable catheter-to-vessel wall sensing distances could improve the accuracy of NIRF measurements. As expected, NIRF imaging sensitivity decreased with increasing blood hematocrit, with maximal sensing distances of the 0.1 μm DiR sample of 1.2 mm and 0.9 mm at hematocrits of 0.40 and 0.50, respectively. Blood attenuation correction of NIRF measurements acquired beyond these sensitivity limits could not recover accurate fluorophore concentration estimates. This sensitivity is in good agreement with other NIRF imaging catheters described in the literature,^{34,266,267,293} but it should be noted that detection sensitivity is also modulated by varying optical properties of the vessel wall tissue, which was not explored in this work.

The least-squares optimization routine used to fit experimental data to Equations A1-1 and A1-2 resulted in a good fit to experimental data ($r^2 = 0.92$), but because the system is over-determined, the solution used in this work is not unique. However, the solution provided an accurate fit to blood attenuation across three hematocrit levels and enabled accurate blood attenuation correction in the phantom studies. An advantage of the analytical light propagation model over Monte Carlo based approaches is that the analytical model can estimate relative fluorophore concentrations from NIRF data in real-time during a catheterization procedure. While a Monte Carlo formulation may improve the accuracy of light attenuation estimates, it is not capable of producing real-time results on the standard computer hardware typically employed within catheterization laboratories.

Model-based correction of NIRF concentration estimates in vessel phantoms reduced average RMSE from 90.5% to 17.5%, comparing well to the results of other analytical models cited in the literature. Diffusion models of light propagation have demonstrated average RMSE between 5 and 25% when measuring fluorescence from tissue-mimicking phantoms,^{283,286,294} and a similar one-dimensional formulation demonstrated less than 10% RMSE when assessing fluorescence from epithelial and stromal tissues within the human cervix.²⁸⁵ A limitation of these approaches is the reliance on *a priori* knowledge of the optical properties of the tissues being studied. The attenuation of whole blood can be measured prior to an imaging procedure, but the optical properties of the vessel wall cannot. Nevertheless, significant effort has been devoted to modeling the optical characteristics of both whole blood and atherosclerotic lesions.^{288,295-297} Furthermore, a variety of techniques for quantitatively measuring fluorophore concentrations with and without *a priori* knowledge of tissue optical properties have been developed for non-catheter based applications,²⁹⁸⁻³⁰⁵ however, it remains to be seen whether these methods are compatible with intravascular imaging through blood and whether they can be integrated into the small form factor of a catheter.

As demonstrated in Figure A1-6, the model-based corrections resulted in a statistically significant improvement in fluorophore spatial distribution estimates in *ex vivo* arteries when compared to relative fluorescence as measured by fluorescence microscopy. While fluorescence microscopy does not provide a quantitative measure of local fluorophore concentration, it does provide an independent measure of relative fluorescence that is unaffected by attenuation of intraluminal blood. The accuracy of the model-based correction technique relies upon accurate catheter-to-vessel wall distance measurements derived from IVUS images, which exhibited a 3.9% RMSE in phantom studies, but were greater in the *ex vivo* studies due to inferior delineation of the

soft vessel wall. This source of measurement error and possible variation in the optical properties of the vessel wall could be limiting factors that reduced the correlation between the two measures of relative fluorescence. Nevertheless, the model-based blood attenuation correction approach improved the correlation of NIRF measurements to fluorescence microscopy in all samples tested.

Temporary vessel occlusion followed by saline flushes or deflection of the catheter towards the vessel wall during NIRF sensing may also improve the accuracy of NIRF measurements, but neither of these approaches are complete solutions.^{275,306} Saline flushes are not appropriate for patients who are sensitive to increases in blood volume, and precise control of the catheter tip is difficult to achieve *in vivo*. The approach demonstrated here is not constrained by these limitations and enables new capabilities. First, independent rotation of the IVUS and NIRF elements enables different IVUS and NIRF acquisition speeds. Conventional IVUS catheters are rotated in excess of 1500 rotations per minute to enable real-time imaging and to reduce non-uniform rotational distortion,³⁰⁷ but NIRF sensing requires longer, variable exposure times to optimize fluorescence signal-to-noise ratios.²⁹⁸ Second, this method of NIRF-IVUS integration does not require significant modifications to existing IVUS instrumentation and can be made more robust through the use of a double lumen catheter.

A1.6 Conclusions

A combined NIRF-IVUS catheter was developed to acquire co-registered molecular and anatomic images of the vessel wall. NIRF-IVUS measurements were corrected for inaccuracies caused by variable catheter-to-vessel wall distances through the use of a light propagation model. The NIRF correction method resulted in an average RMSE of 17.5% when estimating known fluorophore concentrations in vessel phantoms compared to an average RMSE of 90.5% without correction. Furthermore, the NIRF correction method resulted in a statistically significant

improvement in correlation between spatially resolved NIRF measurements and known fluorophore distributions in *ex vivo* arteries ($p < 0.01$, $n = 6$). Future studies are required to determine whether such corrections will enable semi-quantitative assessment of exogenous NIRF fluorophores targeted to biomarkers associated with atherosclerosis and whether such techniques can inform clinical treatment decisions or aid in the study of disease progression in preclinical models.

Chapter A2. Acoustic activation of phase change perfluorocarbon droplets containing solid mesoporous silica nanoparticles within their liquid cores⁷

A2.1 Abstract

Phase change contrast agents (PCCAs) are fluorocarbon liquid droplets that convert into microbubbles when exposed to high acoustic pressures. Given their small size, PCCAs can exit leaky blood vessels and provide exogenous contrast outside of the vascular system, thereby circumventing one of the primary limitations of microbubbles. However, a limitation of PCCAs is the high acoustic pressure required for conversion to gaseous phase, which may restrict their use as a diagnostic imaging agent. The incorporation of solid nanoparticles into the liquid perfluorocarbon phase has been suggested as a means to reduce the pressures required to convert PCCAs, however, this has not been confirmed through rigorous empirical observation. In this work, we sought to determine whether the presence of solid nanoparticles contained within the liquid perfluorocarbon core of PCCAs effects the pressure required for acoustic conversion into a gaseous microbubble. Fluorinated mesoporous silica nanoparticles (FMSNs, diameter = 14 nm) were confirmed to be within the perfluoropentane droplet core by TEM imaging, and acoustic activation of individual droplets was monitored via high speed cinematography. Of the 50 control droplets studied, 2 droplets converted at a peak negative pressure of 12.89 MPa, and of the 46 DFP droplets containing FMSNs, 2 droplets converted at 7.3 MPa and one converted at 10.5 MPa. Thus,

⁷ The content in this chapter appears in the following peer-reviewed conference publications:

AJ Dixon, E Lu, V Chang, JA Hossack, "Synthesis and acoustic conversion of perfluorocarbon nanodroplets containing solid nanoparticles within their liquid cores." International Ultrasonics Symposium (2016), Tours, France.

in this study, there was no statistical difference in acoustic activation of perfluoropentane droplets with FMSNs within their cores.

A2.2 Introduction

Phase change contrast agents (PCCAs) are comprised of a perfluorocarbon liquid core surrounded by a lipid, protein, or polymer shell material. These agents have been fabricated by sonication, agitation, microfluidic devices, and condensation of gaseous microbubbles, which result in droplets with diameters between 0.2 – 5 μm .³⁰⁸⁻³¹¹ Droplets with diameters less than approximate 400 nm may extravasate from leaky tumor vasculature, thereby presenting the opportunity for tumor-specific therapy or targeted molecular imaging. In response to high peak-negative pressures, the liquid perfluorocarbon core undergoes a phase transition from a liquid droplet to a gaseous bubble.³¹² This phase conversion event emits a strong acoustic wave from the droplet that can be detected by an ultrasound imaging system for the purposes of localized contrast enhancement or targeted molecular imaging. However, the use of PCCAs for diagnostic or molecular imaging applications is limited by the high acoustic pressures required for phase conversion. Multiple studies have demonstrated that peak negative pressures in excess of 10 MPa are required to convert the smallest PCCAs, resulting in mechanical index (MI) values significantly higher than current regulatory limits.^{310,313}

Therefore, reducing the pressure required for pressure-mediated phase conversion is of significant academic interest. Sheeran *et al* investigated the effects of mixing perfluorocarbon chains of different lengths (e.g. octofluoropropane, decafluorobutane, dodecafluoropentane) on phase conversion pressures and determined that increasing concentrations of shorter chain perfluorocarbons significantly reduced the pressure required for conversion, but that the MI was still above regulatory limits.³¹⁰ Using a different approach, Lee *et al* investigated the effects of

solid nanoparticles contained within the perfluorocarbon core on acoustic conversion.³¹⁴ Bulk measurements suggested that the presence of iron-oxide nanoparticles within the perfluorocarbon core reduced the pressure required for acoustic conversion, but the effect was not investigated on a per-droplet basis. The central hypothesis is that the presence of solid nanoparticles within the liquid lowers the acoustic energy required for phase conversion by converting the process from a homogeneous to a heterogeneous nucleation process.^{82,83,315,316} In addition, interactions between droplets are known to influence their conversion properties, and more studies are required to investigate single versus group droplet conversion dynamics.³¹⁷

In this work, we investigated the acoustic conversion properties of perfluoropentane droplets that contained fluorinated mesoporous silica nanoparticles (FMSNs) within the liquid perfluorocarbon core. The large surface area of the mesoporous silica nanoparticles was hypothesized to serve as an effective gas nucleation site to promote cavitation via heterogeneous nucleation, thus lowering the acoustic pressure required to convert DFP droplets into microbubbles.³¹⁸ The phase conversion efficiency of this PCCA formulation in response to acoustic pressures was evaluated on a single-droplet basis using a high speed camera to capture the droplet-bubble dynamics immediately following conversion.

A2.3 Materials and Methods

A2.3.1 Preparation of Fluorinated Mesoporous Silica Nanoparticles

To prepare FMSNs, 0.3 g of mesoporous silica nanoparticles (SiO_x, 99.5+%, P-type, 15-20 nm, amorphous, US Research Nanomaterials, Inc.) were dispersed in 10 mL Milli-Q H₂O and sonicated in a bath sonicator for an hour. 100 μ L of this stock solution was then resuspended in 10 mL Milli-Q H₂O in a 25 mL Pyrex jar with a stir bar, and sonicated in the bath sonicator for another hour. A water bath was heated to approximately 55° C and the suspension of dispersed mesoporous

silica nanoparticles (SNPs) were placed in the bath for 20 minutes to allow for temperature equilibration. 188 μL of 1H,1H,2H,2H-perfluorooctyltriethoxysilane (PFOTS, Sigma, 97%) was added dropwise to the Pyrex jar and the mixture was allowed to react overnight, with the stir bar spinning at around 300 RPM.³¹⁹ The nanoparticles were then washed via centrifugation twice in water and twice in perfluorohexane. Anhydrous calcium sulfate was used to remove trace amounts of water after washing. Finally, the FMSNs were resuspended in perfluoropentane. This final re-suspension step could also have been completed in any perfluorocarbon of choice.

A2.3.2 Preparation of Perfluorocarbon Nanodroplets with Fluorinated Silica Nanoparticles

2 mL lipid (4 mg/mL, 9:1 mole ratio 1,2-Distearoyl-sn-glycero-3-phosphocholine: 1,2-distearoyl-sn-glycero-3-phosphoethanol-amine -N-[amino(polyethylene glycol)-2000]) and 100 μL FMSN-perfluoropentane suspension were sonicated on ice for 5 minutes using a tip sonicator and washed via centrifugation in saline to remove any impurities and excess lipid. The droplets

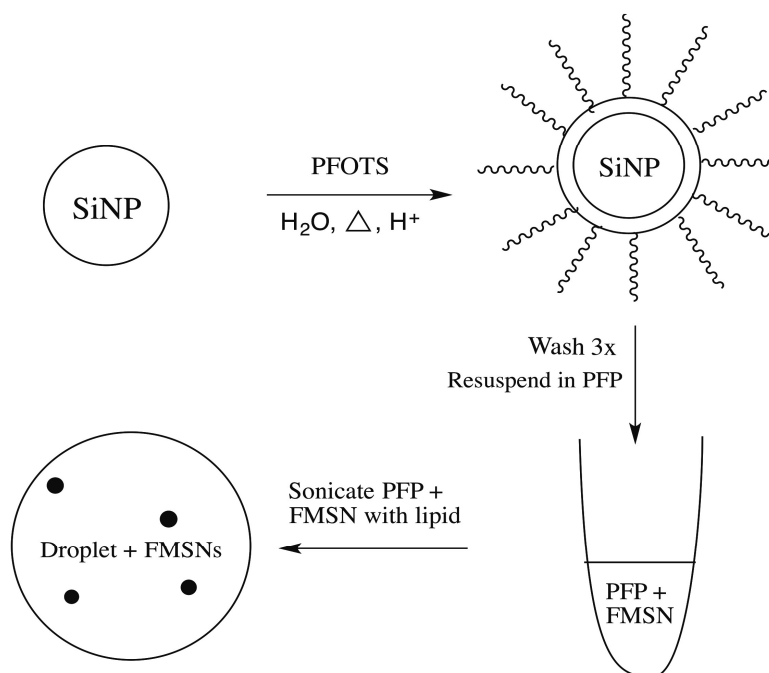


Figure A2-1: Schematic of synthesis of perfluorocarbon droplets with FMSNs in their core

The surface of mesoporous silica nanoparticles was fluorinated by overnight incubation with PFOTS in acidic conditions. The resulting particles were washed and resuspended in perfluoropentane for long-term storage. On the day of experimentation, perfluoropentane containing FMSNs was added to an aqueous solution with lipid surfactant and tip sonicated to form perfluorocarbon nanodroplets.

were kept at 4°C until experiments were performed. The general synthesis method is outlined in Figure A2-1.

A2.3.3. PCCA Acoustic Conversion Apparatus

Acoustic conversion of the droplets was completed using a setup as shown in Figure A2-2. The droplets were first diluted and passed through a 200 μm diameter cellulose tube (Spectrum Labs, Rancho Dominguez, CA). Then, the focus of a high-pressure ultrasound transducer (7.5 MHz, SonicConcepts, Bothell, WA) was aligned with the center of the field of view of a high-speed camera. Acoustic conversion was studied using 5 cycle pulses at 7.5 MHz and increasing peak-negative-pressures, from 2.7 to 12 MPa. The high-speed camera was used to visualize the droplet conversions. The acoustic conversion was studied for control droplets that did not contain FMSNs and droplets that did contain FMSNs. Video sequences were taken of the droplet during this

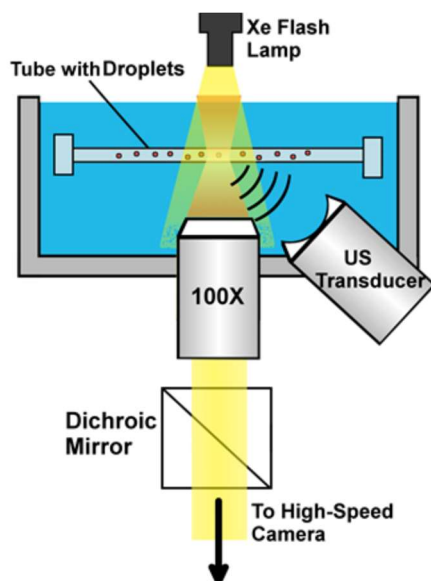


Figure A2-2: Schematic of experimental apparatus used to observe droplet phase conversion

Perfluorocarbon droplets were placed in a 200 μm diameter cellulose tube that was housed in a water bath. The focus of a high-intensity ultrasound and a 100X water-immersion objective were co-aligned using a needle-tip hydrophone to confirm co-alignment of the foci. Individual droplet conversion events were observed using high speed microscopy.

process, and ImageJ was used on component image frames to determine the diameter of droplets and microbubbles pre and post conversion, respectively.

A2.4 Results

A2.4.1 Verification of Nanoparticle Fluorination

A qualitative verification test was performed in order to ensure fluorination of the silica nanoparticles. For this test, the fluorinated and non-fluorinated mesoporous silica nanoparticles were suspended in three tubes. The first tube contained plain deionized water and no nanoparticles, the second tube contained a perfluorohexane phase and a separate deionized water phase (containing blue food coloring) with non-fluorinated nanoparticles suspended, and the third tube contained the same conditions as the second, but using fluorinated nanoparticles. Given their hydrophilic surface, the non-fluorinated silica nanoparticles in the second tube were observed only in the aqueous phase. However, the fluorinated silica nanoparticles were observed in the perfluorohexane phase, indicating at least partial fluorination of their surface. Figure A2-3 shows the results of this verification.

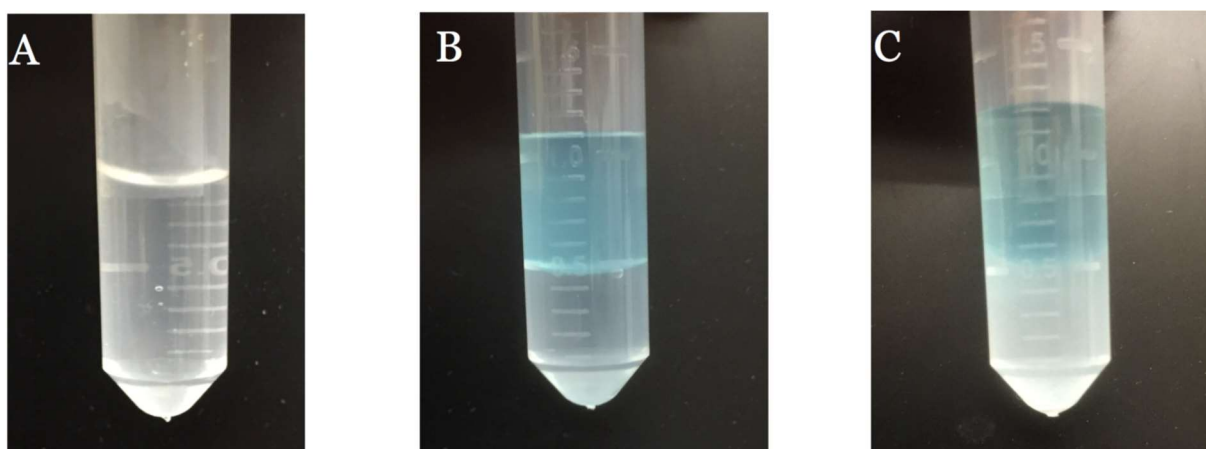


Figure A2-3: Qualitative confirmation of silica nanoparticle fluorination

(A) Plain deionized water. (B) Perfluorohexane (bottom) with unfluorinated nanoparticles in aqueous phase (top). (C) Perfluorohexane (bottom) with fluorinated nanoparticles and deionized water (top).

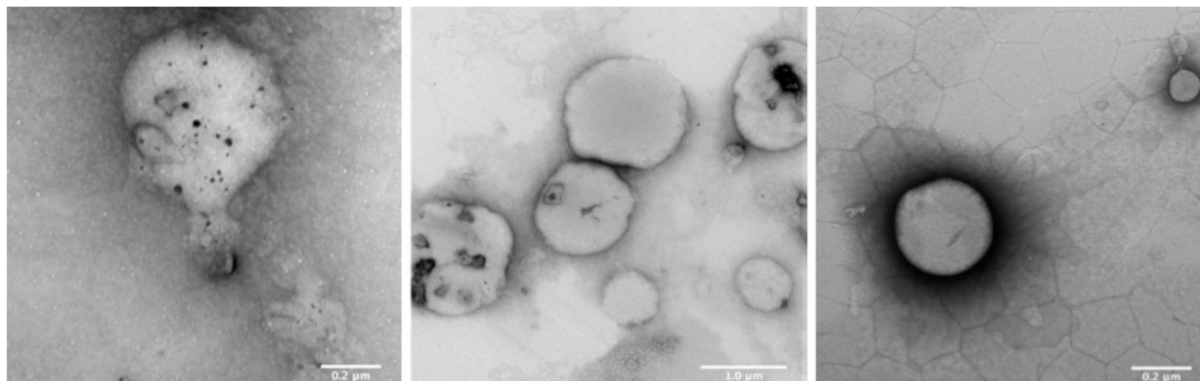


Figure A2-4: TEM imaging of perfluorocarbon droplets and FMSNs
 (Left) DFP droplet containing FMSNs. (Center) DFP droplets with aggregated FMSNs. (Right) Control DFP droplets made without any FMSNs. Scale bar is 0.2 μm in (Left), 1.0 μm in (Center), and 0.2 μm in (Right).

A2.4.2 Verification of FMSN incorporation into PCCAs

After the creation of the droplets, transmission electron microscopy (TEM) was used to confirm that nanoparticles had been successfully loaded within the droplets. TEM was necessary since the silica nanoparticles were 15-20 nm in size, thus making it impossible to visualize using normal optical microscopy. Multiple images were taken of three conditions. The first condition was plain, non-fluorinated silica nanoparticles. These plain silica nanoparticles tended to aggregate together and form large clusters. The second condition was plain perfluoropentane droplets without silica nanoparticles, to serve as a negative control. Finally, the third condition was perfluoropentane droplets synthesized with fluorinated nanoparticles. Black solid structures within the droplets of the third condition confirmed successful fluorination and cohabitation within a perfluorocarbon droplet. A total of 22 droplets containing FMSNs and 27 droplets without FMSNs were imaged using TEM. Droplets containing FMSNs had an average diameter of 723.6 ± 416.3 nm while droplets without FMSNs had an average diameter of 452.2 ± 333.3 nm. All droplets synthesized with FMSNs contained FMSNs within their core, although they were present as aggregates in the TEM images. It is unclear if they were aggregated prior to preparation for TEM or if they were

associated with the lipid membrane or freely dispersed within the droplet core. Figure A2- 4 shows representative results of the TEM imaging.

A2.4.3 Acoustic Conversion of Perfluorocarbon Droplets

Droplets were converted using the setup as shown in Figure A2-2. 50 perfluoropentane droplets without FMSNs were studied to serve as a control, while 46 perfluoropentane droplets containing FMSNs were studied to determine if the presence of solid nanoparticles effected the pressure required for acoustic conversion. All droplets were fabricated on the day of experimentation, and all experiments were performed at 25 C. All droplets studied were between 700 and 1300 nm in diameter. Of the 50 control droplets, 2 droplets converted at a peak negative pressure of 12.89 MPa ($MI = 4.7$). Of the 46 DFP droplets containing FMSNs, 2 droplets converted at a peak negative pressure of 7.3 MPa ($MI = 2.7$) and one converted at a peak negative pressure of 10.5 MPa ($MI = 3.8$). In total, 5% of droplets without FMSNs and 6.5% of droplets with FMSNs converted at the peak negative pressures tested. Using a Student's unpaired t-test, a p -value of 0.4943 was

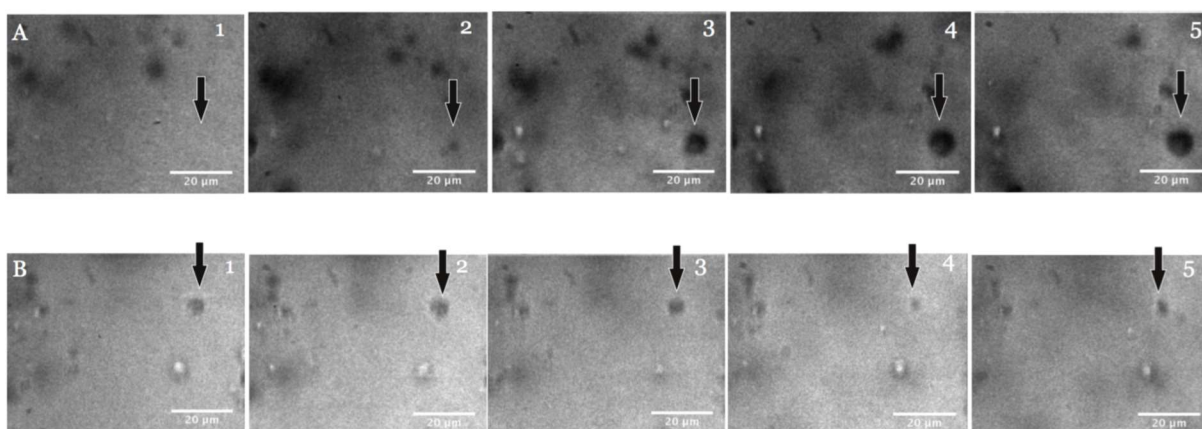


Figure A2-5: High speed camera results of acoustic droplet conversion

(A) Droplets with FMSNs converted in 36° C ambient temperature. Each image is 100 nanoseconds apart. The acoustic pulse used 100 cycles and corresponded to a peak negative pressure of 10 MPa. (B) Droplets with FMSNs converted in 36° C ambient temperature. Each image is 100 nanoseconds apart and correlates to 10 MPa. Scale bar in each image is 20 μm.

calculated, failing to reject the null hypothesis. Droplet conversions were captured using a high-speed camera. Images from this conversion can be seen in Figure A2-5.

A2.5 Discussion and Conclusions

The surface of mesoporous silica nanoparticles was successfully fluorinated to yield FMSNs, and FMSN incorporation into PCCAs was validated via transmission electron microscopy. Acoustic conversion was evaluated using high MI ultrasound excitations of 5 cycles at 7.5 MHz. 5% of the PCCAs without FMSNs converted into gaseous bubbles, while 6.5% of PCCAs with FMSNs converted. This result is not statistically significant and implies that the incorporation of 10 – 20 nm diameter FMSNs into the droplet core does not appreciably influence the acoustic conversion pressure of the PCCAs studied in this work.

Notably, the acoustic conversion efficiencies were low for this droplet formulation. Fewer than 10% of the droplets studied converted into microbubbles, even when exposed to peak negative pressures of up to 12 MPa ($MI = 4.4$). A lack of droplet conversion events limited the ability to analyze the results, and significantly more droplets would have to be studied to draw firm conclusions.

Droplets with decafluorobutane cores are expected to convert in greater numbers and may provide more conversion events in a similarly sized study. This is a future direction that may be explored to determine the effects of solid nanoparticle incorporation into PCCAs on the acoustic conversion efficiency.

Chapter A.3 PZFlex and MATLAB Code for AuMB Oscillation Simulations

The code in the box below simulates the thermal response of a single AuNR of $35 \text{ nm} \times 10 \text{ nm}$ dimensions placed 10 nm from the liquid/gas interface of the microbubble.

Simulation Code A3.1: PZFlex Simulation Code for AuNR near Gas/Liquid Interface

```
c PZFlex Simulation for AuNR near gas/liquid interface
c Author: Adam Dixon
c Date: 9 Sept 2014

c Specify simulation memory usage
mem 4800
mp omp 12

c Setup model geometry and simulation parameters
symb xdim = 200.e-9 /* half of model X extents, [-200, 200] nm
symb ydim = 200.e-9 /* model Y extents, [0, 200] nm
symb zdim = 200.e-9 /* model Z extents, [0, 200] nm
symb simulation_time = 20e-9 /* Simulation time, 20 ns
symb airExtent = 200.e-9 /* extent of gas core to simulate, 200 nm
symb numexec = 5 /* number of timesteps to execute between data dumps
symb freqdamp = 1.e6

c -----
c                               Step 1: Define Model Geometry Size
c -----

symb x1 = - $xdim
symb x7 = $xdim
symb y1 = 0
symb y3 = $ydim
symb z1 = 0
symb z3 = $zdim

c dx, dy, dz are grid size.
symb dx = 0.5e-9 /* note: multiple dx allows sparser regions of model
symb dx2 = 0.5e-9 /* this is not always implemented
symb dx3 = 0.5e-9
symb dy = $dx
symb dy2 = $dx2
symb dz = $dx
symb dz2 = $dx2

symb fineMesh = 70.e-9
symb fineMeshY = 25.e-9
symb fineMeshZ = 15.e-9
```

```

c Convert spatial extents (x,y,z) to model block (i,j,k)
symb i1 = 1 /* start of boundary
symb i2 = $i1 + 160.e-9 / $dx3 /*160 in gas
symb x2 = $x1 + 160.e-9
symb i3 = $i2 + 30.e-9 / $dx2 /*30 in gas
symb x3 = $x2 + 30.e-9
symb i4 = $i3 + 10.e-9 / $dx /*10 in gas
symb x4 = $x3 + 10.e-9
symb i5 = $i4 + 80.e-9 / $dx /* 80 in water
symb x5 = $x4 + 80.e-9
symb i6 = $i5 + 40.e-9 / $dx2 /* 40 in water
symb x6 = $x5 + 40.e-9
symb i7 = $i6 + 80.e-9 / $dx3 /* 80 in water

symb j1 = 1
symb j2 = $j1 + $fineMeshY / $dy
symb y2 = $y1 + $fineMeshY
symb j3 = $j2 + ( $y3 - $fineMeshY ) / $dy2

symb k1 = 1
symb k2 = $k1 + $fineMeshZ / $dz
symb z2 = $z1 + $fineMeshZ
symb k3 = $k2 + ( $z3 - $fineMeshZ ) / $dz2

symb indgrd = $i7
symb jndgrd = $j3
symb kndgrd = $k3

c Set number of grid nodes in i,j,k
grid $indgrd $jndgrd $kndgrd /*

c Set model geometry
geom
  xcrd $x1 $x2 $i1 $i2
  xcrd $x2 $x3 $i2 $i3
  xcrd $x3 $x4 $i3 $i4
  xcrd $x4 $x5 $i4 $i5
  xcrd $x5 $x6 $i5 $i6
  xcrd $x6 $x7 $i6 $i7

  ycrd $y1 $y2 $j1 $j2
  ycrd $y2 $y3 $j2 $j3

  zcrd $z1 $z2 $k1 $k2
  zcrd $z2 $z3 $k2 $k3
end

symb #read gnr_temp_infn.tabl

c -----
c           Step 2: Define material properties
c -----

matr
c -----
c   water
c -----

```

```

type elas
wvsp off
symb xdens_water = 1000. /* kg/m^3
symb c_water = 1480.
symb xvbulk_water = $c_water * $c_water * $xdens_water
symb xvshear_water = 0.
symb hourglas = 0.01
symb damplin = 0.
symb dampquad = 0.
symb bovera = 5.
prop watr $xdens_water $xvbulk_water $xvshear_water $hourglas $damplin
$dampquad
nwtm watr * 1.0e-3 /* Pa*s viscosity of water
thex watr 4.e-4
thrm watr tabl tabl /* load temp varying thermal props from file

c -----
c   DFB : room temp, decafluorobutane
c -----

type elas
wvsp on
symb hourglas = 0.00
symb damplin = 0.
symb dampquad = 0.
/* Chomas dissertation, pg 17. for density of DFB
/* "Velocity of sound measurements in gaseous perfluorocarbon and their
custom mixtures (108 m/s) V. Vacek, G Hallewell S Lindsay
prop dfb 11.2 108. 0. $hourglas $damplin $dampquad
thex dfb 3.4e-3
thrm dfb tabl tabl /*Liessmann, 1995, Data Compilation of the
Saechsische Olefinwerke Boehlen, Germany. Loaded from a file into model.
nwtm dfb * 1.81e-5 /* Pa*s viscosity of gas, generic

c -----
c   gold : Gold , generic   Kino
c -----

type elas
wvsp on
prop gold 19700. 3240. 1200.
vdmp gold $freqdamp db .4 1.2 1000000. 1. 0.01
thex gold 14.4e-6
thrm gold tabl tabl /* load temp varying thermal props from file

c -----
c   intr: water thermal interface, same as water
c -----

type elas
wvsp off
symb xdens_water = 1000. /* kg/m^3
symb c_water = 1480.
symb xvbulk_water = $c_water * $c_water * $xdens_water
symb xvshear_water = 0.
symb hourglas = 0.01
symb damplin = 0.
symb dampquad = 0.
symb bovera = 5.
prop intr $xdens_water $xvbulk_water $xvshear_water $hourglas $damplin
$dampquad

```

```

nwtm intr * 1.0e-3 /* Pa*s viscosity of water
thex intr 4.e-4
thrm intr tabl tabl /* load temp varying thermal props from file
end

c -----
c           Step 3: Map materials to I,J,K locations
c -----

symb spec_heat_cap = 132.

symb airExtentI = $airExtent / $dx
symb airExtentIIR = $airExtentI + 1
symb distanceNR = 10.e-9 if noexist /*denotes distance of NR to air interface
symb distanceNRI = $airExtentI + $distanceNR / $dx
symb radiusNR = 5.e-9 /*denotes NR radius
symb radiusNRI = $radiusNR / $dx
symb radiusNRIR = $radiusNR + $dx
symb widthNR = 35.e-9 /*denotes NR length
symb widthNR2 = ( $widthNR / 2 - $radiusNR )
symb widthNR2I = ( $widthNR / 2 - $radiusNR ) / $dx
symb edge1NR = $x1 + $airExtent + $distanceNR
symb edge2NR = $edge1NR + 2 * $radiusNR + $dx

symb center = ( $x1 + $airExtent + $distanceNR + $radiusNR )
symb centerI = ( $x1 + $airExtent + $distanceNR + $radiusNR ) / $dx

symb edge1NRI = $edge1NR / $dx
symb edge2NRI = $edge2NR / $dx

symb edge1NRig = $edge1NR / $dx + 1
symb edge2NRig = $edge2NR / $dx - 1

symb plotWaterLeft = ( $distanceNR ) / $dx - 1
symb plotWaterRight = ( $distanceNR + 2 * $radiusNR ) / $dx + 1 + 1
symb plotNP = ( $distanceNR + $radiusNR ) / $dx + 1

symb xAir = $x1 + $airExtent
site
    regn watr /* Whole Grid is water
    blok dfb $x1 $xAir $y1 $y3 $z1 $z3
    cyln intr Y -$widthNR2 $widthNR2 0 $center $radiusNRIR $radiusNRIR
    sphr intr $center $widthNR2 0 $radiusNRIR
    sphr intr $center -$widthNR2 0 $radiusNRIR
    cyln gold Y -$widthNR2 $widthNR2 0 $center $radiusNR $radiusNR
    sphr gold $center $widthNR2 0 $radiusNR
    sphr gold $center -$widthNR2 0 $radiusNR
end

symb dzPlot = 1 * $dx
symb X1 = $x1 + $airExtent + $fineMesh - 50.e-9
symb X2 = $x1 + $airExtent + $fineMesh + 50.e-9

c Graph to make sure model geometry looks okay.
grph
    nview 2 2
    eye 0.000 0.000001 1

```

```

        mirr y on
        mirr z on
        wndo elem $x2 $x6 -$y2 $y2 -$z3 $dzPlot
        line yes
        plot matr
        eye 1 1 1
        mirr y on
        mirr z on
        wndo elem $x1 $x7 -$y3 $dzPlot -$z3 $z3
        plot matr
        end

grph
    nview 1
    eye 0.000 0.000001 1
    mirr y on
    mirr z on
    wndo elem $x2 $x6 -$y2 $y2 -$z3 $dzPlot
    line yes
    plot matr
    end

term

c -----
c           Step 4: Turn off mechanical coupling & turn on thermal solver
c -----

heat
c   slvr drct 0.5  /* other solver options. The cgds recommended by PZFlex
c   slvr splu 0.5
c   slvr cgds 0.5 1.e-3
c   cupl off
c   nlin 1 5 5
c   end

c -----
c           Step 5: Set Thermal boundary and apply heat to shell
c -----

data
    hist drv 12000 drive_7p5mJ.dat /* load laser thermal deposition file
    end

func
    hist drv
    end

data
    hist unit 2
    0. 1.
1.e6 1.

data
    hist tinf 2 * 1. 20. /*makes unit function at 20C ... temperature @
infinity
    0. 1.

```

```

1.e6 1.

data
    hist hcof 2 * 1. 5. /*makes h(T), the heat transfer coefficient
water/air
    0. 1.
1.e6 1.

c Set boundary conditions
boun
    side ymin symm
    side zmin symm

    /* Conductive thermal boundary conditions
    side ymax infn norm 0.0 0.0 0.
    side xmax infn norm 0.0 0.0 0.
    side zmax infn norm 0.0 0.0 0.
    side xmin infn norm 0.0 0.0 0.

    defn tone powr func 1. /* these two commands apply the heat function
    mshp matr gold          /* to the gold material
    end

c -----
c          Step 6: Instruct the model to calculate temperature data
c -----
calc
    max tmpr tmin tmax
    end

c -----
c          Step 7: Specify outputs for flxhst file & plotting
c -----

symb #get { im1 im2 jm1 jm2 km1 km2 } matbound ijk gold

pout
    hist func
    hist tmpr $i1 $i4 1 1 1 1 1 1 1
    end

c -----
c          Step 8: Setup simulation duration parameters & number of loops
c -----

time 10e-11
c time * * 0.9
prcs
set tmpr 25.          /* Set temperature in model to initially be 25C
set told 25.          /* Set temperature in model to initially be 25C

c Compute total number of loops to perform
symb #get { step } timestep /* Get timestep
symb nloops = max ( 1 , nint ( $simulation_time / ( $step * $numexec ) ) )

```

```

symb #msg 1
    timestep = $step, nloops = $nloops

symb execNum = 0
symb dataOut = 5.1e-9 / $step
symb dataOutYet = 0

symb icount0 = 0
symb icount1 = 0

c MAIN SIMULATION LOOP
symb #get { clock0 } wtime
do loopi I 1 $nloops 1 /* for each timestep ....

c Compute thermal diffusion for the current timestep after adding laser
contribution.
exec $numexec
symb #get { clock1 } wtime

symb loopTime = $clock1 - $clock0
symb clock0 = $clock1
symb timeRemain = $loopTime * ( $nloops - $I )
symb timeMin = $timeRemain / 60
symb timeSec = $timeRemain - 60 * $timeMin
    symb #msg 1
        $I of $nloops ... $timeMin m $timeSec s remain
symb execNum = $execNum + $numexec

text filename tmpr7p5mj_$I.txt
data
    cddo tmpr $filename $i1 $i7 $j1 $j3 $k1 $k3
end

symb #msg 1
    Save Complete

c if ( $icount0 eq 1 ) then

grph
    nview 6 2
    plot 1 /* 1 plot heating func

    eye 0.000 0.000001 1
    wndo elem $x1 $x7 -$y3 $y3 $z1 $dzPlot
    plot matr

    eye 0 1 0.00001
    wndo elem $x1 $x7 $y1 $dzPlot -$z3 $z3
    plot matr

    plot $plotWaterLeft $plotNP $plotWaterRight /* 4 plot tmpr curves

    eye 0.000 0.000001 1
    wndo elem $x1 $x7 -$y3 $y3 $z1 $dzPlot
    plot tmpr /* 5 tmpr

```

```

        eye 0 1 0.00001
        wndo elem $x1 $x7 $y1 $dzPlot -$z3 $z3
        plot tmpR

    end

symb icount0 = 0
c endif
symb icount0 = $icount0 + 1

end$ loopi

stop

```

The code below solves Equation 3 – 5 under the assumption of a homogenous gas temperature, T_g , within the microbubble.

Simulation Code A3.2: MATLAB Helper Script for Solving Rayleigh-Plesset Model

```

%MATLAB CODE
%14 Sept 2014
%Adam Dixon

%Script #1: This script sets up parameters sent to ode45 solver
%to solve the Rayleigh Plesset Equation
TPTime = 4E-6; %end time of Rayleigh Plesset Simulation
tstep = 1E-11; %time step
timeVector = [0:tstep:TPTime-tstep]; %simulate time vector
R0 = 1E-6; %resting radius of microbubble [m], 1 um
initialConditions = [R0;0]; %initial conditions at T=0
                        %radius = R0;
                        % dradius/dt = 0;

[t, r ] = ode45('RayleighPlessetEquation', ...
                timeVector, ... %simulation time vector
                [R0;0], ... %initial conditions
                [], ...
                gasTemperature, ... %vector of gas temperature,
                thru
                                %time, derived by PZFlex
                                %simulation
                                tstep, ... %time step
                                R0); %initial radius
%The output [t,r] are vectors of the time, radius, and dr/dt

```

Simulation Code A3.3: MATLAB Rayleigh-Plesset Model, Solved by ODE45

```

%MATLAB CODE
%14 Sept 2014
%Adam Dixon

%Rayleigh Plesset model equations
function rdot = RayleighPlessetEquation(t,r, R, gasTemp, tstep,R0)

%Model Physical Parameters. These can be changed to alter MB
%resonance frequency
T0 = 298;
rhoL = 1E3;
sigma = 0.02;
mu = 0.001;
kappaS = 1E-9; %kg/s
P0 = 101325;
kappa = 1.07;

tindex = floor(t/tstep)+1;

%Compute equation sections
c1 = 1./(rhoL*r(1));
c2 = P0 + (2*sigma/R0);
c3 = (r(1)./R0).^(-3*kappa);
c4 = gasTemp(tindex)/T0;
c5 = P0;
c6 = (3*rhoL/2)*r(2).^2;
c7 = 4*mu*r(2)/r(1);
c8 = 2*sigma/r(1);
c9 = 4*kappaS*r(2)/(r(1)).^2;

rdot = [r(2);
        c1* ( c2*c3*c4 - c5 - c6 - c7 - c8 - c9)];

end

```


References

- 1 Overvelde, M. *et al.* Nonlinear shell behavior of phospholipid-coated microbubbles. *Ultrasound in Medicine & Biology* **36**, 2080-2092, (2010).
- 2 Gorce, J. M., Arditi, M. & Schneider, M. Influence of Bubble Size Distribution on the Echogenicity of Ultrasound Contrast Agents: A Study of SonoVue(TM). *Investigative Radiology* **35**, 661-671, (2000).
- 3 Jain, P. K., Eustis, S. & El-Sayed, M. A. Plasmon Coupling in Nanorod Assemblies: Optical Absorption, Discrete Dipole Approximation Simulation, and Exciton-Coupling Model. *The Journal of Physical Chemistry B* **110**, 18243-18253, (2006).
- 4 Crumrine, R. C. *et al.* Intra-arterial administration of recombinant tissue-type plasminogen activator (rt-PA) causes more intracranial bleeding than does intravenous rt-PA in a transient rat middle cerebral artery occlusion model. *Experimental & translational stroke medicine* **3**, 10, (2011).
- 5 Plech, A., Kotaidis, V., Grésillon, S., Dahmen, C. & von Plessen, G. Laser-induced heating and melting of gold nanoparticles studied by time-resolved x-ray scattering. *Phys. Rev. B* **70**, 195423, (2004).
- 6 Smith-Bindman, R., Miglioretti, D. L. & Larson, E. B. Rising Use Of Diagnostic Medical Imaging In A Large Integrated Health System: The use of imaging has skyrocketed in the past decade, but no one patient population or medical condition is responsible. *Health Aff (Millwood)* **27**, 1491-1502, (2008).
- 7 Cosgrove, D. & Lassau, N. Imaging of perfusion using ultrasound. *Eur J Nucl Med Mol Imaging* **37**, 65-85, (2010).
- 8 Feinstein, S. B. Myocardial perfusion imaging: contrast echocardiography today and tomorrow. *Journal of the American College of Cardiology* **8**, 251-253, (1986).
- 9 Kotopoulis, S., Dimcevski, G., Gilja, O. H., Hoem, D. & Postema, M. Treatment of human pancreatic cancer using combined ultrasound, microbubbles, and gemcitabine: A clinical case study. *Medical Physics* **40**, 072902, (2013).
- 10 Abou-Elkacem, L., Bachawal, S. V. & Willmann, J. K. Ultrasound molecular imaging: Moving toward clinical translation. *Eur J Radiol* **84**, 1685-1693, (2015).

- 11 Ferrara, K. W., Pollard, R. & Borden, M. Ultrasound microbubble contrast agents: fundamentals and application to gene and drug delivery. *Annual review of biomedical engineering* **9**, 415-447, (2007).
- 12 Klivanov, A. L. Microbubble Contrast Agents. *Investigative Radiology* **41**, 354-362, (2006).
- 13 Kindberg, G. M., Tolleshaug, H., Roos, N. & Skotland, T. Hepatic clearance of Sonazoid perfluorobutane microbubbles by Kupffer cells does not reduce the ability of liver to phagocytose or degrade albumin microspheres. *Cell Tissue Res.* **312**, 49-54, (2003).
- 14 Kabalnov, A., Klein, D., Pelura, T., Schutt, E. & Weers, J. Dissolution of multicomponent microbubbles in the bloodstream: 1. theory. *Ultrasound in Medicine & Biology* **24**, 739-749, (1998).
- 15 Bouakaz, A., de Jong, N., Cachard, C. & Jouini, K. On the effect of lung filtering and cardiac pressure on the standard properties of ultrasound contrast agent. *Ultrasonics* **36**, 703-708, (1998).
- 16 Willmann, J. K. *et al.* Targeted microbubbles for imaging tumor angiogenesis: assessment of whole-body biodistribution with dynamic micro-PET in mice. *Radiology* **249**, 212-219, (2008).
- 17 Wei, K. *et al.* Quantification of myocardial blood flow with ultrasound-induced destruction of microbubbles administered as a constant venous infusion. *Circulation* **97**, 473-483, (1998).
- 18 Burns, P. N., Wilson, S. R. & Simpson, D. H. Pulse inversion imaging of liver blood flow: improved method for characterizing focal masses with microbubble contrast. *Investigative Radiology* **35**, 58-71, (2000).
- 19 Chapman, C. S. & Lazenby, J. C. Ultrasound imaging system employing phase inversion subtraction to enhance the image. US5632277 A (1997).
- 20 Eckersley, R. J., Chin, C. T. & Burns, P. N. Optimising phase and amplitude modulation schemes for imaging microbubble contrast agents at low acoustic power. *Ultrasound in medicine & biology* **31**, 213-219, (2005).
- 21 de Jong, N., Bouakaz, A. & Frinking, P. Basic Acoustic Properties of Microbubbles. *Echocardiography* **19**, 229-240, (2002).
- 22 Klivanov, A. L. Ligand-carrying gas-filled microbubbles: ultrasound contrast agents for targeted molecular imaging. *Bioconjug. Chem.* **16**, 9-17, (2005).

- 23 van Wamel, A. *et al.* Vibrating microbubbles poking individual cells: drug transfer into cells via sonoporation. *Journal of controlled release : official journal of the Controlled Release Society* **112**, 149-155, (2006).
- 24 Price, R. J., Skyba, D. M., Kaul, S. & Skalak, T. C. Delivery of colloidal particles and red blood cells to tissue through microvessel ruptures created by targeted microbubble destruction with ultrasound. *Circulation* **98**, 1264-1267, (1998).
- 25 Skyba, D. M., Price, R. J., Linka, A. Z., Skalak, T. C. & Kaul, S. Direct in vivo visualization of intravascular destruction of microbubbles by ultrasound and its local effects on tissue. *Circulation* **98**, 290-293, (1998).
- 26 Klibanov, A. L., Shevchenko, T. I., Raju, B. I., Seip, R. & Chin, C. T. Ultrasound-triggered release of materials entrapped in microbubble-liposome constructs: a tool for targeted drug delivery. *Journal of controlled release : official journal of the Controlled Release Society* **148**, 13-17, (2010).
- 27 Vandenbroucke, R. E., Lentacker, I., Demeester, J., De Smedt, S. C. & Sanders, N. N. Ultrasound assisted siRNA delivery using PEG-siPlex loaded microbubbles. *Journal of controlled release* **126**, 265-273, (2008).
- 28 Kilroy, J. P. *et al.* in *Ultrasonics Symposium (IUS), 2014 IEEE International*. 13-16.
- 29 Phillips, L. C., Dhanaliwala, A. H., Klibanov, A. L., Hossack, J. A. & Wamhoff, B. R. Focused ultrasound-mediated drug delivery from microbubbles reduces drug dose necessary for therapeutic effect on neointima formation—brief report. *Arteriosclerosis, thrombosis, and vascular biology* **31**, 2853-2855, (2011).
- 30 Wang, L. V. & Hu, S. Photoacoustic tomography: in vivo imaging from organelles to organs. *Science (New York, N.Y.)* **335**, 1458-1462, (2012).
- 31 Jansen, K., Wu, M., van der Steen, A. F. W. & van Soest, G. Lipid detection in atherosclerotic human coronaries by spectroscopic intravascular photoacoustic imaging. *Optics Express* **21**, 21472-21484, (2013).
- 32 Sethuraman, S., Amirian, J. H., Litovsky, S. H., Smalling, R. W. & Emelianov, S. Y. Spectroscopic intravascular photoacoustic imaging to differentiate atherosclerotic plaques. *Optics Express* **16**, 3362, (2008).
- 33 Erpelding, T. N. *et al.* Sentinel Lymph Nodes in the Rat: Noninvasive Photoacoustic and US Imaging with a Clinical US System. *Radiology* **256**, 102-110, (2010).

- 34 Vinegoni, C. *et al.* Indocyanine Green Enables Near-Infrared Fluorescence Imaging of Lipid-Rich, Inflamed Atherosclerotic Plaques. *Science Translational Medicine* **3**, 1-20, (2011).
- 35 Kim, J.-W., Galanzha, E. I., Shashkov, E. V., Moon, H.-M. & Zharov, V. P. Golden carbon nanotubes as multimodal photoacoustic and photothermal high-contrast molecular agents. *Nat Nano* **4**, 688-694, (2009).
- 36 Alexandrov, A. V. *et al.* A Pilot Randomized Clinical Safety Study of Sonothrombolysis Augmentation With Ultrasound-Activated Perflutren-Lipid Microspheres for Acute Ischemic. *Stroke* **39**, 1464-1469, (2008).
- 37 Alexandrov, A. V. *et al.* Ultrasound-enhanced systemic thrombolysis for acute ischemic stroke. *N. Engl. J. Med.* **351**, 2170-2178, (2004).
- 38 Molina, C. A. *et al.* Transcranial ultrasound in clinical sonothrombolysis (TUCSON) trial. *Annals of neurology* **66**, 28-38, (2009).
- 39 Dayton, P., Allen, J. & Ferrara, K. The magnitude of radiation force on ultrasound contrast agents. *Journal of the Acoustical Society of America* **112**, 2183- 2192, (2002).
- 40 Acconcia, C., Leung, B. Y. C., Hynynen, K. & Goertz, D. E. Interactions between ultrasound stimulated microbubbles and fibrin clots. *Applied Physics Letters* **103**, 053701, (2013).
- 41 Acconcia, C., Leung, B. Y. C., Manjunath, A. & Goertz, D. E. The Effect of Short Duration Ultrasound Pulses on the Interaction Between Individual Microbubbles and Fibrin Clots. *Ultrasound in Medicine & Biology* **41**, 2774-2782, (2015).
- 42 Acconcia, C., Leung, B. Y. C., Manjunath, A. & Goertz, D. E. Interactions between Individual Ultrasound-Stimulated Microbubbles and Fibrin Clots. *Ultrasound in Medicine & Biology* **40**, 2134-2150, (2014).
- 43 Chen, X., Leeman, J. E., Wang, J., Pacella, J. J. & Villanueva, F. S. New Insights into Mechanisms of Sonothrombolysis Using Ultra-High-Speed Imaging. *Ultrasound in Medicine & Biology* **40**, 258-262, (2014).
- 44 Leighton, T. G. *The Acoustic Bubble*. (Elsevier, 1994).
- 45 Medel, R., Crowley, R. W., McKisic, M. S., Dumont, A. S. & Kassell, N. F. Sonothrombolysis: an emerging modality for the management of stroke. *Neurosurgery* **65**, 979-993; discussion 993, (2009).
- 46 Bader, K. B., Bouchoux, G. & Holland, C. K. Sonothrombolysis. *Advances in experimental medicine and biology* **880**, 339-362, (2016).

- 47 Bader, K. B., Gruber, M. J. & Holland, C. K. Shaken and stirred: mechanisms of ultrasound-enhanced thrombolysis. *Ultrasound Med Biol* **41**, 187-196, (2015).
- 48 Beckman, M. G., Hooper, W. C., Critchley, S. E. & Ortel, T. L. Venous Thromboembolism: A Public Health Concern. *American Journal of Preventive Medicine* **38**, S495-S501, (2010).
- 49 Alesh, I., Kayali, F. & Stein, P. D. Catheter-directed thrombolysis (intrathrombus injection) in treatment of deep venous thrombosis: A systematic review. *Catheterization and Cardiovascular Interventions* **70**, 145-150, (2007).
- 50 Enden, T. *et al.* Long-term outcome after additional catheter-directed thrombolysis versus standard treatment for acute iliofemoral deep vein thrombosis (the CaVenT study): a randomised controlled trial. *The Lancet* **379**, 31-38, (2012).
- 51 Enden, T. *et al.* Catheter-directed thrombolysis vs. anticoagulant therapy alone in deep vein thrombosis: results of an open randomized, controlled trial reporting on short-term patency. *J. Thromb. Haemost.* **7**, 1268-1275, (2009).
- 52 Unnikrishnan, S. & Klibanov, A. L. Microbubbles as ultrasound contrast agents for molecular imaging: preparation and application. *AJR. American journal of roentgenology* **199**, 292-299, (2012).
- 53 Garstecki, P., Fuerstman, M. J., Stone, H. a. & Whitesides, G. M. Formation of droplets and bubbles in a microfluidic T-junction-scaling and mechanism of break-up. *Lab on a chip* **6**, 437-446, (2006).
- 54 Kaya, M., Feingold, S., Hettiarachchi, K., Lee, A. P. & Dayton, P. A. Acoustic responses of monodisperse lipid encapsulated microbubble contrast agents produced by flow focusing. *Bubble Science, Engineering & Technology* **2**, 33-40, (2010).
- 55 Hettiarachchi, K., Lee, A. P., Zhang, S., Feingold, S. & Dayton, P. A. Controllable Microfluidic Synthesis of Multiphase Drug-Carrying Lipospheres for Site-Targeted Therapy. *AiIhE: Biotechnology Progress* **25**, (2009).
- 56 Hettiarachchi, K., Talu, E., Longo, M. L., Dayton, P. A. & Lee, A. P. On-chip generation of microbubbles as a practical technology for manufacturing contrast agents for ultrasonic imaging. *Lab on a Chip* **7**, 463, (2007).

- 57 Dhanaliwala, A. H., Chen, J. L., Wang, S. & Hossack, J. A. Liquid Flooded Flow-Focusing Microfluidic Device for in situ Generation of Monodisperse Microbubbles. *Microfluidics and nanofluidics* **14**, 457-467, (2013).
- 58 Chen, J. L., Dhanaliwala, A. H., Dixon, A. J., Klibanov, A. L. & Hossack, J. A. Synthesis and Characterization of Transiently Stable Albumin-Coated Microbubbles via a Flow-Focusing Microfluidic Device. *Ultrasound in Medicine and Biology* **40**, 400-409, (2014).
- 59 Dixon, A. J., Dhanaliwala, A. H., Chen, J. L. & Hossack, J. A. Enhanced intracellular delivery of a model drug using microbubbles produced by a microfluidic device. *Ultrasound in medicine & biology* **39**, 1267-1276, (2013).
- 60 Diebold, G., Sun, T. & Khan, M. Photoacoustic monopole radiation in one, two, and three dimensions. *Physical Review Letters* **67**, 3384-3387, (1991).
- 61 Bell, A. G. The production of sound by radiant energy. *Science (New York, N.Y.)* **2**, 242-253, (1881).
- 62 Laufer, J., Elwell, C., Delpy, D. & Beard, P. In vitro measurements of absolute blood oxygen saturation using pulsed near-infrared photoacoustic spectroscopy: accuracy and resolution. *Physics in Medicine and Biology* **50**, 4409-4428, (2005).
- 63 Wang, X. *et al.* Noninvasive laser-induced photoacoustic tomography for structural and functional in vivo imaging of the brain. *Nature Biotechnology* **21**, 803-806, (2003).
- 64 Li, P.-C. *et al.* In vivo photoacoustic molecular imaging with simultaneous multiple selective targeting using antibody-conjugated gold nanorods. *Optics express* **16**, 18605-18615, (2008).
- 65 Mallidi, S. *et al.* Multiwavelength photoacoustic imaging and plasmon resonance coupling of gold nanoparticles for selective detection of cancer. *Nano Lett.* **9**, 2825-2831, (2009).
- 66 Homan, K. A. *et al.* Silver Nanoplate Contrast Agents for in Vivo Molecular Photoacoustic Imaging. *ACS Nano* **6**, 641-650, (2012).
- 67 Pan, D. *et al.* Molecular photoacoustic imaging of angiogenesis with integrin-targeted gold nanobeacons. *FASEB Journal* **25**, 875-882, (2011).
- 68 Jokerst, J. V., Cole, A. J., Van de Sompel, D. & Gambhir, S. S. Gold Nanorods for Ovarian Cancer Detection with Photoacoustic Imaging and Resection Guidance via Raman Imaging in Living Mice. *ACS Nano* **6**, 10366-10377, (2012).

- 69 Link, S. & El-Sayed, M. A. Spectral Properties and Relaxation Dynamics of Surface Plasmon Electronic Oscillations in Gold and Silver Nanodots and Nanorods. *The Journal of Physical Chemistry B* **103**, 8410-8426, (1999).
- 70 Razansky, D. *et al.* Multispectral opto-acoustic tomography of deep-seated fluorescent proteins in vivo. *Nature Photonics* **3**, 412-417, (2009).
- 71 Wilson, K., Homan, K. & Emelianov, S. Biomedical photoacoustics beyond thermal expansion using triggered nanodroplet vaporization for contrast-enhanced imaging. *Nat Commun* **3**, 618, (2012).
- 72 Wei, C.-w. *et al.* Nonlinear contrast enhancement in photoacoustic molecular imaging with gold nanosphere encapsulated nanoemulsions. *Applied Physics Letters* **104**, 033701, (2014).
- 73 Hannah, A., Luke, G., Wilson, K., Homan, K. & Emelianov, S. Indocyanine Green-Loaded Photoacoustic Nanodroplets: Dual Contrast Nanoconstructs for Enhanced Photoacoustic and Ultrasound Imaging. *ACS Nano* **8**, 250-259, (2014).
- 74 Strohm, E., Rui, M., Gorelikov, I., Matsuura, N. & Kolios, M. Vaporization of perfluorocarbon droplets using optical irradiation. *Biomedical Optics Express* **2**, 1432-1442, (2011).
- 75 Dove, J. D., Murray, T. W. & Borden, M. A. Enhanced photoacoustic response with plasmonic nanoparticle-templated microbubbles. *Soft Matter* **9**, 7743, (2013).
- 76 Winkler, J. *American National Standard for Safe Use of Lasers (ANSI)*. (2007).
- 77 Xu, R. X. Multifunctional microbubbles and nanobubbles for photoacoustic imaging. *Contrast Media Mol. Imaging* **6**, 401-411, (2011).
- 78 Wang, Y.-H., Liao, A.-H., Chen, J.-H., Wang, C.-R. C. & Li, P.-C. Photoacoustic/ultrasound dual-modality contrast agent and its application to thermotherapy. *Journal of biomedical optics* **17**, 045001, (2012).
- 79 Dove, J. D., Borden, M. A. & Murray, T. W. Optically induced resonance of nanoparticle-loaded microbubbles. *Optics Letters* **39**, 3732-3735, (2014).
- 80 Huynh, E. *et al.* Porphyrin shell microbubbles with intrinsic ultrasound and photoacoustic properties. *Journal of the American Chemical Society* **134**, 16464-16467, (2012).
- 81 Wang, Y.-H. *et al.* Synergistic delivery of gold nanorods using multifunctional microbubbles for enhanced plasmonic photothermal therapy. *Sci. Rep.* **4**, (2014).

- 82 Kotaidis, V., Dahmen, C., Plessen, G. v., Springer, F. & Plech, A. Excitation of nanoscale vapor bubbles at the surface of gold nanoparticles in water. *The Journal of Chemical Physics* **124**, 184702, (2006).
- 83 Kotaidis, V. & Plech, A. Cavitation dynamics on the nanoscale. *Applied Physics Letters* **87**, 213102, (2005).
- 84 Zharov, V. P., Galitovskaya, E. N., Johnson, C. & Kelly, T. Synergistic enhancement of selective nanophotothermolysis with gold nanoclusters: Potential for cancer therapy. *Lasers in Surgery and Medicine* **37**, 219-226, (2005).
- 85 Zharov, V. P., Letfullin, R. R. & Galitovskaya, E. N. Microbubbles-overlapping mode for laser killing of cancer cells with absorbing nanoparticle clusters. *J. Phys. D: Appl. Phys.* **38**, 2571, (2005).
- 86 Niidome, T. *et al.* PEG-modified gold nanorods with a stealth character for in vivo applications. *Journal of Controlled Release* **114**, 343-347, (2006).
- 87 Kass, M., Witkin, A. & Terzopoulos, D. Snakes: Active contour models. *International Journal of Computer Vision* **1**, 321-331, (1988).
- 88 Ghosh, S. K. & Pal, T. Interparticle Coupling Effect on the Surface Plasmon Resonance of Gold Nanoparticles: From Theory to Applications. *Chem. Rev.* **107**, 4797-4862, (2007).
- 89 Lajoinie, G. *et al.* Ultrafast vapourization dynamics of laser-activated polymeric microcapsules. *Nat Commun* **5**, (2014).
- 90 Lapotko, D. Optical excitation and detection of vapor bubbles around plasmonic nanoparticles. *Optics Express* **17**, 2538-2556, (2009).
- 91 Lukianova-Hleb, E. Y., Volkov, A. N., Wu, X. & Lapotko, D. O. Transient Enhancement and Spectral Narrowing of The Photothermal Effect of Plasmonic Nanoparticles Under Pulsed Excitation. *Advanced Materials* **25**, 772-776, (2013).
- 92 Lapotko, D. O., Lukianova, E. & Oraevsky, A. A. Selective laser nano-thermolysis of human leukemia cells with microbubbles generated around clusters of gold nanoparticles. *Lasers in Surgery and Medicine* **38**, 631-642, (2006).
- 93 Egerev, S. *et al.* Acoustic signals generated by laser-irradiated metal nanoparticles. *Applied optics* **48**, C38-45, (2009).
- 94 Chen, Y.-S., Frey, W., Aglyamov, S. & Emelianov, S. Environment-Dependent Generation of Photoacoustic Waves from Plasmonic Nanoparticles. *Small* **8**, 47-52, (2012).

- 95 Ju, H., Roy, R. A. & Murray, T. W. Gold nanoparticle targeted photoacoustic cavitation for potential deep tissue imaging and therapy. *Biomedical Optics Express* **4**, 66, (2013).
- 96 Pitsillides, C. M., Joe, E. K., Wei, X., Anderson, R. R. & Lin, C. P. Selective Cell Targeting with Light-Absorbing Microparticles and Nanoparticles. *Biophys J* **84**, 4023-4032, (2003).
- 97 Hleb, E. Y. *et al.* LANTCET: elimination of solid tumor cells with photothermal bubbles generated around clusters of gold nanoparticles. *Nanomedicine* **3**, 647-667, (2008).
- 98 Link, S., Burda, C., Mohamed, M. B., Nikoobakht, B. & El-Sayed, M. A. Laser Photothermal Melting and Fragmentation of Gold Nanorods: Energy and Laser Pulse-Width Dependence. *J. Phys. Chem. A* **103**, 1165-1170, (1999).
- 99 Chen, Y.-S. *et al.* Enhanced thermal stability of silica-coated gold nanorods for photoacoustic imaging and image-guided therapy. *Optics express* **18**, 8867-8878, (2010).
- 100 Zeng, N. & Murphy, A. B. Heat generation by optically and thermally interacting aggregates of gold nanoparticles under illumination. *Nanotechnology* **20**, 375702, (2009).
- 101 Firouzi, K., Stride, E. & Saffari, N. A theoretical investigation of photoacoustic contrast agents. *The Journal of the Acoustical Society of America* **133**, 3853-3862, (2013).
- 102 Sassaroli, E., Li, K. C. P. & O'Neill, B. E. Linear behavior of a preformed microbubble containing light absorbing nanoparticles: insight from a mathematical model. *The Journal of the Acoustical Society of America* **126**, 2802-2813, (2009).
- 103 Dou, Y., Zhigilei, L. V., Winograd, N. & Garrison, B. J. Explosive Boiling of Water Films Adjacent to Heated Surfaces: A Microscopic Description†. *J. Phys. Chem. A* **105**, 2748-2755, (2001).
- 104 Chomas, J. E., Dayton, P., Allen, J., Morgan, K. & Ferrara, K. W. Mechanisms of contrast agent destruction. *IEEE Transactions on Ultrasonics, Ferroelectrics and Frequency Control* **48**, 232-248, (2001).
- 105 Chomas, J. E., Dayton, P., May, D. & Ferrara, K. Threshold of fragmentation for ultrasonic contrast agents. *Journal of Biomedical Optics* **6**, 141-150, (2001).
- 106 Chomas, J. E. *et al.* Optical observation of contrast agent destruction. *Applied Physics Letters* **77**, 1056-1058, (2000).
- 107 Fan, Z., Liu, H., Mayer, M. & Deng, C. X. Spatiotemporally controlled single cell sonoporation. *Proceedings of the National Academy of Sciences of the United States of America* **109**, 1-4, (2012).

- 108 Chakravarty, P., Qian, W., El-Sayed, M. A. & Prausnitz, M. R. Delivery of molecules into cells using carbon nanoparticles activated by femtosecond laser pulses. *Nat Nano* **5**, 607-611, (2010).
- 109 Hynynen, K., McDannold, N., Sheikov, N. A., Jolesz, F. A. & Vykhodtseva, N. Local and reversible blood–brain barrier disruption by noninvasive focused ultrasound at frequencies suitable for trans-skull sonications. *NeuroImage* **24**, 12-20, (2005).
- 110 Dayton, P. A., Allen, J. S. & Ferrara, K. W. The magnitude of radiation force on ultrasound contrast agents. *The Journal of the Acoustical Society of America* **112**, 2183-2192, (2002).
- 111 Davidson, B. P. *et al.* Detection of antecedent myocardial ischemia with multiselectin molecular imaging. *Journal of the American College of Cardiology* **60**, 1690-1697, (2012).
- 112 Kaufmann, B. a. *et al.* High-resolution myocardial perfusion imaging in mice with high-frequency echocardiographic detection of a depot contrast agent. *Journal of the American Society of Echocardiography : official publication of the American Society of Echocardiography* **20**, 136-143, (2007).
- 113 Kaufmann, B. A. *et al.* Molecular imaging of inflammation in atherosclerosis with targeted ultrasound detection of vascular cell adhesion molecule-1. *Circulation* **116**, 276-284, (2007).
- 114 Prentice, P., Cuschieri, A., Dholakia, K., Prausnitz, M. & Campbell, P. Membrane disruption by optically controlled microbubble cavitation. *Nature Physics* **1**, 107-110, (2005).
- 115 Sadauskas, E. *et al.* Protracted elimination of gold nanoparticles from mouse liver. *Nanomedicine: Nanotechnology, Biology and Medicine* **5**, 162-169, (2009).
- 116 Sadauskas, E. *et al.* Kupffer cells are central in the removal of nanoparticles from the organism. *Part Fibre Toxicol* **4**, 10, (2007).
- 117 Longmire, M., Choyke, P. L. & Kobayashi, H. Clearance properties of nano-sized particles and molecules as imaging agents: considerations and caveats. *Nanomedicine* **3**, 703-717, (2008).
- 118 Oelze, M. L., Zachary, J. F. & O'Brien, W. D. Characterization of tissue microstructure using ultrasonic backscatter: Theory and technique for optimization using a Gaussian form factor. *The Journal of the Acoustical Society of America* **112**, 1202, (2002).

- 119 Feinstein, S. B. Contrast ultrasound imaging of the carotid artery vasa vasorum and atherosclerotic plaque neovascularization. *Journal of the American College of Cardiology* **48**, 236-243, (2006).
- 120 Diebold, G. J., Beveridge, A. C. & Hamilton, T. J. The photoacoustic effect generated by an incompressible sphere. *The Journal of the Acoustical Society of America* **112**, 1780, (2002).
- 121 Kumon, R. E., Deng, C. X. & Wang, X. Frequency-domain analysis of photoacoustic imaging data from prostate adenocarcinoma tumors in a murine model. *Ultrasound in medicine & biology* **37**, 834-839, (2011).
- 122 Xu, G. *et al.* Photoacoustic spectrum analysis for microstructure characterization in biological tissue: A feasibility study. *Applied physics letters* **101**, 221102, (2012).
- 123 Dixon, A. J., Hu, S., Klibanov, A. L. & Hossack, J. A. Oscillatory Dynamics and In Vivo Photoacoustic Imaging Performance of Plasmonic Nanoparticle-Coated Microbubbles. *Small* **11**, 3066-3077, (2015).
- 124 Plesset, M. S. & Prosperetti, A. Bubble Dynamics and Cavitation. *Annual Review of Fluid Mechanics* **9**, 145-185, (1977).
- 125 Pustovalov, V. K. Theoretical study of heating of spherical nanoparticle in media by short laser pulses. *Chemical Physics* **308**, 103-108, (2005).
- 126 Pustovalov, V. K. & Babenko, V. A. Computer modeling of optical properties of gold ellipsoidal nanoparticles at laser radiation wavelengths. *Laser Phys. Lett.* **2**, 84, (2005).
- 127 Sassaroli, E., Li, K. C. P. & O'Neill, B. E. Numerical investigation of heating of a gold nanoparticle and the surrounding microenvironment by nanosecond laser pulses for nanomedicine applications. *Physics in Medicine and Biology* **54**, 5541, (2009).
- 128 Ekici, O. *et al.* Thermal analysis of gold nanorods heated with femtosecond laser pulses. *J. Phys. D: Appl. Phys.* **41**, 185501, (2008).
- 129 Patil, A. V., Reynolds, P. & Hossack, J. A. A non-linear three-dimensional model for quantifying microbubble dynamics. *The Journal of the Acoustical Society of America* **127**, EL80-86, (2010).
- 130 Voller, V. R., Swaminathan, C. R. & Thomas, B. G. Fixed grid techniques for phase change problems: A review. *Int. J. Numer. Meth. Engng.* **30**, 875-898, (1990).

- 131 Liessmann, G., Schmidt, W. & Reiffarth, S. Recommended Thermophysical Data; data compilation of the Saechsische Olefinwerke. *Boehlen, Germany*, (1995).
- 132 E.W. Lemmon, M. O. M. & Friend, D. G. in *NIST Chemistry WebBook, NIST Standard Reference Database Number 69* (National Institute of Standards and Technology).
- 133 Brennen, C. E. *Fundamentals of Multiphase Flow*. (Cambridge University Press, 2005).
- 134 Brennen, C. E. *Cavitation and Bubble Dynamics*. (Oxford University Press, 1995).
- 135 de Gennes, P. G. Polymers at an interface; a simplified view. *Advances in Colloid and Interface Science* **27**, 189-209, (1987).
- 136 Park, J., Huang, J., Wang, W., Murphy, C. J. & Cahill, D. G. Heat Transport between Au Nanorods, Surrounding Liquids, and Solid Supports. *Journal of Physical Chemistry C* **116**, 26335-26341, (2012).
- 137 Link, S., Burda, C., Wang, Z. L. & El-Sayed, M. A. Electron dynamics in gold and gold–silver alloy nanoparticles: The influence of a nonequilibrium electron distribution and the size dependence of the electron–phonon relaxation. *The Journal of Chemical Physics* **111**, 1255-1264, (1999).
- 138 Jain, P. K., Lee, K. S., El-Sayed, I. H. & El-Sayed, M. A. Calculated Absorption and Scattering Properties of Gold Nanoparticles of Different Size, Shape, and Composition: Applications in Biological Imaging and Biomedicine. *The Journal of Physical Chemistry B* **110**, 7238-7248, (2006).
- 139 Lin, Z. *et al.* Electron-phonon coupling and electron heat capacity of metals under conditions of strong electron-phonon nonequilibrium. *Phys. Rev. B* **77**, 075133, (2008).
- 140 Barrat, J.-L. & Chiaruttini, F. Kapitza resistance at the liquid—solid interface. *Molecular Physics* **101**, 1605-1610, (2003).
- 141 Bayer, C. L., Nam, S. Y., Chen, Y.-S. & Emelianov, S. Y. Photoacoustic signal amplification through plasmonic nanoparticle aggregation. *Journal of Biomedical Optics* **18**, (2013).
- 142 Nigmatulin, R. I., Akhatov, I. S. & Vakhitova, N. K. Forced oscillations of a gas bubble in a spherical volume of a compressible liquid. *J Appl Mech Tech Phys* **40**, 285-291, (1999).
- 143 Nigmatulin, R. I. & Khabeev, N. S. Heat exchange between a gas bubble and a liquid. *Fluid Dyn* **9**, 759-764, (1974).

- 144 Nigmatulin, R. I., Khabeev, N. S. & Nagiev, F. B. Dynamics, Heat and Mass Transfer of Vapour-Gas Bubbles in a Liquid. *International Journal of Heat and Mass Transfer* **24**, 1033-1044, (1981).
- 145 Gaitan, D. F., Crum, L. A., Church, C. C. & Roy, R. A. Sonoluminescence and bubble dynamics for a single, stable, cavitation bubble. *The Journal of the Acoustical Society of America* **91**, 3166-3183, (1992).
- 146 Prosperetti, A., Crum, L. A. & Commander, K. W. Nonlinear bubble dynamics. *The Journal of the Acoustical Society of America* **83**, 502-514, (1988).
- 147 Leekumjorn, S. & Sum, A. K. Molecular Characterization of Gel and Liquid-Crystalline Structures of Fully Hydrated POPC and POPE Bilayers. *The Journal of Physical Chemistry B* **111**, 6026-6033, (2007).
- 148 Marrink, S. J., Risselada, J. & Mark, A. E. Simulation of gel phase formation and melting in lipid bilayers using a coarse grained model. *Chem. Phys. Lipids* **135**, 223-244, (2005).
- 149 Tissue plasminogen activator for acute ischemic stroke. The National Institute of Neurological Disorders and Stroke rt-PA Stroke Study Group. *N. Engl. J. Med.* **333**, 1581-1587, (1995).
- 150 Watson, L. I. & Armon, M. P. Thrombolysis for acute deep vein thrombosis. *Cochrane Database Syst Rev*, CD002783, (2004).
- 151 Schwamm, L. H. *et al.* Temporal Trends in Patient Characteristics and Treatment With Intravenous Thrombolysis Among Acute Ischemic Stroke Patients at Get With the Guidelines-Stroke Hospitals. *Circ Cardiovasc Qual Outcomes*, (2013).
- 152 Enden, T. *et al.* Catheter-directed Venous Thrombolysis in acute iliofemoral vein thrombosis--the CaVenT study: rationale and design of a multicenter, randomized, controlled, clinical trial (NCT00251771). *Am. Heart J.* **154**, 808-814, (2007).
- 153 Broderick, J. P. & Schroth, G. What the SWIFT and TREVO II Trials Tell Us About the Role of Endovascular Therapy for Acute. *Stroke* **44**, 1761-1764, (2013).
- 154 Nogueira, R. G. *et al.* Trevo versus Merci retrievers for thrombectomy revascularisation of large vessel occlusions in acute ischaemic stroke (TREVO 2): a randomised trial. *The Lancet* **380**, 1231-1240, (2012).
- 155 Vedantham, S. *et al.* Rationale and Design of the ATTRACT Study - A Multicenter Randomized Trial to Evaluate Pharmacomechanical Catheter-Directed Thrombolysis for

- the Prevention of Post-Thrombotic Syndrome in Patients with Proximal Deep Vein Thrombosis. *Am. Heart J.* **165**, 523-530.e523, (2013).
- 156 Saver, J. L. *et al.* Stent-Retriever Thrombectomy after Intravenous t-PA vs. t-PA Alone in Stroke. *New England Journal of Medicine* **372**, 2285-2295, (2015).
- 157 Saver, J. L. *et al.* Solitaire flow restoration device versus the Merci Retriever in patients with acute ischaemic stroke (SWIFT): a randomised, parallel-group, non-inferiority trial. *The Lancet* **380**, 1241-1249, (2012).
- 158 Zaidat, O. O. *et al.* Recommendations on Angiographic Revascularization Grading Standards for Acute Ischemic Stroke A Consensus Statement. *Stroke* **44**, 2650-2663, (2013).
- 159 Chueh, J.-Y. *et al.* Reduction in Distal Emboli With Proximal Flow Control During Mechanical Thrombectomy A Quantitative In Vitro Study. *Stroke* **44**, 1396-1401, (2013).
- 160 Daffertshofer, M. *et al.* Transcranial low-frequency ultrasound-mediated thrombolysis in brain ischemia: increased risk of hemorrhage with combined ultrasound and tissue plasminogen activator: results of a phase II clinical trial. *Stroke* **36**, 1441-1446, (2005).
- 161 Schrijver, A. M. *et al.* Dutch randomized trial comparing standard catheter-directed thrombolysis versus ultrasound-accelerated thrombolysis for thromboembolic infrainguinal disease (DUET): design and rationale. *Trials* **12**, 20, (2011).
- 162 Wang, S., Dhanaliwala, A. H., Chen, J. L. & Hossack, J. A. Production rate and diameter analysis of spherical monodisperse microbubbles from two-dimensional, expanding-nozzle flow-focusing microfluidic devices. *Biomicrofluidics* **7**, 014103, (2013).
- 163 Yeo, J. C., Kenry & Lim, C. T. Emergence of microfluidic wearable technologies. *Lab Chip* **16**, 4082-4090, (2016).
- 164 Scholten, K. & Meng, E. Materials for microfabricated implantable devices: a review. *Lab Chip* **15**, 4256-4272, (2015).
- 165 Johnson, D. G. *et al.* Ultrathin silicon membranes for wearable dialysis. *Advances in chronic kidney disease* **20**, 508-515, (2013).
- 166 Castro-Hernández, E., Hoeve, W. v., Lohse, D. & Gordillo, J. M. Microbubble generation in a co-flow device operated in a new regime. *Lab on a Chip* **11**, 2023-2029, (2011).

- 167 Dietrich, N., Poncin, S., Midoux, N. & Li, H. Z. Bubble formation dynamics in various flow-focusing microdevices. *Langmuir : the ACS journal of surfaces and colloids* **24**, 13904-13911, (2008).
- 168 Gañán-Calvo, A. M. & Gordillo, J. M. Perfectly Monodisperse Microbubbling by Capillary Flow Focusing. *Physical Review Letters* **87**, 274501, (2001).
- 169 Garstecki, P. *et al.* Formation of monodisperse bubbles in a microfluidic flow-focusing device. *Applied Physics Letters* **85**, 2649-2651, (2004).
- 170 van Hoeve, W., Dollet, B., Versluis, M. & Lohse, D. Microbubble formation and pinch-off scaling exponent in flow-focusing devices. *Physics of Fluids* **23**, 092001, (2011).
- 171 Jung, H. C., Lu, W., Wang, S., Lee, L. J. & Hu, X. Etching of Pyrex glass substrates by inductively coupled plasma reactive ion etching for micro/nanofluidic devices. *Journal of Vacuum Science & Technology B* **24**, 3162-3164, (2006).
- 172 Wible, J. H. *et al.* Inhaled gases affect the ultrasound contrast produced by Albunex in anesthetized dogs. *Journal of the American Society of Echocardiography : official publication of the American Society of Echocardiography* **9**, 442-451, (1996).
- 173 Kearon, C. Natural History of Venous Thromboembolism. *Circulation* **107**, I-22-I-30, (2003).
- 174 Go, A. S. *et al.* Heart Disease and Stroke Statistics—2014 Update A Report From the American Heart Association. *Circulation* **129**, e28-e292, (2014).
- 175 Kwiatkowski, T. G. *et al.* Effects of Tissue Plasminogen Activator for Acute Ischemic Stroke at One Year. *New England Journal of Medicine* **340**, 1781-1787, (1999).
- 176 Marler, J. Tissue Plasminogen Activator for Acute Ischemic Stroke. *New England Journal of Medicine* **333**, 1581-1588, (1995).
- 177 Weiss, H. L. *et al.* Mechanical clot damage from cavitation during sonothrombolysis. *The Journal of the Acoustical Society of America* **133**, 3159-3175, (2013).
- 178 Goertz, D., Acconcia, C. & Leung, B. Microscale interactions between ultrasound stimulated microbubbles and the fibrin networks of clots. *The Journal of the Acoustical Society of America* **138**, 1819-1819, (2015).
- 179 Ahadi, G. *et al.* Transcranial sonothrombolysis using high-intensity focused ultrasound: impact of increasing output power on clot fragmentation. *Journal of Therapeutic Ultrasound* **1**, 22, (2013).

- 180 Baron, C., Aubry, J.-F., Tanter, M., Meairs, S. & Fink, M. Simulation of intracranial acoustic fields in clinical trials of sonothrombolysis. *Ultrasound in Medicine & Biology* **35**, 1148-1158, (2009).
- 181 Brown, A. T. *et al.* Microbubbles Improve Sonothrombolysis In Vitro and Decrease Hemorrhage In Vivo in a Rabbit Stroke Model. *Investigative radiology* **46**, (2011).
- 182 Chuang, Y.-H., Cheng, P.-W. & Li, P.-C. Combining radiation force with cavitation for enhanced sonothrombolysis. *IEEE Transactions on Ultrasonics, Ferroelectrics, and Frequency Control* **60**, -, (2013).
- 183 Flores, R., Hennings, L. J., Lowery, J. D., Brown, A. T. & Culp, W. C. Microbubble Augmented Ultrasound Sonothrombolysis Decreases Intracranial Hemorrhage in a Rabbit Model of Acute Ischemic Stroke. *Investigative radiology* **46**, 419-424, (2011).
- 184 Hitchcock, K. E. *et al.* Ultrasound-Enhanced rt-PA Thrombolysis in an ex vivo Porcine Carotid Artery Model. *Ultrasound in Medicine & Biology* **37**, 1240-1251, (2011).
- 185 Petit, B. *et al.* Sonothrombolysis: the contribution of stable and inertial cavitation to clot lysis. *Ultrasound Med Biol* **41**, 1402-1410, (2015).
- 186 Petit, B. *et al.* In vitro sonothrombolysis of human blood clots with BR38 microbubbles. *Ultrasound in medicine & biology* **38**, 1222-1233, (2012).
- 187 Petit, B. *et al.* Fibrin degradation during sonothrombolysis – Effect of ultrasound, microbubbles and tissue plasminogen activator. *Journal of Drug Delivery Science and Technology* **25**, 29-35, (2015).
- 188 Schleicher, N. *et al.* Sonothrombolysis with BR38 Microbubbles Improves Microvascular Patency in a Rat Model of Stroke. *PLoS ONE* **11**, e0152898, (2016).
- 189 Tsivgoulis, G. *et al.* Safety and Efficacy of Ultrasound-Enhanced Thrombolysis A Comprehensive Review and Meta-Analysis of Randomized and Nonrandomized Studies. *Stroke* **41**, 280-287, (2010).
- 190 Borrelli, M. J. *et al.* Influences of microbubble diameter and ultrasonic parameters on in vitro sonothrombolysis efficacy. *Journal of vascular and interventional radiology : JVIR* **23**, 1677-1684.e1671, (2012).
- 191 Zhou, Y., Yang, K., Cui, J., Ye, J. Y. & Deng, C. X. Controlled permeation of cell membrane by single bubble acoustic cavitation. *Journal of Controlled Release* **157**, 103-111, (2012).

- 192 Choi, J. J. *et al.* Microbubble-size dependence of focused ultrasound-induced blood-brain barrier opening in mice in vivo. *IEEE transactions on bio-medical engineering* **57**, 145-154, (2010).
- 193 Dhanaliwala, A. H. *et al.* In vivo imaging of microfluidic-produced microbubbles. *Biomed Microdevices* **17**, 23, (2015).
- 194 Dixon, A. J. *et al.* Microbubble-mediated intravascular ultrasound imaging and drug delivery. *IEEE Transactions on Ultrasonics, Ferroelectrics, and Frequency Control* **62**, 1674-1685, (2015).
- 195 Datta, S. *et al.* Correlation of Cavitation with Ultrasound Enhancement of Thrombolysis. *Ultrasound in medicine & biology* **32**, 1257-1267, (2006).
- 196 Liebeskind, D. S. *et al.* CT and MRI early vessel signs reflect clot composition in acute stroke. *Stroke* **42**, 1237-1243, (2011).
- 197 Roessler, F. C. *et al.* The platelet-rich plasma clot: a standardized in-vitro clot formation protocol for investigations of sonothrombolysis under physiological flows. *Blood Coagulation & Fibrinolysis July 2011* **22**, 407-415, (2011).
- 198 Kim, J. S. *et al.* Volumetric quantification of in vitro sonothrombolysis with microbubbles using high-resolution optical coherence tomography. *Journal of Biomedical Optics* **17**, 0705021-0705023, (2012).
- 199 Cho, K. H., Kim, J. S., Kwon, S. U., Cho, A. H. & Kang, D. W. Significance of susceptibility vessel sign on T2*-weighted gradient echo imaging for identification of stroke subtypes. *Stroke* **36**, 2379-2383, (2005).
- 200 Ribo, M. *et al.* Intra-arterial Administration of Microbubbles and Continuous 2-MHz Ultrasound Insonation to Enhance Intra-arterial Thrombolysis. *Journal of Neuroimaging* **20**, 224-227, (2010).
- 201 Talu, E. *et al.* Maintaining monodispersity in a microbubble population formed by flow-focusing. *Langmuir : the ACS journal of surfaces and colloids* **24**, 1745-1749, (2008).
- 202 Muth, C. M. & Shank, E. S. Gas Embolism. *New England Journal of Medicine* **342**, 476-482, (2000).
- 203 Helps, S. C., Meyer-Witting, M., Reilly, P. L. & Gorman, D. F. Increasing doses of intracarotid air and cerebral blood flow in rabbits. *Stroke* **21**, 1340-1345, (1990).

- 204 Helps, S. C., Parsons, D. W., Reilly, P. L. & Gorman, D. F. The effect of gas emboli on
rabbit cerebral blood flow. *Stroke* **21**, 94-99, (1990).
- 205 Brujan, E. A., Keen, G. S., Vogel, A. & Blake, J. R. The final stage of the collapse of a
cavitation bubble close to a rigid boundary. *Physics of Fluids (1994-present)* **14**, 85-92,
(2002).
- 206 Brujan, E.-A. & Matsumoto, Y. Collapse of micrometer-sized cavitation bubbles near a
rigid boundary. *Microfluidics and Nanofluidics* **13**, 957-966, (2012).
- 207 BRUJAN, E.-A. & VOGEL, A. Stress wave emission and cavitation bubble dynamics by
nanosecond optical breakdown in a tissue phantom. *Journal of Fluid Mechanics* **558**, 281-
308, (2006).
- 208 Krasovitski, B. & Kimmel, E. Shear stress induced by a gas bubble pulsating in an
ultrasonic field near a wall. *IEEE transactions on ultrasonics, ferroelectrics, and frequency
control* **51**, 973-979, (2004).
- 209 Wu, J. Theoretical study on shear stress generated by microstreaming surrounding contrast
agents attached to living cells. *Ultrasound in Medicine & Biology* **28**, 125-129, (2002).
- 210 Marmottant, P. & Hilgenfeldt, S. A bubble-driven microfluidic transport element for
bioengineering. *Proceedings of the National Academy of Sciences of the United States of
America* **101**, 9523-9527, (2004).
- 211 Brujan, E. A., Ikeda, T. & Matsumoto, Y. Jet formation and shock wave emission during
collapse of ultrasound-induced cavitation bubbles and their role in the therapeutic
applications of high-intensity focused ultrasound. *Physics in Medicine and Biology* **50**,
4797, (2005).
- 212 Ohl, C.-D. *et al.* Sonoporation from jetting cavitation bubbles. *Biophys J* **91**, 4285-4295,
(2006).
- 213 Johnson, K. A. *et al.* Experimental verification of theoretical equations for acoustic
radiation force on compressible spherical particles in traveling waves. *Physical review. E*
93, 053109, (2016).
- 214 Marmottant, P. *et al.* A model for large amplitude oscillations of coated bubbles accounting
for buckling and rupture. *The Journal of the Acoustical Society of America* **118**, 3499,
(2005).
- 215 Neppiras, E. A. Acoustic Cavitation. *Phys. Reports* **61**, 159-251, (1980).

- 216 O'Reilly, M. A., Huang, Y. & Hynynen, K. Impact of standing wave effects on transcranial focused ultrasound disruption of the blood-brain barrier in a rat model. *Physics in medicine and biology* **55**, 5251-5267, (2010).
- 217 Bhatia, R. *et al.* Low rates of acute recanalization with intravenous recombinant tissue plasminogen activator in ischemic stroke: real-world experience and a call for action. *Stroke* **41**, 2254-2258, (2010).
- 218 Tomsick, T. TIMI, TIBI, TICI: I Came, I Saw, I Got Confused. *AJNR Am J Neuroradiol* **28**, 382-384, (2007).
- 219 Berkhemer, O. A. *et al.* A Randomized Trial of Intraarterial Treatment for Acute Ischemic Stroke. *New England Journal of Medicine* **372**, 11-20, (2015).
- 220 Goyal, M. *et al.* Randomized Assessment of Rapid Endovascular Treatment of Ischemic Stroke. *New England Journal of Medicine* **Epub**, (2015).
- 221 Jovin, T. G. *et al.* Thrombectomy within 8 Hours after Symptom Onset in Ischemic Stroke. *New England Journal of Medicine* **372**, 2296-2306, (2015).
- 222 Campbell, B. C. V. *et al.* Endovascular Therapy for Ischemic Stroke with Perfusion-Imaging Selection. *New England Journal of Medicine* **Epub**, (2015).
- 223 Powers, W. J. *et al.* 2015 AHA/ASA Focused Update of the 2013 Guidelines for the Early Management of Patients With Acute Ischemic Stroke Regarding Endovascular Treatment: A Guideline for Healthcare Professionals From the American Heart Association/American Stroke Association. *Stroke; a journal of cerebral circulation*, (2015).
- 224 Sakuma, T., Leong-Poi, H., Fisher, N. G., Goodman, N. C. & Kaul, S. Further insights into the no-reflow phenomenon after primary angioplasty in acute myocardial infarction: the role of microthromboemboli. *J Am Soc Echocardiogr* **16**, 15-21, (2003).
- 225 Bekkers, S. C., Yazdani, S. K., Virmani, R. & Waltenberger, J. Microvascular obstruction: underlying pathophysiology and clinical diagnosis. *J Am Coll Cardiol* **55**, 1649-1660, (2010).
- 226 Broderick, J. P. *et al.* Endovascular Therapy after Intravenous t-PA versus t-PA Alone for Stroke. *New England Journal of Medicine* **368**, 893-903, (2013).
- 227 Jayaraman, M. V., Grossberg, J. A., Meisel, K. M., Shaikhouni, A. & Silver, B. The clinical and radiographic importance of distinguishing partial from near-complete reperfusion

- following intra-arterial stroke therapy. *AJNR. American journal of neuroradiology* **34**, 135-139, (2013).
- 228 Alexandrov, A. V. *et al.* Ultrasound-enhanced systemic thrombolysis for acute ischemic stroke. *N Engl J Med* **351**, 2170-2178, (2004).
- 229 Alexandrov, A. V. *et al.* A pilot randomized clinical safety study of sonothrombolysis augmentation with ultrasound-activated perflutren-lipid microspheres for acute ischemic stroke. *Stroke* **39**, 1464-1469, (2008).
- 230 Dinia, M. R., M. Ribo, E. Santamarina, O. Maisterra, R. Delgado-Mederos, & J. Alvarez-Sabin, J. M., C. Molina,. Timing of microbubble-enhanced sonothrombolysis strongly predicts intracranial haemorrhage in acute ischaemic stroke. *European Stroke Conference*, (2008).
- 231 Molina, C. A. *et al.* Microbubble administration accelerates clot lysis during continuous 2-MHz ultrasound monitoring in stroke patients treated with intravenous tissue plasminogen activator. *Stroke; a journal of cerebral circulation* **37**, 425-429, (2006).
- 232 Molina, C. A. *et al.* Transcranial ultrasound in clinical sonothrombolysis (TUCSON) trial. *Annals of neurology* **66**, 28-38, (2009).
- 233 Wu, J. Theoretical study on shear stress generated by microstreaming surrounding contrast agents attached to living cells. *Ultrasound Med Biol* **28**, 125-129, (2002).
- 234 Marmottant, P. & Hilgenfeldt, S. Controlled vesicle deformation and lysis by single oscillating bubbles. *Nature* **423**, 153-156, (2003).
- 235 Marmottant, P., Versluis, M., de Jong, N., Hilgenfeldt, S. & Lohse, D. High-speed imaging of an ultrasound-driven bubble in contact with a wall: “Narcissus” effect and resolved acoustic streaming. *Exp Fluids* **41**, 147-153, (2006).
- 236 Longuet-Higgins, M. S. Viscous streaming from an oscillating spherical bubble. *Proceedings of the Royal Society of London A: Mathematical, Physical and Engineering Sciences* **454**, 725-742, (1998).
- 237 Yueh-Hsun, C., Po-Wen, C. & Pai-Chi, L. Combining radiation force with cavitation for enhanced sonothrombolysis. *Ultrasonics, Ferroelectrics and Frequency Control, IEEE Transactions on* **60**, (2013).
- 238 Shortencarier, M. J. *et al.* A method for radiation-force localized drug delivery using gas-filled lipospheres. *IEEE Trans Ultrason Ferroelectr Freq Control* **51**, 822-831, (2004).

- 239 Brujan, E. A., Ikeda, T. & Matsumoto, Y. Jet formation and shock wave emission during collapse of ultrasound-induced cavitation bubbles and their role in the therapeutic applications of high-intensity focused ultrasound. *Phys Med Biol* **50**, 4797-4809, (2005).
- 240 Li, L. & Zuo, Z. Isoflurane preconditioning improves short-term and long-term neurological outcome after focal brain ischemia in adult rats. *Neuroscience* **164**, 497-506, (2009).
- 241 Haelewyn, B., Risso, J. J. & Abraini, J. H. in *J Cereb Blood Flow Metab* Vol. 30 900-903 (2010).
- 242 Daffertshofer, M. *et al.* Efficacy of sonothrombolysis in a rat model of embolic ischemic stroke. *Neuroscience Letters* **361**, 115-119, (2004).
- 243 Sokal, R. R. & Rohlf, F. J. *Biometry*. 4 edn, (W. H. Freeman, 2012).
- 244 Helfield, B., Chen, X., Watkins, S. C. & Villanueva, F. S. Biophysical insight into mechanisms of sonoporation. *Proc Natl Acad Sci U S A*, (2016).
- 245 Helps, S. C. & Gorman, D. F. Air embolism of the brain in rabbits pretreated with mechlorethamine. *Stroke* **22**, 351-354, (1991).
- 246 Singh, P., Kaur, R. & Kaur, A. Clot composition and treatment approach to acute ischemic stroke: The road so far. *Ann Indian Acad Neurol* **16**, 494-497, (2013).
- 247 Culp, W. C. *et al.* Successful microbubble sonothrombolysis without tissue-type plasminogen activator in a rabbit model of acute ischemic stroke. *Stroke* **42**, 2280-2285, (2011).
- 248 Naghavi, M. & Falk, E. *Asymptomatic Atherosclerosis: From Vulnerable Plaque to Vulnerable Patient*. (Humana Press, 2010).
- 249 Fayad, Z. A. & Fuster, V. Clinical Imaging of the High-Risk or Vulnerable Atherosclerotic Plaque. *Circulation Research* **89**, 305-316, (2001).
- 250 Takano, M. *et al.* Mechanical and structural characteristics of vulnerable plaques: analysis by coronary angioscopy and intravascular ultrasound. *Journal of the American College of Cardiology* **38**, 99-104, (2001).
- 251 Schaar, J. A. *et al.* Characterizing vulnerable plaque features with intravascular elastography. *Circulation* **108**, 2636-2641, (2003).
- 252 Schaar, J. A. *et al.* Intravascular Palpography for High-Risk Vulnerable Plaque Assessment. *Herz* **28**, 488-495, (2003).

- 253 Schaar, J. a. *et al.* Terminology for high-risk and vulnerable coronary artery plaques. Report of a meeting on the vulnerable plaque, June 17 and 18, 2003, Santorini, Greece. *Eur Heart J* **25**, 1077-1082, (2004).
- 254 Moreno, P. R. Vulnerable plaque: definition, diagnosis, and treatment. *Cardiology clinics* **28**, 1-30, (2010).
- 255 Moreno, P. R. *et al.* Detection of lipid pool, thin fibrous cap, and inflammatory cells in human aortic atherosclerotic plaques by near-infrared spectroscopy. *Circulation* **105**, 923-927, (2002).
- 256 Schaar, J. A. *et al.* Incidence of high-strain patterns in human coronary arteries: assessment with three-dimensional intravascular palpography and correlation with clinical presentation. *Circulation* **109**, 2716-2719, (2004).
- 257 Nair, A. *et al.* Coronary Plaque Classification With Intravascular Ultrasound Radiofrequency Data Analysis. *Circulation* **106**, 2200-2206, (2002).
- 258 Yabushita, H. *et al.* Characterization of human atherosclerosis by optical coherence tomography. *Circulation* **106**, 1640-1645, (2002).
- 259 de Korte, C. L., Pasterkamp, G., van der Steen, A. F. W., Woutman, H. A. & Bom, N. Characterization of Plaque Components With Intravascular Ultrasound Elastography in Human Femoral and Coronary Arteries In Vitro. *Circulation* **102**, 617-623, (2000).
- 260 Katouzian, A., Sathyanarayana, S., Baseri, B., Konofagou, E. E. & Carlier, S. G. Challenges in atherosclerotic plaque characterization with intravascular ultrasound (IVUS): from data collection to classification. *IEEE Transactions on Information Technology in Biomedicine* **12**, 315-327, (2008).
- 261 Yin, J. *et al.* Novel combined miniature optical coherence tomography ultrasound probe for in vivo intravascular imaging. *Journal of biomedical optics* **16**, 060505, (2011).
- 262 Kolodgie, F. D. *et al.* Localization of apoptotic macrophages at the site of plaque rupture in sudden coronary death. *The American Journal of Pathology* **157**, 1259-1268, (2000).
- 263 Sangiorgi, G. M., Clementi, F., Cola, C. & Biondi-Zoccai, G. Plaque vulnerability and related coronary event prediction by intravascular ultrasound with virtual histology: "it's a long way to tipperary"? *Catheterization and Cardiovascular Interventions* **70**, 203-210, (2007).

- 264 Karpouk, A. B., Wang, B. & Emelianov, S. Y. Development of a catheter for combined intravascular ultrasound and photoacoustic imaging. *The Review of Scientific Instruments* **81**, 014901, (2010).
- 265 Gardner, C. M. *et al.* Detection of lipid core coronary plaques in autopsy specimens with a novel catheter-based near-infrared spectroscopy system. *JACC. Cardiovascular imaging* **1**, 638-648, (2008).
- 266 Calton, M. A., Vinegoni, C., Ntziachristos, V. & Jaffer, F. A. Intravascular near-infrared fluorescence molecular imaging of atherosclerosis: toward coronary arterial visualization of biologically high-risk plaques. *Journal of Biomedical Optics* **15**, 011107, (2010).
- 267 Jaffer, F. A. *et al.* Two-dimensional intravascular near-infrared fluorescence molecular imaging of inflammation in atherosclerosis and stent-induced vascular injury. *Journal of the American College of Cardiology* **57**, 2516-2526, (2011).
- 268 Jaffer, F. A. *et al.* Real-time catheter molecular sensing of inflammation in proteolytically active atherosclerosis. *Circulation* **118**, 1802-1809, (2008).
- 269 Marcu, L., Fishbein, M. C., Maarek, J. M. & Grundfest, W. S. Discrimination of Human Coronary Artery Atherosclerotic Lipid-Rich Lesions by Time-Resolved Laser-Induced Fluorescence Spectroscopy. *Arteriosclerosis, Thrombosis, and Vascular Biology* **21**, 1244-1250, (2001).
- 270 Jansen, K., van der Steen, A. F. W., van Beusekom, H. M. M., Oosterhuis, J. W. & van Soest, G. Intravascular photoacoustic imaging of human coronary atherosclerosis. *Optics Letters* **36**, 597-599, (2011).
- 271 Weissleder, R., Tung, C. H., Mahmood, U. & Bogdanov, A. In vivo imaging of tumors with protease-activated near-infrared fluorescent probes. *Nature Biotechnology* **17**, 375-378, (1999).
- 272 Jaffer, F. A. & Weissleder, R. Molecular Imaging in the Clinical Arena. *Journal of the American Medical Association* **293**, 855-862, (2005).
- 273 Jaffer, F. A., Libby, P. & Weissleder, R. Molecular and cellular imaging of atherosclerosis: emerging applications. *Journal of the American College of Cardiology* **47**, 1328-1338, (2006).

- 274 Warren, S. *et al.* Combined Ultrasound and Fluorescence Spectroscopy for Physico-Chemical Imaging of Atherosclerosis. *IEEE Transactions on Biomedical Engineering* **42**, 121-132, (1995).
- 275 Stephens, D. N., Park, J., Sun, Y., Papaioannou, T. & Marcu, L. Intraluminal fluorescence spectroscopy catheter with ultrasound guidance. *Journal of Biomedical Optics* **14**, 030505, (2011).
- 276 Liang, S. *et al.* Intravascular atherosclerotic imaging with combined fluorescence and optical coherence tomography probe based on a double-clad fiber combiner. *Journal of Biomedical Optics* **17**, 070501, (2012).
- 277 Twersky, V. Interface Effects in Multiple Scattering by Large, Low-Refracting, Absorbing Particles. *Journal of the Optical Society of America* **60**, 908, (1970).
- 278 Twersky, V. Absorption and Multiple Scattering by Biological Suspensions. *Journal of the Optical Society of America* **60**, 1084-1093, (1970).
- 279 Anderson, N. M. & Sekelj, P. Light-absorbing and scattering properties of non-haemolysed blood. *Physics in Medicine and Biology* **12**, 173-184, (1967).
- 280 Steinke, J. M. & Shepherd, a. P. Diffusion model of the optical absorbance of whole blood. *Journal of the Optical Society of America. A, Optics and image science* **5**, 813-822, (1988).
- 281 Steinke, J. M. & Shepherd, A. P. Role of Light Scattering in Whole Blood Oximetry. *IEEE Transactions on Biomedical Engineering* **BME-33**, 294-301, (1986).
- 282 Cope, M. *The application of near infrared spectroscopy to non invasive monitoring of cerebral oxygenation in the newborn infant*, University College London, (1991).
- 283 Wu, J., Feld, M. S. & Rava, R. P. Analytical model for extracting intrinsic fluorescence in turbid media. *Applied optics* **32**, 3585-3595, (1993).
- 284 Ishimaru, a. Diffusion of light in turbid material. *Applied optics* **28**, 2210-2215, (1989).
- 285 Chang, S. K., Arifler, D., Drezek, R., Follen, M. & Richards-Kortum, R. Analytical model to describe fluorescence spectra of normal and preneoplastic epithelial tissue: comparison with Monte Carlo simulations and clinical measurements. *Journal of Biomedical Optics* **9**, 511-522, (2004).
- 286 Diamond, K. R., Farrell, T. J. & Patterson, M. S. Measurement of fluorophore concentrations and fluorescence quantum yield in tissue-simulating phantoms using three

- diffusion models of steady-state spatially resolved fluorescence. *Physics in medicine and biology* **48**, 4135-4149, (2003).
- 287 Cook, J. R., Bouchard, R. R. & Emelianov, S. Y. Tissue-mimicking phantoms for
photoacoustic and ultrasonic imaging. *Biomedical Optics Express* **2**, 3193-3206, (2011).
- 288 Keijzer, M., Richards-Kortum, R. R., Jacques, S. L. & Feld, M. S. Fluorescence
spectroscopy of turbid media: Autofluorescence of the human aorta. *Applied Optics* **28**,
4286, (1989).
- 289 Alvarez, L., Lions, P.-L. & Morel, J.-M. Image Selective Smoothing and Edge Detection
by Nonlinear Diffusion. II. *SIAM Journal on Numerical Analysis* **29**, 845-866, (1992).
- 290 Chenyang, X. & Prince, J. L. Gradient vector flow: a new external force for snakes.
*Proceedings of IEEE Computer Society Conference on Computer Vision and Pattern
Recognition* **2**, 66-71, (1997).
- 291 Patil, A. V., Rychak, J. J., Klibanov, A. L. & Hossack, J. A. A real-time technique for
improving molecular imaging and guiding drug delivery in large blood vessels: in vitro and
ex vivo results. *Molecular Imaging* **10**, 238-247, (2011).
- 292 Li, Y. *et al.* Direct labeling and visualization of blood vessels with lipophilic carbocyanine
dye DiI. *Nature protocols* **3**, 1703-1708, (2008).
- 293 Mallas, G. *et al.* Progress on multimodal molecular / anatomical intravascular imaging of
coronary vessels combining near infrared fluorescence and ultrasound. *IEEE EMBS
Proceedings* **2011**, 1117-1120, (2011).
- 294 Diamond, K. R., Patterson, M. S. & Farrell, T. J. Quantification of Fluorophore
Concentration in Tissue-Simulating Media by Fluorescence Measurements with a Single
Optical Fiber. *Applied Optics* **42**, 2436-2442, (2003).
- 295 Roggan, A., Friebel, M., Dörschel, K., Hahn, A. & Müller, G. Optical Properties of
Circulating Human Blood in the Wavelength Range 400–2500 nm. *Journal of Biomedical
Optics* **4**, 36, (1999).
- 296 Meinke, M., Müller, G., Helfmann, J. & Friebel, M. Optical properties of platelets and
blood plasma and their influence on the optical behavior of whole blood in the visible to
near infrared wavelength range. *Journal of Biomedical Optics* **12**, 014024, (2007).

- 297 van Soest, G. *et al.* Atherosclerotic tissue characterization in vivo by optical coherence tomography attenuation imaging. *Journal of Biomedical Optics* **15**, 011105-011101–011109.
- 298 Upadhyay, R., Sheth, R. A., Weissleder, R. & Mahmood, U. Quantitative real-time catheter-based fluorescence molecular imaging in mice. *Radiology* **245**, 523-531, (2007).
- 299 Sheth, R. A., Tam, J. M., Maricevich, M. A., Josephson, L. & Mahmood, U. Quantitative Endovascular Fluorescence-based Molecular Imaging through Blood of Arterial Wall Inflammation. *Radiology* **251**, 813-821, (2009).
- 300 Valdés, P. A. *et al.* Quantitative, spectrally-resolved intraoperative fluorescence imaging. *Sci. Rep.* **2**, 798, (2012).
- 301 Valdés, P. A. *et al.* Quantitative fluorescence in intracranial tumor: implications for ALA-induced PpIX as an intraoperative biomarker. *J Neurosurg* **115**, 11-17, (2011).
- 302 Saager, R. B., Cuccia, D. J., Saggese, S., Kelly, K. M. & Durkin, A. J. Quantitative fluorescence imaging of protoporphyrin IX through determination of tissue optical properties in the spatial frequency domain. *Journal of biomedical optics* **16**, 126013, (2011).
- 303 Bradley, R. S. & Thorniley, M. S. A review of attenuation correction techniques for tissue fluorescence. *Journal of the Royal Society, Interface / the Royal Society* **3**, 1-13, (2006).
- 304 Hyde, D. E., Farrell, T. J., Patterson, M. S. & Wilson, B. C. A diffusion theory model of spatially resolved fluorescence from depth-dependent fluorophore concentrations. *Physics in Medicine and Biology* **46**, 369-383, (2001).
- 305 Hull, E. *et al.* Noninvasive, optical detection of diabetes: model studies with porcine skin. *Optics express* **12**, 4496-4510, (2004).
- 306 Fujimoto, J. G. *et al.* High resolution in vivo intra-arterial imaging with optical coherence tomography. *Heart* **82**, 128-133, (1999).
- 307 Tuzcu, E. M., Bayturan, O. & Kapadia, S. Invasive imaging: Coronary intravascular ultrasound: a closer view. *Heart (British Cardiac Society)* **96**, 1318-1324, (2010).
- 308 Bardin, D. *et al.* High-speed, clinical-scale microfluidic generation of stable phase-change droplets for gas embolotherapy. *Lab on a Chip* **11**, 3990-3998, (2011).
- 309 Martz, T. D., Bardin, D., Sheeran, P. S., Lee, A. P. & Dayton, P. A. Microfluidic Generation of Acoustically Active Nanodroplets. *Small* **8**, 1876-1879, (2012).

- 310 Sheeran, P. S., Luo, S. H., Mullin, L. B., Matsunaga, T. O. & Dayton, P. a. Design of ultrasonically-activatable nanoparticles using low boiling point perfluorocarbons. *Biomaterials* **33**, 3262-3269, (2012).
- 311 Sheeran, P. S., Matsunaga, T. O. & Dayton, P. A. Phase change events of volatile liquid perfluorocarbon contrast agents produce unique acoustic signatures. *Physics in Medicine and Biology* **59**, 379, (2014).
- 312 Kripfgans, O. D., Fowlkes, J. B., Miller, D. L., Eldevik, O. P. & Carson, P. L. Acoustic Droplet Vaporization For Therapeutic and Diagnostic Applications. *Ultrasound in Med. & Biol.* **26**, 1177-1189, (2000).
- 313 Matsunaga, T. O. *et al.* Phase-Change Nanoparticles Using Highly Volatile Perfluorocarbons: Toward a Platform for Extravascular Ultrasound Imaging. *Theranostics* **2**, 1185-1198, (2012).
- 314 Lee, J. Y. *et al.* Nanoparticle-Loaded Protein–Polymer Nanodroplets for Improved Stability and Conversion Efficiency in Ultrasound Imaging and Drug Delivery. *Advanced Materials* **27**, 5484-5492, (2015).
- 315 Borkent, B. M., Gekle, S., Prosperetti, A. & Lohse, D. Nucleation threshold and deactivation mechanisms of nanoscopic cavitation nuclei. *Physics of Fluids* **21**, (2009).
- 316 Pu, G., Borden, M. A. & Longo, M. L. Collapse and Shedding Transitions in Binary Lipid Monolayers Coating Microbubbles. *Langmuir* **22**, 2993-2999, (2006).
- 317 Kang, S.-T. & Yeh, C.-K. Intracellular acoustic droplet vaporization in a single peritoneal macrophage for drug delivery applications. *Langmuir : the ACS journal of surfaces and colloids* **27**, 13183-13188, (2011).
- 318 Holland, C. K. & Apfel, R. E. Thresholds for transient cavitation produced by pulsed ultrasound in a controlled nuclei environment. *The Journal of the Acoustical Society of America* **88**, (1990).
- 319 Yildirim, A., Budunoglu, H., Daglar, B., Deniz, H. & Bayindir, M. One-Pot Preparation of Fluorinated Mesoporous Silica Nanoparticles for Liquid Marble Formation and Superhydrophobic Surfaces. *ACS Appl. Mater. Interfaces* **3**, 1804-1808, (2011).